Karlsruhe Series in Photonics & Communications, Vol. 24

Tobias Harter

Wireless THz Communications: Optoelectronic Devices and Signal Processing

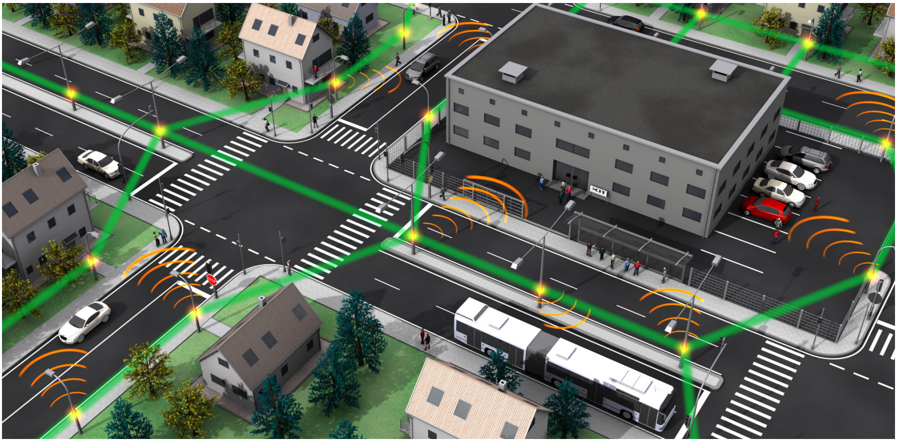

KIT Scientific Publishing

Tobias Harter

Wireless Terahertz Communications: Optoelectronic Devices and Signal Processing

Karlsruhe Series in Photonics & Communications, Vol. 24
Edited by Profs. C. Koos, W. Freude and S. Randel

Karlsruhe Institute of Technology (KIT)
Institute of Photonics and Quantum Electronics (IPQ)
Germany

Wireless Terahertz Communications: Optoelectronic Devices and Signal Processing

by
Tobias Harter

KIT Scientific Publishing

Karlsruher Institut für Technologie
Institut für Photonik und Quantenelektronik

Wireless Terahertz Communications:
Optoelectronic Devices and Signal Processing

Zur Erlangung des akademischen Grades eines Doktor-Ingenieurs
von der KIT-Fakultät für Elektrotechnik und Informationstechnik des
Karlsruher Instituts für Technologie (KIT) genehmigte Dissertation

von Tobias Harter, M.Sc.

Mündliche Prüfung: 28. November 2019
Hauptreferent: Prof. Dr. Christian Koos
Korreferenten: Prof. Dr. Dr. h. c. Wolfgang Freude
Prof. Dr. Guillermo Carpintero-del-Barrio

Impressum

KIT Scientific
Publishing

Karlsruher Institut für Technologie (KIT)
KIT Scientific Publishing
Straße am Forum 2
D-76131 Karlsruhe

www.ksp.kit.edu

Print on Demand 2021 – Gedruckt auf FSC-zertifiziertem Papier

ISSN 1865-1100
ISBN 978-3-7315-1083-3
DOI 10.5445/KSP/1000128941

Table of Contents

Kurzfassung

Telekommunikation ist ein Grundpfeiler der heutigen Informationsgesellschaft und hat signifikanten Einfluss auf alle Bereiche des sozialen Lebens. Der stetig ansteigende Bedarf an Vernetzung erfordert eine digitale Infrastruktur, mit welcher hohe Übertragungsraten erzielt werden können. Durch die Verwendung von Lichtwellenleitern können heutzutage große Datenraten übertragen werden. Diese optischen Netzwerke werden durch flexible Funknetzwerke ergänzt. Da herkömmliche kabellose Verbindungen jedoch lediglich Trägerfrequenzen im Gigahertz-Bereich einsetzen, sind die übertragbaren Datenraten wesentlich geringer als bei optischen Lichtwellenleitern und führen somit zu einem Engpass im Gesamtnetzwerk. Eine mögliche Lösung hierfür ist die Verwendung von Trägerfrequenzen im Terahertz-Bereich von 0.1 THz bis 1 THz, sogenannte T-Wellen. Ihr entscheidender Vorteil: Auf Grund ihrer hohen Trägerfrequenz können größere Bandbreiten genutzt und dadurch die Übertragungsraten bedeutend erhöht werden. Des Weiteren ist die atmosphärische T-Wellen-Dämpfung noch immer gering genug, um Signale über einige hundert Meter übertragen zu können. Tatsächlich wurden in Laborexperimenten Datenraten von über 100 Gbit/s gemessen. Um Systeme für die THz-Kommunikation jedoch noch flexibler, ökonomischer und weniger komplex zu gestalten, werden neuartige Ansätze sowohl auf Bauteilebene als auch im Hinblick auf die zugrundeliegenden Signalverarbeitungsverfahren benötigt.

Da sich das Spektrum der T-Wellen im Bereich zwischen Mikrowellen (elektrisch) und dem nahen Infrarot (optisch) befindet, ermöglichen es innovative T-Wellen-Systeme, die Stärken der elektrischen und optischen Signalverarbeitung vorteilhaft miteinander zu verbinden. Als besonders nützlich für die T-Wellen-Kommunikation haben sich optoelektronische T-Wellen-Sender erwiesen, mit denen Rekord-Datenraten erzielt wurden. Auf der Empfänger-Seite konnten die Vorzüge der optoelektronischen Signalverarbeitung bisher jedoch noch nicht gezeigt werden. Neben einer effizienten Umwandlung der Signale zwischen den unterschiedlichen Frequenzbereichen ist es zudem entscheidend, dass die Bauteile auf Halbleiter-Chips integriert

werden können, einen geringen Leistungsverbrauch aufweisen und sich kostengünstig in großen Stückzahlen herstellen lassen.

In der vorliegenden Arbeit werden unterschiedliche Ansätze diskutiert, mit denen sich die Leistungsfähigkeit von T-Wellen-Systemen erhöhen lässt. Dies umfasst sowohl neuartige Bauteil-Technologien für Sende- und Empfangssysteme als auch neuartige Signalverarbeitungstechniken und Systemkonzepte. Die technische Tragfähigkeit der untersuchten Ansätze wurde in einer Reihe von Experimenten unter Beweis gestellt. Teile dieser Arbeit wurden in den internationalen Fachzeitschriften *Nature Photonics* und *Optica* veröffentlicht [J2]-[J4].

In *Kapitel 1* wird eine allgemeine Einführung in das Gebiet der T-Wellen-Kommunikation gegeben und die Limitierung aktuell existierender T-Wellen-Systeme aufgezeigt.

Kapitel 2 führt die fachlichen Grundlagen der T-Wellen-Kommunikation sowie verschiedener Sender- und Empfänger-Technologien ein. Die Termini Basisband- und Bandpass-Signal werden definiert, und es werden die Grundsätze der digitalen Kommunikation sowie die Besonderheiten des T-Wellen-Kanals erörtert. Die darauffolgenden Abschnitte zeigen aktuell verwendete T-Wellen-Sender und -Empfänger, die elektrische oder optische Methoden verwenden. Das Kapitel endet mit einem Vergleich zwischen den Erfolgen dieser Arbeit und dem Stand der Technik der T-Wellen-Kommunikation.

Kapitel 3 zeigt, wie ein Hüllkurvendetektor in Verbindung mit digitaler Signalverarbeitung dazu verwendet werden kann, ein in Amplitude und Phase moduliertes Datensignal zu empfangen. Dazu wird der sogenannte Kramers-Kronig-Empfänger, der ursprünglich für die optische Kommunikation über Glasfasern entwickelt wurde, an die T-Wellen-Kommunikation angepasst. Die Qualität des empfangenen Signals kann dabei erheblich verbessert werden, indem die Nichtidealität des Hüllkurvendetektors mithilfe digitaler Signalverarbeitung kompensiert wird. Mit diesem angepassten Kramers-Kronig-Empfänger konnte die erste THz-Verbindung mit einer Datenrate von mehr als 100 Gbit/s über eine Entfernung von mehr als 100 m demonstriert werden.

Kapitel 4 zeigt, dass optoelektronische Signalverarbeitung nicht nur am T-Wellen-Sender, sondern auch am T-Wellen-Empfänger bedeutende Vorteile bietet. Zum ersten Mal wird in einem Kommunikations-Experiment ein durchstimmbarer optoelektronischer T-Wellen-Sender mit einem durchstimmbaren optoelektronischen Empfänger ergänzt. Diese Kombination erhöht die Flexibilität des Systems erheblich, da die bisher verwendeten elektronischen T-Wellen-Sender und -Empfänger jeweils für eine bestimmte Trägerfrequenz optimiert werden mussten. In dieser Arbeit wird gezeigt, dass der optische Empfänger über einen Frequenzbereich von 0.03 THz bis 0.34 THz, das heißt in einem Bereich von mehr als einer Dekade, abgestimmt werden kann.

Für die optoelektronische T-Wellen-Signalverarbeitung wurden bisher Bauelemente aus speziellen III-V-Verbindungshalbleitern benötigt. In *Kapitel 5* wird ein neuartiger Ansatz gezeigt, der es erlaubt, optoelektronische T-Wellen-Sender und -Empfänger auf der Silizium-Plattform zu integrieren. Dadurch lassen sich kompakte T-Wellen-Systeme auf einem Chip herstellen, die alle Vorteile der skalierbaren Silizium-Photonik nutzen können. Um das Konzept zu demonstrieren, verwenden wir integrierte T-Wellen-Sender und -Empfänger und messen die frequenzabhängige komplexe Impedanz von T-Wellen-Leitungen in einem Frequenzbereich von 0.05 THz bis 0.8 THz.

Kapitel 6 fasst die Arbeit zusammen, gibt einen Ausblick auf weitere Möglichkeiten, T-Wellen-Systeme für die drahtlose Kommunikation zu verbessern, und führt zusätzliche Anwendungsgebiete an.

Preface

Data transmission at carrier frequencies between 0.1 THz and 1 THz (T-waves) has the potential to overcome the current limitations of wireless networks. The large carrier frequencies provide large data bandwidths, while the atmospheric attenuation is still sufficiently low. In laboratory experiments, data rates of more than 100 Gbit/s have already been shown. Widespread deployment of T-wave links in real systems, however, still requires novel signal processing schemes and device concepts that reduce the footprint, cost, and energy consumption of T-wave systems. T-waves occupy the spectral range between microwaves and near infrared. Advanced T-wave systems therefore allow to combine the advantages of both electronic and photonic signal processing schemes. In this context, efficient signal conversion between the various frequency ranges is essential. These goals are accomplished by chip-scale systems with low power consumption that can be realized in large quantities at low cost. Optoelectronic T-wave signal generation is already utilized in T-wave communication links and enabled record-high data rates. On the receiver side, the advantages of optoelectronic signal processing could not be shown yet.

This work addresses various approaches to enhance the performance of T-wave systems. We show novel signal processing concepts and investigate novel optoelectronic devices for T-wave transmitters and receivers. The viability of our systems is confirmed by data transmission experiments. Parts of this thesis has been published in the international journals *Nature Photonics* und *Optica* [J2]-[J4].

In *Chapter 1*, a general introduction to the topic of T-wave communications is given, and the limitations of current T-wave systems are pointed out.

Chapter 2 discusses the fundamentals of wireless T-wave communication systems and gives an overview of existing transmitter and receiver technologies. The terms baseband and bandpass signals are defined, and the principles of digital communications as well as the special properties of a T-wave channel are shown. In the subsequent sections, current T-wave transmitters and receivers using electronic or photonic methods are outlined. The chapter ends by comparing the achievements in this work with the present state of T-wave communications.

Chapter 3 demonstrates how a simple THz envelope detector in combination with advanced digital signal processing can be used to receive amplitude- and phase-modulated data signals. To this end, the so-called Kramers-Kronig receiver concept, originally developed in the context of fibre-optic communication, is adapted to T-wave communications. The quality of the received signal is drastically enhanced by accounting for the measured characteristics of the envelope detector. Using this receiver scheme, record-high data rates of 115 Gbit/s are wirelessly transmitted over a distance of 110 m at a carrier frequency of 0.3 THz.

Chapter 4 shows that optoelectronic signal processing is not only beneficial for T-wave signal generation but also for T-wave reception. For the first time, a tunable optoelectronic T-wave transmitter is complemented with a tunable optoelectronic receiver in a T-wave communication link. This enhances the flexibility compared to electronic receivers, which need to be optimized for a certain T-wave carrier frequency. In this work, the same optoelectronic receiver is used in a frequency range from 0.03 THz to 0.34 THz, i.e., a range of more than a decade. At a carrier frequency of 0.3 THz, a line rate of 30 Gbit/s is transmitted over a distance of 58 m.

So far, current optoelectronic T-wave signal processing techniques require devices made from special III-V semiconductors. *Chapter 5* introduces plasmonic internal-photoemission detectors (PIPEDs) which can be integrated on silicon allowing the exploitation of all the advantages of the highly-developed silicon-photonic platform. PIPEDs can be used as optoelectronic T-wave transmitters and receivers, and they enable compact T-wave systems on a single silicon chip. In a proof-of-principle experiment, we use a T-wave transmitter and a receiver for measuring various co-integrated T-wave transmission lines.

Chapter 6 summarizes this work, provides an outlook on possible enhancements of T-wave communication systems, and shows additional applications.

Achievements of the present work

In this thesis, novel device concepts and signal processing schemes for T-wave communications are presented. Advanced T-wave systems are discussed which combine electronic methods with optoelectronic and digital signal processing. Thereby, record-high data rates are demonstrated, while the complexity of the receiver hardware can be significantly reduced. Furthermore, a T-wave communication system using an optoelectronic receiver and a photonic local oscillator is shown. Moreover, we propose a new kind of T-wave transmitter and receiver, which can be integrated on the silicon platform. This allows to monolithically co-integrate T-wave devices with advanced silicon photonic circuits.

In the following, an overview of the achievements of this work is given:

First demonstration of a Kramers-Kronig receiver in a wireless T-wave communication experiment: We show coherent data transmission on a T-wave carrier using a Schottky-barrier diode as an envelope detector together with a generalized version of a Kramers-Kronig phase reconstruction. The work has been published in Nature Photonics [J4].

Wireless T-wave transmission over more than 100 m with a record-high data rate: Using the Kramers-Kronig receiver scheme, a net data rate of 115 Gbit/s is demonstrated, which is the highest data rate achieved with a T-wave transmission link that spans more than 100 m. This result is also part of the previously mentioned publication [J4].

First T-wave communication system with optoelectronic downconversion at the receiver: A T-wave link with optoelectronic signal processing both at the transmitter and at the receiver side is demonstrated for the first time. We show that the wireless T-wave receiver benefits greatly from optoelectronic signal processing techniques, especially if wideband tunability and large carrier frequencies are required. In a proof-of-principle demonstration we were able to transmit up to 30 Gbit/s over a distance of 58 m. The work has been published in Optica [J3].

First optoelectronic T-wave generation and downconversion on the silicon platform: A novel class of ultra-fast photodetectors that exploit internal photoemission at a metal-semiconductor interface is investigated for signal generation and coherent detection of T-waves. The transmitter and the receiver are characterized over a broad range of frequencies from 0.05 THz to 1 THz. These devices allow T-wave signal processing on the silicon platform, offering the possibility of co-integrating monolithic T-wave components with the full portfolio of silicon photonic devices. The work has been published in Nature Photonics [J2].

Demonstration of integrated T-wave systems: Integrated T-wave systems which combine T-wave transmitters and receivers on the silicon platform are demonstrated. With these systems, on-chip transmission lines are characterized over a broad frequency range from 0.05 THz to 0.8 THz. This result is also part of the previously mentioned publication in Nature Photonics [J2].

1 Introduction

Powerful communication systems are the backbone of modern society, in which ubiquitous access to information has become a matter of course. The number of devices connected to communication networks is rapidly increasing and already today exceeds the global population [1]. This leads to an explosive growth of the overall internet traffic and especially of the wireless data traffic, which is currently doubling every 22 months. By 2022, wireless traffic will account for more than 70 % of the overall internet traffic [1]. Sustaining this growth requires a dense mesh of small radio cells to guarantee to each user a broadband service. Connecting these small cells efficiently, however, is still challenging and should be done with high-speed wireless links. For providing the necessary bandwidth for these connections, high carrier frequencies in the range from 0.1 THz to 1 THz (so-called T-waves) could be used. T-wave links offer data rates beyond 100 Gbit/s, while the atmospheric attenuation is small enough to bridge transmission distances of hundreds of meters. Implementation of free-space T-wave links in future networks requires novel concepts for compact, energy-efficient, and inexpensive transmitters and receivers, which can be easily interconnected with fibre-optic transmission links. To achieve high data rates, spectrally efficient modulation formats are required that encode information on both the amplitude and the phase of a carrier. In this context, optoelectronic technologies have emerged as a particular attractive solution to process high-speed T-wave signals. Over the previous years, record-high data rates have been demonstrated in a series of experiments in which high-quality T-wave signals were generated by photomixing. For the detection of these signals, however, the benefits of optoelectronic signal processing have not been demonstrated so far.

This thesis addresses novel device concepts and signal processing schemes for T-wave communications. By combining photonic, electronic and digital signal processing, powerful T-wave transmitters and receivers are demonstrated. A coherent receiver with greatly reduced complexity is shown. The receiver requires simply a single Schottky-barrier diode (SBD) as an envelope detector, followed by digital signal processing (DSP) to recover the phase information of the T-wave data signal. This receiver is adapted from the Kramers-Kronig (KK) receiver originally developed for optical communications. Here we demonstrate for the first time that KK receivers can be used also for T-wave communications. We account for the measured nonlinear characteristics of the SBD and transmit record-high net data rates of 115 Gbit/s over a free-space distance of 110 m. This is the highest data rate which has so far been transmitted over more than 100 m at T-wave carrier frequencies.

The KK receiver relies on a self-coherent approach, where the local oscillator (LO) is transmitted along with the data signal, thus allowing to greatly simplify the receiver hardware. However, if the overall transmit power is limited, the power in the data signal is reduced, because a strong LO needs to be sent along with the data signal. As an alternative, we investigate a coherent receiver where we use a photoconductor driven by a photonic LO for downconversion of the T-wave signal to an intermediate-frequency (IF) band. The arrangement replaces costly fixed-frequency electronic LO and electronic mixers. This type of receiver with photonic LO features advantages such as the ability to downconvert high carrier frequencies of hundreds of GHz, and to tune the LO frequency over more than a decade. In a proof-of-principle demonstration, we show wireless data transmission at line rates up to 30 Gbit/s over a distance of 58 m.

While these experiments represent a first demonstration of high-speed wireless communication links with optoelectronic T-wave transmitters and receivers, the associated devices still rely on special III-V semiconductors. This prevents a co-integration of the transmitters and the receivers, and it impedes advanced T-wave systems that combine photonic signal processing with optoelectronic frequency conversion on a common chip. To overcome this problem, we investigate optoelectronic T-wave transmitters and receivers which can be directly integrated on silicon, allowing to exploit the opportunities of the silicon platform. We develop plasmonic internal-photoemission detectors (PIPEDs) which can be used as T-wave transmitters and as T-wave receivers. If the newly developed PIPEDs are used as receivers, they already show a similar performance as the well-developed III-V receivers. Possibilities for further optimizations are suggested in this work. If the PIPEDs are used as transmitters, the T-wave output power is inferior to the one of III-V uni-travelling carrier photodiodes (UTC-PD). However, our silicon-based approach allows the co-integration of a T-wave transmitter and a receiver in form of a transceiver, and on-chip T-wave signal processing enables new applications where small T-wave power suffice. In a proof-of-principle experiment, T-wave transmitters are combined with T-wave receivers on a single silicon chip. We measure the frequency-dependent characteristics of interconnecting T-wave transmission lines in a frequency range between 0.05 THz and 0.8 THz.

The experimental results in this work demonstrate the potential of advanced T-wave systems which combine electronics with photonics and digital signal processing.

2 THz communications and devices

This chapter introduces the fundamentals of T-wave communications and the associated basic devices. Furthermore, an overview of the recently published experimental demonstrations are given, and are compared in terms of data rates and transmission distances with the results from this work.

T-waves as defined here are electromagnetic waves with frequencies ranging from 0.1 THz to 1 THz. This frequency range is particularly interesting for wireless communications. Due to the high carrier frequency, large data rates can be achieved even with moderate relative bandwidths and moderate spectral efficiencies. T-waves are located in the so-called terahertz (THz) range, which is commonly defined [2] as the frequency regime between 0.1 THz and 10 THz, connecting the microwave and the optical regions. Depending on the definition also frequencies of up to 30 THz might be included [3,4]. For simplicity, the terms THz and T-waves are used interchangeably in this work. Figure 2.1 illustrates the position of the THz range in the electromagnetic spectrum. The THz region could not be accessed for a long time because electronic devices were not fast enough to process these high frequencies. At the same time, the energy of THz photons is too small to use conventional devices with band-to-band transitions as sources and detectors. In the last decades, the progress in electronics and in photonics made it possible to close the gap. In analogy to the

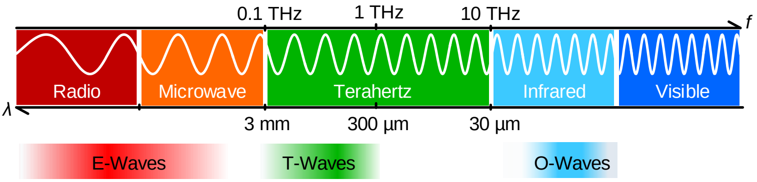

Figure 2.1: Electromagnetic spectrum. The terahertz (THz) region is located between the microwave region and the infrared region. For wireless communications, the lower THz region is very promising because the atmospheric attenuation is still reasonably small while the high carrier frequencies allow transmitting large data rates. We refer to the signals with spectral components in the frequency range from 0.1 THz to 1 THz as *T-waves*. Similarly, *E-waves* are defined for frequencies below 100 GHz, and *O-waves* with frequencies in the range from 190 THz to 250 THz.

definition of *T-waves*, we define the term *E-waves* if the signals have frequencies below 100 GHz, which is typically the case for baseband signals. Moreover, we define *O-waves* as optical waves that are suitable for glass fibre transmission with frequencies in the range of 190 THz and 250 THz.

2.1 Fundamentals of T-wave communications

Figure 2.2 illustrates a schematic of a T-wave communication system. The information source often contains low-frequency components, which does not match the requirements of the communication channel. Therefore, the signal needs to be upconverted at the transmitter (Tx) and downconverted at the receiver (Rx) for recovering the original signal. In this work, T-wave carrier frequencies are used to transmit the data over the communication channel.

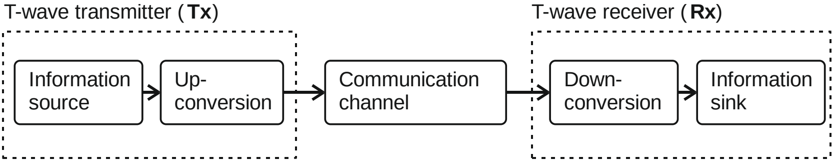

Figure 2.2: Schematic of a T-wave communication system. At the T-wave transmitter (Tx), the information signal is upconverted to T-wave frequencies to match the frequency characteristics of the T-wave communication channel. At the T-wave receiver (Rx), the signal is downconverted to recover the information.

2.1.1 Baseband and bandpass signals

The spectrum of an information signal is typically located around the frequency zero and is called baseband or lowpass signal [5]. In general, all physical signals are real-valued. However, it is convenient to define a complex baseband signal $\underline{s}(t)$ having a real in-phase component $s_\mathrm{I}(t)$ and a real quadrature component $s_\mathrm{Q}(t)$, or, equivalently, a real amplitude $A(t)$ and a real phase $\varphi(t)$,

$$\underline{s}(t) = s_\mathrm{I}(t) + \mathrm{j}s_\mathrm{Q}(t) = A(t)\mathrm{e}^{\mathrm{j}\varphi(t)}, \tag{2.1}$$

where both descriptions are related by

$$A(t)=\sqrt{s_{\mathrm{I}}^2(t)+s_{\mathrm{Q}}^2(t)}, \qquad \varphi(t)=\operatorname{Arg}\left(\underline{s}(t)\right). \tag{2.2}$$

It is assumed that the complex baseband signal spans a frequency region from $[-B,+B]$ and is zero for all other frequencies. For upconversion, the complex baseband signal is mixed with a complex carrier $\exp\left(\mathrm{j}2\pi f_0 t\right)$ at frequency f_0 with $f_0 > B$. The upconverted complex signal $\underline{s}(t)\exp\left(\mathrm{j}2\pi f_0 t\right)$ is a bandpass signal and occupies a spectral region $[f_0 - B,\ f_0 + B]$.

The physical reality, e.g., an electric field $E(t)$, is described by the real part $\Re\left\{\underline{s}(t)\exp\left(\mathrm{j}2\pi f_0 t\right)\right\}$ of the multiplication of the slowly varying complex baseband amplitude $\underline{s}(t)$ and the fast oscillating carrier at frequency f_0,

$$\begin{aligned} E(t) &= \Re\left\{\underline{s}(t)\mathrm{e}^{\mathrm{j}2\pi f_0 t}\right\} = \Re\left\{s_{\mathrm{I}}(t)\mathrm{e}^{\mathrm{j}2\pi f_0 t} + \mathrm{j}s_{\mathrm{Q}}(t)\mathrm{e}^{\mathrm{j}2\pi f_0 t}\right\} \\ &= s_{\mathrm{I}}(t)\cos\left(2\pi f_0 t\right) - s_{\mathrm{Q}}(t)\sin\left(2\pi f_0 t\right). \end{aligned} \tag{2.3}$$

Equation (2.3) explains the naming “in-phase” and “quadrature”, because with reference to $\cos\left(2\pi f_0 t\right)$ the real part $s_{\mathrm{I}}(t)$ is in phase, while the imaginary part is out of phase by 90°, i.e., in quadrature. In practice, the upconversion of a complex signal can be obtained by an in-phase/quadrature phase (IQ) mixer. The block diagram of an IQ-mixer is shown in Figure 2.3a. The in-phase component $s_{\mathrm{I}}(t)$ of the complex baseband signal is mixed with the carrier at frequency f_0, and the quadrature component $s_{\mathrm{Q}}(t)$ is mixed with a 90°-phase-shifted copy of the carrier. The output signals of both mixers are subtracted to form the real bandpass signal $E(t)$.

To recover the complex baseband signal at the receiver, a similar technique is applied, see Figure 2.3b. The received real signal is first split and sent to two arms. The signal in one arm is multiplied by a LO, and the signal in the other arm is mixed with a 90°-phase-shifted version of the LO. The output $i_{\mathrm{I}}(t)$ of the upper arm and the output $i_{\mathrm{Q}}(t)$ of the lower arm are given by

$$\begin{aligned} i_{\mathrm{I}}(t) &= \left(s_{\mathrm{I}}(t)\cos\left(2\pi f_0 t\right) - s_{\mathrm{Q}}(t)\sin\left(2\pi f_0 t\right)\right)\cos\left(2\pi f_0 t\right) \\ &= s_{\mathrm{I}}(t)\left(\tfrac{1}{2} + \tfrac{1}{2}\cos\left(4\pi f_0 t\right)\right) - \tfrac{1}{2}s_{\mathrm{Q}}(t)\sin\left(4\pi f_0 t\right), \end{aligned} \tag{2.4}$$

$$\begin{aligned} i_{\mathrm{Q}}(t) &= -\left(s_{\mathrm{I}}(t)\cos(2\pi f_0 t) - s_{\mathrm{Q}}(t)\sin(2\pi f_0 t)\right)\sin(2\pi f_0 t) \\ &= -\tfrac{1}{2} s_{\mathrm{I}}(t)\sin(4\pi f_0 t) + s_{\mathrm{Q}}(t)\left(\tfrac{1}{2} - \tfrac{1}{2}\cos(4\pi f_0 t)\right). \end{aligned} \tag{2.5}$$

For simplicity, the amplitudes of the carrier and the LO are set to 1. After removing the carrier harmonics at $2f_0$, the in-phase $s_{\mathrm{I}}(t)$ and quadrature component $s_{\mathrm{Q}}(t)$ of the complex baseband signal are recovered. Note that the LO and the transmitter carrier must be locked in phase, which could be achieved by an analog phase lock loop. For free-running oscillators, the phase-locking is not given, but phase drifts can still be compensated with digital signal processing.

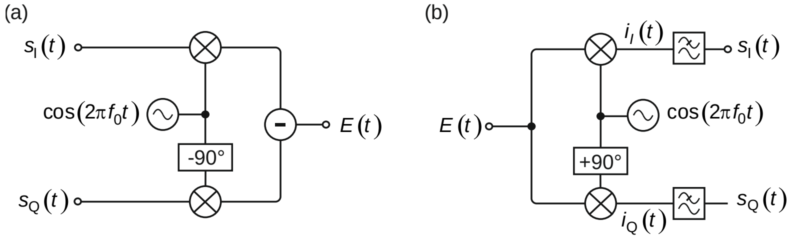

Figure 2.3: IQ mixer schematic. (a) IQ transmitter. The bandpass signal $E(t)$ is obtained by mixing the in-phase component $s_{\mathrm{I}}(t)$ with the carrier at frequency f_0, and the quadrature component $s_{\mathrm{Q}}(t)$ with a 90° phase-shifted copy of the carrier. Both mixer outputs are subtracted. **(b)** IQ receiver. To recover real and imaginary part of the complex baseband signal, the bandpass signal is split and sent to two arms. The signal in one arm is mixed with a local oscillator (LO) at f_0, and the signal in the other arm is mixed with a 90°-phase-shifted version of the LO. After lowpass filtering of the mixer outputs $i_{\mathrm{I}}(t)$ and $i_{\mathrm{Q}}(t)$, the in-phase component $s_{\mathrm{I}}(t)$ and the quadrature component $s_{\mathrm{Q}}(t)$ are recovered.

2.1.2 Mixer and balanced mixer

In Figure 2.3 mixing of two signals is illustrated by a cross symbol. In general, a mixer multiplies two quantities $s_{\mathrm{a}}(t)$ and $s_{\mathrm{b}}(t)$ to form the output signal $i(t)$. In a practical implementation of a mixer, a nonlinear interaction between the signals is required. This can be achieved by the multiplication of $s_{\mathrm{a}}(t)$ and $s_{\mathrm{b}}(t)$, which is called *multiplicative mixing*. Alternatively, the signals can first be added, and then a nonlinear operation can be applied. For a simple squaring operation, the mixer output $i(t)$ is given by

$$i(t) \propto \left[s_\mathrm{a}(t) + s_\mathrm{b}(t)\right]^2 = s_\mathrm{a}^2(t) + s_\mathrm{b}^2(t) + 2\underbrace{s_\mathrm{a}(t)s_\mathrm{b}(t)}_{\text{mixing}}, \tag{2.6}$$

and contains the mixing product of $s_\mathrm{a}(t)$ and $s_\mathrm{b}(t)$. This kind of mixing is called *additive mixing*. In comparison to the case of multiplicative mixing, the signals $s_\mathrm{a}(t)$ and $s_\mathrm{b}(t)$ are also multiplied with themselves. These product terms are called *signal-signal beat interference* (SSBI) and might affect the received signal. A balanced mixer as illustrated in Figure 2.4 eliminates the SSBI. In this case, a directional coupler combines $s_\mathrm{a}(t)$ and $s_\mathrm{b}(t)$, where both output ports of the directional coupler are used. By assuming a lossless coupler and a proper choice of the reference planes, the outputs of the coupler can be described by $\frac{1}{\sqrt{2}}\left[s_\mathrm{a}(t)+s_\mathrm{b}(t)\right]$ and $\frac{1}{\sqrt{2}}\left[s_\mathrm{a}(t)-s_\mathrm{b}(t)\right]$. The output signals $i_1(t)$ and $i_2(t)$ of the mixers are given by

$$i_{1,2}(t) \propto \tfrac{1}{2}\left[s_\mathrm{a}(t) \pm s_\mathrm{b}(t)\right]^2 = \tfrac{1}{2}s_\mathrm{a}^2(t) + \tfrac{1}{2}s_\mathrm{b}^2(t) \pm s_\mathrm{a}(t)s_\mathrm{b}(t). \tag{2.7}$$

After subtraction of the output signals $i_1(t)$ and $i_2(t)$, the SSBI from each of the mixers compensate, and the output $i(t)$ of the balanced mixer is given by

$$i(t) = i_1(t) - i_2(t) \propto 2s_\mathrm{a}(t)s_\mathrm{b}(t). \tag{2.8}$$

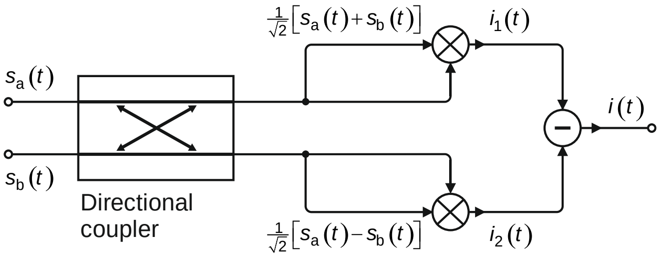

Figure 2.4: A balanced mixer reduces the effect of signal-signal beat interference (SSBI) which occurs in additive mixers. At the outputs of the directional coupler, the input signals $s_\mathrm{a}(t)$ and $s_\mathrm{b}(t)$ are superimposed with a phase difference of π. At the output ports this can be written as $\frac{1}{\sqrt{2}}\left[s_\mathrm{a}(t)+s_\mathrm{b}(t)\right]$ and $\frac{1}{\sqrt{2}}\left[s_\mathrm{a}(t)-s_\mathrm{b}(t)\right]$, if the reference planes are chosen properly. By subtracting the outputs $i_1(t)$ and $i_2(t)$ of both mixers, the SSBI-terms compensate each other, and the output $i(t) \propto 2s_\mathrm{a}(t)s_\mathrm{b}(t)$ contains only the product of $s_\mathrm{a}(t)$ and $s_\mathrm{b}(t)$.

Balanced mixers are often used in coherent receivers, where one of the input signals is the data and the other one the LO. If a high-power LO is used, the influence of the SSBI might be neglectable even with a single mixer but the balanced scheme still reduces the effect of relative intensity noise of the LO considerably.

For T-wave receivers, balanced mixers are complicated to realize because they require a LO at T-wave frequencies. An envelope detector where the LO is remotely provided by the transmitter could be easier to implement. In this case, however, the SSBI introduced at the receiver reduces the signal quality. One method to deal with SSBI is to make sure that their spectral regions are different from the ones of the signal, e.g. by using a guard band between the signal and the LO. This reduces the spectral efficiency and increases the bandwidth requirements of the components. In this work, we show that this problem can be overcome by using a T-wave Kramers-Kronig receiver, where a guard band is not required. Details can be found in Chapter 3. The photoconductive mixer and the PIPED mixer described in Chapter 4 and 5 establish multiplicative mixing so that SSBI does not occur.

2.1.3 Digital communications

In this work, we focus on digital communications where the information signal is encoded into a sequence of binary digits [5]. The binary information is mapped to one of *M* symbols of an alphabet. The symbols of the alphabet differ in amplitude, phase or in a combination of both and can be written in complex notation as $\underline{a}_k = a_{k,\mathrm{I}} + \mathrm{j}a_{k,\mathrm{Q}}$, where $k = 1, 2 \ldots M$. The rate at which different symbols are transmitted is called the symbol rate R_s and has the unit *Baud* (Bd) with $1\,\mathrm{Bd} = 1\,\mathrm{Symbol/s}$. The symbol duration T_s is given by $T_\mathrm{s} = 1/R_\mathrm{s}$. Each symbol can encode $\log_2 M$ bits of information. The rate R_b of transmitted bits per second is connected to the symbol rate by $R_\mathrm{b} = R_\mathrm{s} \log_2 M$.

The graphical representation of the in-phase component $a_{k,\mathrm{I}}$ and the quadrature component $a_{k,\mathrm{Q}}$ for all symbols of the alphabet is called a constellation diagram. The constellation diagrams for commonly used modulation formats are shown in Figure 2.5. The simplest modulation format is on-off keying (OOK), which is shown in Figure 2.5a. In this case, only the amplitude of the carrier is changed and only two states are allowed. This modulation format is also called two-level pulse amplitude modulation (2PAM). Typically, the amplitude of the carrier is varied by modulating the carrier power. The reception of these signals is especially simple because no information is encoded in the phase, and simple envelope detectors are sufficient. With each symbol, only 1 bit can be transmitted. The number of bits can be increased by using more amplitude levels, however the noise tolerance of the transmission is also reduced. If the modulation format contains four amplitude levels, it is called 4PAM and allows transmitting 2 bit per symbol. More advanced modulation formats use not only the in-phase component of the carrier but also the quadrature component. This is called quadrature amplitude modulation (QAM). Frequently, QAM signals with 4 phase states are used. In this case, the modulation format is also called quadrature phase-shift keying (QPSK), which allows transmitting 2 bit per symbol as shown in Figure 2.5b. The last example is a 16-state QAM signal, which is illustrated in Figure 2.5c and allows transmitting 4 bit per symbol. The number of bits per symbol could be further increased by using, e.g. 32QAM (5 bit/symbol) or 64QAM (6 bit/symbol).

The time-continuous complex baseband signal $\underline{s}(t)$ is obtained by multiplying the i^{th}-symbol $\underline{a}_{k,i}$ with the time-continuous pulse $p(t-iT_s)$ and summing over all symbols

$$\underline{s}(t)=\sum_{i=-\infty}^{+\infty}\underline{a}_{k,i}\,p(t-iT_s). \tag{2.9}$$

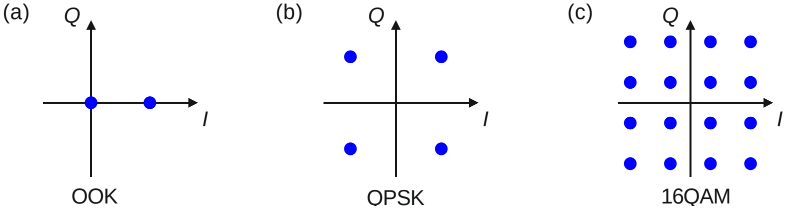

Figure 2.5: The constellation diagram shows all possible symbols of a certain digital modulation format. **(a)** For on-off keying (OOK), only the amplitude, or equivalently the intensity of the signal is varied. This modulation format has only two discrete levels and allows transmitting of 1 bit per symbol. **(b)** For quadrature phase-shift keying (QPSK) only the phase of the carrier is modulated. It allows to transmit 2 bit/symbol. **(c)** In 16-state quadrature amplitude modulation (16QAM) the amplitude and the phase are modulated, allowing to transmit 4 bits/symbol.

The pulses $p(t-iT_s)$ can be adjusted to shape the spectrum of the signal. This can be achieved by an analog waveform or in the digital domain by using a digital filter.

2.1.4 T-wave communication channel

Shannon's theoretical investigations [6] revealed an upper limit for the maximum capacity $\mathcal{C}$ (measured in bit/s) which can be reliably transmitted over a linear channel in the presence of noise. This limit can only be achieved by arbitrarily complex encoding schemes and arbitrarily complex error correction techniques for error-free transmission. Shannon assumed a Gaussian distributed signal with average signal power P_s and additive white Gaussian noise (AWGN) with power P_n. For a signal bandwidth B, the maximum channel capacity can be written as

$$\mathcal{C} = B\log_2\left(1+\frac{P_\mathrm{s}}{P_\mathrm{n}}\right), \tag{2.10}$$

where the ratio $P_\mathrm{s}/P_\mathrm{n}$ is called the signal-to-noise power ratio (SNR). From Eq. (2.10) it is obvious that the capacity of a link can be increased by improving the SNR. The logarithmic relation between the SNR and the capacity, however, reduces the effect of the SNR enhancement. Increasing the bandwidth B is often more effective because the bandwidth is linearly connected to the link capacity. Note that increasing the bandwidth also reduces the SNR. For a constant noise power density N_0 the total noise power within the transmission bandwidth of the signal can be written as $P_\mathrm{n} = N_0 B$.

Typically, electronic circuits and matching networks are limited to a spectral range of roughly 10 % centered about the carrier frequency f_0, and the available bandwidth corresponds to $B \approx 0.1 f_0$. Therefore, higher carrier frequencies f_0 increase the capacity of a link. However, the carrier frequency also has a large impact on the loss and the directivity of the link. Figure 2.6 illustrates the attenuation of a free-space link for various carrier frequencies and weather conditions. The blue curve shows the attenuation due to atmospheric gases [7] for standard conditions, i.e. a temperature of 15 °C and water-vapor content of 7.5 g/m^3. The resonant peaks come from absorption of oxygen and water molecules. The absorption increases for heavy fog. The gray curve shows the attenuation for fog with a visibility in the order of 50 m [8]. Heavy rain with a rain rate of 31 mm/h increases the attenuation even further [9], see the red curve. In Karlsruhe, where the experiments were performed, only in 0.01 % of the year the rain rate exceeds this value [10]. The purple curve shows the attenuation if both rain and fog are present. Various spectral windows with small atmospheric attenuation can be used for wireless communication links. For example, for frequencies in the range of 220 GHz to 315 GHz, which are mainly used as carrier frequencies in this work, the attenuation is below 30 dB/km even for the unlikely case that heavy rain and fog is combined.

Free-space optical (FSO) links could alternatively be used to achieve high data rates [11]. However, these links are typically more susceptible to attenuation by fog, scintillation, and misalignment [12–14]. For the same fog conditions as assumed in Figure 2.6 with a visibility in the order of 50 m, the atmospheric attenuation for FSO links is considerably higher and can be more than 350 dB/km [15–17]. As a reference, this value is shown as a green dashed line in Figure 2.6. For good weather conditions, even higher data rates compared to

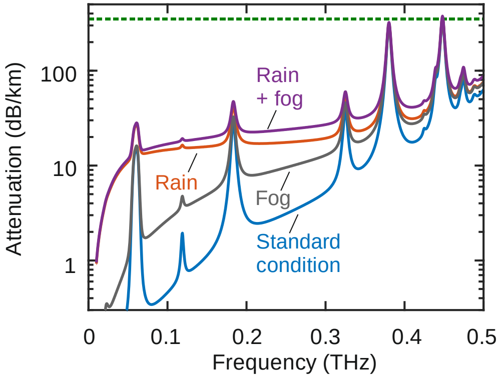

Figure 2.6: Free-space attenuation for various weather conditions. The blue curve shows the attenuation of gases [7] for standard conditions (temperature of 15 °C, water-vapour content of 7.5 g/m^3). The gray curve shows the attenuation for thick fog [8] with a visibility in the order of 50 m. The red curve shows the attenuation [9,10] for a rain rate of 31 mm/h, and the purple curve displays the attenuation if both rain and fog are present. As a reference, the green dashed line shows the attenuation of 350 dB/km of a free-space optical link under the same fog conditions as assumed for the gray curve.

T-wave links might be achieved with FSO links [11], and in future, a combination of both T-wave links and free-space optical links could be the optimum solution [13].

The T-wave attenuation due to atmospheric absorption can be compared to the free-space path loss (FSPL), which describes the loss between an isotropic radiator and an isotropic receiver due to the decrease of the power flux density with larger distance d between the transmitter and the receiver,

$$\begin{aligned} \mathrm{FSPL} &= \left(4\pi d \frac{f_0}{c}\right)^2, \\ \mathrm{FSPL}_{\mathrm{dB}} &= 10\log_{10}\left(4\pi d \frac{f_0}{c}\right)^2, \end{aligned} \tag{2.11}$$

where f_0 is the carrier frequency and c the speed of light. A derivation of the FSPL can be found in Appendices A.1 and A.2. By using a simple link budget analysis, the power P_{Rx} at the receiver can be estimated if the isotropic radiated power P_{Tx} at the transmitter and the antenna gain G_{Tx} and G_{Rx} are known,

$$\begin{aligned} P_{\mathrm{Rx}} &= \frac{P_{\mathrm{Tx}} G_{\mathrm{Tx}} G_{\mathrm{Rx}}}{L_{\mathrm{a}}\,\mathrm{FSPL}}, \\ P_{\mathrm{Rx,dBm}} &= P_{\mathrm{Tx,dBm}} + G_{\mathrm{Tx,dB}} + G_{\mathrm{Rx,dB}} - L_{\mathrm{a,dB}} - \mathrm{FSPL}_{\mathrm{dB}}. \end{aligned} \tag{2.12}$$

In this relation, L_{a} stands for the atmospheric loss of the transmission link with distance d, see Figure 2.6. This formula is only valid if the distance between the transmitter and the receiver is large enough and the receiver is in the far field of the transmitter antenna. For a distance d = 100 m and a frequency f_0 = 0.3 THz, the free-space path loss corresponds to 120 dB without considering the antenna gain, while the atmospheric loss is only 3 dB even for bad weather condition. The total loss can be greatly reduced by using highly directive antennas at the transmitter and the receiver, which can easily have a combined antenna gain of 100 dB or more [2]. With high-gain antennas, transmission distances of a couple of hundred meters are possible. Equation (2.12) is closely related to Friis transmission equation [18]. In this equation the atmospheric loss is not considered, $L_\mathrm{a}=1$, and the performance of the transmitter and receiver antenna is specified in terms of effective areas A_Tx and A_Rx, leading to

$$P_\mathrm{Rx}=P_\mathrm{Tx}\frac{A_\mathrm{Tx}A_\mathrm{Rx}}{\left(d\lambda\right)^2}. \tag{2.13}$$

The connection between antenna gain and antenna aperture is given in Appendix A.

2.2 T-wave transmitters: State of the art

In this section, the most common techniques for generating continuous-wave (c.w.) T-wave carriers are discussed. Pulsed T-waves are not part of the following discussion, because their relevance for T-wave communication is limited. Furthermore, only compact transmitters, which can be operated at room temperature, are discussed and sources such as free electron lasers, backward-wave oscillators, or quantum cascade lasers are excluded. The transmitter types can be divided into electronic transmitters, which upconvert an electronic signal to the THz range, and photonic transmitters, which downconvert an optical signal to the THz range. Both techniques are frequently used for T-wave communications. More information on T-wave transmitters can be found in [19,20].

2.2.1 Electronic transmitters

Various electronic methods can be used to generate T-wave signals by electronic circuits:

- **Transistor technologies:** Transistors are mainly used to amplify T-waves [21–24], but they can also be used for generation of T-wave signals [25,26]. They are continuously improving and nowadays achieve maximum oscillation frequencies f_max exceeding 1 THz [21]. To reach such high frequencies, the most commonly used architecture [27] is the metamorphic high-electron-mobility transistor (mHEMT), which is a special kind of field-effect transistor. By using a heterostructure and appropriate doping of the high-bandgap material, a two-dimensional electron gas can be generated at the low-bandgap material right at the interface to the high-bandgap material. The mobility of the two-dimensional electron gas inside the undoped region exceeds the mobility in bulk material and enables transistors with very high f_{max}. Heterojunction bipolar transistors (HBT) are also able to operate at frequencies beyond 1 THz [28–30], but typically lead to higher noise figures [19].

- **Resonant structures:** Resonant structures allow the generation of high-frequency radiation. One promising approach is the resonant tunneling diode (RTD), which can be used to generate radiation with frequencies exceeding 1 THz [31,32]. In such a diode, a quantum film is located between two thin high-bandgap semiconductors, which serve as potential barriers. If a certain voltage is applied to the diode, the conduction band edge aligns with the resonant state of the quantum film [33], and the electrons can tunnel through the potential barrier. This leads to an increase in the current. If a larger voltage is applied, the energy states of the conduction band and of the quantum film become misaligned, and the current decreases. In this voltage region, the RTD features a negative differential conductance (NDC), which can be used to compensate the ohmic loss of an oscillator circuit. The oscillator can be integrated with an antenna to couple the radiation to free space [32]. The output power can be increased further by using large-scale arrays of RTD [31].

  Other methods to obtain an NDC are to use impact ionization avalanche transit-time (IMPATT) diodes, tunneling transit-time (TUNNETT) diodes, or Gunn diodes. The IMPATT diode introduces a time delay between the voltage and the current, which effectively leads to a NDC in a certain range of frequencies. In the avalanche region, the electron-hole pairs are generated statistically, which leads to a large noise contribution [34]. TUNNETT diodes are used for very high frequencies, where the transit time region becomes small. They also exploit transit-time delays but instead of an avalanche effect, they make use of a tunneling mechanism. The noise of TUNNETT diodes is typically smaller than for IMAPTT diodes, but also the power output and efficiency are reduced [34]. Gunn diodes use the field-dependent velocity, which can lead to

instabilities through which current pulses can be generated. Gunn diodes with good noise performance can be realized by using an optimized resonator design [35]. Such diode oscillators are often used as c.w. sources for microwave test instruments or radar applications [34].
The resonant T-wave transmitters have in common that they are compact, and high T-wave power can be achieved. However, the tunability is limited [36].

- **Multipliers:** A third method to generate T-waves is to use a low-frequency source and upconvert the signal with a nonlinear electronic device such as Schottky-barrier diodes (SBDs), heterostructure barrier varactors (HBVs), or mHEMTs. Each conversion stage reduces the output power, and increases the phase noise [36].

2.2.2 Optoelectronic transmitters

In an optoelectronic T-wave transmitter, the data signal is first modulated on an optical carrier. The optical signal is then downconverted to the THz range. Various methods can be used for this downconversion:

- **Optical nonlinear crystals:** Frequency conversion can be achieved in optical nonlinear crystals. By using difference-frequency generation, the resulting wave can contain frequencies in the THz range. This process allows adjusting the THz frequency in a broad range. However, the conversion efficiency is inherently limited by the conversion from high energy photons at optical frequencies f_{opt} to photons with much smaller energies at THz frequencies f_{THz} and the conversion efficiency cannot be better than $f_{\text{opt}} / f_{\text{THz}} \approx 0.001$. To achieve high THz output power levels, optical signals with very high power are required, which makes this method not attractive for T-wave communications.

- **Photomixers:** Mixing of two optical signals oscillating at frequencies f_{a} and f_{b} in a photodetector leads to a current oscillating at the difference frequency $f_{\text{THz}} = \left| f_{\text{a}} - f_{\text{b}} \right|$. Any modulation of the amplitude and the phase of one of the optical signals is then converted to a modulated T-wave carrier. In most cases, high-speed photodiodes are used for downconversion. The most important properties of photomixers for T-wave generation are bandwidth, sensitivity, and saturation power. A particularly attractive implementation of a photodiode is the uni-travelling-carrier photodiode (UTC-PD), which enables high-speed operation and large saturation levels of the photocurrent. The various semiconductor layers are designed in a way that only the electrons travel ballistically through the depletion region, while the holes are quickly captured by the p-contact. Because the velocity of electrons in the semiconductor is larger than the velocity of holes, the response of the UTC-PD is faster than the one of conventional photodiodes. In addition, the effect of charge accumulation is reduced, which increases the maximum photocurrent. A comparison between a conventional pin-photodiode and an UTC-PD is given in Appendix B.

Photoconductors can also be used for c.w. T-wave generation. However, their T-wave output power is still below the power levels of photodiodes [20,37]. So far, there is no demonstration where photoconductors are used as transmitters in high-speed T-wave communication links. The main difficulty in designing photoconductors is to reduce the carrier lifetime but still maintain a high mobility. Furthermore, there is always a DC bias voltage needed to accelerate the carriers and the associated DC current might lead to a thermal failure of the devices. Recently, optimized photoconductors have been demonstrated as transmitters in a c.w. spectroscopy system [38] and further optimization might also make them suitable for communication applications.

2.3 T-wave receivers: State of the art

T-wave receivers can be categorized in electronic receivers and optoelectronic receivers, similar to the case of T-wave transmitters. However, for T-wave communications until now electronic receivers were used exclusively. In this work, we report on the first demonstration of optoelectronic receivers used for high-speed T-wave communications, see Chapter 4. The optoelectronic receivers reviewed in the following have so far been used in sensing applications only. In this summary, we only discuss concepts that are potentially suitable for high-speed data communications, whereas rather slow T-wave receivers such as bolometers, calorimeters and pyroelectric detectors are excluded.

2.3.1 Electronic receivers

Electronic T-wave receivers can be divided into two groups. The first one comprises envelope detectors, which can be used for direct detection. The second group is represented by mixers, which allow coherent reception of the signals.

- **Envelope detectors:** A device with a nonlinear current-voltage characteristic can be used to detect the envelope of a T-wave signal, see Appendix C.3 for details. This can be used for direct detection of, e.g., OOK or 4PAM signals. Furthermore, self-coherent schemes could be used to recover also the phase information, see Chapter 3. Typically, SBD or RTD are used as envelope detectors.

- **Mixers:** The T-wave multipliers described in Section 2.2.1 can also be used to receive a T-wave signal. To this end, a T-wave LO is generated by a first multiplier chain. The T-wave LO is mixed with the incoming T-wave in an additional nonlinear element which leads to a downconversion of the T-wave signal. This approach is most frequently used in current T-wave links, but the mixers are costly and often represent the bandwidth bottleneck of the transmission link [39]. Therefore, alternative concepts are investigated in this work.

2.3.2 Optoelectronic receivers

Optoelectronic T-wave receivers are frequently used for spectroscopy and imaging applications. This work is the first demonstration of their use in T-wave communications. Methods for optoelectronic T-wave reception are:

- **Electro-optic (EO) sampling:** The incoming T-wave signal can modulate the index of refraction of an EO crystal via the Pockels effect. This change can be probed by an optical beam, which allows measuring the amplitude and the phase of the T-wave signal. This method is mainly used for pulsed systems [40], but also c.w. systems have been demonstrated [41]. The EO sampling offers an extremely large tuning range, but the small conversion efficiency makes this solution unattractive for T-wave communications.

- **Photoconductors:** Photoconductors are often used as receivers in c.w. THz spectroscopy systems and can be driven by lasers at the telecommunication wavelength [42]. The T-wave signal leads to a time-dependent voltage $U(t)$ at the photoconductor. At the same time, the conductivity $G(t)$ is modulated by the power beat signal of two laser tones. The output current is given by the multiplication of both quantities $I(t)=U(t)G(t)$ and therefore leads to a downconversion by multiplicative mixing of the T-wave signal and the optical LO, see Appendix D.1 for details.
- **Photodiodes:** In photodiodes, the output current is hardly affected by an applied voltage, and a downconversion similar to the downconversion in photoconductors is not possible. Only for very large optical powers mixing becomes possible due to the dynamic capacitance associated with the charge storage in the photo-absorption layer [43]. This effect has been used to downconvert data signals at a carrier frequency of 35 GHz [44] and 60 GHz [45] but not at T-wave frequencies.

2.4 T-wave communications: State of the art

In this section, the recent achievements of T-wave communication links are summarized. The experiments differ greatly in the underlying device technology, the carrier frequency, the transmission distance, the number of channels and the data rate. In addition, multiple-input-multiple-output (MIMO) systems with a number of *N*-Tx antennas and *N*-Rx antennas are often used, which in effect leads to nearly *N*-fold increase of the data rate. For comparison of the results, the total data rates are therefore divided by *N*. Figure 2.7 summarizes the recent demonstrations with T-wave links and compares them to the achievements of this work. The net data rates shown in the experiments are indicated with respect to the occupied frequency range and wireless transmission distance *d*. The color code indicates the different receiver technologies used in the experiments. The highest data rates are achieved with electronic mixers and electronic LO at the Rx (olive) [39,46–62]. Such Rx circuits are costly, and often limit the bandwidth which can be used for transmission [39]. Much simpler receiver hardware designs use only a single envelope detector, e.g. a Schottky-barrier diode (SBD), at the receiver (green) [63–66]. So far, the data rates achieved with SBD-Rx where much smaller in comparison to the electronic mixer Rx. In this work, it is demonstrated that the combination of a SBD with so-called Kramers-Kronig processing allows for data rates of 115 Gbit/s transmitted over a distance of 110 m. This is the first demonstration of data rates above 100 Gbit/s transmitted over a distance larger than 20 m. The blue lines show the results achieved with optoelectronic Rx [J3], [44,45]. The data rates are still below the data rates achieved with electronic mixers. However, this work represents a first proof-of-principle experiment,

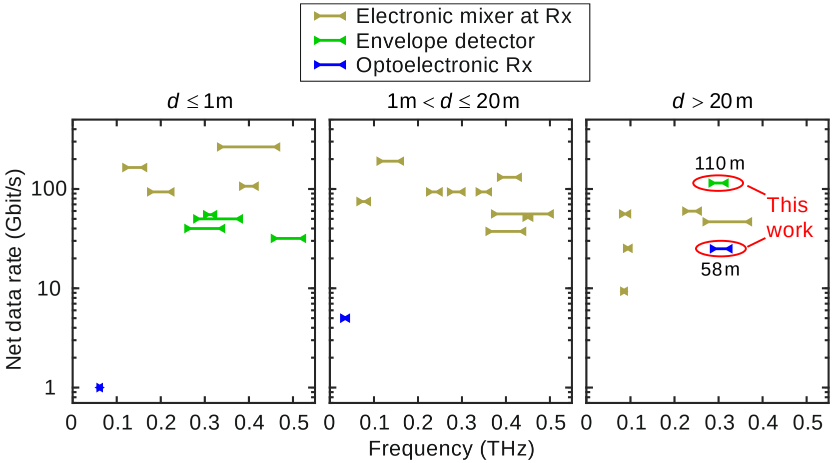

Figure 2.7: Overview of T-wave communication experiments. Net data rate as a function of occupied frequency range and wireless transmission distance *d*. The olive lines show the experiments where an electronic mixer in combination with an electronic local oscillator (LO) is used as a T-wave receiver (Rx) [39,46–62]. The green lines show the reception with a simple envelope detector as receiver [J4], [63–66] and the blue lines the reception with an optoelectronic Rx [J3], [44,45]. Encircled are the results from this work, demonstrating the highest data rates received with an envelope detector, the highest data rate received with an optoelectronic Rx, and the highest data rate transmitted over a T-wave link over a distance of more than 20 m for any kind of receiver.

and the receiver technology is not yet optimized. In the future, comparable or even higher data rates could be achieved with optoelectronic Rx.

3 Kramers-Kronig receiver for coherent THz communications

This chapter discusses a coherent THz data transmission link using a Schottky-barrier diode as a technically simple envelope detector at the receiver in combination with a generalized version of Kramers-Kronig signal processing for reconstructing the phase of the complex data signal. A comparison of the Kramers-Kronig approach with iterative phase retrieval algorithms is shown in Appendix C.12.

This chapter is taken from a publication in *Nature Photonics* [J4]. In order to fit the structure and layout of this document, it was adapted accordingly. Methods and Supplementary Information associated with the manuscript can be found in Appendix C.

[start of paper [J4]]

Generalized Kramers-Kronig Receiver for Coherent THz Communications

Nature Photonics, Volume 14, pages 601–606 (2020)
DOI: 10.1038/s41566-020-0675-0

T. Harter[1,2*], C. Füllner[1*], J. N. Kemal[1], S. Ummethala[1,2],
J. L. Steinmann[3], M. Brosi[3], J. L. Hesler[4], E. Bründermann[3],
A.-S. Müller[3], W. Freude[1], S. Randel[1], C. Koos[1,2]

[1] Institute of Photonics and Quantum Electronics (IPQ), Karlsruhe Institute of Technology (KIT), Germany
[2] Institute of Microstructure Technology (IMT), Karlsruhe Institute of Technology (KIT), Germany
[3] Institute for Beam Physics and Technology (IBPT), Karlsruhe Institute of Technology (KIT), Germany
[4] Virginia Diodes, Inc. (VDI), Charlottesville, United States of America
[*] These authors contributed equally to this work

Modern communication systems rely on efficient quadrature amplitude modulation formats that encode information on both the amplitude and phase of an electromagnetic carrier. Coherent detection of such signals typically requires complex receivers that contain a continuous-wave local oscillator as a phase reference and a mixer circuit for spectral downconversion. In optical communications, the so-called Kramers–Kronig scheme has been demonstrated to simplify the receiver, reducing the hardware to a single photodiode [67–69]. In this approach, a local-oscillator tone is transmitted along with the signal, and the amplitude and phase of the complex signal envelope are digitally reconstructed from the photocurrent by exploiting their Kramers–Kronig-type relation [70–72]. Here, we transfer the Kramers–Kronig scheme to high-speed wireless communications at terahertz carrier frequencies. To this end, we generalize the approach to account for non-quadratic receiver characteristics and employ a Schottky-barrier diode as a nonlinear receiver element. Using 16-state quadrature amplitude modulation, we transmit a net data rate of 115 Gbit/s at a carrier frequency of 0.3 THz over a distance of 110 m.

3.1 Introduction

Future mobile communication networks will crucially rely on wireless backbone networks with high-speed point-to-point links [2,73]. To offer data rates of 100 Gbit/s or more, these links will have to exploit unoccupied spectral resources at carrier frequencies [2,39,46,55,74–76] above 0.1 THz, where frequency windows of low atmospheric attenuation enable transmission over practically relevant distances of a few hundred metres [48,77]. To generate the underlying terahertz data signals, coherent downconversion of optical waveforms in high-speed photodiodes has been demonstrated as a particularly promising approach [2,39,46,55,63,75,76,78,79]. This concept opens a simple path towards quadrature amplitude modulation (QAM) formats that offer fast transmission at high spectral efficiencies. Coherent reception of these signals, however, largely relies on relatively complex terahertz circuits, which comprise, for example, high-speed mixers along with terahertz local oscillators (LOs). These circuits are costly and often represent the bandwidth bottleneck of the transmission link [39].

Here we demonstrate a greatly simplified coherent receiver scheme for terahertz data signals that relies on a simple envelope detector and subsequent digital signal processing [80] (DSP). The scheme allows reconstruction of the phase of the terahertz waveform from the measured envelope and relies on a generalization of the so-called Kramers-Kronig (KK) receiver in optical communications [67,68]. In our experiments, we use a high-speed Schottky-barrier diode (SBD) as a broadband and compact envelope detector. In contrast to a conventional photodetector used in optical communications, the SBD features non-quadratic rectification characteristics, which must be accounted for in our generalized KK algorithm. We demonstrate transmission of quadrature phase-shift keying (QPSK) and 16-state QAM (16QAM) signals at a carrier frequency $f_{\mathrm{THz}} = 0.3$ THz over a distance of 110 m, achieving line rates of up to 132 Gbit/s and net data rates of up to 115 Gbit/s after subtraction of the error-correction overhead. To the best of our knowledge, this is the first experiment using an envelope detector and subsequent KK processing in wireless communications, leading to the highest data rate so far demonstrated for terahertz transmission over distances of more than 100 m. Our simplified terahertz receiver perfectly complements optoelectronic wireless transmitters [2,39,46,55,63,75,76,78,79], thereby paving the way towards terahertz transmission systems that do not need any electronic terahertz circuits for signal generation and detection.

3.2 Future wireless backbone networks

The vision of a future wireless backbone network is shown in Figure 3.1. Small radio cells [81,82] with coverage of only a few tens of metres enable frequency reuse and guarantee broadband service for large numbers of terminal devices. The various cells are connected by high-capacity terahertz backhaul links in a mesh configuration, thus increasing network resilience and flexibility while decreasing installation costs in comparison with fibre-based connections. With expected per-cell peak data rates of 20 Gbit/s in fifth-generation (5G) networks [83] and 100 Gbit/s in sixth-generation networks [84], wireless terahertz backhaul links will have to offer transmission capacities of 100 Gbit/s or more to allow for flexible traffic aggregation. The inset of Figure 3.1 shows a schematic of the terahertz link using a KK receiver scheme. The KK approach

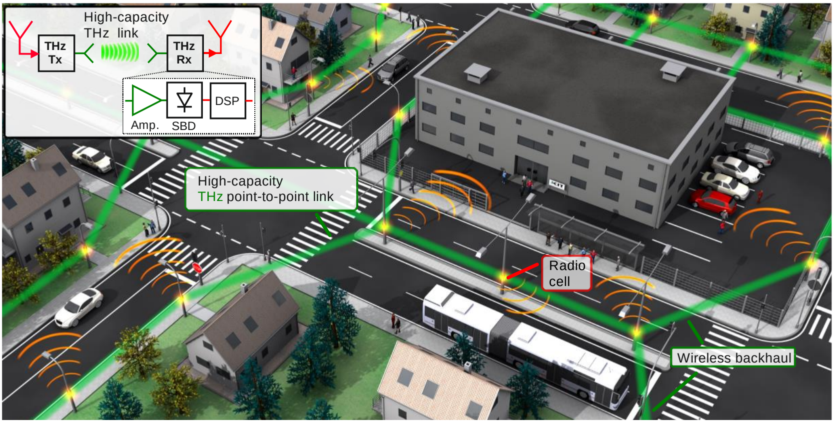

Figure 3.1: Vision of a future wireless backbone network. High-capacity terahertz line-of-sight links connect small radio cells with coverage of only a few tens of metres. Each of these cells locally guarantees ultra-broadband wireless services. The wireless connections allow flexible and efficient installation without the need for deploying optical fibres or changing fibre installations if reconfigurations are required. The inset shows a schematic of a terahertz link based on a KK-type receiver. This scheme greatly reduces the complexity of the receiver hardware by replacing technically complex terahertz LOs and mixer circuits with a simple SBD. Antennas and waveguides for terahertz signals are coloured in green, whereas red is used for radio-frequency components. Tx, transmitter; Rx, receiver; Amp., amplifier. *Copyright © Springer Nature.*

greatly reduces the complexity of the receiver hardware, which consists of only an amplifier and an SBD and does not require any technically complex terahertz LOs and mixer circuits.

3.3 Generalized Kramers-Kronig processing

On a fundamental level, KK processing [67] relies on the fact that the real and imaginary parts of an analytic time-domain signal represent a Hilbert transform pair. This relationship can be translated into an equivalent relationship that allows the phase of a complex signal to be retrieved once its amplitude has been measured, see Appendix C.1 for details. For the KK-based reception described here, the terahertz signal incident at the receiver can be described as

$$u_{\mathrm{THz}}(t) = \Re\left\{\underline{U}(t)\mathrm{e}^{\mathrm{j}2\pi f_{\mathrm{THz}}t}\right\}, \tag{3.1}$$

where j is the imaginary unit, $\Re\{.\}$ denotes the real part, and where the complex envelope as a function of time *t*, $\underline{U}(t)$, consists of a strong real-valued constant part U_0 and an analytic data signal $\underline{U}_\mathrm{s}(t)$ with a single-sided power spectrum,

$$\underline{U}(t) = U_0 + \underline{U}_\mathrm{s}(t) = \left|\underline{U}(t)\right|\mathrm{e}^{\mathrm{j}\Phi(t)}. \tag{3.2}$$

To ensure correct reconstruction of the phase $\Phi(t)$ from the measured amplitude $|\underline{U}(t)|$, $\underline{U}(t)$ must be a minimum-phase signal in the time domain, which is ensured by [67]

$$\left|\underline{U}_\mathrm{s}(t)\right| < U_0 \;\forall\; t. \tag{3.3}$$

The phase $\Phi(t)$ can then be reconstructed by a KK-type relation,

$$\Phi(t) = \frac{1}{\pi}\mathcal{P}\int_{-\infty}^{\infty}\frac{\ln\left(\left|\underline{U}(\tau)\right|\right)}{t-\tau}\mathrm{d}\tau, \tag{3.4}$$

where $\mathcal{P}$ denotes the Cauchy principal value of the otherwise undefined improper integral. A more detailed derivation can be found in Appendix C.1.

In optical communications, a photodiode is commonly used as an envelope detector for KK reception. Since the photocurrent is proportional to the incident optical power, the magnitude of the optical amplitude can be digitally reconstructed from the electrical signal by a simple square-root operation. In contrast to this, SBDs feature complex rectification characteristics, thus requiring a generalization of the KK-based signal reconstruction algorithm. To this end, we assume that the relationship between the amplitude of the terahertz signal at the SBD receiver input $|\underline{U}(t)|$ and the current $i(t)$ at the output can be described by a bijective function *g*,

$$i(t) = g\left(|\underline{U}(t)|\right), \tag{3.5}$$

see Appendix C.3 for details.

The amplitude $|\underline{U}(t)|$ can then be reconstructed by applying the inverse function $g^{-1}(i)$ to the measured output current, and the phase $\Phi(t)$ can be found by replacing $\ln\left(\left|\underline{U}(t)\right|\right)$ in Eq. (3.4) with the generalized expression $\ln\left(g^{-1}(i)\right)$,

$$\Phi(t) = \frac{1}{\pi}\mathcal{P}\int_{-\infty}^{\infty} \frac{\ln\left(g^{-1}\left(i(\tau)\right)\right)}{t-\tau}\mathrm{d}\tau \,. \tag{3.6}$$

In contrast to square-law photodetectors, the exact rectification characteristics of SBDs depend crucially on the operating point as well as on the peripheral terahertz and baseband circuits and are hence hard to describe analytically. We therefore express $g^{-1}(i)$ as a power series with $N+1$ initially unknown coefficients a_n,

$$\left|\underline{U}_{\mathrm{R}}\right| = g^{-1}(i) = \sum_{n=0}^{N} a_n i^n \,. \tag{3.7}$$

In this relation, $\left|\underline{U}_{\mathrm{R}}\right|$ denotes the terahertz voltage amplitude that is reconstructed from a measured current i at the SBD output. The coefficients a_n have to be determined from measured data. To this end, we use test signals with known amplitudes $\left|\underline{U}(t)\right|$ and measure the associated current $i(t)$ at discrete times t_m, with $m = 1, 2, \ldots M$ and $M \gg N$. The coefficients a_n are obtained from a least-squares fit of the polynomial function $\left|\underline{U}_{\mathrm{R}}(t_m)\right| = g^{-1}\left(i(t_m)\right)$, given by Eq. (3.7), to the known data set $\left|\underline{U}(t_m)\right|$, see Appendix C.4 for details. The result is shown in Figure 3.2, together with the square-root characteristics that would be used in conventional KK processing of optical signals. While the square-root characteristics can be used as an approximation for small signal amplitudes, the generalized approach accounts for the actual behaviour of the SBD receiver over a large range of signal levels. In addition, the generalized function comprises an offset $a_0 \neq 0$ that assigns a zero output current $i = 0$ to a non-zero terahertz amplitude $\left|\underline{U}_{\mathrm{R}}\right| = g^{-1}(0)$, see Appendix C.4. This offset avoids small values of the reconstructed terahertz amplitude, which would otherwise require artificial clipping [85] of the signals at low reconstructed voltages to mitigate large uncertainties in the phase reconstruction according to Eq. (3.4) due to the singularity of $\ln\left(\left|\underline{U}_{\mathrm{R}}\right|\right)$ at $\left|\underline{U}_{\mathrm{R}}\right| = 0$. Note that the measurement data used for the least-squares fit were obtained from an SBD in combination with a terahertz amplifier at its input. The extracted receiver characteristics $g^{-1}(i)$ hence not only account for the SBD but can also compensate the saturation behaviour of the terahertz amplifier. More details on the characterization of the SBD and the terahertz amplifier can be found in Appendices C.4 and C.5. Note also that the non-quadratic characteristics of the SBD can broaden the received signal spectrum and might increase the bandwidth requirements of the receiver circuits. This effect, however, is not very prominent, see Appendix C.6.

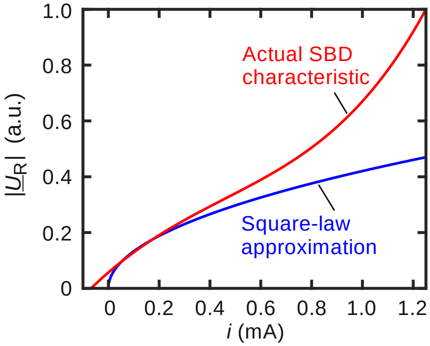

Figure 3.2: SBD receiver characteristics. The SBD rectifies the incident terahertz signal, leading to an output current i that depends on the voltage amplitude $|\underline{U}|$. We describe the actual receiver characteristics $|\underline{U}_\mathrm{R}| = g^{-1}(i)$ (red) by a power-series approximation according to Eq. (3.7). The coefficients a_n are determined from measured test signals, see Appendix C.4. As a reference, we show the square-root relationship (blue) that is assumed in conventional KK processing and that leads to a relationship of the form $|\underline{U}_\mathrm{R}| \propto \sqrt{i}$. The generalized approach describes the actual behaviour of the SBD receiver for all signal levels, whereas the square-root characteristics can be used as an approximation for small signal levels only. The terahertz amplitude $|\underline{U}_\mathrm{R}|$ is indicated in arbitrary units (a.u.), normalized to a maximum value of 1. Note that the generalized function comprises an offset $a_0 \neq 0$ that assigns a non-zero terahertz amplitude $|\underline{U}_\mathrm{R}| = g^{-1}(0)$ to a zero output current $i = 0$, thereby effectively clipping small signal amplitudes [85], see Appendix C.4 for details. *Copyright © Springer Nature.*

3.4 Experimental setup and results

To demonstrate the viability of generalized KK processing, we perform wireless transmission experiments at $f_{\text{THz}} = 0.3$ THz. Figure 3.3 depicts a simplified sketch of the experimental set-up (for a comprehensive description, see Appendix C.2). At the transmitter, the terahertz signal is generated by frequency downconversion of an optical signal via photomixing. An arbitrary-waveform generator (AWG) is used to drive an electro-optic in-phase/quadrature-phase (IQ) modulator, which encodes data signals with bandwidth B on an optical carrier with frequency f_0. The optical data signal is combined with two continuous-wave tones at optical frequencies f_1 and f_2 and then fed to a high-speed uni-travelling-carrier photodiode (UTC-PD) [86] for photomixing. The

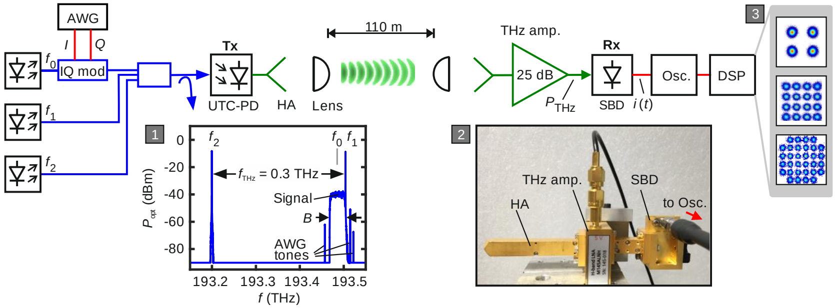

Figure 3.3: Experimental setup. An optical data signal centred at frequency f_0 is generated by an IQ modulator (‘IQ mod.’) driven by an AWG. The optical data signal is then combined with two continuous-wave tones at f_1 and f_2. The tone at f_1 is placed at the edge of the data spectrum and will eventually act as an LO for KK reception, whereas the tone at f_2 serves as a reference tone for down-converting the data signal to $f_{\text{THz}} = f_1 - f_2$ by photomixing in a high-speed UTC-PD. At the output of the UTC-PD, the terahertz signals are radiated into free space by a horn antenna (‘HA’) and a subsequent polytetrafluoroethylene collimation lens. After a transmission distance of 110 m, the terahertz signal is received by a second lens and another horn antenna and fed to a terahertz amplifier providing a 25 dB gain. The SBD is connected to the output of the amplifier, and a real-time oscilloscope (‘Osc.’) is used to capture the output current of the SBD for further offline processing (‘DSP’). **Inset 1**: corresponding optical spectrum (resolution bandwidth 180 MHz) recorded after a monitoring tap. The optical spectrum also exhibits spurious tones generated by the AWG (‘AWG tones’). **Inset 2**: photograph of the receiver, including the horn antenna, the terahertz amplifier and the SBD. **Inset 3**, top to bottom: exemplary constellation diagrams for QPSK, 16QAM and 32QAM at symbol rates of 30 GBd, 15 GBd and 5 GBd, respectively. *Copyright © Springer Nature.*

overall optical power entering the UTC-PD is between 10 dBm and 14 dBm, depending on the desired terahertz power (P_{THz}). The optical spectrum at the input of the photodiode is shown in Inset 1 of Figure 3.3. The first optical continuous-wave tone, at frequency f_1, serves as an LO for KK reception, whereas the second continuous-wave tone, at frequency f_2, is used for down-converting the data signal and the LO tone to the THz carrier frequency $f_{\mathrm{THz}} = f_1 - f_2$. The LO tone at f_1 is placed at the edge of the data signal spectrum, and the data signal can hence be represented by a complex analytic signal $\underline{U}_{\mathrm{s}}(t)$ with respect to the carrier frequency f_{THz}. The total voltage envelope is then given by $\underline{U}(t) = U_0 + \underline{U}_{\mathrm{s}}(t)$, see Eq. (3.2), where U_0 denotes the LO amplitude generated by the optical tone at f_1. For distortion-free KK processing, the chosen power of the continuous-wave LO tone has to be large enough to guarantee that the resulting $\underline{U}(t)$ fulfils the minimum-phase condition according to Eq. (3.3). Note that in contrast to conventional SBD-based self-coherent transmission [66,87], generalized KK processing avoids unused guard bands between the LO tone and the payload signal, which would occupy at least half of the available transmission bandwidth.

After photomixing, the terahertz signals are radiated into free space by a horn antenna. A subsequent polytetrafluoroethylene lens collimates the beam. After a transmission distance of 110 m, the terahertz signal is collected by a second lens and another horn antenna. The transmission loss of the free-space section amounts to 17 dB and is (over-) compensated by a low-noise amplifier with 25 dB gain. The SBD is connected to the output of the amplifier (Inset 2 of Figure 3.3), and a real-time oscilloscope with 80 GHz bandwidth is used to record the output current $i(t)$. After data acquisition, we apply the generalized KK algorithm, followed by blind coherent DSP, see Appendix C.1. This leads to the constellation diagrams shown in Inset 3 of Figure 3.3. All experiments are performed indoors under laboratory conditions. For outdoor operation, additional attenuation due to adverse weather conditions must be considered. At heavy rain of, for example, 40 mm/h, the path loss of a 110-m-long link operated at a carrier frequency of 0.3 THz would increase by approximately 2.4 dB, see Appendix C.11. This attenuation can be easily compensated by, for example, an additional terahertz amplifier at the transmitter.

In our experiments, we explore QPSK, 16QAM and 32-state QAM (32QAM) as modulation formats. The results of QPSK and 16QAM are summarized in Figure 3.4 and Figure 3.5, respectively. We use generalized KK processing (gen. KK) as described above and compare it with the results obtained by conventional KK processing when assuming a square-root relationship between the SBD output current and the terahertz amplitude (conv. KK). We also consider evaluation assuming heterodyne reception without any KK processing (w/o KK). In this case, downconversion leads to an LO-signal mixing product that is impaired by the nonlinear mixing of the signal with itself (see Appendix C.1). In a first series of experiments, we analyse the influence of the optical carrier-to-signal power ratio (CSPR) on the signal quality for QPSK modulation (Figure 3.4). The CSPR, expressed in decibels, is given by the power ratio between the LO tone and the data signal,

$$\mathrm{CSPR} = 10\log\left(\left|U_0\right|^2 \Big/ \overline{\left|U_\mathrm{s}(t)\right|^2}\right), \tag{3.8}$$

where $\overline{\left|U_\mathrm{s}(t)\right|^2}$ denotes the time average of the squared signal voltage. When changing the CSPR, the sum of carrier and signal power is kept constant at $P_\mathrm{THz} = 260\,\mu\mathrm{W}$, measured at the input port of the SBD. For QPSK signalling, the high quality of the received constellation diagram leads to a small number of errors for the 3×10^5 evaluated symbols, and the measured bit error ratio (BER) does not represent a reliable estimate for the bit error probability. We therefore use the error vector magnitude (EVM) as a quality metric [88,89] (see Appendix C.1). We find an optimum CSPR of approximately $6-7\,\mathrm{dB}$ for both generalized and conventional KK processing as well as for heterodyne reception without KK processing. For smaller CSPRs, the EVM obtained from KK processing increases because, for a given overall terahertz power P_THz, the LO magnitude becomes smaller, and the minimum-phase condition according to Eq. (3.3) is violated. For heterodyne reception without KK processing, the nonlinear interaction of the signal with itself can no longer be neglected if the CSPR is too small, thus impairing the signal quality. For larger CSPRs and constant overall terahertz power P_THz, the data signal becomes weaker and is finally dominated by receiver noise.

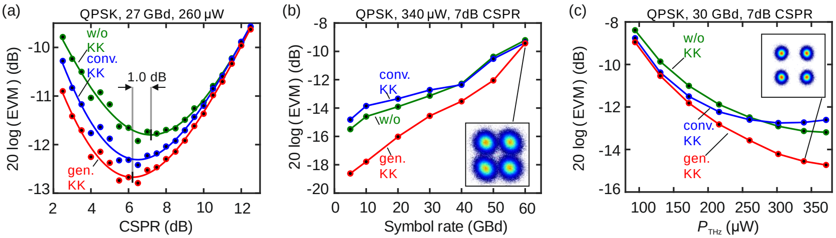

Figure 3.4: Results of the QPSK transmission experiments bridging a distance of 110 m. **(a)** EVM as a function of the CSPR for QPSK signals measured at a symbol rate of 27 GBd for constant terahertz power P_THz = 260 µW. For generalized KK processing (‘gen. KK’), the actual SBD receiver characteristics are taken into account and are compensated, see Eqs. (3.5) and (3.7) , leading to the best transmission performance. As a reference, we consider conventional KK reception (‘conv. KK’), assuming a quadratic relationship between the SBD current and $|\underline{U}|$, as well as heterodyne reception without any KK processing and without a guard band between the signal and the LO (‘w/o KK’), which suffers from impairments due to nonlinear interaction of the signal with itself. For all processing schemes, an optimum CSPR of around 6 - 7 dB is found, representing an ideal trade-off between low signal power at high CSPR and low LO power at small CSPR. The generalized KK processing shows a 1.0 dB reduction of the optimum CSPR compared with heterodyne reception without KK processing. **(b)** EVM as a function of the symbol rate for a CSPR of 7 dB and a total incident THz power of P_THz = 340 µW. The inset shows the constellation diagram for a symbol rate of 60 GBd, for which an EVM of -9.4 dB is recorded. **(c)** EVM as a function of P_THz for a symbol rate of 30 GBd and a CSPR of 7 dB. The performance advantages of generalized KK processing are most pronounced at high terahertz powers, where the SBD receiver characteristics cannot be approximated by a square-root relationship. An exemplary constellation diagram for a 30 GBd QPSK signal is shown in the inset. *Copyright © Springer Nature.*

Next, we evaluate the EVM for various symbol rates of up to 60 GBd at a total THz power of P_THz = 340 µW and for a CSPR of 7 dB (Figure 3.4b). For lower symbol rates, generalized KK processing clearly improves the signal quality. At higher symbol rates, thermal noise and quantization noise are the dominant limitations, and the three processing schemes converge in their performance. The inset of Figure 3.4b shows the constellation diagram for the 60 GBd transmission, for which an EVM of −9.4 dB is measured. For this case, the bit error probability could be reliably estimated by measuring the BER. The BER of 1.9×10^{-3} is below the threshold of 4.4×10^{-3} for forward error correction (FEC) with 7% overhead [90] and leads to a net data rate of 112 Gbit/s.

In a third measurement, we investigate the dependence of the EVM on the incident terahertz power for a symbol rate of 30 GBd and a CSPR of 7 dB (Figure 3.4c). For small terahertz powers, where the SBD characteristics can be approximated by a square-root relationship, the performance of generalized KK processing is similar to that of the conventional KK scheme. In this regime, KK processing does not show a strong advantage over heterodyne reception, because the unwanted interaction products of the signal with itself are comparable to or even smaller than the receiver noise power. At large terahertz powers, we observe an improvement in the EVM from -12.6 dB obtained from conventional KK processing to -14.7 dB for the generalized KK scheme. Assuming that the signal impairments can be modelled as additive white Gaussian noise, this would correspond to a BER improvement [88,89] from 1×10^{-5} to 3×10^{-8}.

The same set of measurements is repeated with 16QAM signalling, that is, at double the spectral efficiency. In these experiments, we were able to directly measure the BER for a sequence of 1.6×10^{5} received symbols. For better comparison with the QPSK results, we also show the EVM evaluation in Appendix C.10. The CSPR analysis (Figure 3.5a) exhibits a behaviour similar to that for QPSK. In both cases, the generalized KK processing shows a slight reduction of the optimum CSPR compared with heterodyne reception without KK processing. This reduction amounts to 1.0 dB for QPSK and to 1.9 dB for 16QAM and is less pronounced than usually observed in optical communications [91]. Note that a direct comparison of our generalized terahertz KK receiver with its conventional optical counterpart is difficult – the underlying nonlinearity in our experiment has pronounced third- and fourth-order contributions, whereas an optical receiver exhibits a nearly perfect quadratic characteristic. This leads to different spectral shapes of the signal-signal mixing products and hence to different CSPR-dependent impairments.

The evaluation of the BER for various symbol rates at a terahertz power $P_{\mathrm{THz}} = 340\ \mu\mathrm{W}$ and a CSPR of 7 dB is shown in Figure 3.5b. When using heterodyne reception without KK processing, the BER is larger than the FEC limit for 7% overhead, even for symbol rates as small as 10 GBd. Conventional KK processing does not noticeably improve the BER, because higher-order

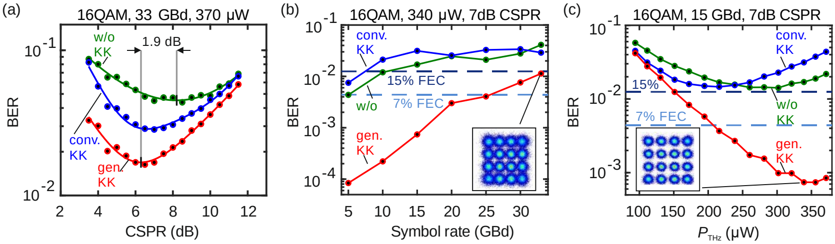

Figure 3.5: Results of the 16QAM transmission experiments bridging a distance of 110 m. **(a)** BER as a function of the CSPR for 16QAM transmission at a symbol rate of 33 GBd at a terahertz power $P_{\text{THz}} = 370$ µW. The CSPR analysis compares generalized KK processing ('gen. KK'), conventional KK reception ('conv. KK'), and heterodyne detection without any KK processing ('w/o KK') and exhibits similar behaviour to that for QPSK (Figure 3.4a). Here also, the generalized KK processing shows a slight reduction of the optimum CSPR with respect to heterodyne reception without KK processing. This reduction amounts to 1.9 dB. **(b)** BER as a function of the symbol rate at a CSPR of 7 dB and a terahertz power $P_{\text{THz}} = 340$ µW. Employing generalized KK reception, the BER stays below the 15% FEC limit and leads to a line rate of 132 Gbit/s and a net data rate of 115 Gbit/s when accounting for FEC overhead. The inset shows a constellation diagram for a symbol rate of 33 GBd. **(c)** BER as a function of the terahertz power P_{THz} for a symbol rate of 15 GBd and a CSPR of 7 dB. For high terahertz powers, generalized KK processing allows the BER to be reduced by more than an order of magnitude. This leads to clearly distinguishable constellation points as shown in the inset. *Copyright © Springer Nature.*

mixing products of the SBD have strong impact for the comparatively high terahertz power of 340 µW. In contrast to this, generalized KK processing allows for substantial improvement of the BER, achieving a reduction of more than an order of magnitude for small symbol rates. For higher symbol rates, thermal noise again limits the performance of the reception, reducing the performance advantage of generalized KK processing. Nevertheless, for a 16QAM symbol rate of 33 GBd and generalized KK processing, the BER is still below the 15% FEC limit of 1.25×10^{-2} [92]. This leads to a line rate of 132 Gbit/s before FEC and to a net data rate of 115 Gbit/s, which represents the highest data rate so far demonstrated for wireless terahertz transmission over distances of more than 100 m.

Finally, we investigate the dependence of the BER on the incident terahertz power for a symbol rate of 15 GBd and a CSPR of 7 dB (Figure 3.5c). We find that generalized KK processing leads to a clear performance advantage over a wide range of incident terahertz powers. This demonstrates the capability of our approach, especially if phase-noise-sensitive spectrally efficient QAM formats are used.

Note that the 16QAM net data rate of 115 Gbit/s is even slightly larger than the 112 Gbit/s achieved for QPSK. This result may seem counterintuitive at first glance: by going from QPSK (2 bit per symbol) to 16QAM (4 bit per symbol), the symbol rate and hence the analogue signal bandwidth can be reduced by a factor of two, which improves the signal-to-noise ratio (SNR) by 3 dB, assuming a spectrally white noise floor. At the same time, the reduced spacing of the 16QAM constellation points increases the SNR requirement [93] by more than 6 dB. Hence, for a communication channel without bandwidth limitations, the overall transmission performance for QPSK should be better than that for 16QAM. In our case, however, the channel is bandwidth-limited by the baseband circuitry at the SBD output, which deteriorates the QPSK signal at high symbol rates, but which does not affect the less broadband 16QAM signal. We believe that the improved spectral efficiency of 16QAM will become important in view of future regulations of the terahertz spectrum [94], which will require more efficient use of this scarce resource. We therefore also tested 32QAM transmission, leading to a smaller data rate than 16QAM, which is well in line with the expectations based on the high SNR requirements [93], see Appendix C.8. Still, we observe clear performance advantages of the generalized KK scheme compared with its conventional counterpart. In the future, 32QAM transmission might benefit from advances in terahertz amplifier technology, leading to higher saturation output powers and lower noise figures.

3.5 Summary

In summary, we have demonstrated a greatly simplified coherent receiver scheme for terahertz data signals, combining an SBD as a simple envelope detector with generalized KK signal processing. Our scheme accounts for the real characteristics of the SBD and leads to a substantial performance improvement compared with conventional square-root KK processing or with heterodyne reception without guard band. We demonstrate the viability of the scheme using QPSK, 16QAM, and 32QAM signalling, and achieve line rates of up to 132 Gbit/s, which correspond to net data rates of up to 115 Gbit/s when accounting for the overhead of FEC. We believe that the technical simplicity of the presented KK receiver is a unique advantage, which, in combination with further advances of terahertz technology, may be key to making terahertz communication systems a viable option for future high-capacity wireless infrastructures.

[end of paper [J4]]

4 Wireless THz link with optoelectronic transmitter and receiver

This chapter reports on a wireless T-wave data transmission experiment that complements optoelectronic signal generation at the transmitter by optoelectronic downconversion at the receiver and is taken from a publication in *Optica* [J3]. In order to fit the structure and layout of this document, it was adapted accordingly. Supplementary Information associated with the manuscript can be found in Appendix D.

[start of paper [J3]]

Wireless THz link with optoelectronic transmitter and receiver

Optica, Volume 6, pages 1063–1070 (2019)
DOI: 10.1364/OPTICA.6.001063

T. Harter[1,2], S. Ummethala[1,2], M. Blaicher[1,2], S. Muehlbrandt[1,2], S. Wolf[1], M. Weber[1], M. M. H. Adib[1], J. N. Kemal[1], M. Merboldt[1], F. Boes[3], S. Nellen[4], A. Tessmann[5], M. Walther[5], B. Globisch[4], T. Zwick[3], W. Freude[1], S. Randel[1], C. Koos[1,2]

[1] Karlsruhe Institute of Technology, Institute of Photonics and Quantum Electronics, 76131 Karlsruhe, Germany
[2] Karlsruhe Institute of Technology, Institute of Microstructure Technology 76344 Eggenstein-Leopoldshafen, Germany
[3] Institute of Radio Frequency Engineering and Electronics (IHE), Karlsruhe Institute of Technology (KIT), 76131 Karlsruhe, Germany
[4] Fraunhofer Institute for Telecommunications, Heinrich Hertz Institute (HHI), 10587 Berlin, Germany
[5] Fraunhofer Institute for Applied Solid State Physics (IAF), 79108 Freiburg, Germany

Photonics might play a key role in future wireless communication systems that operate at THz carrier frequencies. A prime example is the generation of THz data streams by mixing optical signals in high-speed photodetectors. Over previous years, this concept has enabled a series of wireless transmission experiments at record-high data rates. Reception of THz signals in these experiments, however, still relied on electronic circuits. In this paper, we show that wireless THz receivers can also greatly benefit from optoelectronic signal processing techniques, in particular when carrier frequencies beyond 0.1 THz and wideband tunability over more than an octave is required. Our approach relies on a high-speed photoconductor and a photonic local oscillator for optoelectronic downconversion of THz data signals to an intermediate frequency band that is easily accessible by conventional microelectronics. By tuning the frequency of the photonic local oscillator, we can cover a wide range of carrier frequencies between 0.03 and 0.34 THz. We demonstrate line rates of up to 10 Gbit/s on a single channel and up to 30 Gbit/s on multiple channels transmitted over a distance of 58 m. To the best of our knowledge, our experiments represent the first demonstration of a THz communication link that exploits optoelectronic signal processing techniques both at the transmitter and the receiver.

4.1 Introduction and background

Data traffic in wireless communication networks is currently doubling every 22 months [1] and will account for more than 70 % of the overall internet traffic by 2022. Sustaining this growth requires advanced network architectures that combine massive deployment of small radio cells [81,95,96] with powerful backhaul infrastructures that exploit high-capacity wireless point-to-point links. Such links may be efficiently realized by exploiting THz carriers in low-loss atmospheric transmission windows [97], thereby offering data rates of tens or even hundreds of Gbit/s. To generate the underlying communication signals at the THz transmitter, optoelectronic signal processing [2,79,98–101] has emerged as a particularly promising approach, leading to demonstrations of wireless transmission at line rates of 100 Gbit/s and beyond [39,46,55,58,60,76,80]. At the THz receiver, however, the advantages of optoelectronic signal processing have not yet been exploited.

In this paper, we show that wireless THz Rx can benefit from optoelectronic signal processing techniques as well, in particular when carrier frequencies beyond 0.1 THz and wideband tunability are required [102,103]. We exploit a high-speed photoconductor and a photonic local oscillator (LO) for terahertz-to-electrical downconversion over a broad range of frequencies between 0.03 and 0.34 THz. In our experiments, we demonstrate a coherent wireless link that operates at a carrier frequency of 0.31 THz and allows line rates of up to 10 Gbit/s on a single channel and up to 30 Gbit/s on multiple channels, transmitted over a distance of 58 m. To the best of our knowledge, this represents the first demonstration of a THz communication link that complements optoelectronic signal generation at the Tx by optoelectronic downconversion at the Rx.

The vision of a future wireless network architecture is shown in Figure 4.1a. The increasing number of terminal devices and the advent of new data-hungry applications require a dense mesh of small radio cells to provide ubiquitous broadband wireless access [81,95,96]. Backhauling of these cells relies on high-speed wireless point-to-point links, which are seamlessly integrated into fibre-optic networks [104,105]. The high data rates required for wireless backhauling infrastructures are achieved by using carrier frequencies in the range of 0.1 THz to 1 THz (T-waves). Figure 4.1b shows the atmospheric T-wave attenuation as a function of frequency [7], revealing several transmission windows with low loss which can be used for wireless communications. For highest flexibility and performance, T-wave Tx and Rx should be able to switch between various windows depending on channel occupancy and weather conditions. At the Tx, this can be achieved by optoelectronic T-wave signal generation, Figure 4.1c, which relies on mixing of an optical data signal at a carrier frequency with a continuous-wave (c.w.) tone at a frequency $f_{\mathrm{S,b}}$ in a high-speed photodiode (optical-to-T-wave, O/T conversion). This leads to a T-wave data signal centred at the carrier frequency $f_{\mathrm{S}} = \left| f_{\mathrm{S,a}} - f_{\mathrm{S,b}} \right|$, which can be widely tuned by changing the frequency $f_{\mathrm{S,b}}$ of the unmodulated optical tone. Note that similar optoelectronic Tx concepts have been used in earlier demonstrations [39,46,55,58,76,80], but were complemented by an electronic Rx that cannot match the wideband tunability of the Tx. To overcome this limitation, we have implemented an optoelectronic Rx that requires neither an electronically generated local oscillator nor an electronic mixer for coherent reception, but

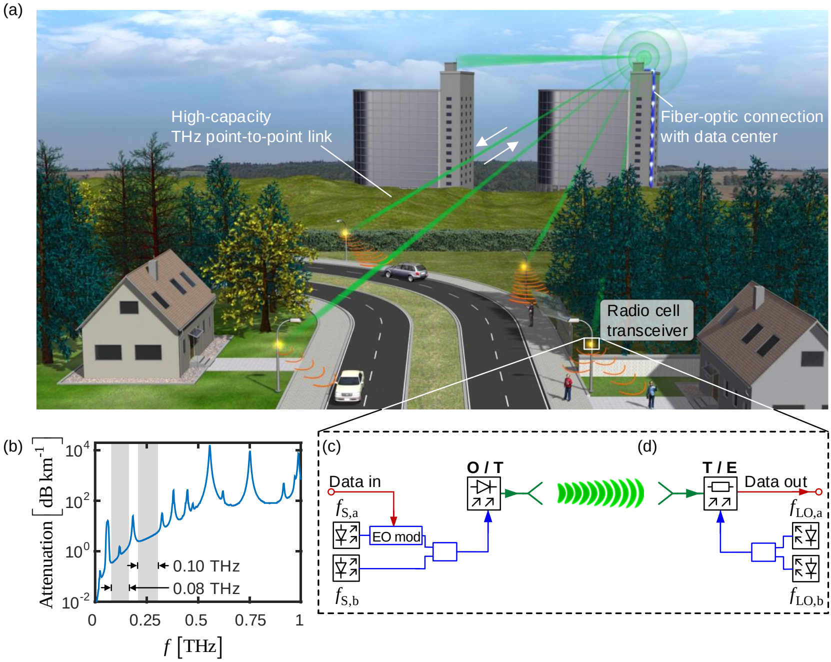

Figure 4.1: T-wave wireless infrastructure using optoelectronic signal processing techniques. **(a)** Vision of a future wireless network architecture. A dense mesh of small radio cells provides broadband wireless access to a vast number of users and devices. The high data rates required for the underlying wireless backhauling infrastructures are provided by high-speed wireless point-to-point links that are operated at THz frequencies and that can be efficiently interfaced with fibre-optic networks. **(b)** T-wave atmospheric attenuation [7] for standard conditions (temperature of 15 °C, water-vapour content of 7.5 g/m^3). Various windows with low attenuation can be used for T-wave communications. Our Rx allows operation over a wide range of frequencies between 0.03 THz and 0.34 THz, in which the atmospheric attenuation is small enough to permit transmission over technically relevant distances. **(c)** Optoelectronic T-wave signal generation. The data signal is modulated on an optical continuous-wave (c.w.) tone with frequency $f_{\mathrm{S,a}}$ by an electro-optic modulator (EO mod). The modulated signal is superimposed with an unmodulated c.w. tone $f_{\mathrm{S,b}}$, and the optical signal is converted to a T-wave signal in a high-speed photodiode (optical-to-T-wave conversion, O/T), where the carrier frequency of the T-wave is given by the frequency difference $f_{\mathrm{S}} = \left| f_{\mathrm{S,a}} - f_{\mathrm{S,b}} \right|$. The T-wave is radiated into free space by an antenna. **(d)** Optoelectronic coherent T-wave reception. The T-wave data signal is downconverted in a photoconductor where the optical power beat $f_{\mathrm{LO}} = \left| f_{\mathrm{LO,a}} - f_{\mathrm{LO,b}} \right|$ of two unmodulated c.w. tones acts as photonic local oscillator (T-wave-to-electric conversion, T/E). *Reprinted with permission from [J3] © The Optical Society.*

relies on a photoconductor that is driven by a photonic LO instead, Figure 4.1d. The photonic LO is generated by superimposing two optical c.w. tones with frequencies $f_{\mathrm{LO,a}}$ and $f_{\mathrm{LO,b}}$ and coupling them to the photoconductor [106–108] for downconversion of the T-wave data signal to an intermediate frequency band that is easily accessible by conventional microelectronics (T-wave-to-electric, T/E conversion). Note that optically driven photoconductors have previously been used for downconversion of T-waves in spectroscopy systems [106–110]. These demonstrations, however, are usually based on T-wave Tx and Rx that are driven by a common pair of lasers ($f_{\mathrm{S,a}} = f_{\mathrm{LO,a}}$, $f_{\mathrm{S,b}} = f_{\mathrm{LO,b}}$) for homodyne reception, and they rely on narrowband detection schemes with typical averaging times of the order of 1 ms. This corresponds to bandwidths of a few kilohertz and allows for highly sensitive reception of small T-wave power levels. In our work, we advance these concepts to enable wireless data transmission at gigahertz bandwidth over technically relevant distances, using amplitude and phase-modulated T-wave carriers for transmitting information. To this end, we make use of advanced photoconductors with engineered carrier lifetime [108], and we mount them together with high-speed transimpedance amplifiers (TIAs) [111] in a metal housing. We exploit heterodyne detection in combination with advanced digital signal processing to overcome phase noise and frequency drift associated with the free-running photonic LO at the Rx. In the following, we discuss the details of the optoelectronic Rx module, and we demonstrate a T-wave communication system.

4.2 Implementation of optoelectronic receiver

The concept and the implementation of the optoelectronic Rx is illustrated in Figure 4.2a. The T-wave data signal, oscillating at an angular carrier frequency $\omega_{\mathrm{S}} = 2\pi f_{\mathrm{S}}$, is received by a bow-tie antenna, resulting in a T-wave voltage $U(t)$ across the antenna feed points,

$$U(t) = \hat{U}_{\mathrm{S}}(t)\cos\left(\omega_{\mathrm{S}} t + \varphi_{\mathrm{S}}(t)\right). \tag{4.1}$$

In this relation, $\hat{U}_{\mathrm{S}}(t)$ is the modulated T-wave voltage amplitude, and $\varphi_{\mathrm{S}}(t)$ is the associated modulated phase. The antenna feed points are connected to the photoconductor G, which is illuminated by the photonic LO that provides a time-dependent optical power. The optical power oscillates at a frequency $\omega_{\mathrm{LO}} = 2\pi \left| f_{\mathrm{LO,a}} - f_{\mathrm{LO,b}} \right|$ with amplitude $\hat{P}_{\mathrm{LO,1}}$ and phase $\varphi_{\mathrm{P,LO}}$,

$$P_{\mathrm{LO}}(t) = P_{\mathrm{LO,0}} + \hat{P}_{\mathrm{LO,1}} \cos\left(\omega_{\mathrm{LO}} t + \varphi_{\mathrm{P,LO}}\right). \tag{4.2}$$

The free carriers generated by the absorbed optical power change the photoconductance according to

$$G(t) = \mathcal{G} P_{\mathrm{LO}}(t) = G_0 + \hat{G}_{\mathrm{LO}} \cos\left(\omega_{\mathrm{LO}} t + \varphi_{\mathrm{LO}}\right), \tag{4.3}$$

where $\mathcal{G}$ denotes a proportionality constant that describes the sensitivity of the photoconductor. Note that the phase φ_{LO} of the conductance oscillation might differ from the phase of the optical power oscillation $\varphi_{\mathrm{P,LO}}$ if the period of the LO power oscillation is in the same order of magnitude as the lifetime of the free carriers of the photoconductor. The resulting current $I(t)$ through the photoconductor is given by the product of the time-varying conductance $G(t)$ and the T-wave voltage $U(t)$, leading to mixing of the T-wave signal centred around ω_{S} and the optical LO power oscillating at ω_{LO}. After processing of the current by subsequent electronics such as a transimpedance amplifier (TIA), only the low-frequency components of the mixing product remain, leading to a downconverted current at an intermediate frequency $\omega_{\mathrm{IF}} = \left|\omega_{\mathrm{S}} - \omega_{\mathrm{LO}}\right|$,

$$I_{\mathrm{IF}}(t) = \tfrac{1}{2} \hat{G}_{\mathrm{LO}} \hat{U}_S(t) \cos\left(\omega_{\mathrm{IF}} t + \varphi_{\mathrm{S}}(t) - \varphi_{\mathrm{LO}}\right). \tag{4.4}$$

This intermediate signal contains the amplitude and phase information of the T-wave data signal. A more detailed derivation of Eqs. (4.1) - (4.4) can be found in Appendix D.1.

Figure 4.2b illustrates the technical implementation of the Rx module used for our experiments. The photoconductor [106] is connected to a bow-tie antenna, which is electrically coupled to a TIA by a metal wire bond. The photoconductor is operated without any additional DC bias, and a decoupling capacitor $C = 1$ nF is used to isolate the device from the bias that is effective at the input of the TIA, see Appendix D.2. The output of the TIA is electrically connected to a printed circuit board (PCB). The photoconductor is illuminated from the top with the optical power $P_{\mathrm{LO}}(t)$, which is coupled to the device from the

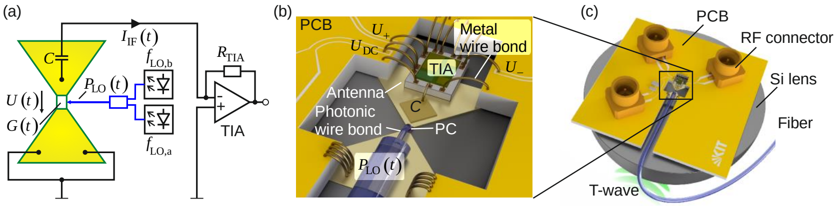

Figure 4.2: Concept and implementation of the optoelectronic coherent T-wave Rx. **(a)** Schematic of the Rx. The T-wave signal centred around a carrier frequency f_S is received by a bow-tie antenna with a photoconductor between the antenna feed points. This leads to a T-wave voltage signal $U(t)$ applied to the photoconductor. At the same time the photoconductance $G(t)$ is modulated at a frequency f_{LO} by the power beat of two unmodulated laser tones, $f_{LO} = |f_{LO,a} - f_{LO,b}|$. Both effects combined lead to a downconverted current $I_{IF}(t)$ oscillating at the difference frequency $|f_S - f_{LO}|$. The current is amplified by a transimpedance amplifier ('TIA') having a transimpedance R_{TIA}. The capacitor $C = 1\,\text{nF}$ blocks direct currents at the input circuit of the TIA. **(b)** Schematic of Rx module. The photoconductor ('PC') and the antenna are electrically connected to the input of the TIA by metal wire bonds. The differential outputs of the TIA (U_+ and U_-) are connected to a printed circuit board ('PCB'), realized as a gold-plated alumina ceramic substrate which includes RF connectors to feed the signals to a high-speed oscilloscope for further analysis. The photoconductor is illuminated with the optical power $P_{LO}(t)$ by a fibre and a 3D-printed photonic wire bond. **(c)** The Rx assembly of photoconductor, antenna, TIA, and PCB is glued on a silicon lens. This lens capture the T-wave signal incoming from the bottom and focuses it to the antenna on the surface of the photoconductor chip. *Reprinted with permission from [J3] © The Optical Society.*

horizontally positioned fibre by a photonic wire bond [112]. The entire assembly is glued on a silicon lens which captures the T-wave signal incoming from the bottom and focuses it to the antenna on the chip surface, see Figure 4.2c. The assembly is placed in a metal housing for effective electromagnetic shielding. A microscope image of the fabricated device and a more detailed description of the Rx module in terms of conversion efficiency, bandwidth and noise can be found in Appendix D.2.

4.3 Demonstration of wireless T-wave links

In the following, we demonstrate the viability of our receiver concept in a series of experiments, covering both single-channel and multi-channel transmission of THz data signals. For the single-channel experiments, our focus was on demonstrating the wideband tunability of the carrier frequency. The multi-channel experiment shows the scalability of the approach towards high-throughput parallel transmission.

4.3.1 Single-channel transmission and wideband tunability

The wireless transmission system for single-channel transmission is illustrated in Figure 4.3a. As a data source we use an arbitrary waveform generator (AWG), which provides a quadrature phase-shift-keying (QPSK) signal to an optical in-phase/quadrature phase (IQ) modulator. The modulator is fed with an optical carrier at frequency $f_{\mathrm{S,a}}$ generated by a tunable laser. The modulated data signal is superimposed with an unmodulated optical carrier at frequency $f_{\mathrm{S,b}}$. The optical power spectrum of the data signal and the unmodulated laser tone for a 3 GBd QPSK signal and a frequency spacing of $f_{\mathrm{S}} = \left| f_{\mathrm{S,a}} - f_{\mathrm{S,b}} \right| = 0.310\,\mathrm{THz}$ is shown in Inset 1 of Figure 4.3a. For O/T-conversion, the superimposed optical signals are fed to a commercially available uni-travelling-carrier photodiode (UTC-PD) [86]. The T-wave signal is then radiated into free space by a horn antenna and a subsequent THz lens made from polytetrafluoroethylene (PTFE) collimates the radiation. The transmission distance amounts to 58 m and is only limited by the size of our building. At the Rx, we use another lens and a horn antenna to couple the T-wave signal into a WR 3.4 hollow waveguide that is connected to a two-stage T-wave amplifier [22]. At the output of the amplifier, another horn antenna is used to feed the signal to the photoconductor via a silicon lens and a bow-tie antenna that is co-integrated with the device. For T/E-conversion, the photoconductor is illuminated by a photonic LO, see power spectrum in Inset 2 of Figure 4.3a. A comprehensive description of the transmission setup is given in Appendix D.3, and a discussion of the link budget as well as of the noise contributions of T-wave amplifiers and the baseband circuits can be found in Appendix D.5. The total gain of the two-stage T-wave amplifier ranges from 42 dB to 49 dB in a frequency range from 0.260 THz to 0.335 THz, thereby overcompensating the loss of the 58 m-long free-space link. The noise figure of the amplifier cascade amounts to approximately 10 dB, see Appendix D.4 for details.

The output signal of the photoconductor is fed to a TIA, Figure 4.2b, and the amplified signals are then recorded by a real-time oscilloscope (Osc.) and stored

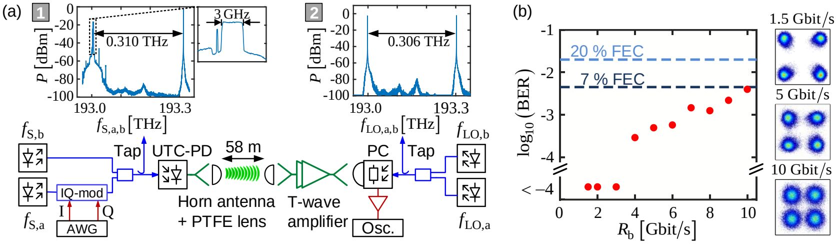

Figure 4.3: Experimental demonstration of T-wave wireless transmission. **(a)** Experimental setup. At the Tx, an optical quadrature phase shift keying (QPSK) signal at a carrier frequency $f_{S,a}$ is generated by an IQ-modulator driven by an arbitrary-waveform generator (‘AWG’). The optical signal is then superimposed with an unmodulated optical c.w. tone at frequency $f_{S,b}$ and converted to a T-wave data signal by a high-speed uni-travelling carrier photodiode (‘UTC-PD’). The T-wave is radiated into free space by a horn antenna and a subsequent PTFE lens. The frequency of the T-wave carrier depends on the frequency difference of the lasers $f_S = \left| f_{S,a} - f_{S,b} \right| = 0.310\,\mathrm{THz}$. At the Rx, two c.w. laser tones with frequencies $f_{LO,a}$ and $f_{LO,b}$ are superimposed to generate an optical power beat, which acts as local oscillator (photonic LO) for coherent downconversion of the T-wave by an antenna-coupled photoconductor. The wireless transmission link spans a distance of 58 m. To compensate the transmission loss, we use a two-stage T-wave amplifier in front of the Rx. The received data signal is recorded by a real-time oscilloscope (‘Osc.’) and offline digital signal processing is used to analyze the data. **Inset 1:** Optical spectrum (180 MHz resolution bandwidth, RBW) at the Tx for a 3 GBd QPSK data stream and a T-wave carrier frequency of $f_S = 0.310\,\mathrm{THz}$. The spectrum was recorded after a monitoring tap (‘Tap’) introducing an attenuation of 12 dB. The overall optical power entering the UTC-PD amounts to 12.8 dBm (19 mW). **Inset 2:** Optical spectrum (180 MHz RBW) of the photonic LO at the Rx for $f_{LO} = 0.306\,\mathrm{THz}$. The spectrum was recorded after an optical tap introducing an attenuation of 18 dB. The overall optical power coupled to the photoconductor amounts to 19 dBm (80 mW). **(b)** Measured bit error ratio (BER) for QPSK data streams with various line rates R_b transmitted at a T-wave carrier frequency of around 0.310 THz. For line rates up to 10 Gbit/s, a BER below the threshold for forward-error correction (FEC) with 7% overhead is achieved. For the data points shown at the bottom ($\log_{10}(\mathrm{BER}) < -4$), no errors were measured in our recording length of 10^5 symbols. Constellation diagrams for selected data rates of 1.5 Gbit/s, 5 Gbit/s, and 10 Gbit/s are shown on the right. Note that for an optical input power of 19 mW into the UTC-PD at the Tx, the T-wave power received by the Rx horn antenna after the free-space link was already sufficient to partially saturate the T-wave amplifier cascade. This leads to an asymmetric distribution of the noise around the various constellation points at 1.5 Gbit/s, where the limited TIA bandwidth does not play a role. *Reprinted with permission from [J3] © The Optical Society.*

for offline digital signal processing (DSP). The T-wave Rx relies on a heterodyne detection scheme $(f_S \neq f_{LO})$, where the photonic LO is placed at the edge of the T-wave data spectrum, which leads to electrical signals centred around the intermediate frequency $f_{\mathrm{IF}} = \left| f_{\mathrm{S}} - f_{\mathrm{LO}} \right|$. The in-phase and the quadrature components of the QPSK baseband signals are then extracted from the intermediate signals by DSP, comprising standard procedures such as digital frequency downconversion, timing recovery, constant-modulus equalization, frequency offset compensation, and carrier phase estimation.

Figure 4.3b shows the bit error ratio (BER) measured for various line rates R_{b} at a carrier frequency of 0.31 THz. For line rates below 3 Gbit/s, no errors are measured in our recording length of 10^5 symbols, demonstrating the excellent performance of the optoelectronic Rx. The constellation diagrams for line rates of 1.5 Gbit/s, 5 Gbit/s and 10 Gbit/s are shown in the insets. For larger line rates, the received signal quality decreases mainly due to limitations of the TIA in the intermediate-frequency circuit. The TIA has a specified bandwidth of only 1.4 GHz and larger line rates would require a more broadband device. With the current TIA, we could transmit 10 Gbit/s with a BER below the threshold of forward-error correction (FEC) with 7% overhead. Note that in these experiments, the T-wave power received by the horn antenna after the free-space link was already sufficient to partially saturate the T-wave amplifier cascade. This leads to an asymmetric distribution of the noise around the various constellation points at low data rates, where the limited TIA bandwidth does not play a role, see Figure 4.3b. A more detailed discussion of T-wave amplifier saturation can be found in Appendix D.3. Note also that the transmission distance of 58 m was dictated by space limitations. With the current components, it would be possible to bridge at least twice the distance by increasing the optical power at the Tx and by using slightly lower input power levels at the Rx to avoid saturation of the T-wave amplifier cascade.

To the best of our knowledge, our experiments represent the first demonstration of a THz transmission link that complements optoelectronic generation of T-wave signals at the Tx by optoelectronic downconversion at the Rx. Similar schemes have also been demonstrated [44,45] at lower carrier frequencies, relying on a UTC-PD for optoelectronic T/E conversion. Using this Rx, a line rate of 5 Gbit/s at a carrier frequency of 35.1 GHz and a line rate of 1 Gbit/s at a carrier frequency of 60 GHz have been demonstrated with transmission distances of 1.3 m and 0.55 m, respectively. Our work relies on photoconductors with excellent linearity both with respect to the voltage and the applied optical power [102,103] and clearly demonstrates the vast potential of optoelectronic downconversion for T-wave communications at tens of Gbit/s over extended distances. To further demonstrate the flexibility of the optoelectronic Rx, we transmit 2 Gbit/s data streams at various carrier frequencies covering the entire range between 0.03 THz and 0.34 THz. Note that the setup shown in Figure 4.3a only allows to address the frequency range between 0.24 THz and 0.34 THz due to bandwidth limitations of both the UTC-PD and the T-wave amplifiers. For transmission at frequencies between 0.03 THz and 0.18 THz, we therefore omitted the amplifiers and replaced the UTC-PD by a pin-PD. The measured BER and some exemplary constellation diagrams of the transmission experiments are shown in Figure 4.4. For carrier frequencies between 0.24 THz and 0.34 THz, no errors were measured in our recordings such that we can only specify an upper limit of 10^{-4} for the BER. For carrier frequencies between 0.03 THz and 0.18 THz, comparable performance was obtained. For simplicity, the transmission experiments in the lower frequency range were performed over

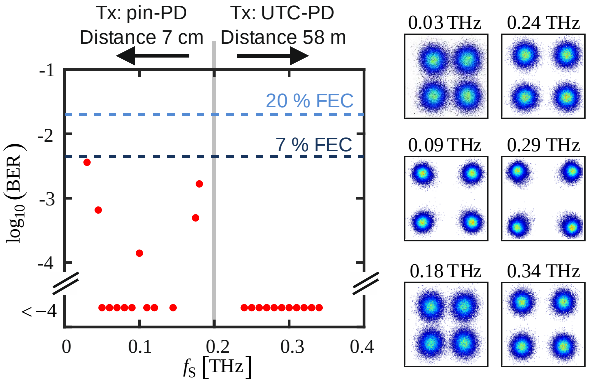

Figure 4.4: BER and constellation diagrams for various carrier frequencies at a line rate of $R_b = 2\,\text{Gbit/s}$. For the Tx we used two different types of photodiodes depending on the T-wave frequency. For T-wave frequencies $0.03\,\text{THz} \le f_S \le 0.18\,\text{THz}$ we use a lens-coupled pin photodiode (pin-PD). For simplicity, the transmission experiments in this frequency range were performed over a reduced transmission distance of 7 cm only, which could be bridged without any amplifiers. For T-wave frequencies $0.24\,\text{THz} \le f_S \le 0.34\,\text{THz}$, a waveguide-coupled uni-travelling-carrier photodiode (UTC-PD) is used in combination with a cascade of two T-wave amplifiers, as described in Figure 4.3. In both cases, the same Rx module as in Figure 4.2 was used, demonstrating its exceptional wide-band tunability. *Reprinted with permission from [J3] © The Optical Society.*

a transmission distance of 7 cm only, which could be bridged without any amplifiers. The range could be easily extended to tens or hundreds of meters by using Rx antennas that are optimized for lower frequencies in combination with amplifiers. Note also that the data points between 0.03 THz and 0.18 THz were taken on a slightly irregular frequency grid, thereby avoiding some carrier frequencies for which the free-space link of our setup features low transmission. This does not represent a fundamental problem and was caused by fading due to uncontrolled reflections in the beam path. The associated power variations could be overcome by using amplifiers with adaptive gain or by optimizing the beam path for each frequency point individually. This fading in combination with frequency-dependent Tx power and a decreasing gain of the on-chip bow-tie antenna for low frequencies is also the reason for the degraded performance of the transmission experiments at carrier frequencies of 0.03 THz, 0.04 THz, 0.10 THz, and 0.18 THz. Still, these experiments demonstrate that the same receiver concept as in Figure 4.2 can be used for carrier frequencies in a range of $0.03\,\mathrm{THz} \le f_\mathrm{S} \le 0.340\,\mathrm{THz}$, i.e. over more than a decade.

4.3.2 Multi-channel transmission

We also investigate the receiver in a multicarrier transmission experiment at carrier frequencies between 0.287 THz and 0.325 THz. We simultaneously transmit up to 20 T-wave channels (Ch 1 … 20) spaced by 2 GHz, where each channel is operated with independent QPSK signals at a symbol rate (line rate) of 0.75 GBd (1.5 Gbit/s). To keep the experimental setup simple, we use a single broadband AWG and a single IQ-modulator to generate an optical signal that simultaneously contains all channels, which is then converted to the THz range by a UTC-PD. This approach allows us to re-use the experimental setup shown on Figure 4.3a. Alternatively, multiple optical carriers and less broadband devices in combination with optical multiplexing could have been used to generate the optical channels [39]. Figure 4.5a shows the optical spectrum containing all 20 channels, measured at the monitoring tap before the UTC-PD. For compensating the spectral roll-off of the UTC-PD and the T-wave amplifiers, the channels at the edges of the T-wave transmission band are pre-emphasized, see inset of Figure 4.5a. Figure 4.5b shows the spectrum of the two optical lines which are used as photonic LO for reception of Ch 20, which

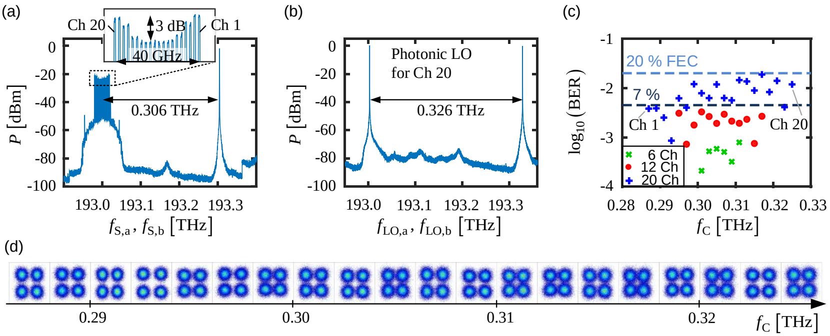

Figure 4.5: Multi-channel T-wave transmission. **(a)** Optical spectrum (180 MHz RBW) at the Tx for a signal containing 20 channels. Each channel is modulated with pulses having a raised-cosine spectrum with a roll-off factor of 0.1 and carries a 0.75 GBd QPSK signal. The channels are spaced by 2 GHz. In the UTC-PD, the channels are simultaneously downconverted to a T-wave frequency band centred at 0.306 THz. The spectrum was recorded at the optical monitoring tap after the power combiner at the Tx, Figure 4.3a, introducing an attenuation of 12 dB. The overall optical power contained in the spectrum amounts to 12.7 dBm (18.5 mW). **(b)** Optical LO spectra (180 MHz RBW) at the receiver for detection of Ch 20. For heterodyne detection, the T-wave LO frequency $f_{\mathrm{LO}} = 0.326\,\mathrm{THz}$ is chosen close to the spectral edge of the channel. The spectrum was recorded at the optical monitoring tap after the power combiner at the Rx which introduces an attenuation of 16 dB. The overall optical power contained in the spectrum amounts to 19 dBm (80 mW). **(c)** Measured BER for various numbers of channels. For 12 (20) channels, the BER is below the 7% (20%) threshold for forward error correction (FEC). This corresponds to an aggregate line rate of 18 Gbit/s (30 Gbit/s). **(d)** Constellation diagrams for all 20 channels leading to an aggregate line rate of 30 Gbit/s. *Reprinted with permission from [J3] © The Optical Society.*

features the highest THz carrier frequency of $f_S = 0.325\,\mathrm{THz}$. Note that we again used heterodyne detection at the receiver and hence chose a T-wave LO frequency $f_{\mathrm{LO}} = 0.326\,\mathrm{THz}$ close to the spectral edge of Ch 20. It is also worth mentioning that the 0.75 GBd T-wave channels were transmitted on a 2 GHz grid to avoid interference of data signals from neighbouring channels after downconversion to the intermediate frequency band. This leads to un-used spectral regions of approximately 1.2 GHz between the T-wave channels, which could be avoided by optoelectronic downconversion schemes that allow simultaneous extraction of the in-phase and the quadrature component of the T-wave signal. Figure 4.5c shows the BER for transmission experiments with 6, 12, and 20 channels. For transmission of 12 channels (aggregate line rate

18 Gbit/s), the BER stays below the 7% FEC limit, whereas for 20 channels (30 Gbit/s), 20% FEC overhead is required. Figure 4.5d shows the constellation diagrams of the 20-channel experiment. The BER degradation with increasing channel count is mainly caused by the fact that the overall power available at the output of the Rx T-wave amplifier cascade is limited. A higher number of channels thus leads to a reduced power per channel and hence to a reduced signal-to-noise power ratio (SNR). Compared to the single-channel transmission experiment, we expect an SNR reduction of 7.8 dB, 10.8 dB and 13 dB, respectively, through the splitting of the power among 6, 12, and 20 channels. This is in good agreement with our measurement, where we find an SNR reduction of approximately 6.5 dB, 9.8 dB and 12.3 dB, respectively, see Appendix D.3 for details. Note that the different channels in our multi-channel experiments were measured sequentially. While this is a usual approach in multi-channel THz transmission experiments [39,60,76], parallel reception of the entire data stream would be desirable. In this context, T-wave demultiplexers might become highly relevant in the future [113,114].

4.3.3 Potential for further improvements

While optoelectronic signal processing features a series of conceptual advantages such as wideband tunability of the carrier frequency and the ability to address high carrier frequencies at hundreds of GHz, the data rates demonstrated in our proof-of-concept experiments are still smaller than those achieved with best-in-class all-electronic devices. Competing all-electronic approaches may, e.g., rely on advanced millimetre-wave integrated circuits (MMIC) operating in the V-band (57 … 66 GHz) or the E-bands (71 … 76 GHz and 81 … 86 GHz) [115]. For single-input-single-output (SISO) transmission in this frequency range, impressive data rates of up to 80 Gbit/s were demonstrated [47] using a transmission bandwidth of approximately 20 GHz centred at a carrier frequency of 77 GHz. In this context, it is important to note that the data rates of 30 Gbit/s achieved by our proof-of-concept experiment is a first step but represents by no means the highest achievable performance and leaves substantial room for further improvements both on a device and a system level.

The main limitation of the current implementation is the small conversion efficiency of the photoconductor, ranging between – 51 dB and – 64 dB depending on the carrier frequency and power of the photonic LO, see Appendix D.2. Improving the conversion efficiency is subject to current research [106,116] and might drastically enhance the performance of the optoelectronic receiver. In this context, plasmonic photoreceivers with strongly bias-dependent responsivity [101,117] might be a particularly compact alternative to conventional photoconductors. Note that the conversion efficiency specified for our current experiment also includes the coupling losses introduced by the free-space section between the output of the T-wave amplifier cascade and the photoconductor, see Appendix D.5 for details. Co-integrating or co-packaging of the T-wave amplifiers and the subsequent photoconductor using, e.g., hollow waveguides in metallic split-block assemblies [118], could not only avoid these losses, but also improve the spectral uniformity of the receiver characteristics. Further improvements are expected from constantly improving T-wave amplifiers and TIA. Specifically, the per-channel symbol rate in our current experiments was only limited by the bandwidth of the TIA. Using more broadband devices [119], symbol rates of more than 25 GBd may be achieved in the future. Photoconductors with increased conversion efficiency, improved T-wave amplifiers with higher saturation output power, and faster TIA with optimized baseband circuitry could allow more broadband systems with significantly better SNR and hence higher margin to FEC thresholds. This would also pave the path towards advanced modulation formats, such as 16-state quadrature amplitude modulation (16QAM), which are frequently used in fibre-optic communication systems. Taken together, these improvements could allow for data rates beyond 100 Gbit/s per channel. Regarding the transmission distance, the demonstrated 58 m are only limited by the available space and could be further increased, e.g., by using higher transmitter power levels.

Besides improved performance, a real system implementation would also require a compact integrated receiver assembly. Our experiment already demonstrates compact integration of the photoconductor with the subsequent TIA in a single metal housing, and co-integration with the T-wave amplifiers might be the next step [21]. In the future, the photoconductor might even be combined with advanced photonic circuitry [120,121] into chip-scale optoelectronic T-wave transceiver modules, comprising, e.g., the photonic LO or additional passive optical circuits [101,122].

4.4 Summary

In summary, we showed a first demonstration of a coherent wireless THz communication system using optoelectronic signal processing both at the transmitter and at the receiver. Our experiments show that the same receiver concept can be used over a broad frequency range $0.03\,\text{THz} \leq f_\text{S} \leq 0.340\,\text{THz}$, spanning more than a decade. We transmit a line rate of 10 Gbit/s using a single T-wave channel at a carrier frequency of 0.31 THz with a BER below the 7% FEC limit. In this experiment, the line rate was limited by the bandwidth of the transimpedance amplifier, but not by the transmitter and receiver scheme. We further demonstrate multi-channel transmission using up to 20 carriers with frequencies in the range between 0.287 THz and 0.325 THz. This leads to an aggregate line rate of 30 Gbit/s with a BER below the threshold for a FEC with 20% overhead. The single and the multi-channel T-wave link bridges a distance of 58 m, limited by the available space. Our findings demonstrate that coherent T-wave receivers with an widely tunable optoelectronic local oscillator may build the base of a novel class of THz communication systems.

[end of paper [J3]]

5 Silicon-plasmonic integrated circuits for THz signal generation and coherent detection

In this chapter, a new concept for T-wave transmitters and receivers is suggested, which can be implemented on the silicon platform. This is attractive for integrated T-wave systems which combine T-wave devices with advanced silicon photonic circuits.

This chapter is taken from a publication in *Nature Photonics* [J2]. In order to fit the structure and layout of this document, it was adapted accordingly. Methods and Supplementary Information associated with the manuscript can be found in Appendix E. This article was also discussed in the News & Views of Nature Photonics [123].

[start of paper [J2]]

Silicon-plasmonic integrated circuits for terahertz signal generation and coherent detection

Nature Photonics, Volume 12, pages 625–633 (2018)
DOI: 10.1038/s41566-018-0237-x

T. Harter[1,2], S. Muehlbrandt[1,2], S. Ummethala[1,2], A. Schmid[1],
S. Nellen[3], L. Hahn[2], W. Freude[1], and C. Koos[1,2]

[1] Karlsruhe Institute of Technology, Institute of Photonics and Quantum Electronics, 76131 Karlsruhe, Germany
[2] Karlsruhe Institute of Technology, Institute of Microstructure Technology 76344 Eggenstein-Leopoldshafen, Germany
[3] Fraunhofer Institute for Telecommunications, Heinrich Hertz Institute, 10587 Berlin, Germany

Optoelectronic signal processing offers great potential for generation and detection of ultra-broadband waveforms in the terahertz range (so-called T-waves). However, fabrication of the underlying devices still relies on complex processes using dedicated III–V semiconductor substrates. This severely restricts the application potential of current T-wave transmitters and receivers and impedes co-integration of these devices with advanced photonic signal processing circuits. Here, we demonstrate that these limitations can be overcome by plasmonic internal-photoemission detectors (PIPEDs). PIPEDs can be realized on the silicon photonic platform, which allows exploiting the enormous opportunities of the associated device portfolio. In our experiments, we demonstrate both T-wave signal generation and coherent detection at frequencies up to 1 THz. To prove the viability of our concept, we monolithically integrate PIPED transmitters and receivers on a common silicon chip and use them to measure the complex transfer impedance of an integrated T-wave device.

5.1 Introduction

Terahertz signals (T-waves) offer promising perspectives for a wide variety of applications, including high-speed communications [2,39,113], microwave photonics [124], spectroscopy [125,126], life sciences [4,127], as well as industrial metrology [128,129]. Optoelectronic signal processing techniques are particularly attractive for both T-wave generation [2,37,130] and detection [106,131], especially when broadband tunability of the terahertz frequency is required. On a conceptual level, optoelectronic generation of continuous-wave (c.w.) terahertz signals relies on mixing two optical signals oscillating at frequencies f_a and f_b in a high-speed photodetector, for which the photocurrent depends on the incident optical power [130]. The photocurrent oscillates with a difference frequency $f_{\mathrm{THz}} = |f_a - f_b|$ in the terahertz region, which can be relatively easily adjusted over the full bandwidth of the photodetector by frequency-tuning one of the two lasers. In many practical applications, the optical signal oscillating at f_a carries an amplitude or phase modulation, whereas the optical signal at f_b is simply a c.w. carrier. In this case, the phase and amplitude modulation of the optical carrier is directly transferred to the T-wave carrier. This concept shows great potential for high-speed wireless communications at terahertz carrier frequencies and has been at the heart of a series of transmission experiments, in which record-high data rates of 100 Gbit/s and above have been reached [39,55,76]. Similarly, optoelectronic techniques can be used for detection of T-wave signals. In this case, the T-wave signal is applied to a high-speed photoconductor and the optical power oscillation at the difference frequency $f_{\mathrm{THz}} = |f_{\mathrm{a}} - f_{\mathrm{b}}|$ is used as a local oscillator (LO) for coherent downconversion to the baseband [106,131]. This technique was initially developed for frequency-domain terahertz spectroscopy systems offering a widely tunable frequency range and a high signal-to-noise ratio [106,132,133], and has recently been transferred to terahertz communications [103].

To exploit the tremendous application potential of optoelectronic T-wave processing, monolithic co-integration of photonic devices and T-wave transmitters and receivers is of vital importance. From the technology side, however, optoelectronic T-wave transmitters and receivers are still rather complex, relying on high-speed photodiodes [134–136] or photoconductors [38,106,137] that require dedicated III–V semiconductor substrates (obtained, for example, through low-temperature growth of InGaAs/InAlAs multilayer structures [106]) and which are not amenable to large-scale photonic integration. This not only hampers the co-integration of T-wave transmitter and receiver circuitry on a common chip, but also hinders the exploitation of highly developed photonic integration platforms to build advanced optoelectronic T-wave systems that combine photonic signal processing with optoelectronic frequency conversion on a common chip.

In this Article, we demonstrate an approach that allows the integration of T-wave transmitters and receivers directly on the silicon photonic platform, thereby exploiting the outstanding technical maturity, scalability and the comprehensive device portfolio [138–140] of this material system. The approach exploits internal photoemission at the metal–semiconductor interfaces of plasmonic structures [117,141] which can be directly integrated into widely used silicon-on-insulator (SOI) waveguides. Our experiments show that these plasmonic internal-photoemission detectors (PIPEDs) are not only suited for photomixing at the T-wave transmitter, but also lend themselves to highly sensitive optoelectronic reception. In a proof-of-concept experiment, we monolithically co-integrated a PIPED transmitter and a PIPED receiver on a common silicon photonic chip and used them to measure the complex transfer function of an integrated T-wave transmission line. In this context, we also developed and experimentally verified a mathematical model of optoelectronic T-wave conversion that allows us to quantitatively describe T-wave generation and detection over a wide range of frequencies.

5.2 Silicon-plasmonic T-wave systems

The vision of an integrated silicon-plasmonic T-wave system is illustrated in Figure 5.1 using a wireless high-speed transceiver as an exemplary application case. The system combines a T-wave transmitter, a T-wave receiver and a variety of other silicon photonic devices [138,139] such as phase shifters [142–144] or high-performance modulators [145–148] on a common substrate. C.w. lasers are coupled to the chip using photonic wire bonds [112], and electrical circuits such as field-programmable gate arrays (FPGA), digital-to-analog and analog-to- digital converters (DAC and ADC) are used to drive the modulators and to further process the received signals. T-wave generation is accomplished by photomixing the modulated optical signals with an optical c.w. tone in a high-speed antenna-coupled PIPED acting as an optical-to-T-wave (O/T) converter [117]. Large-scale monolithic integration of advanced silicon photonic devices with O/T converters opens up rich opportunities for advanced T-wave signal processing. Note that, for integrated T-wave systems, the generation and detection of c.w. signals offers various advantages over pulsed operation (see Appendix E.1 for details). In the example, the transmitter comprises a T-wave antenna array, fed by an array of O/T converters that are driven by a series of optical signals. The phases of the optical signals and hence those of the T-waves can be precisely defined by an electrically driven optical phase shifter network [142,143], thereby enabling broadband beam steering and shaping. Optionally, integrated T-wave amplifiers can be used to boost the T-wave signals [149]. At the receiver, optoelectronic downconversion (T/E-conversion) is used for coherent detection of the T-wave signal, using the power beat of two optical waves as a LO. For O/T and T/E conversion, the concept relies on PIPEDs that are coupled to dipole antennas (inset 1 of

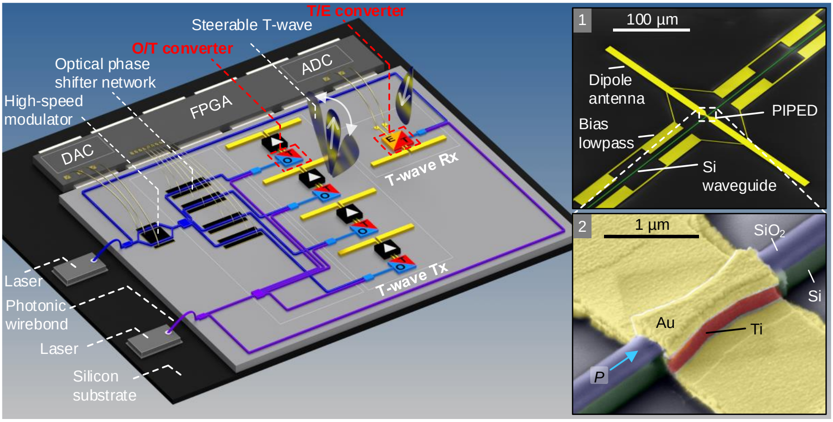

Figure 5.1: Vision of an integrated silicon-plasmonic T-wave wireless transceiver that exploits optoelectronic signal processing both at the transmitter and at the receiver. The system combines optical-to-T-wave (O/T) and T-wave-to-electronic (T/E) converters with advanced silicon photonic devices such as phase shifters or high-performance modulators. Continuous-wave lasers are coupled to the chip using photonic wire bonds [202], and electrical circuits such as field-programmable gate arrays (FPGAs), DACs and ADCs are used to drive the modulators and to process the received signals. The transmitter comprises a T-wave antenna array, fed by an array of O/T converters that are driven by a series of optical signals. The phases of the optical and hence the T-wave signals can be precisely defined by an electrically driven optical phase shifter network, thereby enabling broadband beam steering. Optionally, additional T-wave amplifiers could boost the power of the generated signals. Coherent detection of the T-wave signal relies on a pair of optical carriers, the power beat of which serves as a LO for T/E conversion. **Inset 1**: false-colour scanning electron microscopy (SEM) image of an O/T or T/E converter. The devices rely on PIPEDs [117] coupled to dipole antennas. The PIPEDs are fed through silicon photonic waveguides and biased via low-pass structures that are directly connected to the arms of the antennas. **Inset 2**: detailed view of a fabricated PIPED. The device consists of a narrow silicon nanowire waveguide that is combined with overlays of Au and Ti to form an ultrasmall plasmonic structure with two metal-semiconductor interfaces. Optical power *P* is fed to the PIPED by a silicon photonic waveguide. *Copyright © Springer Nature.*

Figure 5.1). The PIPEDs are fed through silicon photonic waveguides and electrically biased by dedicated low-pass structures that are directly connected to the arms of the dipole antennas. A more detailed view of a PIPED is shown in inset 2 of Figure 5.1. The device consists of a narrow silicon nanowire waveguide that is combined with overlays of gold (Au) and titanium (Ti) to form an ultrasmall plasmonic structure with two metal–semiconductor interfaces. Note that the PIPED concept does not rely on the use of gold as a plasmonic material – this was chosen only for ease of fabrication in the current experiment. When combined with large-scale silicon photonic circuits, gold-free designs may be used that allow processing in a state-of-the-art CMOS line [150].

5.3 PIPED for optoelectronic T-wave processing

The PIPED concept is illustrated and explained in Figure 5.2. Figure 5.2a presents a schematic cross-section of the device. The Si nanowire waveguide core is contacted by an Au layer on the left and by a Ti layer on the right (for details of the fabrication see ref. [117]). To drive the device, light at infrared telecommunication wavelengths ($\lambda \approx 1.5\ \mu\text{m}$) is coupled to the Si waveguide core, leading to excitation of surface plasmon polaritons (SPPs) both at the Au-Si and Si–Ti interfaces. The associated energy levels are sketched in Figure 5.2b for a forward bias voltage $U > 0$, which is counted positive from the Au to Ti electrode. Free-carrier absorption generates hot electrons in the titanium with carrier energies above the Fermi level $W_{\mathrm{F,Ti}}$. An equivalent effect occurs for holes at the Au–Si interface (the relative magnitude of the two contributions is currently under investigation). The hot electrons and holes have an increased probability to cross the $d = 100$ nm wide Si barrier, leading to a photocurrent I from the Au to the Ti side. The photocurrent I depends linearly on optical power P with a sensitivity (or responsivity) $S = I / P$. Note that, in contrast to conventional photodiodes, the measured sensitivity $S(U)$ of the PIPED depends strongly on the applied voltage U, as shown in Figure 5.2c. This voltage dependence is a key aspect for efficient optoelectronic T/E conversion as it allows mixing of an oscillating optical input power with a time-dependent voltage applied to the PIPED contacts. For a forward bias $U > 0$, the band edges tilt inside the Si core (Figure 5.2b), which reduces the effective width of the potential barrier such that the sensitivity S increases with U. For a reverse bias $U < 0$, the carrier emission probability is small, and so the photocurrent remains small. The strong absorption of the SPP allows junction lengths ℓ of less than 1 μm and device capacitances smaller than $C = 1$ fF (ref. [117]). With a load resistance of $R = 50\,\Omega$, this would lead to an RC limiting frequency of 3 THz. In the current device designs, this limitation is not relevant because the speed is limited by the carrier transit times, for which we estimate 1 ps for electrons and

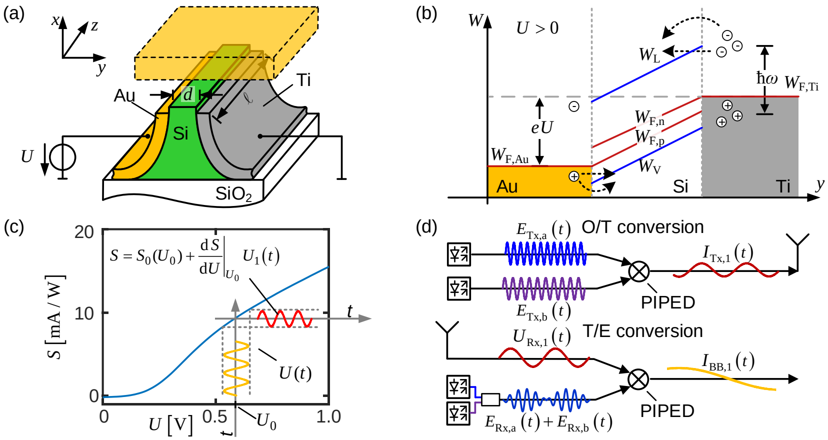

Figure 5.2: Operating principle of PIPED-based T-wave transmitters and coherent receivers. **(a)** Schematic of the PIPED, consisting of a silicon core with Au and Ti sidewalls. SPPs propagating along the z direction are mostly absorbed in the Ti due to the large imaginary part of its complex electric permittivity ε_r. A voltage U is applied between the Au and Ti electrodes. **(b)** Band diagram of the Au–Si–Ti junction. W_C and W_V denote the edges of the conduction and valence bands in the silicon core, and the Fermi levels in Au and Ti are denoted $W_\mathrm{F,Au}$ and $W_\mathrm{F,Ti}$, respectively. An applied voltage $U>0$ and the injection of carriers due to absorption of light lead to an interband non-equilibrium, which is described by the separation of the quasi-Fermi levels of conduction-band electrons and valence-band holes, denoted $W_\mathrm{F,n}$ and $W_\mathrm{F,p}$, respectively. Photons absorbed in the Ti layer excite hot electrons, which can overcome or tunnel through the Schottky potential barrier, leading to a photocurrent $I=SP$. An equivalent effect occurs for holes at the Au–Si interface. The relative magnitude of the two contributions is still under investigation. The carrier emission probability into the Si waveguide core and therefore the sensitivity $S(U)$ can be increased ($U>0$) or decreased ($U<0$) by varying bias voltage U. **(c)** Measured sensitivity $S(U)$ of the PIPED in dependence on applied voltage U. In the vicinity of a bias voltage, the sensitivity $S(U)$ can be linearized. **(d)** In essence, the PIPED can be used as a mixer that multiplies two signals to generate a waveform at the difference frequency. **Top:** when used for photomixing (O/T conversion) at the T-wave transmitter (Tx), the PIPED acts as a power detector, and the output photocurrent corresponds to the product of two time-dependent optical signals $E_\mathrm{Tx,a}(t)$ and $E_\mathrm{Tx,b}(t)$. **Bottom:** when used for optoelectronic downconversion (T/E conversion) at the T-wave receiver (Rx), the PIPED combines two functionalities, namely the generation of a terahertz LO from two optical carriers $E_\mathrm{Tx,a}(t)$ and $E_\mathrm{Tx,b}(t)$ and the downconversion of the received T-wave to the baseband. To this end, the PIPED is fed by a superposition of two unmodulated optical carriers, oscillating at frequencies $f_\mathrm{Rx,a}$ and $f_\mathrm{Rx,b}$, while a time-dependent voltage $U_\mathrm{Rx,1}(t)$ modulates the device sensitivity. The PIPED photocurrent is then given by the product of the time-variant sensitivity with the time-variant optical power $P_\mathrm{Rx}(t)$. *Copyright © Springer Nature.*

1.5 ps for holes. This estimate is based on a voltage drop of $U = 0.5\,\mathrm{V}$ within the 100-nm-wide barrier, leading to drift velocities of $10^7\,\mathrm{cm\,s^{-1}}$ for electrons and $6.5 \cdot 10^5\,\mathrm{cm\,s^{-1}}$ for holes [151], close to the respective saturation velocities. This limits the bandwidth to ~0.44 THz assuming dominating electron transport and to ~0.29 THz in case hole transport dominates [151]. The fast device response makes the PIPED an excellent candidate for T-wave generation and reception at frequencies of 1 THz and above. It is worth noting that the sensitivity of the PIPED can be increased beyond the values depicted in Figure 5.2c by applying larger bias voltages. We have previously demonstrated sensitivities of up to $0.12\,\mathrm{AW^{-1}}$ (ref. [117]) - the highest value so far demonstrated for photodetectors based on internal photoemission. This sensitivity is still below the $0.2 - 0.3\,\mathrm{AW^{-1}}$ typically achieved for the uni-travelling carrier photodiodes (UTC-PD) designed to operate at frequencies around 0.3 THz (refs. [135,152,153]), and we expect that further improvements are possible by optimizing the materials and geometries of the PIPED. Note that the sensitivity of the photodetector is not of utmost importance for the generation and detection of T-wave signals, because a smaller sensitivity can be compensated by launching a higher optical power.

For O/T conversion, the transmitter (Tx) essentially acts as a mixer multiplying two time-dependent optical signals $E_{\mathrm{Tx,a}}(t)$ and $E_{\mathrm{Tx,b}}(t)$ to produce a photocurrent $I_{\mathrm{Tx}}(t)$ that corresponds to the difference-frequency waveform, (Figure 5.2d, top). In the following, we only give a short mathematical description of photomixing and optoelectronic downconversion in the PIPED. A rigorous analysis is provided in Appendix E.2. We assume that the optical signal $E_{\mathrm{Tx,a}}(t)$ oscillates at angular frequency $\omega_{\mathrm{Tx,a}}$ and carries an amplitude modulation $\hat{E}_{\mathrm{Tx,a}}(t)$ and/or a phase modulation $\varphi_{\mathrm{Tx,a}}(t)$, whereas the optical signal $E_{\mathrm{Tx,b}}(t)$ is simply a c.w. carrier with constant amplitude $\hat{E}_{\mathrm{Tx,b}}$, frequency $\omega_{\mathrm{Tx,b}}$ and phase $\varphi_{\mathrm{Tx,b}}$:

$$\begin{aligned} E_{\mathrm{Tx,a}}(t) &= \hat{E}_{\mathrm{Tx,a}}(t)\cos\left(\omega_{\mathrm{Tx,a}}t + \varphi_{\mathrm{Tx,a}}(t)\right), \\ E_{\mathrm{Tx,b}}(t) &= \hat{E}_{\mathrm{Tx,b}}\cos\left(\omega_{\mathrm{Tx,b}}t + \varphi_{\mathrm{Tx,b}}\right). \end{aligned} \tag{5.1}$$

The optical power $P_{\mathrm{Tx}}(t)$ then oscillates at the difference frequency $\omega_{\mathrm{Tx,THz}} = \left|\omega_{\mathrm{Tx,a}} - \omega_{\mathrm{Tx,b}}\right|$,

$$P_{\mathrm{Tx,1}}(t)=\hat{P}_{\mathrm{Tx,1}}(t)\cos\left(\omega_{\mathrm{Tx,THz}}t+\varphi_{\mathrm{Tx,THz}}(t)\right), \tag{5.2}$$

here the amplitude $\hat{P}_{\mathrm{Tx,1}}(t)$ and phase $\varphi_{\mathrm{Tx,THz}}(t)$ of the oscillation are directly linked to the normalized amplitude and to the phase of the optical wave:

$$\hat{P}_{\mathrm{Tx,1}}(t)=\hat{E}_{\mathrm{Tx,a}}(t)\hat{E}_{\mathrm{Tx,b}}, \qquad \varphi_{\mathrm{Tx,THz}}(t)=\varphi_{\mathrm{Tx,a}}(t)-\varphi_{\mathrm{Tx,b}}. \tag{5.3}$$

When detected by the PIPED (sensitivity S_{Tx}), this leads to an oscillating component in the photocurrent $I_{\mathrm{Tx}}(t)$, featuring the same frequency and the same phase as the optical power oscillation:

$$I_{\mathrm{Tx,1}}(t)=\hat{I}_{\mathrm{Tx,1}}(t)\cos\left(\omega_{\mathrm{Tx,THz}}t+\varphi_{\mathrm{Tx,THz}}(t)\right), \tag{5.4}$$

where

$$\hat{I}_{\mathrm{Tx,1}}(t)=S_{\mathrm{Tx}}\hat{E}_{\mathrm{Tx,a}}(t)\hat{E}_{\mathrm{Tx,b}}. \tag{5.5}$$

Hence, any modulation of the amplitude $\hat{E}_{\mathrm{Tx,a}}(t)$ or phase $\varphi_{\mathrm{Tx,a}}(t)$ of the optical signal translates directly into an amplitude and phase modulation of the T-wave. The amplitude of the emitted terahertz field is linearly connected to the sensitivity S_{Tx} and can be increased by applying a larger forward bias to the PIPED. Exploiting this concept, broadband high-quality terahertz signals can be generated by using widely available optical communication equipment. The terahertz field is radiated by an antenna or coupled to a transmission line.

Similarly, PIPEDs can be used for T/E conversion in the T-wave receiver (Rx) (Figure 5.2d, bottom). In this case, the device combines two functionalities, namely the generation of a terahertz LO from two optical carriers and the downconversion of the received T-wave to the baseband. To this end, the PIPED is fed by a superposition of two unmodulated optical tones, oscillating at frequencies $\omega_{\mathrm{Rx,a}}$ and $\omega_{\mathrm{Rx,b}}$:

$$\begin{aligned}E_{\mathrm{Rx,a}}(t)&=\hat{E}_{\mathrm{Rx,a}}\cos\left(\omega_{\mathrm{Rx,a}}t+\varphi_{\mathrm{Rx,a}}\right),\\E_{\mathrm{Rx,b}}(t)&=\hat{E}_{\mathrm{Rx,b}}\cos\left(\omega_{\mathrm{Rx,b}}t+\varphi_{\mathrm{Rx,b}}\right).\end{aligned} \tag{5.6}$$

This leads to an oscillating power at frequency $\omega_{\mathrm{Rx,THz}} = \left|\omega_{\mathrm{Rx,a}} - \omega_{\mathrm{Rx,b}}\right|$ with phase $\varphi_{\mathrm{Rx,THz}}$:

$$P_{\mathrm{Rx,1}}(t) = \hat{P}_{\mathrm{Rx,1}} \cos\left(\omega_{\mathrm{Rx,THz}} t + \varphi_{\mathrm{Rx,THz}}\right), \tag{5.7}$$

where

$$\hat{P}_{\mathrm{Rx,1}} = \hat{E}_{\mathrm{Rx,a}} \hat{E}_{\mathrm{Rx,b}}, \quad \varphi_{\mathrm{Rx,THz}} = \varphi_{\mathrm{Rx,a}} - \varphi_{\mathrm{Rx,b}} \ . \tag{5.8}$$

At the same time, the PIPED is biased with a DC voltage $U_{\mathrm{Rx,0}}$, which is superimposed by the time-variant terahertz signal $U_{\mathrm{Rx,1}}(t)$ generated by the terahertz antenna. The overall time-dependent voltage applied to the PIPED hence reads

$$U_{\mathrm{Rx}}(t) = U_{\mathrm{Rx,0}} + U_{\mathrm{Rx,1}}(t), \tag{5.9}$$

where

$$U_{\mathrm{Rx,1}}(t) = \hat{U}_{\mathrm{Rx,1}}(t) \cos\left(\omega_{\mathrm{Tx,THz}} t + \varphi_{\mathrm{Tx,THz}}(t) - \varphi_{\mathrm{TxRx}}\right). \tag{5.10}$$

In this relation, the phase at the receiver depends on the phase delay φ_{TxRx} that the T-wave experiences when propagating from the Tx to the Rx. Due to the voltage-dependent PIPED sensitivity, the time-varying voltage $U_{\mathrm{Rx,1}}(t)$ leads to a temporal variation of the sensitivity $S_{\mathrm{Rx}}\left(U_{\mathrm{Rx,1}}(t)\right)$, oscillating at frequency $\omega_{\mathrm{Tx,THz}}$ of the incident T-wave. The PIPED photocurrent is given by the product of the time-variant sensitivity with the time-variant optical power $P_{\mathrm{Rx,1}}(t)$. For the case of homodyne detection, $\omega_{\mathrm{Rx,THz}} = \omega_{\mathrm{Tx,THz}} = \omega_{\mathrm{THz}}$, the baseband current at the output of the Rx PIPED is given by

$$\begin{aligned} I_{\mathrm{BB}}(t) &= I_{\mathrm{BB,0}} + I_{\mathrm{BB,1}}(t) \\ &= I_{\mathrm{BB,0}} + \hat{I}_{\mathrm{BB,1}}(t) \cos\left(\varphi_{\mathrm{BB}}(t)\right), \end{aligned} \tag{5.11}$$

where the amplitude $\hat{I}_{\mathrm{BB,1}}(t)$ of the time-variant part of the baseband photocurrent and the associated time-variant phase $\varphi_{\mathrm{BB}}(t)$ are connected to the amplitude and phase of the time-variant terahertz signal $U_{\mathrm{Rx,1}}(t)$:

$$\begin{aligned} \hat{I}_{\mathrm{BB},1}(t) &= \tfrac{1}{2} \left. \frac{\mathrm{d}S_{\mathrm{Rx}}}{\mathrm{d}U_{\mathrm{Rx}}} \right|_{U_{\mathrm{Rx},0}} \hat{P}_{\mathrm{Rx},1} \hat{U}_{\mathrm{Rx},1}(t) \ , \\ \varphi_{\mathrm{BB}}(t) &= \varphi_{\mathrm{Tx,THz}}(t) - \varphi_{\mathrm{Rx,THz}} + \varphi_{\mathrm{TxRx}} \, . \end{aligned} \tag{5.12}$$

For sensitive detection, the slope $\mathrm{d}S_{\mathrm{Rx}}/\mathrm{d}U_{\mathrm{Rx}}\big|_{U_{\mathrm{Rx},0}}$ of the sensitivity as a function of voltage has to be maximized such that small variations of the terahertz voltage translate into large variations of the baseband photocurrent amplitude. The phase $\varphi_{\mathrm{BB}}(t)$ may be properly adjusted with the variable time delay τ_{opt} (Figure 5.3a). A more convenient alternative measurement technique is explained in Appendix E.1.

5.4 Demonstration of T-wave generation and detection

For an experimental demonstration of the PIPED performance in O/T and T/E conversion, we first characterized the Tx and Rx separately. To this end, we fabricated a PIPED that was connected to an on-chip dipole antenna as shown in inset 1 of Figure 5.1. To supply a bias voltage $U_{\mathrm{Tx},0}$ to the PIPED, we used bias lines equipped with terahertz chokes that prevent leakage of terahertz signals from the antenna; see Appendix E.4 for details of the antenna design. Note that the dipole antenna is not optimum for transmitting and receiving terahertz power over a broad frequency range. We still decided to use this antenna concept due to its small footprint, which allowed us to densely integrate a large number of PIPEDs on a test chip. The dipole antennas may be replaced by bigger spiral or bow-tie structures in future devices. To measure the device performance, we used the set-up depicted in Figure 5.3a, where the Tx and Rx are driven by the same lasers for homodyne detection. To increase the sensitivity of T-wave detection, we used a modulated bias voltage $U_{\mathrm{Tx},0}$ that leads to a modulated terahertz power and helps in detecting the received T-wave with a lock-in amplifier. The T-wave is transmitted via a silicon lens and redirected to the lensed Rx antenna by an off-axis parabolic mirror.

To characterize the PIPED Tx performance, we determined the emitted power as a function of frequency by comparison to a commercially available terahertz reference Tx (Toptica, EK – 000724) (see Appendix E.1). To ensure traceability, the emitted power $P_{\text{THz, ref}}$ of the reference Tx was measured using a calibrated pyroelectric thin-film sensor. We then detected the emission of the PIPED and the reference Tx with a commercially available photoconductive terahertz receiver (Toptica, EK – 000725). The terahertz power $P_{\text{THz,PIPED}}$ generated by the PIPED Tx leads to a current $I_{\text{Rx,PIPED}}$ in the reference receiver, while the emission of the reference Tx generates a receiver current $I_{\text{Rx,ref}}$. The PIPED terahertz output power can then be estimated by

$$P_{\text{THz,PIPED}} = P_{\text{THz, ref}} \left(I_{\text{Rx,PIPED}} / I_{\text{Rx,ref}} \right)^2 . \tag{5.13}$$

The frequency dependence of the terahertz power emitted by the PIPED is shown in Figure 5.3b. The PIPED is capable of generating radiation at frequencies of up to 1 THz. The measured transmitted power $P_{\text{THz,PIPED}}$ obtained according to Eq. (5.13) is depicted as a blue solid line. For comparison,

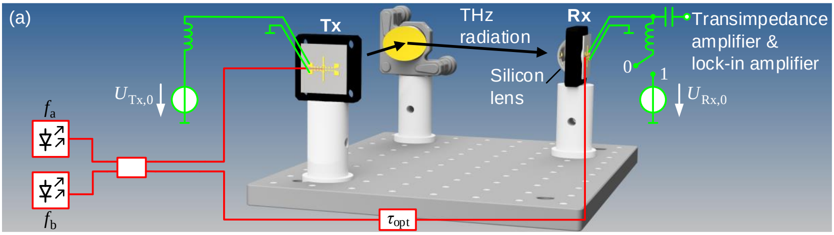

Figure 5.3A: Demonstration of PIPED performance for O/T and T/E conversion. **(a)** Experimental set-up. To measure the PIPED Tx and Rx separately, the respective other component is replaced by a commercially available device in a free-space set-up. Light from two lasers with frequencies f_a and f_b is superimposed to obtain an optical power beat at $f_{\text{THz}} = |f_a - f_b|$, which generates a T-wave in the PIPED Tx or acts as a LO for homodyne detection in the PIPED Rx. When using the PIPED at the Tx, the device is biased by a DC voltage $U_{\text{Tx,0}}$, which is modulated by an AC signal for lock-in detection. The bias is applied to the PIPED Tx via dedicated on-chip low-pass structures (terahertz chokes), see inset 1 of Figure 5.1. The same structures are used at the PIPED Rx, along with an additional bias-T in the feed circuit that allows the DC bias to be separated from the AC lock-in signal. The AC signal is fed to a transimpedance amplifier and detected by a lock-in amplifier. When operating the PIPED as a T-wave Rx, we either apply a defined bias voltage $U_{\text{Rx,0}}$ by connecting an external voltage source (switch position 1), or we leave the bias contacts open (switch position 0, ‘zero bias current’), which leads to a build-up of an internal forward bias of $U_{\text{Tx,0}}$ upon illumination of the PIPED. (Figure continues on the next page)

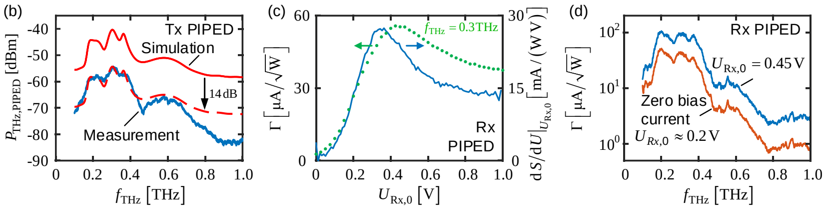

Figure 5.3B: (b) PIPED as a T-wave Tx. The radiated power (blue) was determined by a commercial reference Rx (Toptica, EK 000725). The Tx antenna and terahertz chokes were designed for a resonance frequency of 0.385 THz (see Appendix E.4). The peaks at lower frequencies are caused by unwanted resonances on the choke structures. For comparison, we also plot the simulated terahertz power (solid red) emitted by the PIPED via the silicon substrate and an adjacent silicon lens. The shape of the measured frequency characteristic coincides reasonably well with its simulated counterpart, while the absolute power levels obtained from the measurement are ~14 dB below the simulated values. We attribute this to losses in the set-up and to imperfect coupling of the PIPED terahertz beam to the reference Rx. For better comparison of the shapes, we shifted the simulated characteristic by 14 dB (dashed red) to coincide with the measurement. Details of the simulation are provided in Appendices E.1 and E.10. **(c)** PIPED as T-wave Rx. Measured conversion factor $\Gamma = \hat{I}_{\mathrm{BB},1} \big/ \sqrt{P_{\mathrm{THz}}}$ (green) as a function of Rx bias voltage $U_{\mathrm{Rx,0}}$. The bias-dependent sensitivity slope $\mathrm{d}S/\mathrm{d}U|_{U_{\mathrm{Rx,0}}}$ (blue) features a maximum that deviates slightly from the maximum of the conversion factor Γ at a carrier frequency of 0.3 THz. We attribute this effect to the voltage dependence of the transit time. **(d)** Conversion factor Γ of the Rx as a function of the terahertz frequency both for zero-bias-current operation ($U_{\mathrm{Rx,0}} \approx 0.2\,\mathrm{V}$) and for an externally applied DC bias of $U_{\mathrm{Rx,0}} = 0.45\,\mathrm{V}$, which leads to the maximum conversion factor (c). *Copyright © Springer Nature.*

we perform a simulation of the terahertz power that the PIPED emits into free space via the silicon substrate and an adjacent silicon lens; the results are plotted as a solid red line. Details of the simulation are provided in Appendices E.1 and E.10. The shapes of the measured and simulated frequency characteristics coincide reasonably well, but the absolute power levels obtained from the measurement are ~14 dB below the simulated values. We attribute this effect to losses in the set-up and to imperfect coupling of the PIPED terahertz beam to the reference Rx. The peaks in the simulated and measured frequency characteristic are caused by antenna and bias line resonances. The roll-off at larger frequencies is predominantly caused by the carrier transit time in the 100 nm-wide silicon core of the PIPED (Appendix E.10). This width can be further reduced [117], for example to 75 nm, which would decrease the transit time accordingly. To avoid irreversible damage to the device in our Tx experiments, we chose to limit the optical power such that the mean photocurrent did not exceed 50 µA. The measured radiated output power exhibits a maximum of approximately -55 dBm at 0.3 THz. Note that this value, as well as its simulated counterpart of approximately -40 dBm, are still well below the power levels that can be achieved by state-of-the-art discrete terahertz sources. As an example, commercially available electronic multipliers (www.vadiodes.com) permit output powers of tens of milliwatts at 0.3 THz when operated with input powers of hundreds of milliwatts at 150 GHz, and similar levels can be achieved with IMPATT diodes (www.terasense.com). However, these devices are limited to certain frequency bands or even to single-frequency operation for the case of IMPATT diodes. Photomixing in high-speed UTC-PDs on III–V substrates allows for broadband operation, with power levels of up to 1.2 mW at 0.3 THz achieved for a pair of devices operated in parallel [135]. The power level of our commercial terahertz reference Tx is −19 dBm at 0.3 THz, measured by a calibrated pyroelectric detector (Appendix E.3). In comparison to these established terahertz generators, our current PIPED devices are still inferior in terms of maximum output power. Note, however, that the PIPED approach exploits the intrinsic scalability advantages of highly mature silicon photonic integration and is hence perfectly suited for integrated T-wave signal processing systems that combine the T-wave Tx and Rx on a common chip. These systems can be operated at very low power levels as shown in the next section. In addition, the output power of PIPED systems can be further increased. For instance, the maximum applied current of 50 µA is still well below the actual damage threshold of the PIPED, and we expect that much higher operating currents can be safely applied provided that the devices are thermally connected to a proper heat sink (Appendix E.6). Moreover, the output power can be increased by connecting an array of devices to a single antenna or transmission line (Appendix E.13). Exploiting the coherent superposition of the individual terahertz currents, an array of n synchronously pumped PIPEDs connected in parallel would increase the terahertz output power of the Tx by a factor of n^2. The small PIPED length of roughly 1 µm, the small capacitance below 1 fF, and the large resistance in excess of 10 kΩ would easily allow the connection of $n = 10$ PIPEDs to the antenna feed point, leading to a power gain of 20 dB. Moreover, the intrinsic scalability of silicon photonics allows large-scale antenna arrays to be built on a single chip, which could further increase the output power as well as the directivity of the emitted terahertz power.

To evaluate the PIPED Rx performance, we used a commercially available Tx (Toptica, EK – 000724). According to Eq. (5.12), the baseband photocurrent amplitude $\hat{I}_{\mathrm{BB},1}$ depends linearly on the amplitude $\hat{U}_{\mathrm{Rx},1}$ of the terahertz voltage, which is proportional to the square root of terahertz power P_{THz}. As a metric for Rx sensitivity, we can hence define the ratio

$$\Gamma = \frac{\hat{I}_{\mathrm{BB},1}}{\sqrt{P_{\mathrm{THz}}}} \propto \left.\frac{\mathrm{d}\,S_{\mathrm{Rx}}}{\mathrm{d}U_{\mathrm{Rx}}}\right|_{U_{\mathrm{Rx},0}} \hat{P}_{\mathrm{Rx},1}, \tag{5.14}$$

which describes the conversion factor from the terahertz signal to the baseband photocurrent. The linear relationship between $\hat{I}_{\mathrm{BB},1}$ and $\sqrt{P_{\mathrm{THz}}}$ was confirmed experimentally (Appendix E.5). The conversion factor depends on the sensitivity slope $\mathrm{d}\,S_{\mathrm{Rx}}/\mathrm{d}\,U_{\mathrm{Rx}}\big|_{U_{\mathrm{Rx},0}}$; see Eq. (5.12). This was experimentally confirmed by measuring the conversion factor Γ in dependence on the bias voltage $U_{\mathrm{Rx},0}$ at a frequency of 0.3 THz. The result is depicted in Figure 5.3c (green, left axis) along with the slope of the sensitivity (blue, right axis) derived from the static $S(U)$ characteristic in Figure 5.2. The two curves are in fair agreement. We also verified that the conversion factor depends linearly on the incident optical power $\hat{P}_{\mathrm{Rx},1}$ (Appendix E.5). These findings confirm the validity of our PIPED model used to describe the Rx.

Similarly, we demonstrate the ability of a PIPED to perform broadband T/E conversion at the Rx. To this end, we measured the conversion factor Γ as a function of terahertz frequency for two cases. In a first measurement, we left the bias contacts open, which corresponds to switch position 0 in Figure 5.3a (zero-bias-current operation). This leads to the build-up of an internal forward bias of $U_{\mathrm{Rx},0} \approx 0.2\,\mathrm{V}$ when illuminating the PIPED (Appendix E.7). For the second measurement, we turned the switch in Figure 5.3a to position 1 and connected an external DC voltage source $U_{\mathrm{Rx},0} = 0.45\,\mathrm{V}$. The results of the measured conversion efficiencies Γ are shown in Figure 5.3d. The PIPED is able to receive radiation at frequencies up to 1 THz and beyond. At a frequency of 0.3 THz, the devices exhibit a conversion factor of $95\,\mu\mathrm{A}/\sqrt{\mathrm{W}}$ for bias voltages of $U_{\mathrm{Rx},0} = 0.45\,\mathrm{V}$ and $44\,\mu\mathrm{A}/\sqrt{\mathrm{W}}$ for zero bias current, that is, internal bias voltages of $U_{\mathrm{Rx},0} \approx 0.2\,\mathrm{V}$. As expected from Figure 5.3c, the bias voltage of 0.45 V leads to a larger slope $\mathrm{d}S_{\mathrm{Rx}}/\mathrm{d}U_{\mathrm{Rx}}\big|_{U_{\mathrm{Rx},0}}$ of the sensitivity and hence to a higher conversion factor as compared to the 0.2 V bias. The resonances in Figure 5.3d and the drop of the conversion factor for larger frequencies are caused by the frequency response of the antenna, the PIPED and the bias lines.

If we assume a 50 Ω load, the conversion factor Γ can be translated to a conversion gain of $\frac{1}{2}\Gamma^2 \times 50\,\Omega$, which corresponds to – 73 dB for zero-bias-current operation and – 66 dB for a bias voltage of 0.45 V. This is clearly below the conversion gain of − 8.5 dB that can be achieved by state-of-the art electronic subharmonic mixers (www.vadiodes.com) operating at 300 GHz with a 150 GHz electronic local oscillator. Note, however, that the PIPED T-wave receivers can be tuned across a large range of operation frequencies that exceeds that of discrete mixers, which are usually limited to the specific transmission band of the waveguides needed to package the discrete devices and to block unwanted frequency components. Regarding optoelectronic downconversion of T-wave signals, InP-based UTC-PDs have been exploited [152,154,155], leading to a conversion gain of – 30 dB at a frequency of 0.3 THz (ref. [152]). However, downconversion in UTC-PDs relies on the dynamic capacitance associated with accumulation of carriers in the absorption region and is hence only efficient for very high optical powers (for example, 80 mW) [152]. This leads to large DC currents and hence a strong noise background in the baseband current (for example, $28\,\mathrm{nA}/\sqrt{\mathrm{Hz}}$,); see Appendix E.1 for details. Hence, despite the large conversion gain, the baseband signal-to-noise power ratio (SNR) of UTC-PD T-wave receivers is limited, and levels of 57 dB Hz^{-1} have been demonstrated at a frequency of 0.3 THz for the devices of ref. [155]. In contrast to that, PIPEDs exploit an intrinsically voltage-dependent sensitivity (Figure 5.2c) and thus require only relatively small optical power levels. For a PIPED operated with zero bias current, we measured a noise current of $9\,\mathrm{pA}/\sqrt{\mathrm{Hz}}$ and a SNR of $85\,\mathrm{dB\,Hz}^{-1}$ at 0.3 THz. These figures compare very well to the noise current of $15\,\mathrm{pA}/\sqrt{\mathrm{Hz}}$ and SNR of $91\,\mathrm{dB\,Hz}^{-1}$ reported for state-of-the-art photoconductors [106] as well as to the $18\,\mathrm{pA}/\sqrt{\mathrm{Hz}}$ and $84\,\mathrm{dB\,Hz}^{-1}$ that we measured when replacing the PIPED Rx with photoconductive reference Rx. The conversion gain of the reference Rx is – 67 dB at 0.3 THz (Figure E.1b in Appendix E.3) and hence is comparable to that of the PIPED Rx.

Based on these findings, we conclude that a PIPED T-wave Rx can already provide conversion factors and SNR levels that are comparable to those of conventional III–V devices while offering an ultra-compact footprint. It is also worth noting that the PIPEDs reported here are first-generation devices that still feature large potential for further performance improvements. As an example, using parallel arrays of n PIPEDs connected to a single Rx antenna would allow boosting the power conversion factor in proportion to n^2, hence allowing improvements of the conversion gain by one to two orders of magnitude (Appendix E.13). Note also that the load resistance of 50 Ω assumed for translating the conversion factor Γ into a conversion gain is not the optimum choice: the PIPED itself features a large output impedance well above 10 kΩ, and the conversion gain would hence increase if load resistances larger than 50 Ω could be used. Given the ultrasmall capacitance of the PIPED (Appendix E.10), this would be possible without imposing significant RC limitations to the bandwidth of the device. These aspects indicate that the PIPED-based T-wave Rx has the clear potential to unlock a wide variety of applications that rely on optoelectronic T-wave signal processing in compact integrated systems.

The SNR achieved with our PIPED Rx is sufficient for many spectroscopic or diagnostic applications, where lock-in detection and large integration times lead to a small detection bandwidth. Application of Rx PIPEDs in high-speed terahertz communication would still require higher SNR, dictated by the large bandwidth of the data signal. Assuming that a viable transmission link requires a signal power that is at least 10 dB larger than the noise power in a 10 GHz signal bandwidth, the SNR needs to be larger than 110 dB Hz^{-1}. By using a high-power transmitter, for example, an UTC-PD [135], or by using a T-wave amplifier [149], T-wave powers of more than 0 dBm can be achieved, which would increase the SNR to more than 100 dB Hz^{-1}. Combining these transmitters with parallel arrays of PIPEDs connected to the same Rx antenna would lead to SNR values suitable for wireless communication links.

5.5 Monolithically integrated T-wave system

To demonstrate the technological advantages of the PIPED concept, we monolithically integrate arrays of PIPED Tx and PIPED Rx on a common silicon chip. Tx and Rx are coupled by short T-wave transmission lines having various lengths L between 10 µm and ~1 mm. An SEM image of such a Tx–Rx pair is displayed in Figure 5.4a. A 1-µm-wide gap in the middle of the T-wave transmission line acts as a DC block to decouple the bias voltages of the Tx and Rx. The insets in Figure 5.4a show magnified pictures of the Tx, the Rx, and the gap. In the experiment, we used the PIPED Tx and Rx to measure the amplitude and phase transfer characteristics of the transmission line at terahertz frequencies; the associated set-up is shown in Figure 5.4b. Optical signals are fed to the Tx and the Rx PIPED by separate silicon photonic waveguides equipped with grating couplers. As in the previous experiments, the Tx and Rx are fed with two optical spectral lines f_a and f_b at varying frequency separations. The Tx is biased in the forward direction $U_{\mathrm{Tx},0} > 0$ and feeds the T-wave transmission line. At the end of the transmission line, the Rx PIPED acts as a homodyne receiver to coherently detect the T-wave signal and to downconvert it to a baseband current $I_{\mathrm{BB},1}$, Eqs. (5.11) and (5.12). The Rx PIPED is operated under zero-bias-current conditions to minimize noise. Because the PIPED features a large impedance at terahertz frequencies, all transmission lines are essentially terminated by open circuits at both ends and thus act as T-wave resonators, for which the resonance frequencies are dictated by the respective geometric length L. At the Rx, we measure the baseband photocurrent $I_{\mathrm{BB},1}$. By sweeping the Tx frequency, we can separate the amplitude $\hat{I}_{\mathrm{BB},1}$ from the phase φ_BB (see Appendix E.1 for details). To quantify the transmission line transfer characteristics, we used the complex transfer impedance $\underline{Z}_{21} = |\underline{Z}_{21}| \mathrm{e}^{\,\mathrm{j}\varphi_{21}}$, which is defined as the ratio of the complex T-wave voltage amplitude at the Rx PIPED and the complex T-wave current amplitude at the Tx PIPED. The magnitude of the complex transfer impedance is directly proportional to the baseband current amplitude $\hat{I}_{\mathrm{BB},1}$.

$$|\underline{Z}_{21}| = a\hat{I}_{\mathrm{BB},1}, \tag{5.15}$$

where the proportionality factor a depends on the operation conditions of the Tx and Rx PIPED (Appendix E.8):

$$a = \left(\tfrac{1}{2} \frac{\mathrm{d}S_{\mathrm{Rx}}}{\mathrm{d}U_{\mathrm{Rx}}} \bigg|_{U_{\mathrm{Rx},0}} \hat{P}_{\mathrm{Rx},1} \, S_{\mathrm{Tx}} \left(U_{\mathrm{Tx},0} \right) \hat{P}_{\mathrm{Tx},1} \right)^{-1} . \tag{5.16}$$

The corresponding phase φ_{21} is obtained from φ_{BB} by swapping the role of the Tx and Rx PIPEDs, thus allowing us to eliminate the influence of the unknown group delay in the optical fibres (see Appendix E.1). The measured magnitude and phase characteristics of the transfer impedance $\underline{Z}_{21,\mathrm{meas}}$ are depicted as blue traces Figure 5.4c-e. For comparison, we also numerically calculated the transfer impedance of the T-wave transmission lines using a commercially available time-domain solver. The results of the simulated transfer impedance $\underline{Z}_{21,\mathrm{sim}}$ are shown as red traces in Figure 5.4c-e. Note that calculating the proportionality factor a according to Eq. (5.16) is subject to large uncertainties because the experimental operating conditions of the Tx and Rx PIPED at terahertz frequencies are only known approximately. To estimate $|\underline{Z}_{21}|$ from the measured baseband photocurrent amplitude $\hat{I}_{\mathrm{BB},1}$, we therefore chose a such that we obtained the best agreement between the simulation and measurement (Appendix E.9). Moreover, we numerically corrected for the frequency roll-off of the PIPED when deriving the measured transfer impedance $\underline{Z}_{21,\mathrm{meas}}$ from the baseband photocurrent amplitude $\hat{I}_{\mathrm{BB},1}$. To this end, the transit-time limited frequency response of both PIPEDs was approximated by an *RC* low-pass characteristic with a corner frequency of 0.3 THz, obtained from a least-squares fit of the measurement data (Appendix E.9). The measured and simulated transmission line characteristics show perfect agreement with respect to amplitude and phase over the entire frequency range $f_{\mathrm{THz}} = 0.05 - 0.8\,\mathrm{THz}$, corresponding to a span of 1.5 decades. The field distributions along the transmission lines were investigated by numerical simulations of the structures, see Appendix E.11. These findings show that signal processing in PIPED can be quantitatively described by a reliable mathematical model, thus enabling deterministic photonic–electronic signal processing over an ultra-broadband frequency range.

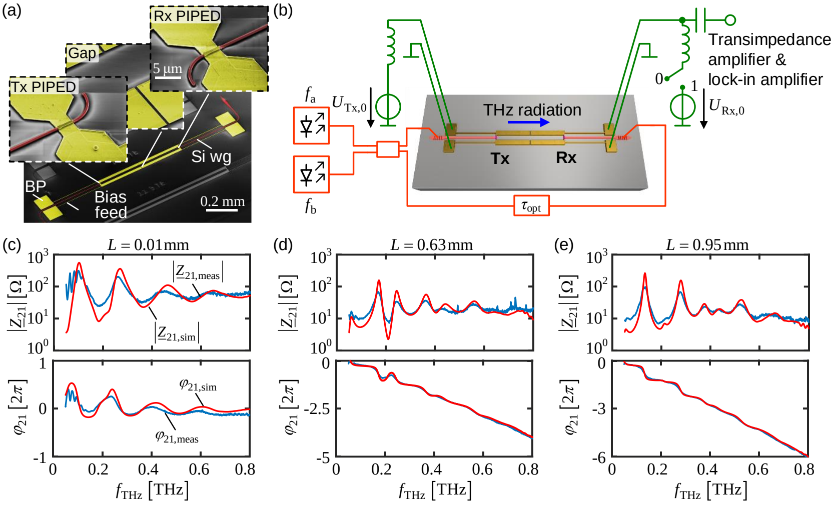

Figure 5.4: Demonstration of T-wave system on a silicon chip. **(a)** False-colour SEM image of the terahertz system, consisting of a T-wave Tx, a coplanar transmission line, and a T-wave Rx. Light is coupled to the PIPED Tx and Rx by silicon waveguides (Si wg) and grating couplers (GC). Bias pads (BP) and terahertz-blocking bias feeds (terahertz chokes) allow a voltage to be applied to or a signal current to be extracted from the PIPED. A gap in the middle of the transmission line separates the bias voltages of Tx and Rx. **Insets:** magnified SEM images of Tx, Rx and the transmission line gap. **(b)** Experimental set-up for on-chip transmission-line measurements. Tx and Rx are fed with two optical spectral lines f_a and f_b at varying frequency separations. The Tx is biased in the forward direction $U_{Tx,0} > 0$ and feeds the T-wave transmission line. At the end of the transmission line, the Rx PIPED acts as a homodyne receiver to coherently detect the T-wave signal by downconversion to the baseband current $I_{BB,1}$. To reduce the noise, the switch is set to 0 to operate the Rx PIPED with zero-bias current. **(c)–(e)** Magnitude and phase characteristics of the complex transfer impedance $\underline{Z}_{21} = |\underline{Z}_{21}| \exp(j\varphi_{21})$. Red curves show simulated frequency characteristics of $|\underline{Z}_{21,sim}|$ and $\varphi_{21,sim}$ for three transmission line lengths $L = 0.01$, 0.63 and 0.95 mm, and blue curves represent corresponding measurement results $|\underline{Z}_{21,meas}|$ and $\varphi_{21,meas}$. The frequency roll-off of the PIPED is modelled by an RC low-pass filter with a 3 dB frequency of $f_{3dB} = 0.3\,\text{THz}$ (Appendix E.9). Measurements (blue) agree very well with the simulation (red). *Copyright © Springer Nature.*

5.6 Summary and outlook

We have demonstrated a novel approach to T-wave signal processing that exploits internal photoemission at metal–semiconductor interfaces of silicon–

plasmonic structures. This approach allows to monolithically co-integrate T-wave transmitters and receivers on the silicon photonic platform, thus enabling a novel class of photonic-electronic signal processors that may exploit the outstanding technical maturity and performance of the silicon photonic device portfolio. When used as a T-wave Rx, the performance of our current PIPED devices can already compete with state-of-the-art III–V photoconductors, while further improvements are still possible by optimized device geometry and materials. The devices are analysed and described by a quantitatively reliable mathematical model. In a proof-of-concept experiment, we use co-integrated PIPED transmitters and receivers to measure the complex transfer function of an integrated T-wave transmission line.

[end of paper [J2]]

6 Summary and Outlook

6.1 Summary

T-wave links are likely to become an essential part of future communication networks. Compact and energy-efficient transmitters and receivers are key to the success of T-wave technology. Moreover, it is important that T-wave links can be easily integrated into existing fibre-optic infrastructure. In this respect, optoelectronic devices are especially promising. This thesis investigated new chip-scale transmitter and receiver solutions, which combine the advantages of electronic and photonic signal processing. The performance of the devices was verified in T-wave links. These experiments led to a number of demonstrations with outstanding results. Key accomplishments of this thesis cover the following aspects:

First demonstration of T-wave Kramers-Kronig receiver: By adapting the Kramers-Kronig phase retrieval scheme that was originally developed for optical communications, we showed that a simple envelope detector, e.g., a Schottky-barrier diode, can be used as a receiver for high-speed T-wave signals.

Record-high data rates at large transmission distances: The performance of the Kramers-Kronig receiver was demonstrated by transmitting data at a net rate of 115 Gbit/s over a 110 m-long T-wave transmission link. To the best of our knowledge, this represents the highest data rate so far for a T-wave transmission link with distances of more than 20 m.

First demonstration of optoelectronic downconversion of THz data signals: Optoelectronic signal processing at the receiver is attractive because it offers the possibility to downconvert T-wave signals over a broad range of carrier frequencies. We showed for the first time that optoelectronic receivers cannot only be used for spectroscopy applications, but are also useful for T-wave communications. Data streams with bit rates up to 30 Gbit/s are transmitted over a 58 m-long T-wave link consisting of an optoelectronic T-wave transmitter and an optoelectronic T-wave receiver. We demonstrated that the receiver can be tuned from 0.03 THz to 0.34, i.e., over a frequency range spanning more than a decade. These experiments show the potential of T-wave receivers that exploit optoelectronic signal processing.

First demonstration of T-wave generation and downconversion on the silicon-plasmonic platform: In this work, a novel class of T-wave ultra-fast silicon-plasmonic photodetectors was experimentally demonstrated. The devices lend themselves to T-wave signal generation and coherent detection, and can be monolithically co-integrated with silicon photonic devices. By leveraging the advanced toolbox of the silicon photonic platform, this approach opens up new opportunities for T-wave signal processing.

Demonstration of integrated T-wave systems based on silicon-plasmonic devices: T-wave transmitters and receivers were integrated on a single silicon chip and were used to measure the complex impedance of an on-chip T-wave transmission line in a frequency range between 0.05 THz and 0.8 THz.

6.2 Outlook and future work

The achievements summarized in the previous section largely represent proof-of-concept demonstrations that emphasize the potential of novel device concepts and signal processing schemes in the field of T-wave communications. Further steps towards complementing the portfolio of devices and methodologies could focus on the following aspects:

Direct T-wave-to-optical (T/O) conversion: The full advantage of combined electronic and photonic signal processing can only be exploited if efficient converters exist to flexibly convert between electronic, T-wave and photonic signals. In this work, we demonstrated the conversion from optical signals to T-wave signals (O/T conversion) and the conversion from T-wave signals to electrical signals (T/E conversion). The flexibility of T-wave systems can be further increased by combining the converters with optical ultra-broadband plasmonic modulators, for directly converting T-wave signals to optical signals [105]. Depending on the application, the T-wave signals can then be upconverted to optical frequencies, or downconverted to the electrical domain.

Beam-steering, spatial and frequency multiplexing of T-wave signals: Advanced T-wave systems with smart antennas require beam steering capabilities. This can be achieved by combining an array of optoelectronic T-wave transmitters with an optical phase shifter array. Multiple antennas could further boost the performance of T-wave links by making use of multiple-input, multiple-output (MIMO) processing. MIMO transmission increases the system robustness and/or the data rates by spatial multiplexing. Frequency multiplexing is another method to increase the transmitted data rate. This requires the development of efficient and broadband T-wave multiplexers and demultiplexers [113,114].

Compact and efficient T-wave systems: Monolithic or hybrid integration of electronic, photonic, and T-wave circuits can reduce the system size and the interconnecting loss of the components. Fully integrated circuits might offer a compact and energy-efficient solution to process broadband signals.

Exploration of new application fields for T-wave signals: In the present work, the capabilities of T-wave transmitters and receivers were demonstrated in T-wave communication links. Compact and efficient T-wave systems, however, go beyond communications and impact other fields such as medicine, material sciences, engineering and chemistry. For instance, it has been shown recently that THz radiation can be used for cancer or diabetes detection [156,157], and that it potentially enables future cancer treatment [157]. Further research on T-wave devices and systems is crucial to realize these novel applications not only in proof-of-principle experiments but also in real-world application scenarios.

Appendices

A. Important antenna parameters

This section gives a short overview of important antenna parameters. In general, an antenna is used to couple electromagnetic waves from a guided mode to free space. Important quantities are the antenna directivity, gain and aperture. In the following, the definitions from the IEEE standards association [158] are given and afterwards their relations are explained. All three quantities depend on the direction. Often these quantities are given without the specification of a direction. In this case, the direction of maximum radiation intensity is implied [158].

Antenna directivity D: "The ratio of the radiation intensity in a given direction from the antenna to the radiation intensity averaged over all direction." [158]

Antenna gain G_A: "The ratio of the radiation intensity in a given direction to the radiation intensity that would be produced if the power accepted by the antenna were isotopically radiated." [158]

Antenna aperture (or area) A: "In a given direction, [the antenna aperture is] the ratio of the available power at the terminals of a receiving antenna to the power flux density of a plane wave incident on the antenna from that direction, the wave being polarization matched to the antenna." [158]

The antenna gain G_A is connected to the directivity D by the efficiency η of the antenna, $G_\mathrm{A} = \eta D$. The effective aperture A of the antenna is connected to the gain G_A by [158]

$$A = G_\mathrm{A} \frac{\lambda^2}{4\pi}, \tag{A.1}$$

where λ is the operating wavelength.

A.1 Aperture of an isotropic antenna

The aperture of an isotropic antenna can be calculated by thermodynamic considerations [159,160]. Figure A.1 illustrates the approach. An isotropic radiating (or receiving) antenna is located in a cavity A and is connected by a transmission line to a resistor *R* that is located in cavity B. The antenna and the transmission line are matched to the resistor *R* and both cavities are in thermodynamic equilibrium at temperature *T*. A bandpass filter allows transmission of frequencies in the range between f and $f+\Delta f$.

The unpolarized spectral black-body radiance $B_f\left(f,T\right)$ for a certain frequency *f* and temperature *T* is given by Planck's law

$$B_f\left(f,T\right)=2\frac{f^2}{c^2}\underbrace{\left(\exp\left(\frac{hf}{kT}\right)-1\right)^{-1}}_{\bar{n}}hf\,, \tag{A.2}$$

where *h* is Planck's constant, *hf* the photon energy and $\bar{n}$ the mean number of photons. Equation (A.2) describes the amount of power radiated per unit solid angle, per unit area and per unit frequency. The antenna with the effective area A_eff receives the power P_r in the full solid angle 4π and in the bandwidth Δ*f*:

$$P_\text{r}=\tfrac{1}{2}A_\text{eff}\,4\pi B_f\left(f,T\right)\Delta f=\frac{4\pi}{\lambda^2}A_\text{eff}\bar{n}hf\,\Delta f\,. \tag{A.3}$$

The factor $\tfrac{1}{2}$ is required because the antenna receives only one polarization while the black-body radiance is given for unpolarized radiation. The resistor emits in one polarization in the bandwidth Δf and the thermal noise power P_th is given by

$$P_\text{th}=\bar{n}hf\,\Delta f\,. \tag{A.4}$$

The system including cavity A and B is in thermal equilibrium and therefore the net power transfer between both cavities must be zero, which leads to

$$P_\text{r}=P_\text{th},\quad A_\text{eff}=\frac{\lambda^2}{4\pi}. \tag{A.5}$$

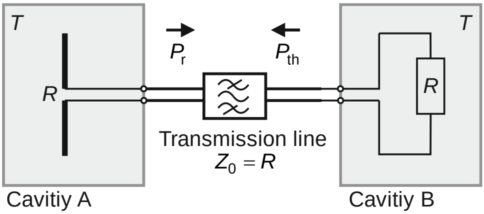

Figure A.1: Thermodynamic considerations for calculation of the aperture A_{eff} of an isotropic antenna. The antenna is placed in a cavity A and is connected with a transmission line to a resistor R that is located in cavity B. The antenna impedance is matched to the transmission line impedance and the resistor R. A bandpass filter allows only the frequencies from f to $f + \Delta f$ to be transmitted along the transmission line. Both cavities are at temperature T and are in thermal equilibrium. Therefore the thermal power P_{th} emitted by the resistor must be the same as the power P_r received by the antenna. With this relation the antenna aperture $A_{eff} = \lambda^2/4\pi$ is calculated, see Eq.(A.5).

A.2 Free-space path loss

The free-space path loss FSPL gives the ratio of the power P_{Tx} transmitted by an isotropic radiator and the power P_{Rx} received by an isotropic antenna, which is separated by a distance d from the transmitter. At the distance d, the spherical wave front of the transmitter covers an area

$$A_{Sph} = 4\pi d^2 . \tag{A.6}$$

The aperture of the isotropic antenna $A_{eff} = \lambda^2/4\pi$ was derived in the previous section. The received power is by a factor A_{eff}/A_{Sph} smaller than the transmitted power. By using Eq. (A.6) the FSPL is given by

$$\mathrm{FSPL} = \frac{P_{Tx}}{P_{Rx}} = \frac{P_{Tx}}{\frac{A_{eff}}{A_{Sph}} P_{Tx}} = \frac{4\pi d^2}{\lambda^2/4\pi} = \left(\frac{4\pi d}{c} f \right)^2 . \tag{A.7}$$

B. Photodiode implementations

In this section the details of the pin-photodiode (pin-PD) and uni-travelling carrier photodiode (UTC-PD) are given, which are used as a T-wave transmitters for the data transmissions experiments shown in Chapter 3 and Chapter 4. The photodiode converts the optical power to an electrical current. The most important photodiode parameters for our applications are the sensitivity, the bandwidth and the saturation power. Photodiodes are restricted in their bandwidth by the carrier drift times and/or by RC limitations.

A typical implementation of the photodetector is the pin-PD. The corresponding band diagram for a reverse bias is shown in Figure B.1a. Light is absorbed in the intrinsic region (light absorption layer) of width w_a. The absorption of the photons leads to generation of electron-hole-pairs. The absorption layer is depleted, and the applied electric field leads to a drift of the electrons and the holes to the contacts. The drift time τ_a is proportional to the length of the absorption region w_a. However, reducing the length of the absorption region leads to an increase of the capacitance $C \propto 1/w_\text{a}$ and the RC-limitation might reduce the bandwidth of the device. Typically, the hole velocity is smaller than the electron velocity and the hole transit time limits the overall response time of the device.

The UTC-PD design decreases the response time of the device by using the semiconductor stack shown in Figure B.1b. The active region consists of a p-doped light-absorption layer of width w_a, and an intrinsic carrier collection layer of width w_c. The bandgap of the collection layer is larger than the photon energy and electron-hole pairs are only generated in the absorption layer. The holes generated in the p-doped absorption layer are majority carriers and the response time is given by the dielectric relaxation time. This time can be very short and the speed of the UTC-PD is only limited by the speed of the electrons.

The electrons diffuse towards the intrinsic carrier collection layer and continue drifting through the intrinsic carrier collection layer to the n-contact. The wide-bandgap material to the left of the absorption layer is used to prevent electrons to diffuse to the p-contact (diffusion block). By applying a reverse bias, the speed of the electrons in the collection layer can be much larger than the speed of the holes due to the large electron mobility and the velocity overshoot effect. This allows increasing the width of the collection layer w_c and therefore reducing the influence of the RC limitations. The speed of the device is then mainly limited by the transit time of the electrons through the absorption layer. The width of the absorption layer w_a can be made small without being RC limited and therefore photodiodes with very high bandwidth can be achieved.

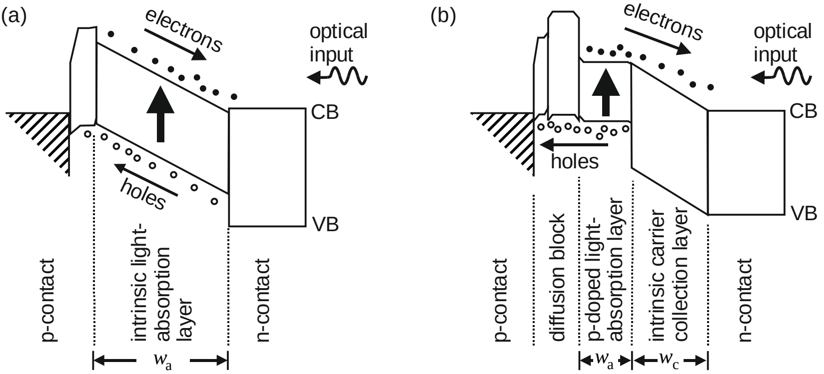

Figure B.1: Band diagram for a **(a)** pin-PD **(b)** UTC-PD. CB: Conduction band, VB: valence band. (drawn after [161])

The UTC-PD not only offers large bandwidth but also large saturation power level [161,162]. The saturation results from the space charge effect [163]. For a conventional pin-PD, the fast electrons leave the absorption region faster than the holes and holes accumulate in the absorption layer at the p-contact-side. The charge accumulation decreases the field inside the depletion region and reduces the hole velocity further. This reduces the bandwidth and eventually limits the output current of the photodetector. In the UTC-PD only the electrons contribute to the current. The large electron velocity leads a reduced space charge effect and to higher saturation levels. A 3 dB-bandwidth above 0.3 THz and an output power level above 1 mW at a frequency of 0.3 THz has been demonstrated with the UTC-PD [135,153,164].

For broadband operation, the absorption layer in the UTC-PD must be kept thin - otherwise the time the electrons require to diffuse from the absorption layer to the collection layer would limit the photodetector response. This reduces the efficiency of the UTC-PD. Typically DC responsivities between $0.1\ \mathrm{A/W}$ and $0.3\ \mathrm{A/W}$ are achieved at a wavelength of $1.55\ \mu\mathrm{m}$ for UTC-PDs operating at a frequency around 0.3 THz [135,153,164]. This is much smaller than the DC responsivities of $1\ \mathrm{A/W}$, which have been achieved with pin-PD [165,166]. However, also the bandwidth and the saturation power of the pin-PD is much smaller. To increase the sensitivity, modified versions of the UTC-PD could be used. By adding an undoped absorption layer, responsivities of up to $0.75\ \mathrm{A/W}$ are demonstrated. In this case, however, the bandwidth is reduced considerably to around 30 GHz [136,167,168].

C. Kramers-Kronig receiver

The content of the following Appendices C.1 - C.11 are taken from Methods and Supplementary Information of a submission [J4] to *Nature Photonics*. In order to fit the structure and layout of this document, it was adapted accordingly.

T. Harter, C. Füllner, J. N. Kemal, S. Ummethala, J. L. Steinmann,
M. Brosi, J. L. Hesler, E. Bründermann, A. S. Müller, W. Freude,
S. Randel, C. Koos,
"Generalized Kramers-Kronig Receiver for Coherent THz
Communications," *Nature Photonics* ***14***, 601–606 (2020).
DOI: 10.1038/s41566-020-0675-0 © Springer Nature

[start of Methods and Supplementary Information of submission [J4]]

C.1 Methods

Schottky-barrier diode (SBD)

We use a zero-bias SBD [169,170] (Virginia Diodes, WR3.4ZBD-F) as a terahertz envelope detector. This device offers high responsivity of the order of 2000 V/W along with broadband output circuitry (bandwidth approximately 40 GHz) for downconversion of high-speed data signals. The rectangular waveguide input port (WR 3.4) of the SBD allows us to directly connect the device to the output of a terahertz low-noise amplifier [171], designed for operation in the submillimetre H-band (0.220 THz - 0.325 THz), see Appendix C.5 for details.

Phase reconstruction by Kramers-Kronig (KK) processing

On a fundamental level, KK processing [67] relies on data signals that are analytic. For an arbitrary analytic time-domain signal $\underline{s}(t) = s_\mathrm{r}(t) + \mathrm{j}s_\mathrm{i}(t)$ the imaginary part $s_\mathrm{i}(t)$ and the real part $s_\mathrm{r}(t)$ are connected by a Hilbert transform,

$$s_\mathrm{i}(t) = \frac{1}{\pi}\mathcal{P}\int_{-\infty}^{\infty} \frac{s_\mathrm{r}(\tau)}{t-\tau}\,\mathrm{d}\tau = \mathcal{P}\left\{\frac{1}{\pi t} * s_\mathrm{r}(t)\right\}, \tag{C.1}$$

$$s_\mathrm{r}(t) = -\frac{1}{\pi}\mathcal{P}\int_{-\infty}^{\infty}\frac{s_\mathrm{i}(\tau)}{t-\tau}\mathrm{d}\tau = -\mathcal{P}\left\{\frac{1}{\pi t} * s_\mathrm{i}(t)\right\}, \tag{C.2}$$

where the asterisks denote a convolution, and where the operator $\mathcal{P}$ stands for the Cauchy principal value of the subsequent improper integral. Equations (C.1) and (C.2) can be interpreted as the time-domain analogue of the KK relations [71,72] that connect the real and the imaginary part of a transfer function belonging to a system that is causal in the time domain [172].

Analytic signals as defined by Eqs. (C.1) and (C.2) feature single-sided power spectra, which do not contain any spectral components for negative frequencies $\omega < 0$. Note that the mutual relationships between the imaginary and the real part of an analytic signal are defined only if both the real and the imaginary part are zero mean. To understand this, let us consider a signal with real part $s'_\mathrm{r}(t) = s_\mathrm{r}(t) + C_\mathrm{r}$ that consists of a constant DC part C_r and a zero-mean signal $s_\mathrm{r}(t)$. When introducing $s'_\mathrm{r}(t)$ into Eq. (C.1), the integral has to be evaluated in the sense of a Cauchy principal value to ensure convergence both for the singularity at $t = \tau$ and for the infinite integration limits,

$$s_\mathrm{i}(t) = \frac{1}{\pi}\lim_{\varepsilon\to 0}\left(\int_{t-1/\varepsilon}^{t-\varepsilon}\frac{s'_\mathrm{r}(\tau)}{t-\tau}\mathrm{d}\tau + \int_{t+\varepsilon}^{t+1/\varepsilon}\frac{s'_\mathrm{r}(\tau)}{t-\tau}\mathrm{d}\tau\right). \tag{C.3}$$

In this case, the constant C_r does not contribute to $s_\mathrm{i}(t)$, and when using equation Eq. (C.2) to reconstruct the real part, we would obtain $s_\mathrm{r}(t)$ rather than $s'_\mathrm{r}(t)$. Similarly, using Eq. (C.2) to reconstruct $s_\mathrm{r}(t)$ from an imaginary part $s'_\mathrm{i}(t) = s_\mathrm{i}(t) + C_\mathrm{i}$ with non-zero mean value C_i would suppress the constant DC part C_i and produce the real part $s_\mathrm{r}(t)$ that belongs to the corresponding zero-mean signal $s_\mathrm{i}(t)$. Hence, signals with non-zero mean value, that is, non-zero spectral power at frequency $f = 0$, are not analytic signals in the sense of Eqs. (C.1) and (C.2).

For KK-based transmission, the analytic data signal $\underline{U}_\mathrm{s}(t)$ is superimposed with a carrier tone, represented by a constant voltage U_0 in the baseband. Without loss of generality, we assume U_0 to be real-valued and positive. The overall complex envelope $\underline{U}(t)$ can then be written as

$$\underline{U}(t) = U_0 + \underline{U}_\mathrm{s}(t) = \left|\underline{U}(t)\right| \mathrm{e}^{\mathrm{j}\Phi(t)}, \tag{C.4}$$

where $\left|\underline{U}(t)\right|$ and $\Phi(t)$ denote the amplitude and the phase of the overall complex envelope $\underline{U}(t)$, comprising the data signal $\underline{U}_\mathrm{s}(t)$ and the carrier amplitude U_0.

In technical implementations of KK reception, the amplitude $\left|\underline{U}(t)\right|$ can be directly measured through some sort of envelope detector with nonlinear characteristics such as a photodiode or, as in our case, an SBD. To establish a relation between the amplitude $\left|\underline{U}(t)\right|$ and the phase $\Phi(t)$ of the complex envelope $\underline{U}(t)$, we derive an auxiliary signal $\underline{s}(t)$ by applying the complex natural logarithm to Eq. (C.4),

$$\underline{s}(t) = \ln\left(\underline{U}(t)\right) = \ln\left(\left|\underline{U}(t)\right|\right) + \mathrm{j}\Phi(t). \tag{C.5}$$

For our further analysis, we exploit the fact that $\underline{s}(t)$ is an analytic signal if the complex data signal $\underline{U}_\mathrm{s}(t)$ is an analytic signal too and if, in addition, the overall complex envelope $\underline{U}(t)$ is minimum phase [67]. A necessary condition for $\underline{U}(t)$ being minimum phase is that the associated time-dependent trajectory described by $\underline{U}(t)$ in the complex plane does not encircle the origin, which is ensured if $\left|\underline{U}_\mathrm{s}(t)\right| < U_0, \forall t$. In this case, we may apply Eq. (C.2) to the auxiliary analytic signal $\underline{s}(t)$ and obtain

$$\Phi(t) = \frac{1}{\pi} \mathcal{P} \int_{-\infty}^{\infty} \frac{\ln\left(\left|\underline{U}(\tau)\right|\right)}{t-\tau} \mathrm{d}\tau. \tag{C.6}$$

This relation allows us to reconstruct the phase of $\underline{U}(t)$ if only the magnitude $\left|\underline{U}(t)\right|$ is known. The complex data signal $\underline{U}_\mathrm{s}(t) = \left|\underline{U}_\mathrm{s}(t)\right| \exp\left(\mathrm{j}\varphi_\mathrm{s}(t)\right)$ with magnitude $\left|\underline{U}_\mathrm{s}(t)\right|$ and phase $\varphi_\mathrm{s}(t)$ is then recovered from $\underline{U}(t)$ by subtracting the constant DC voltage U_0 corresponding to the amplitude of the carrier tone, see Eq. (C.4),

$$\underline{U}_\mathrm{s}(t) = \left|\underline{U}_\mathrm{s}(t)\right| \mathrm{e}^{\mathrm{j}\varphi_\mathrm{s}(t)} = \left|\underline{U}(t)\right| \mathrm{e}^{\mathrm{j}\Phi(t)} - U_0. \tag{C.7}$$

Note that the voltage magnitude $\left|\underline{U}(t)\right|$ in Eq. (C.6) can be scaled with an arbitrary constant factor ζ without changing the reconstructed $\Phi(t)$. This becomes plausible when considering that $\ln\left(\zeta\left|\underline{U}(t)\right|\right)=\ln\left(\left|\underline{U}(t)\right|\right)+\ln(\zeta)$ and that the constant $\ln(\zeta)$ is suppressed when applying the Hilbert transform according to Eq. (C.6), see discussion after Eq. (C.3).

Heterodyne reception without guard band.

In our evaluation in Chapter 3, we also consider single-ended heterodyne reception without any KK processing (w/o KK), which does not account for nonlinear interaction of the signal with itself. According to Eq. (3.5), the SBD current $i(t)$ depends on the magnitude of the complex envelope $|\underline{U}(t)|$. For the sake of simplicity, we assume a square-law relationship $i(t)\propto\left|\underline{U}(t)\right|^2$ in the following derivation. With Eq. (3.2) we obtain

$$i(t)\propto\left|U_0+\underline{U}_\mathrm{s}(t)\right|^2=U_0^2+\left|\underline{U}_\mathrm{s}(t)\right|^2+2U_0\Re\left(\underline{U}_\mathrm{s}(t)\right), \tag{C.8}$$

where $\Re\{\cdot\}$ denotes the real part. The component $2U_0\Re\left\{\underline{U}_\mathrm{s}(t)\right\}$ corresponds to the mixing product of the LO tone with amplitude U_0 and the analytic data signal $\underline{U}_\mathrm{s}(t)$ and allows us to recover the data signal. However, there is also the mixing product $\left|\underline{U}_\mathrm{s}(t)\right|^2$ of the signal with itself, which covers the same spectral region as the mixing product $2U_0\Re\left\{\underline{U}_\mathrm{s}(t)\right\}$, unless a guard band between U_0 and the data spectrum is used. This mixing product degrades the received signal quality and can be compensated by using KK processing, as described in Chapter 3. For large carrier-to-signal power ratios (CSPRs), that is, large values of U_0, the data can still be recovered without using KK processing, because the data signal $2U_0\Re\left(\underline{U}_\mathrm{s}(t)\right)$ dominates over the unwanted mixing product for $\left|U_0\right|\gg\left|U_\mathrm{s}(t)\right|$.

In Appendix C.9, we compare the generalized KK scheme to heterodyne detection with a guard band and find that both schemes offer similar transmission performances, while the generalized KK scheme overcomes the need for a guard band.

Digital signal processing chain

In our experiments, we digitize the receiver currents using a real-time oscilloscope (Keysight UXR0804A) and store the recorded waveforms for subsequent offline DSP and signal-quality evaluation. The transmitted data signal $|\underline{U}_\mathrm{s}(t)|\exp\left(\mathrm{j}\varphi_\mathrm{s}(t)\right)$ is reconstructed from the digitally captured SBD current *i* by generalized KK processing, Eqs. (3.5) and (3.6). We first calculate the THz voltage amplitude $|\underline{U}(t)|$ from the captured signal by inverting Eq. (3.5). For the phase reconstruction, Eq. (3.6), the Hilbert transform is implemented as a convolution with a discrete-time finite-impulse-response filter [173]. For the processing, an oversampling of six samples per symbol is used to avoid performance penalties due to spectral broadening [174] introduced by the natural logarithm in Eq. (3.6) and by the function in Eq. (3.7). Note that the rather large oversampling was chosen to guarantee optimum performance in the proof-of-principle demonstration. The system, however, performs equally well for a sampling with only three samples per symbol, see Appendix C.7. After phase reconstruction, the complex signal $\underline{U}(t)$ is down-sampled to a ratio of two samples per symbol, and the analytic signal $\underline{U}_\mathrm{s}(t)$ is obtained according to Eq. (C.7). The original QAM signal is then recovered by down-converting $\underline{U}_\mathrm{s}(t)$ to the baseband. The KK receiver DSP is followed by the DSP blocks of a fully blind coherent optical receiver [175], with the exception that only a single polarization is evaluated. Specifically, we perform a timing-error estimation in the frequency domain, followed by a compensation with a Lagrange interpolator in a Farrow [176] structure. We then apply an adaptive feed-forward equalizer, whose coefficients are adapted blindly using the constant-modulus algorithm [177]. The remaining frequency offset originating from frequency drifts of the LO laser at f_1 as well as of the signal laser at f_0 is removed, and a subsequent phase recovery using the blind phase search algorithm [178] combats laser phase noise. Finally, we apply a real-valued multiple-input multiple-output feed-forward equalizer with the in-phase (I) and the quadrature (Q) components of the complex baseband as individual inputs to compensate IQ imbalances of the transmitter hardware [179]. The feed-forward equalizer coefficients are adapted by a decision-directed least-mean-square algorithm [180]. Eventually, the BER and EVM are calculated. Compared with conventional terahertz receiver concepts, the KK scheme comes at the cost of extra DSP for the phase reconstruction. However, the outputs of the DSP blocks containing $g^{-1}(i)$ and the natural logarithm in Eq. (3.6) as well as the complex exponential in Eq. (3.2) can be stored in look-up tables. Furthermore, the Hilbert transform can be implemented without considerable performance degradation [173] by a convolution of the reconstructed $|\underline{U}(t)|$ with a discrete-time finite-impulse-response filter that has only a small number of taps. By considering an advanced implementation of the KK processing that works at a reduced oversampling ratio of two samples per symbol, the DSP complexity can be reduced even further [181,182]. The overall DSP effort, also including steps such as timing recovery, phase estimation and FEC, will hence not be substantially increased by KK-type phase reconstruction. We therefore believe that the additional KK-related DSP complexity will be overcompensated by the reduced hardware complexity.

Error vector magnitude (EVM) and bit error ratio (BER)

The EVM and BER are standard metrics to evaluate the quality of communication signals and are widely used in the optical and terahertz communications community [88,89]. Assuming data-aided reception of N randomly transmitted symbols, the EVM is a measure for the effective distance of the received complex symbols $\underline{E}_\mathrm{r}$ from their ideal positions $\underline{E}_\mathrm{t}$ in the constellation diagram. Specifically, it relates the root-mean-square value σ_err of the error vector amplitude $\left|\underline{E}_\mathrm{r}-\underline{E}_\mathrm{t}\right|$ to the root-mean-square value $\left|\underline{E}_\mathrm{t,a}\right|$ of the N ideal constellation points,

$$\begin{aligned} &\mathrm{EVM}=\frac{\sigma_\mathrm{err}}{\left|\underline{E}_\mathrm{t,a}\right|}, \quad \mathrm{EVM_{dB}}=20\log\left(\mathrm{EVM}\right), \\ &\left|\underline{E}_\mathrm{t,a}\right|^2=\frac{1}{N}\sum_{n=1}^{N}\left|\underline{E}_{\mathrm{t},n}\right|^2, \quad \sigma_\mathrm{err}^2=\frac{1}{N}\sum_{n=1}^{N}\left|\underline{E}_{\mathrm{r},n}-\underline{E}_{\mathrm{t},n}\right|^2. \end{aligned} \tag{C.9}$$

In these relations, $\mathrm{EVM_{dB}}$ is the EVM expressed in decibels, $\underline{E}_{\mathrm{t},n}$ and $\underline{E}_{\mathrm{r},n}$ with $n=1,2,\ldots N$ correspond to the complex amplitudes of the ideal transmitted and the actual received symbols, and $\left|\underline{E}_\mathrm{t,a}\right|^2$ corresponds to the average power of the signal. The BER is obtained by comparing the digitally processed bit sequence with the known transmitter bit sequence and by relating the number of counted errors to the total number of bits. For the results shown in Figure 3.4 and Figure 3.5 in Section 3.4, a random pattern of length 2^{15} (QPSK) or 2^{14} (16QAM) symbols is periodically repeated. The real-time oscilloscope records a sequence of 8×10^6 samples at a sampling rate of 128 GSa/s (‘Sa’ stands for samples) for symbol rates smaller than 20 GBd, and at a sampling rate of 256 GSa/s for symbol rates $\geq 20\,\mathrm{GBd}$. These correspond to recording lengths of 31.25 µs, and 62.5 µs, respectively. The BER and EVM evaluation is restricted to the last ten transmit pattern periods to ensure that the equalizers have already converged. In the case of QPSK modulation, the signal quality is so good that only very few errors can be found for the given recording length. Generally, if fewer than 13 errors are counted in a recording, the measured BER is not a reliable estimate [183] of the actual bit error probability due to poor statistics. Moreover, since the constellation points seen in Figure 3.4 and Figure 3.5 are not perfectly circular, the assumption of additive white Gaussian noise is violated, and we refrain from estimating the BER from the EVM. Therefore, the measured EVM itself is used as a quality metric for QPSK signals.

C.2 Experimental setup

The experimental setup is depicted in Figure C.1a. An arbitrary-waveform generator (AWG, Keysight M8194A) is used to drive an IQ-modulator to encode a quadrature-amplitude modulated signal onto an optical carrier at frequency f_0. The data pulses have a raised-cosine spectrum with bandwidth B and roll-off factor 0.1. The modulated optical signal is amplified by an erbium-doped fibre amplifier (EDFA), followed by a 0.6 nm optical bandpass filter to suppress amplified spontaneous emission (ASE) noise. A 50/50-coupler combines the modulated optical carrier with an unmodulated optical continuous-wave (c.w.) tone at frequency $f_1 = f_0 + B/2 + \Delta$, where $\Delta = 1 \ldots 2.5$ GHz denotes an additional offset required due to the roll-off of the data signal spectrum. This tone will form the THz local oscillator (LO) for generalized Kramers-Kronig (KK) reception. The optical spectrum is shown in Inset 1 of Figure 3.3 on Page 30. The optical carrier-to-signal power ratio (CSPR) is adjusted by varying the gain of the EDFA while keeping the power of the c.w. tone at optical frequency f_1 constant. A second 50/50-coupler is used to add another c.w. tone at optical frequency $f_2 = f_1 - f_{\mathrm{THz}}$, which is used as a reference for downconversion of the data signal and the LO tone to the THz carrier frequency f_{THz}. For downconversion, we use a high-speed uni-travelling-carrier photodiode [86] (UTC-PD), which is designed for operation in the H-band (0.220 … 0.325 THz). The tunable laser sources (Keysight, N7714A) used to provide the optical tones f_0 and f_2 feature linewidths of less than

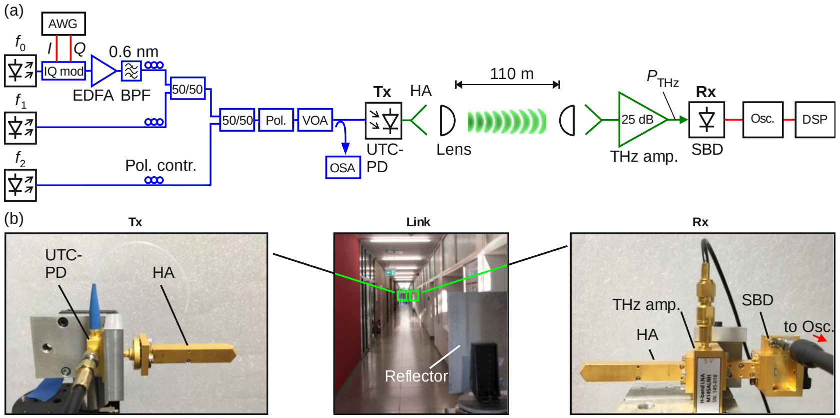

Figure C.1: (a) The data signal is modulated on an optical carrier at frequency f_0. The optical data signal is superimposed with an unmodulated optical tone f_1, which, after downconversion, will form the THz local oscillator (LO) for generalized Kramers-Kronig (KK) reception. The optical data signal and the LO are converted to the THz domain by photomixing with an unmodulated carrier $f_2 = f_1 - f_{THz}$ in a high-speed uni-travelling carrier photodiode (UTC-PD), see Inset 1 of Figure 3.3 on Page 30 for an optical spectrum measured at the input of the UTC-PD. Horn antenna (HA) / lens combinations are used to radiate and receive the THz signals. The transmission distance amounts to 110 m. After amplification by 25 dB, a Schottky-barrier diode (SBD) rectifies the THz signal. A real-time oscilloscope (Osc.) is used to capture the RF signal at the SBD output for off-line processing. AWG: arbitrary waveform generator. IQ mod: in-phase and quadrature modulator. EDFA: Erbium-doped fibre amplifier. BPF: optical bandpass filter. Pol.: polarizer. VOA: variable optical attenuator. OSA: optical spectrum analyser. DSP: digital signal processing. **(b)** Image of the transmission link. A mid-way THz reflector doubles the transmission distance within our 60 m-long building. Details of the Tx and Rx (focusing lenses not visible) are shown in the left and right image, respectively. *Copyright © Springer Nature.*

100 kHz, and the source (NKT Photonics, Koheras Adjustik) used for generating the LO tone at f_1 has a specified linewidth smaller than 0.1 kHz. We adjust the polarization using three polarization controllers (Pol. contr.) to maximize the power after a polarizer (Pol.) to ensure perfect interference of the optical signals. A variable optical attenuator (VOA, Keysight, N7764A) is used to set the optical power level of the overall signal entering the UTC-PD, and the optical spectrum is measured by an optical spectrum analyser (OSA). After downconversion of the optical signals by the UTC-PD, the THz signals are radiated into free space by a horn antenna (HA) and collimated by a

polytetrafluoroethylene (PTFE) lens. After a transmission distance of 110 m, the THz signal is collected by a second lens and a horn antenna. The resulting transmission loss of 17 dB is (over-) compensated by a low-noise amplifier with 25 dB gain, which is coupled to a Schottky-barrier diode (SBD) via a hollow waveguide. The SBD rectifies the THz signal, and a real-time oscilloscope (Keysight UXR0804A) with 80 GHz bandwidth records the SBD output current. Figure C.1b shows photographs of the transmitter, the receiver, and the transmission link. For doubling the distance of 55 m available in our building, a metal plate reflects the THz beam from the transmitter back to the receiver, which is positioned side by side with the transmitter. In our measurement, we did not observe any cross-talk between the THz transmitter and the receiver.

C.3 Model of the Schottky-barrier diode receiver

In this section, we describe the principle and the underlying mathematical model of the SBD envelope detector. The block diagram in Figure C.2 illustrates the system model consisting of an idealized THz transmitter (Ideal THz Tx), a THz band-pass filter (THz-BP) with impulse response $h_1(t)$, a nonlinear element followed by an idealized THz low-pass jointly representing the SBD, an additional low-pass (BB-LP) with impulse response $h_2(t)$ modelling the behaviour of the baseband circuits, and an analogue-to-digital converter (ADC) with subsequent digital signal processing (DSP) for KK phase reconstruction. In this model, the ideal THz Tx is assumed to generate the perfect THz data signal $u_{\mathrm{THz}}(t)$ according to Eq. (3.1) in Section 3.3, while $h_1(t)$ accounts for all impairments due to bandwidth limitations of the various components such as the AWG and the IQ modulator of the optical transmitter, the UTC-PD, the passive THz components such as antennae and waveguides, as well as the THz amplifier and the THz circuits at the SBD input, see Figure C.1. The SBD is modelled by a nonlinear element that represents the relation between the THz voltage and the associated current, followed by an ideal low-pass filter (THz-LP). The role of the ideal THz-LP is to suppress signals at the THz frequency and at harmonics thereof, which are generated in addition to the rectified current $i(t)$ by mathematically applying a nonlinear function to the time-dependent THz voltage $u_{\mathrm{THz}}(t)$. In our analysis, the THz-LP is assumed to take the average over several cycles of the THz signal and can be represented

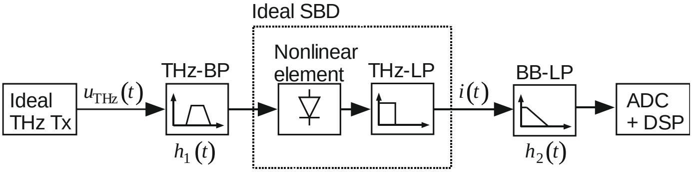

Figure C.2: Model of the SBD receiver. An idealized THz transmitter (Ideal THz Tx) generates a perfect THz data signal $u_{\mathrm{THz}}(t)$ while a bandpass filter (THz-BP) with impulse response $h_1(t)$ accounts for the bandwidth limitations of the transmitter, of the passive THz components such as antennas and waveguides, as well as of the THz amplifier and the THz circuits at the SBD input. The idealized SBD receiver is described by a nonlinear element followed by an idealized THz low-pass filter (THz-LP). The SBD output current $i(t)$ then enters a baseband low-pass filter (BB-LP) characterized by an impulse response $h_2(t)$, which accounts for the bandwidth limitations of the baseband circuits at the SBD output. The baseband receiver signal is then digitized by an analogue-to-digital converter (ADC), and digital signal processing (DSP) is used for KK phase reconstruction. *Copyright © Springer Nature.*

by an ideal low-pass filter with cut-off frequency $f_{\mathrm{THz}}/2$, see discussion of the mathematical description below. Note that in our consideration, the THz- LP is a merely theoretical construct, which is introduced for the sake of a simplified mathematical description. In addition, the baseband circuits at the SBD output are subject to physical bandwidth limitations caused, e.g., by the K-connector used at the SBD package, the subsequent RF cable, and potentially the ADC of the real-time-oscilloscope. The overall effect of these devices is described by another low-pass filter with impulse response $h_2(t)$ and affects the rectified signal $i(t)$.

The effect of the filter with impulse response $h_1(t)$ can be compensated by conventional adaptive feed-forward DSP algorithms applied after KK processing, see Appendix C.1 for details. The filter with impulse response $h_2(t)$, however, impairs the signal reconstruction [69,184] according to Eq. (3.5) of Section 3.3. The performance of our receiver could hence be further improved by implementing a digital compensation of $h_2(t)$ prior to KK processing [184].

For a mathematical description of the rectification in the SBD, the nonlinear element is described by a function $\tilde{g}$ that connects the THz voltage at the input to a current at the output of the nonlinear element. This connection is assumed to be instantaneous, and the rectified output current $i(t)$ of the ideal SBD is obtained by subsequent averaging over a few THz cycles,

$$\begin{aligned} i(t) &= \left\langle \tilde{g}\left(u_{\mathrm{THz}}(t)\right)\right\rangle, \\ \tilde{g}\left(u_{\mathrm{THz}}(t)\right) &= \sum_{l=0}^{L} c_l u_{\mathrm{THz}}^{l}(t). \end{aligned} \tag{C.10}$$

In this relation, the time averaging of the ideal THz-LP is denoted as $\langle\cdot\rangle$, and c_l denote the coefficients of a power series expansion of the instantaneous input-output characteristics $\tilde{g}$. According to Eq. (3.1) in Section 3.3, the THz voltage $u_{\mathrm{THz}}(t)$ incident at the ideal SBD can be written as

$$\begin{aligned} u_{\mathrm{THz}}(t) &= \Re\left\{\underline{U}(t)\mathrm{e}^{\mathrm{j}2\pi f_{\mathrm{THz}}t}\right\} \\ &= \tfrac{1}{2}\left[\underline{U}(t)\mathrm{e}^{\mathrm{j}2\pi f_{\mathrm{THz}}t} + \underline{U}^{*}(t)\mathrm{e}^{-\mathrm{j}2\pi f_{\mathrm{THz}}t}\right], \end{aligned} \tag{C.11}$$

where $\underline{U}^{*}(t)$ denotes the complex conjugate of the envelope $\underline{U}(t)$. Inserting Eq. (C.11) into Eq. (C.10) leads to

$$i(t) = \left\langle \sum_{l=0}^{L}\sum_{k=0}^{l} c_l \left(\tfrac{1}{2}\right)^{l} \binom{l}{k} \underline{U}(t)^{l-k}\, \underline{U}^{*}(t)^{k}\, \mathrm{e}^{\mathrm{j}2\pi f_{\mathrm{THz}}t(l-2k)} \right\rangle, \tag{C.12}$$

where $\binom{l}{k}$ denotes the binomial coefficients. Time-averaging suppresses all signal components at the THz carrier frequency and its harmonics $(l-2k)\, f_{\mathrm{THz}}$ for $l \neq 2k$. Retaining only expressions with $l = 2k$ allows us to express the ideal SBD output current $i(t)$ by the magnitude $\left|\underline{U}(t)\right|$ of the complex envelope, equivalently to Eq. (3.5) in Section 3.3,

$$i(t) = \sum_{k=0}^{K} c_{2k}\left(\tfrac{1}{2}\right)^{2k} \binom{2k}{k} \left|\underline{U}(t)\right|^{2k} = g\left(\left|\underline{U}(t)\right|\right), \tag{C.13}$$

where $K = \lfloor L/2 \rfloor$ with $\lfloor\cdot\rfloor$ denoting the floor function. Note that g represents a bijective function, the inverse of which is expanded into a power series with coefficients a_n according to Eq. (3.7) of Section 3.3.

C.4 Characterization of SBD receiver

For the generalized KK processing scheme, we need to reconstruct the THz voltage amplitude $\left|\underline{U}_{\mathrm{R}}\right|$ from the measured current i. The rectification characteristics of the SBD receiver crucially depend on the operating point as well as on the peripheral THz and baseband circuits and are difficult to describe analytically. We therefore approximate the receiver characteristics $g^{-1}(i)$ according to Eq. (3.7) in Section 3.3 as a power series with N+1 initially unknown coefficients a_n,

$$\left|\underline{U}_{\mathrm{R}}\right| = g^{-1}(i) = \sum_{n=0}^{N} a_n i^{\,n} \,. \tag{C.14}$$

The coefficients a_n are obtained by a least-squares fit of the power series expansion to measured data, which are obtained from the measurement setup shown in Figure C.3a. This setup is a slightly modified version of the setup described in Appendix C.2 without a free-space section between the THz transmitter and the receiver. Note that for this measurement, the unmodulated c.w. tone at f_1 is not needed and the associated laser is hence not part of the setup. Note also that the receiver characteristics $g^{-1}(i)$ according to Eq. (C.14) do not only account for the nonlinear characteristics of the SBD itself, but also for those of the preceding THz amplifier, see Figure C.3a. It is also worth noting that, while only even orders of $\left|\underline{U}(t)\right|$ contribute to the SBD current $i(t)$, see Eq. (C.13), the power series expansion of the inverse function $g^{-1}(i)$ in general contains even and odd orders, see Eq. (C.14).

As test signals for characterizing the SBD receiver, we use QPSK signals with a symbol rate of 0.5 GBd. The data pulses have a raised-cosine spectrum with a roll-off factor of 0.1. The symbol rate is intentionally chosen rather small to mitigate the influence of bandwidth limitations of the various devices, which are modelled by band-pass and low-pass filters with impulse responses $h_1(t)$ and $h_2(t)$ in Figure C.2 and which cannot be accounted for by an instantaneous input-output characteristic according to Eq. (C.10). Both the transmitted and the received signals are oversampled by a factor of 32, leading to a sequence of known voltages $U_{\mathrm{I}}(t_m)$ and $U_{\mathrm{Q}}(t_m)$ applied to the in-phase (I) and quadrature (Q) arm of the IQ modulator and to a sequence of corresponding SBD currents

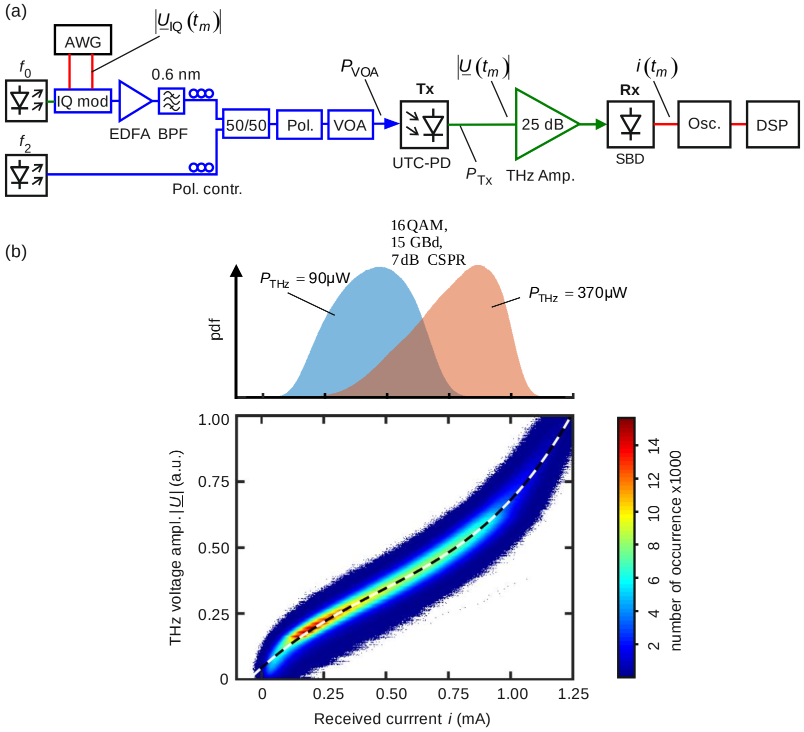

Figure C.3: Characterization of SBD receiver. **(a)** Measurement setup used to determine the characteristics of the SBD and the preceding THz amplifier. In the experiment, we feed QPSK test signals with varying THz voltage amplitudes to the input of the THz amplifier and measure the resulting currents at the SBD output. The setup is a slightly modified version of the one described in Figure C.1. Specifically, the free-space section between the THz transmitter and the receiver and the laser generating the unmodulated c.w. tone at optical frequency f_1 are omitted. AWG: arbitrary waveform generator. IQ mod: in-phase and quadrature modulator. EDFA: Erbium-doped fibre amplifier. BPF: optical bandpass filter. Pol.: polarizer. VOA: variable optical attenuator. UTC-PD: uni-travelling carrier photodiode. Osc.: oscilloscope. DSP: digital signal processing. **(b)** Measurement results and fitted SBD characteristics. We record $M = 10^8$ pairs of THz voltage amplitudes at the input of the SBD receiver along with the associated receiver currents i at the output. The graph in the lower part shows the associated histogram, based on bin sizes of 2.5 µA and 2 mV for the receiver current i and the THz voltage amplitude $|\underline{U}|$ respectively. The dashed curve shows the least-squares fit of a power series according to Eq. (C.14) with $N = 4$. The power series reliably describes the behaviour of the SBD over a broad range of THz voltage amplitudes. The graph on the top shows probability density functions (pdf) obtained from 16QAM data signals transmitted at THz powers of $P_{\mathrm{THz}} = 90\ \mu\mathrm{W}$ and $P_{\mathrm{THz}} = 370\ \mu\mathrm{W}$. Even for the low THz power, the vast majority of measured receiver currents are in the region where the fit is reliable. *Copyright © Springer Nature.*

$i(t_m)$, all measured at discrete times t_1, t_2, … t_M. Assuming that the IQ modulator and the UTC-PD are both operated in the linear regime, we can define a complex voltage signal $\underline{U}_{\mathrm{IQ}}(t_m) = U_{\mathrm{I}}(t_m) + \mathrm{j}U_{\mathrm{Q}}(t_m)$, the magnitude $|\underline{U}_{\mathrm{IQ}}(t_m)|$ of which is connected to the magnitude $|\underline{U}(t_m)|$ of the THz voltage incident at the SBD receiver by a linear relationship,

$$|\underline{U}(t_m)| = \xi |\underline{U}_{\mathrm{IQ}}(t_m)|. \tag{C.15}$$

Note that, as long as the scaling factor ξ is constant during a measured symbol sequence, its exact magnitude is of no consequence for the KK receiver, see Section "Phase reconstruction by Kramers-Kronig (KK) processing" in Appendix C.1.

To cover a broad range of THz amplitudes in our characterization of the SBD receiver, we record time sequences of $|\underline{U}_{\mathrm{IQ}}(t_m)|$ and $i(t_m)$ for different optical power levels at the input of the UTC-PD. These levels are adjusted by a variable optical attenuator (VOA) in front of the UTC-PD, see Figure C.3a. Varying the optical output power P_{VOA} of the VOA corresponds to changing the scaling factor ξ in Eq. (C.15) in proportion to P_{VOA}. We perform a series of measurements at various THz power levels P_{Tx} ranging from 0.1 µW to 1.4 µW to finally obtain a data set comprising a total of $M = 10^8$ voltage magnitudes $|\underline{U}(t_m)|$ along with the associated SBD receiver currents $i(t_m)$.

The histogram of this data set is shown in Figure C.3b. The coefficients a_n of Eq. (C.14) are obtained by minimizing a cost function $\gamma(a_1, \ldots a_{\mathrm{N}})$ that is given by the sum of the squared deviations of the measured values $|\underline{U}(t_m)|$ from the values $|\underline{U}_{\mathrm{R}}(t_m)|$ reconstructed according to Eq. (3.7) in Section 3.3,

$$\gamma(a_1, \ldots a_{\mathrm{N}}) = \sum_{m=1}^{M} \left(|\underline{U}(t_m)| - |\underline{U}_{\mathrm{R}}(t_m)| \right)^2 . \tag{C.16}$$

The result for a power series with $N = 4$ is shown as a dashed curve in Figure C.3b. The dashed curve corresponds to the red curve shown in Figure 3.2 in Section 3.3. The power series reliably describes the behaviour of the receiver in a broad range of incident THz voltage amplitudes. Only for very small voltage amplitudes, the fitted model function differs from the peak line of the measured histogram. This is a consequence of the fitting procedure, which minimizes the fit error of the THz voltage amplitudes $\left|\underline{U}\left(t_m\right)\right|$ and does not account for observational errors of the measured receiver currents $i\left(t_m\right)$. A positive effect of this approach is the fact that the resulting function comprises an offset $a_0 \neq 0$, that assigns a zero output current $i = 0$ to a non-zero reconstructed THz amplitude $\left|\underline{U}_\mathrm{R}\right| = g^{-1}\left(0\right)$. This offset avoids small values of the reconstructed THz amplitude, which would lead to large uncertainties in the phase reconstruction according to Eq. (3.4) due to the singularity of $\ln\left(\left|\underline{U}_\mathrm{R}\right|\right)$ at $\left|\underline{U}_\mathrm{R}\right| = 0$, and which would otherwise require artificial clipping of the signals at low reconstructed voltages [85]. Note that, in an actual transmission experiment, only a very small share of data points is affected by this offset. This can be understood from typical probability density functions (pdf) of the receiver current, which are exemplarily shown at the top of Figure C.3b. These pdfs refer to 16QAM signals with a symbol rate of 15 GBd transmitted at THz powers of $P_\mathrm{THz} = 90\,\mu\mathrm{W}$ and $P_\mathrm{THz} = 370\,\mu\mathrm{W}$, respectively. These THz powers correspond to the leftmost and rightmost point of the plots shown in Figure 3.5c on page 35. Even for the smallest THz power, the vast majority of measured receiver currents is in the region where the fit is reliable.

As an alternative to using QPSK test signals for characterization of the SBD and the associated THz amplifier, we also tried operating the device with c.w. THz tones at $f_\mathrm{THz} = 0.3\,\mathrm{THz}$ to extract the nonlinear relationship $\left|\underline{U}_\mathrm{R}\right| = g^{-1}(i)$. The result is plotted as a green trace in Figure C.4 together with the characteristics obtained from QPSK test signals, red trace. Except for the above-mentioned offset of the red trace at $i = 0$, the two characteristics coincide well, thereby confirming the validity of our approach. Note that the QPSK test signal, which consists of pulses with raised-cosine power spectra (roll-off 0.1), features a fairly high peak-to-average power ratio (PAPR) of around 7 dB. This PAPR allows sampling of the nonlinear SBD characteristics also at higher THz amplitudes without being forced to increase the power of a c.w. THz tone close to the maximum allowed input level of the THz amplifier.

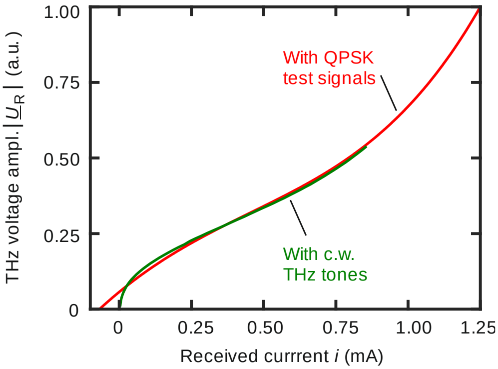

Figure C.4: Comparison of receiver characterization with QPSK test signals (red trace) and continuous-wave (c.w.) THz tones (green trace). Except for a small offset of the red trace at $i = 0$, the two characteristics coincide well. The increased peak-to-average power ratio (PAPR) of the QPSK test signal allows sampling of the nonlinear SBD characteristic also at higher THz amplitudes, whereas the c.w. tones were kept below the maximum allowed power level of the THz amplifier. *Copyright © Springer Nature.*

C.5 THz link budget and noise analysis

To measure the THz link budget, we use the setup shown in Figure C.5. Two unmodulated c.w. laser tones having equal powers and different frequencies f_1 and f_2 are superimposed in a 50/50 coupler and fed to the UTC-PD for photomixing. The resulting THz signal is then radiated to free space, transmitted over the link distance of 110 m and amplified by the low-noise amplifier (LNA) at the receiver. The THz output power P_{Tx} after the UTC-PD and the THz power P_{THz} after the LNA are measured with a calorimeter (VDI, Erickson PM4). The results for an optical input power of $P_{\text{opt}} = 10$ dBm at the input of the UTC-PD and a THz frequency of $f_{\text{THz}} = f_2 - f_1 = 0.3\,\text{THz}$ are summarized in Table C1. The THz power P_{Rx} at the input of the receiver is below the detection limit of the calorimeter and cannot be measured directly. We therefore measure the power P_{THz} after the LNA and calculate the power P_{Rx} by considering the gain of the LNA. From the differences of P_{Tx} and P_{Rx} we find a total loss of the link of 17 dB. The theoretical isotropic free-space path loss (FSPL) for the transmission distance of $d = 110$ m is given by

$$\mathrm{FSPL}_{\mathrm{dB}} = 10\log\left(4\pi d\frac{f_s}{c}\right)^2 = 123\,\mathrm{dB}\,. \tag{C.17}$$

We thus estimate a total gain of the antennas of 106 dBi. The antenna gain results from the Tx/Rx horn antennas, each with a gain of 25 dBi, and from two plano-convex polytetrafluoroethylene lenses (PTFE, model LAT200, 4” diameter).

Table C1: THz link budget for f_{THz} = 0.3 THz

P_{opt}	10 dBm
P_{Tx}	-16 dBm
$\mathrm{FSPL}_{\mathrm{dB}}$	123 dB
Total antenna gain	106 dBi
Link loss	17 dB
P_{Rx}	-33 dBm
G_{LNA}	25 dB
P_{THz}	-8 dBm

The LNA is designed for operation in the sub-millimetre H-band [171] (0.220 THz - 0.325 THz). It compensates the link loss of 17 dB and boosts the received THz signal prior to coupling it to the SBD. The measurement results for the *S*-parameters and the noise of the LNA are shown in Figure C.6. At a frequency of 0.3 THz the gain of the amplifier is 25 dB, and the noise figure is

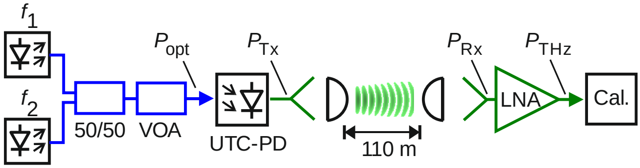

Figure C.5: Experimental setup for measuring the THz link budget. The THz signal at the transmitter is generated by superimposing two unmodulated optical c.w. tones with equal power and by feeding them to a UTC-PD for photomixing (combined optical power P_{opt}). A calorimeter is used to measure the transmitted THz power P_{Tx} as well as the THz power P_{THz} at the LNA output. The power P_{Rx} is calculated by considering the 25 dB gain of the LNA. *Copyright © Springer Nature.*

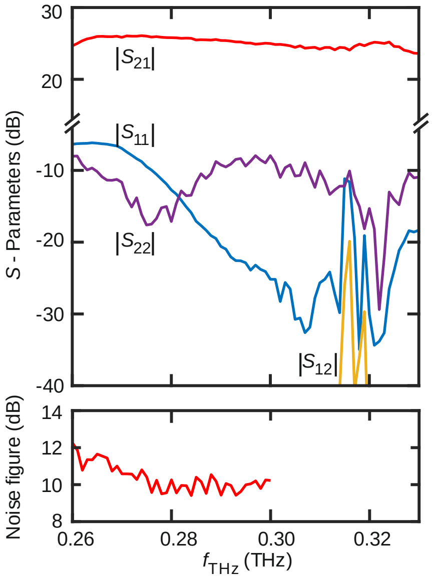

Figure C.6: *S*-Parameter and noise measurement results of the low-noise amplifier (LNA). The measurement was done by the manufacturer (Fraunhofer Institute for Applied Solid State Physics, IAF) using a vector network analyser. *Copyright © Springer Nature.*

$F \approx 10$. With a bandwidth of $B \approx 100$ GHz, the equivalent noise power at the input of the LNA is estimated to be

$$P_{\mathrm{n}} = k_{\mathrm{B}} T F B = 4.1\,\mathrm{nW} \mathrel{\hat{=}} \text{-}54\,\mathrm{dBm}\,. \tag{C.18}$$

For a received THz power P_{Rx} of -33 dBm, the estimated THz signal-to-noise power ratio amounts to 21 dB.

When characterizing the SBD receiver, Section C.4 and Figure 3.2 in Section 3.3, we do not discriminate between the nonlinear contribution of the LNA and the SBD because only the combined effect of both is relevant for KK processing. To get a better understanding of the amplifier and its saturation behaviour, we also characterized the device individually. To this end, we use the setup shown in Figure C.5. Figure C.7 shows the measured amplifier output power P_{THz} as a function of the transmitted THz power P_{Tx} measured after the

UTC-PD. For large transmitted THz power P_{Tx}, the amplifier output power P_{THz} saturates and the measured dependence of P_{THz} on P_{Tx} deviates from the initially linear relationship, see upper graph of Figure C.7. The corresponding gain compression of the THz amplifier is shown in the lower graph of Figure C.7. The maximum compression is 1.5 dB. We hence conclude that the compression of the LNA only contributes weakly to the nonlinear receiver response shown in Figure 3.2 on page 29.

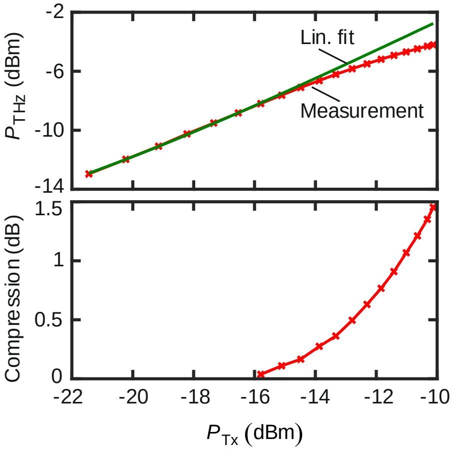

Figure C.7: THz amplifier compression. The experimental setup for measuring the THz power after a 110 m-long free-space transmission link and a 25 dB LNA is shown in Figure C.5. The transmitted THz power P_{Tx} is varied by a VOA which adjusts the optical input power delivered to the UTC-PD. **Upper graph:** THz power P_{THz} at the output of the THz amplifier as a function of P_{Tx}. The compression of the amplifier gain leads to a deviation from the linear characteristics. The green curve is obtained from a linear fit of the data points at low power levels $P_{\mathrm{Tx}} \leq -16$ dBm. **Lower graph:** Gain compression obtained from the deviation of the measured output power from the power expected according to the extrapolated linear relationship. The maximum compression amounts to 1.5 dB, measured for a transmitted THz power P_{Tx} of -10 dBm. *Copyright © Springer Nature.*

C.6 Spectral broadening by non-quadratic SBD characteristics

The non-quadratic characteristics of the SBD can lead to a spectral broadening of the rectified output current beyond the bandwidth B of the THz data signal. This effect might increase the bandwidth requirements of the receiver electronics. To investigate this influence, we artificially decrease the receiver bandwidth by introducing a digital 10th -order Butterworth low-pass filter at the beginning of our digital signal processing chain. As a test, we use QPSK signals with symbol rate $f_{\text{symb}} = 30\,\text{GBd}$ and 16QAM signals with symbol rate $f_{\text{symb}} = 15\,\text{GBd}$. The influence of the cut-off frequency f_{3dB} of the low-pass filter on the error vector magnitude (EVM) of the QPSK signal and on the BER of the 16QAM signal is depicted in Figure C.8a and Figure C.8b, respectively. The insets show the recorded spectrum (blue) of the received signal and the spectrum obtained after digital low-pass filtering (orange) with a cut-off frequency of $f_{\text{3dB}} = 1.3\,f_{\text{symb}}$. Note that the BER and the EVM increase sharply for cut-off frequencies of $f_{\text{3dB}} < 1.2\,f_{\text{symb}}$ because considerable spectral fractions of the down-converted signals are removed for lower cut-off frequencies due to the roll-off of 0.1 that was chosen for raised-cosine pulse shaping.

As expected, the results obtained for heterodyne reception and conventional KK processing are less influenced by low-pass filtering than generalized KK processing, which accounts for the actual non-quadratic characteristics of the SBD and which hence relies on third and higher-order signal-signal mixing products that are partially suppressed by the low-pass. Still, for QPSK signalling, the differences are negligible as long as a filter bandwidths of $f_{\text{3dB}} \geq 1.2\,f_{\text{symb}}$ is used. For 16QAM signals, Figure C.8b, we observe a slight degradation of the signal quality if the cut-off frequency is too small. However, even if the receiver bandwidth is restricted to $f_{\text{3dB}} = 1.2\,f_{\text{symb}}$, the signal quality obtained with the generalized KK receiver is much better than with heterodyne reception or conventional KK processing. We therefore conclude that the effect of spectral broadening is not very prominent and is not a fundamental drawback of generalized KK processing.

C.7 Oversampling requirements in the DSP

In the Kramers-Kronig processing, the amplitude $|U|$ first needs to be calculated from the measured SBD current i by applying the inverse function $g^{-1}(i)$ according to Eq. (3.7) of Section 3.3. In a second step, the phase is reconstructed by Eq. (3.6), which involves the calculation of the natural logarithm of the voltage amplitude $|\underline{U}(t)|$. The nonlinear nature of these relations leads to broadening of the signal spectrum and thus to performance penalties due to aliasing, unless the signal is sufficiently oversampled in the time domain. In the proof-of-principle demonstration discussed in the main manuscript, we used a rather large oversampling ratio of 6 samples per symbol to eliminate any influence of the spectral broadening. In a practical implementation, however, large oversampling would increase the complexity of the DSP chain. In the following, we investigate the system performance also for smaller oversampling ratios. Figure C.9 summarizes the results obtained for 16QAM signaling at a symbol rate of 15 GBd for different numbers of samples per symbol. Figure C.9a shows the BER as a function of the incident THz power for six samples per symbol (6 Sa/Symbol, transparent curves) and compares the results to the case when only three samples per symbol (3 Sa/Symbol, opaque curves) are used. The transparent curves obtained with six samples per symbol are identical to the curves shown in Figure 3.5c in Section 3.4. As expected, an increased oversampling ratio does not provide any benefit for heterodyne reception. For Kramers-Kronig processing, we find that three samples per symbol still provide good performance that is essentially identical to the one obtained for six samples per symbol. Figure C.9b and Figure C.9c show the BER for various numbers of samples per symbol for an incident THz power of 170 µW and 340 µW, respectively.

We also investigate the individual impact of the nonlinear relationship according to Eq. (3.7) and of the log-function in Eq. (3.6) of Section 3.3 on the required oversampling ratio. We observe that the spectrum of the reconstructed data-signal magnitude $\left|\underline{U}(t)\right|$ is less broadband than the spectrum of the associated SBD current $i(t)$, i.e., application of the nonlinear function $\left|\underline{U}(t)\right| = g^{-1}(i)$ according to Eq. (3.7) even leads to a spectral narrowing of $\left|\underline{U}(t)\right|$ with respect to the SBD current $i(t)$. We hence conclude that the required digital oversampling ratio is mainly dictated by the log-function in the phase

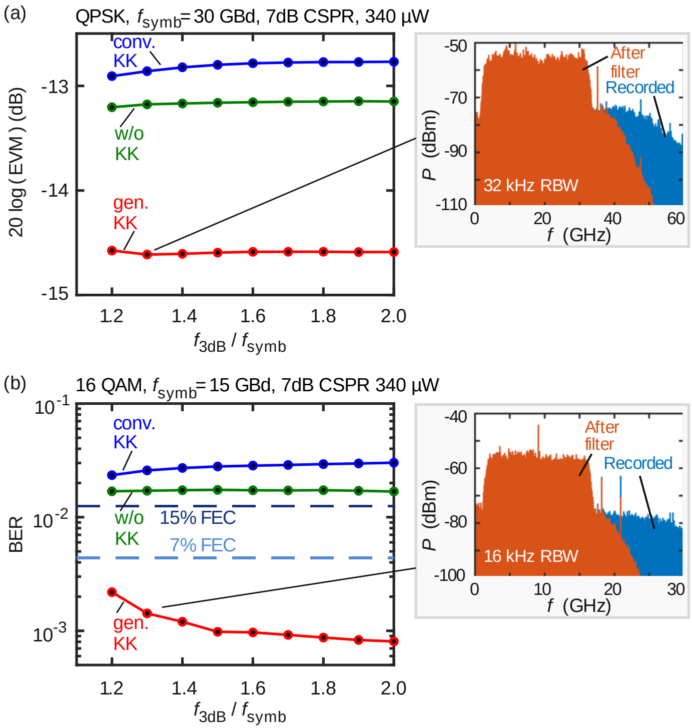

Figure C.8: Influence of spectral broadening. **(a)** Error vector magnitude (EVM) as a function of the cut-off frequency $f_{3\mathrm{dB}}$ of an artificially introduced low-pass filter for a 30 GBd QPSK data signal. The signal quality is essentially independent of the filter bandwidth as long as $f_{3\mathrm{dB}} \geq 1.2\, f_{\mathrm{symb}}$. The inset shows the recorded spectrum of the receiver current and the spectrum obtained after applying a digital low-pass filter with a cut-off frequency $f_{3\mathrm{dB}} = 1.3\, f_{\mathrm{symb}}$. **(b)** Bit error ratio (BER) as a function of the cut-off frequency $f_{3\mathrm{dB}}$ for a 15 GBd 16QAM data signal. The inset shows again the recorded spectrum of the receiver current and the spectrum obtained after applying a digital low-pass filter with a cut-off frequency $f_{3\mathrm{dB}} = 1.3\, f_{\mathrm{symb}}$. For generalized KK processing, a slight increase of the BER can be seen if the receiver bandwidth is not large enough. Still, even for $f_{3\mathrm{dB}} = 1.2\, f_{\mathrm{symb}}$ the signal quality of the generalized KK is much better than with heterodyne reception or conventional KK processing. *Copyright © Springer Nature.*

reconstruction according to Eq. (3.6) and not by the amplitude reconstruction according to Eq. (3.7) of Section 3.3. We attribute this observation to the fact that the application of the inverse function $\left|\underline{U}(t)\right| = g^{-1}(i)$ to the measured SBD current $i(t)$ undoes major parts of the spectral broadening that is introduced by the nonlinear SBD characteristic $i(t)=g\left(\left|\underline{U}(t)\right|\right)$ during detection of the band-limited data signal. Note that the magnitude operation $|.|$ still may cause some spectral broadening of $\left|\underline{U}(t)\right|$ with respect to $\underline{U}(t)$, but this effect seems to be not very significant for the data signals used in our experiments.

In summary, we may conclude that three samples per symbol are sufficient to obtain a good performance with the generalized KK receiver. These findings together with the results on the required ADC bandwidth, Figure C.8, indicate

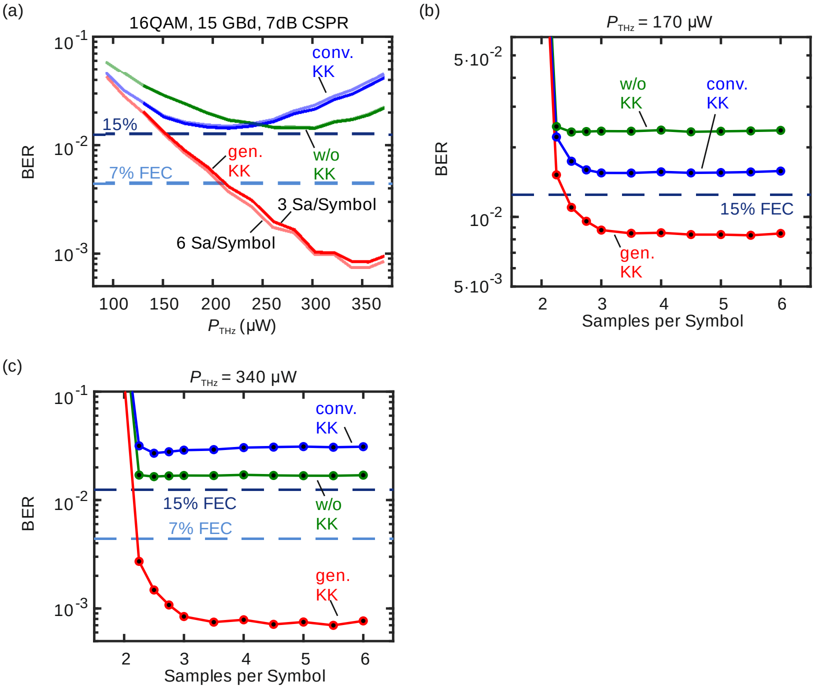

Figure C.9: Influence of oversampling in the DSP on transmission performance at 15GBd 16QAM. **(a)** BER as a function of the incident THz power P_{THz} for sampling with six samples per symbol (6 Sa/Symbol, transparent curves) and with three samples per symbol (3 Sa/Symbol, opaque curves). The transparent curves are identical to those in Figure 3.5c in Section 3.4. The results indicate that three samples per symbol still provide good performance which is essentially identical to the one obtained for six samples per symbol. **(b)** and **(c)** BER as a function of sampling rate for an incident THz power of 170 µW and 340 µW, respectively. The results confirm that a sampling rate of three samples per symbol is sufficient to achieve good performance of the generalized KK receiver. *Copyright © Springer Nature.*

that the additional KK-related DSP complexity can be minimized and will thus be overcompensated by the advantages of THz receiver circuits with reduced complexity.

C.8 32QAM measurements

In Section 3.4, we show the data transmission results for QPSK and 16QAM signals, Figure 3.4 and Figure 3.5. We also investigate the system performance with 32QAM signals. Figure C.10 displays the measured BER as a function of the symbol rate and as a function of the incident THz power P_{THz}. Also here, the generalized KK scheme shows clear performance advantages over conventional KK processing and heterodyne reception. We reach symbol rates of 5 GBd with a BER below the 7% FEC limit. Note that the resulting net data rate of 23 Gbit/s is significantly lower than the 115 Gbit/s achieved with QPSK and 16QAM modulation. This is partially caused by an erroneous non-optimum setting of the oscilloscopes used for sampling the SBD output signal in these

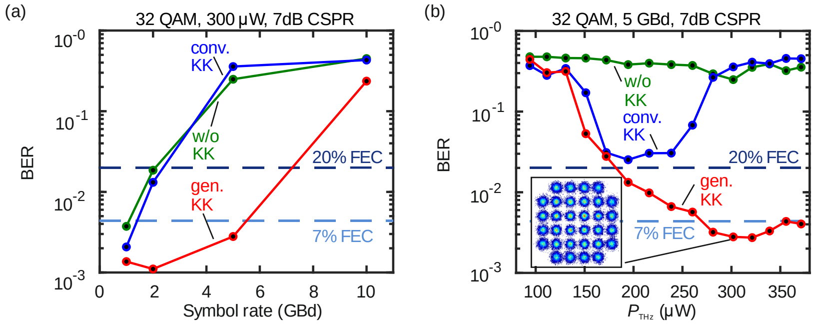

Figure C.10: Experimental results for 32 QAM measurements. **(a)** BER as a function of symbol rate with a CSPR = 7 dB and P_{THz} = 340 µW. The generalized KK scheme shows clear performance advantages over conventional KK processing and heterodyne reception. Employing generalized KK reception, the BER stays below the threshold for forward error correction with 7% FEC overhead for symbol rates of up to 5 GBd. For 5 GBd, we reach a net data rate of 23 Gbit/s. This data rate was limited by a non-ideal setting of the oscilloscopes in our measurement and does not represent a fundamental limit of generalized KK processing. **(b)** BER as a function of the incident THz power P_{THz} for a symbol rate of 5 GBd and a CSPR = 7 dB. Also here, the generalized KK scheme shows clear performance advantages over conventional KK processing and heterodyne reception. The constellation diagram for an incident THz power of 300 µW is shown in the inset. *Copyright © Springer Nature.*

experiments. Specifically, the sampling rate was reduced from 256 GSa/s to 128 GSa/s and 64 GSa/s without using a suitable anti-aliasing filter and without increasing the averaging time per sample accordingly. This leads to an aliasing of noise signals and hence to an increase of the noise floor. A more careful choice of device settings could allow for higher symbol rates and better signal qualities. Note that the results shown in Figure 3.4b and Figure 3.5b of Section 3.4 are also slightly impaired by this effect, leading to a slight performance degradation of symbol rates below 20 GBd, for which the sampling rate was reduced to 128 GSa/s without suitable anti-aliasing filter and without increasing the averaging time per sample accordingly, see Appendix C.1.

C.9 Comparison of generalized Kramers-Kronig processing and heterodyne detection with guard band

For the ideal generalized KK processing scheme, the phase of the complex envelope $\underline{U}(t)$, Eq. (3.2) of Section 3.3, is perfectly reconstructed, and the reception quality compares well to that obtained from heterodyne detection using an appropriate guard band. To demonstrate the equivalence of the reception techniques, we perform back-to-back transmission experiments with different signal processing approaches and compare the result of conventional and generalized KK reception with those obtained for heterodyne reception with and without guard band, see Figure C.11. These experiments were performed using the setup described in Figure 3.3 on page 30 without the 110 m transmission link and with a THz transmit power that was accordingly reduced by 17 dB. Figure C.11a shows the BER as a function of the incident THz power for conventional KK processing (‘conv. KK’, blue curve), generalized KK processing (‘gen. KK’, red curve) and heterodyne reception without a guard band (‘w/o KK’, green curve) and compares them to conventional heterodyne detection using an appropriate guard band of 15 GHz (‘heterodyne w/ 15 GHz guard band’, black curve). For signalling without guard band (conv. KK, w/o KK, gen. KK), the back-to-back transmission with reduced transmit power reproduces the results obtained from the 110 m-wireless link, see Figure 3.5c

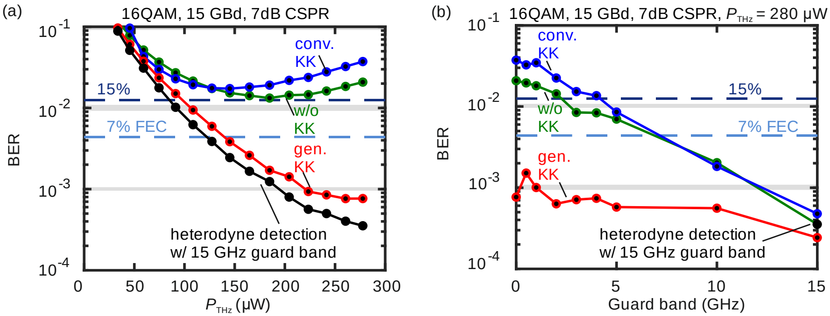

Figure C.11: Comparison of generalized KK processing with heterodyne detection with guard band. **(a)** BER as a function of the incident THz power P_{THz} for a symbol rate of 15 GBd and a CSPR of 7 dB. The curves 'gen. KK', 'conv. KK' refer to the generalized and the conventional KK phase reconstruction, and 'w/o KK' gives the results for heterodyne detection without guard band or KK processing, see Section 3.4 for details of the processing techniques. The curve 'heterodyne detection w/ 15 GHz guard band' was obtained for conventional heterodyne detection using an appropriate guard band of 15 GHz and without KK processing. We find that the generalized KK scheme offers a transmission performance comparable to that obtained from conventional heterodyne reception while overcoming the need for a guard band. **(b)** BER obtained for the various receiver schemes as a function of guard band width for an incident THz power P_{THz} = 280 µW. The rightmost data point of the green curve ('w/o KK') corresponds to the case of conventional heterodyne detection with an appropriate 15 GHz guard band (black dot). We find that the introduction of a guard band can slightly improve the performance of the generalized KK receiver. We attribute this effect to a still imperfect characterization of the SBD characteristics, leading to residual impairments from signal-signal mixing products that decrease once a guard band is introduced. *Copyright © Springer Nature.*

on page 35, thereby confirming the comparability of the two experiments. We also find that the generalized KK scheme offers a transmission performance comparable to that obtained from conventional heterodyne reception while overcoming the need for a guard band. The slightly better performance of the heterodyne reception with guard band is attributed to a still imperfect characterization of the nonlinear transfer characteristics of the SBD, which leads to residual impairments from signal-signal mixing products in the generalized KK processing scheme. In Figure C.11b the influence of the guard band width is investigated. The rightmost data point of the green curve (w/o KK) corresponds to the case of conventional heterodyne detection with an appropriate 15 GHz guard band (black dot). As expected, the generalized KK scheme does not require a guard band, whereas the performance of conventional

KK processing (conv. KK, blue curve) and of heterodyne detection (w/o KK, green curve) improves greatly with increasing guard band width and hence reduced detrimental impact of signal-signal mixing products. Note that a slight performance improvement with increasing guard band width is also observed for the generalized KK scheme, which we attribute again to a still imperfect characterization of the SBD characteristics and the associated residual impairments from signal-signal mixing products.

C.10 Comparison of EVM for QPSK and 16QAM

In Section 3.4, we used the EVM as a quality metric for QPSK modulation, since the limited recording length did not allow for a reliable measurement of the BER. For better comparison of both modulation formats, we show in

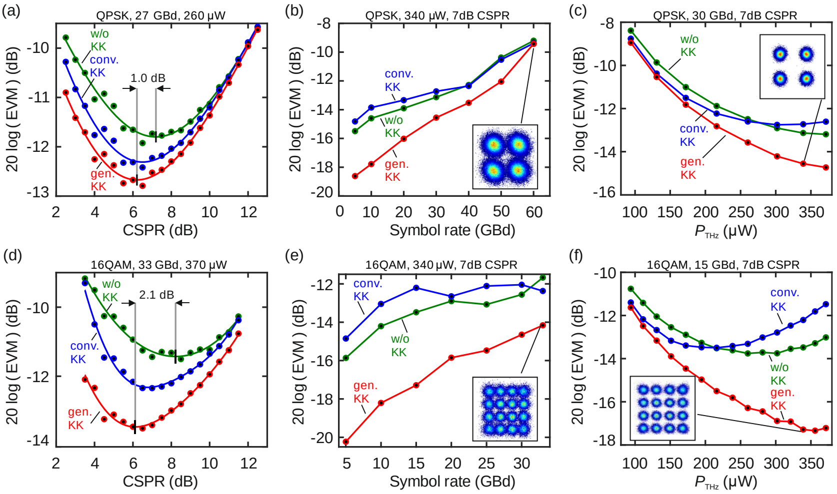

Figure C.12: Results of the transmission experiments using QPSK and 16QAM signals, all transmitted over a free-space distance of 110 m. **(a-c)** Error vector magnitude (EVM), for QPSK transmission as a function of the carrier-to-signal power ratio (CSPR), the symbol rate, and the incident THz power P_{THz}. The curves are identical to the ones shown in Figure 3.4a-c in Section 3.4, and are repeated here for better comparison to the results for 16QAM signalling. **(d-f)** EVM for 16QAM signalling as a function of the CSPR, the symbol rate, and the incident THz power P_{THz}. The EVM is derived from the same recordings as the BER in Figure 3.5 in Section 3.4. *Copyright © Springer Nature.*

Figure C.12 the EVM for QPSK together with the results for 16QAM transmission. The curves in Figure C.12a-c are identical to the curves in Figure 3.4a-c in Section 3.4

C.11 Outdoor performance

Our experimental results are achieved under laboratory conditions in an indoor environment. Nevertheless, the results give a good indication of the performance that can be expected for outdoor operation since the transmission link is only weakly impaired by adverse weather conditions. Figure C.13 shows the frequency-dependent atmospheric attenuation for various weather conditions [7–9]. At a carrier frequency of 0.3 THz, the atmospheric absorption along a 110 m-long transmission link amounts to 0.6 dB for clear sky, to 1.4 dB for heavy fog (visibility 50 m), and to 2.4 dB in case of heavy rain with rates of 40 mm/h. These attenuations are much lower than those expected for optical links for heavy fog [185] (visibility 50 m), see dashed line in Figure C.13, and can be easily compensated by an additional THz amplifier at the transmitter [22]. Note that in temperate climate, rain rates of 40 mm/h or more are

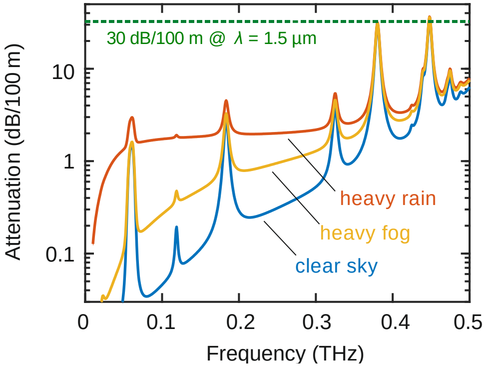

Figure C.13: Free-space atmospheric attenuation under different weather conditions. The blue curve shows the atmospheric attenuation for a clear sky [7] (temperature of 15 °C, water-vapour content of 7.5 g/m^3). The yellow curve shows the attenuation for thick fog [8] with a visibility in the order of 50 m. The red curve shows the attenuation [9,10] for a rain rate of 40 mm/h. As a reference, the green dashed line shows the attenuation of a free-space optical link operated at a wavelength of 1.5 µm under heavy fog (visibility 50 m). *Copyright © Springer Nature.*

extremely rare and typically occur only for less than 0.01% of the time [10] such that wireless THz links should offer highly reliable connectivity.

[end of Methods and Supplementary Information of submission [J4]]

C.12 Comparison of phase retrieval algorithms

In Chapter 3, we show that the KK receiver allows recovering the complex signal by only measuring its intensity. Recovering the phase of a signal is not only important in T-wave communications but also in other fields such as astronomy, wave front sensing, and imaging. Various algorithms to retrieve the phase information have been proposed [186–189].

The *Gerchberg-Saxton algorithm* recovers the phase information from intensity measurements in the image plane and the diffraction plane [186]. At first, the amplitude information from the image picture is combined with random phase values. The resulting complex waveform is propagated to the diffraction plane by using the Fourier transform (FT). The calculated phase is combined with the amplitude values measured in the diffraction plane. The complex wave front is then propagated back to the image plane. The calculated phase information in the image plane is combined with the measured amplitudes, and the complex wave front is again propagated to the diffraction plane. The procedure of propagating between the image plane and the diffraction plane is repeated. Gerchberg and Saxton demonstrated that with each iteration the error is decreasing [186]. Fienup [187] formulated a generalization of the Gerchberg-Saxton algorithm and called it the *error-reduction algorithm*. This algorithm allows the phase reconstruction of a single intensity measurement if certain a priori information of the Fourier Domain are given.

In principle, iterative algorithms could also be used to recover the phase of the data signal in a communication application. However, the calculation effort of the iterative phase recovery might not be acceptable for a real-time implementation of these algorithms. In addition, a priori information of the spectrum is required. In [189] it is demonstrated that iterative techniques can be used to reconstruct the phase of a minimum-phase signal. It therefore replaces the Hilbert transform by iterative computation.

This approach can also be used to recover the phase of the analytic data signal $\underline{U}_\mathrm{s}(t)$ of the complex envelope $\underline{U}(t)$, see Eq. (3.2) in Section 3.3. In this case, we know that $\underline{U}_\mathrm{s}(t)$ has a single-sided amplitude spectrum. Figure C.14 illustrates the phase-reconstruction algorithm. To simplify the description, we assume time-continuous signals. In an actual implementation, the signal is sampled at discrete times and the FT needs to be replaced with the discrete-time FT. The current $i(t) = g(|\underline{U}(t)|)$ at the output of the SBD receiver depends on the amplitude $|\underline{U}(t)|$ of the THz signal at the SBD receiver input, see Eq. (3.5) . By inverting the function g the amplitude $|\underline{U}(t)|$ is obtained. In the n^th-iteration the complex envelope is estimated by $\underline{U}_{n-1}(t) = |\underline{U}(t)|\,\mathrm{e}^{\mathrm{j}\Phi_{n-1}(t)}$, where the initial phase $\Phi_0(t)$ is set to zero. A FT is performed to obtain the spectra $\underline{\tilde{U}}_n(f)$ and the negative frequency components are set to 0, to fulfill the single-sideband constrain. After this, the inverse FT (IFT) is performed and the phase $\Phi_n(t)$ of the signal $\underline{U}_n(t)$ gives a new estimate of the phase of the complex envelope $\underline{U}(t)$. This procedure is repeated N-times.

Figure C.15 shows a comparison of the iterative phase retrieval approach with the KK processing as explained in Chapter 3 for the case of 16QAM signals with a symbol rate of 15 GBd and a CSPR of 7 dB. The blue, green, and red curve are identical to the ones shown in Figure 3.5c on Page 35. For the iterative process (black curves), two cases are investigated. The first case (‘iterative 1’)

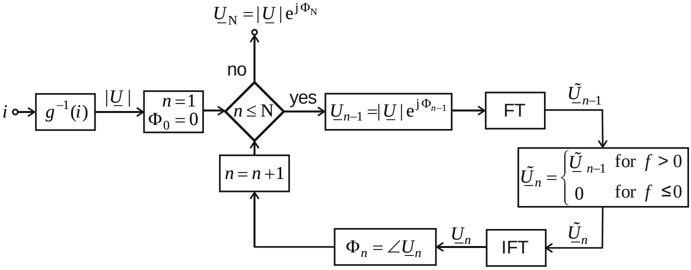

Figure C.14: Error-reduction algorithm to recover the phase of an analytic signal. First the inverse function g^{-1} is applied to the measured SBD current $i(t)$ to get the amplitude $|\underline{U}(t)|$. The phase $\Phi(t)$ of the complex amplitude $\underline{U}(t)$ is obtained iteratively. In each iteration, the Fourier transformation (‘FT’) is applied to the complex amplitude $\underline{U}_{n-1}(t)$ to get the spectral information $\underline{\tilde{U}}_{n-1}(f)$. Afterwards the spectral components $\underline{\tilde{U}}_{n-1}(f)$ are set to zero for all negative frequencies. The inverse FT (‘IFT’) is applied to the spectrum $\underline{\tilde{U}}_n(f)$ and the phase Φ_n is obtained from the complex amplitude $\underline{U}_n(t)$. These steps are repeated N times.

considers a square relation of the SBD current and the voltage amplitude, $i(t)=|\underline{U}(t)|^2$. The second case ('iterative 2') considers the measured SBD characteristic, see Eq. (3.7). The algorithm converges typically after 20 to 80 iterations. In our evaluation, we used $N=200$ iterations to ensure convergence. After the iterative phase reconstruction, the complex amplitude $\underline{U}_\mathrm{N}$ is analyzed using the same DSP steps as for the other processing types. The results of the first iterative approach are almost identical to the ones with conventional KK processing, and the results of the second iterative approach are almost identical to the generalized KK processing. Therefore, the iterative phase retrieval works as good as the KK processing, see Eq. (3.6). The KK processing, however, allows to directly calculating the phase $\Phi(t)$ and requires less calculation steps than the iterative approach. This makes the KK processing the preferable solution for high-speed communications.

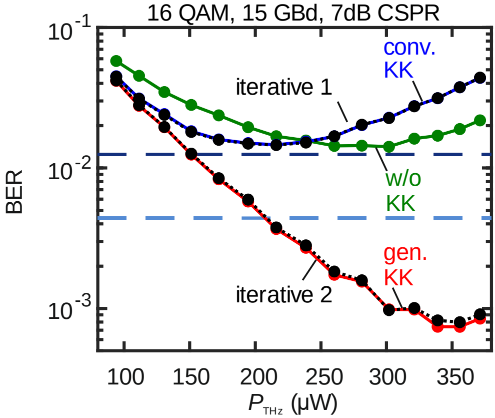

Figure C.15: Comparison of various processing techniques. BER as a function of the incident THz power P_THz for a symbol rate of 15 GBd and a CSPR of 7 dB. The curves for generalized Kramers-Kronig processing ('gen. KK'), conventional KK reception ('conv. KK') and for heterodyne reception without any KK processing ('w/o KK') are equivalent to the results shown in Figure 3.5c. In black, the results of the iterative phase retrieval are shown. The first method ('iterative 1') considers a square relation of the SBD current $i(t)$ and the amplitude $|\underline{U}(t)|$ and shows a similar performance than the conventional KK. The second method ('iterative 2') considers the measured SBD characteristic according to Eq. (3.7) and shows a similar performance than the generalized KK. The KK processing requires less computation than the iterative process and is therefore the preferred solution.

Recently, it was also demonstrated that the KK signal processing can be applied to holographic imaging [190]. This allows to reduce the interferogram bandwidth, enables fast processing times and does not require information on the sample [190].

D. Optoelectronic THz receiver

The content of the following sections has been published in the Supplementary Information of the journal publication [J3]. In order to fit the structure and layout of this document, it was adapted accordingly.

> **T. Harter**, S. Ummethala, M. Blaicher, S. Muehlbrandt, S. Wolf,
> M. Weber, M. M. H. Adib, J. N. Kemal, M. Merboldt, F. Boes,
> S. Nellen, A. Tessmann, M. Walther, B. Globisch, T. Zwick, W.
> Freude, S. Randel, C. Koos, "Wireless THz link with optoelectronic
> transmitter and receiver," *Optica*, **6**, 1063–1070 (2019).
> DOI: 10.1364/OPTICA.6.001063 © The Optical Society.

[start of the Supplementary Information of paper [J3]]

D.1 Mathematical model

In Chapter 4, we show coherent wireless THz communications using an optoelectronic receiver [42,106,108] and a tunable photonic local oscillator (LO). The concept of optoelectronic downconversion in a photoconductive T-wave receiver (Rx) is illustrated in Figure 4.2a on Page 45. In the following, we give a detailed derivation of the associated mathematical model.

The T-wave data signal from the transmitter (Tx) at an angular carrier frequency $\omega_\mathrm{S} = 2\pi\, f_\mathrm{S}$ is received by a bow-tie antenna resulting in a T-wave voltage across its feed points,

$$U(t) = \hat{U}_\mathrm{S}(t)\cos\left(\omega_\mathrm{S} t + \varphi_\mathrm{S}(t)\right). \tag{D.1}$$

In this relation, $\hat{U}_\mathrm{S}(t)$ is the modulated T-wave voltage amplitude, and $\varphi_\mathrm{S}(t)$ is the associated modulated phase. The antenna feed points are connected to a photoconductor G, which is illuminated by the superposition of two unmodulated optical fields $E_\mathrm{LO,a}(t)$ and $E_\mathrm{LO,b}(t)$ with frequencies $\omega_\mathrm{LO,a}$, $\omega_\mathrm{LO,b}$, amplitudes $\hat{E}_\mathrm{LO,a}$, $\hat{E}_\mathrm{LO,b}$, and phases $\varphi_\mathrm{LO,a}$, $\varphi_\mathrm{LO,b}$,

$$\begin{aligned} E_{\mathrm{LO,a}}(t) &= \hat{E}_{\mathrm{LO,a}} \cos\left(\omega_{\mathrm{LO,a}} t + \varphi_{\mathrm{LO,a}}\right), \\ E_{\mathrm{LO,b}}(t) &= \hat{E}_{\mathrm{LO,b}} \cos\left(\omega_{\mathrm{LO,b}} t + \varphi_{\mathrm{LO,b}}\right). \end{aligned} \tag{D.2}$$

This leads to an optical power, which oscillates at a frequency $\omega_{\mathrm{LO}} = \left|\omega_{\mathrm{LO,a}} - \omega_{\mathrm{LO,b}}\right|$ and has an amplitude $\hat{P}_{\mathrm{LO,1}}$,

$$P_{\mathrm{LO}}(t) = P_{\mathrm{LO,0}} + \hat{P}_{\mathrm{LO,1}} \cos\left(\omega_{\mathrm{LO}} t + \varphi_{\mathrm{P,LO}}\right). \tag{D.3}$$

The quantities $P_{\mathrm{LO,0}}$, $\hat{P}_{\mathrm{LO,1}}$ are expressed by the (normalized) electrical field strengths, and the phase $\varphi_{\mathrm{P,LO}}$ is given by the relative phases of the optical tones,

$$\begin{aligned} P_{\mathrm{LO,0}} &= \tfrac{1}{2}\left(\hat{E}_{\mathrm{LO,a}}^2 + \hat{E}_{\mathrm{LO,b}}^2\right), \\ \hat{P}_{\mathrm{LO,1}} &= \hat{E}_{\mathrm{LO,a}}\, \hat{E}_{\mathrm{LO,b}}, \\ \varphi_{\mathrm{P,LO}} &= \varphi_{\mathrm{LO,a}} - \varphi_{\mathrm{LO,b}}. \end{aligned} \tag{D.4}$$

The photocarriers generated by the absorbed optical power change the photoconductance according to

$$G(t) = \mathcal{G} P_{\mathrm{LO}}(t) = G_0 + \hat{G}_{\mathrm{LO}} \cos\left(\omega_{\mathrm{LO}} t + \varphi_{\mathrm{LO}}\right), \tag{D.5}$$

where $\mathcal{G}$ denotes a proportionality constant that describes the sensitivity of the photoconductor. Note that the phase φ_{LO} of the conductance oscillation might differ from the phase of the optical power oscillation $\varphi_{\mathrm{P,LO}}$ in case the period of the LO power oscillation is of the same order of magnitude as the lifetime of the free carriers in the photoconductor. The resulting current $I(t)$ through the photoconductor is then given by the product of the time-varying conductance $G(t)$ and the time-varying voltage $U(t)$,

$$\begin{aligned} I(t) &= G(t)U(t) \\ &= \underbrace{G_0 \hat{U}_\mathrm{S}(t)\cos\left(\omega_\mathrm{S} t + \varphi_\mathrm{S}(t)\right)}_{(1)} \\ &\quad + \underbrace{\tfrac{1}{2}\hat{G}_\mathrm{LO}\hat{U}_\mathrm{S}(t)\cos\left((\omega_\mathrm{S}+\omega_\mathrm{LO})t + \varphi_\mathrm{S}(t) + \varphi_\mathrm{LO}\right)}_{(2)} \\ &\quad + \underbrace{\tfrac{1}{2}\hat{G}_\mathrm{LO}\hat{U}_\mathrm{S}(t)\cos\left((\omega_\mathrm{S}-\omega_\mathrm{LO})t + \varphi_\mathrm{S}(t) - \varphi_\mathrm{LO}\right)}_{(3)}. \end{aligned} \tag{D.6}$$

After amplification of the current $I(t)$ using a transimpedance amplifier (TIA), only the low-frequency-part (3) of Eq. (D.6) remains. This leads to a downconverted current at the intermediate frequency $\omega_\mathrm{IF} = |\omega_\mathrm{S} - \omega_\mathrm{LO}|$,

$$I_\mathrm{IF}(t) = \tfrac{1}{2}\hat{G}_\mathrm{LO}\hat{U}_\mathrm{S}(t)\cos\left(\omega_\mathrm{IF} t + \varphi_\mathrm{S}(t) - \varphi_\mathrm{LO}\right). \tag{D.7}$$

The intermediate signal hence contains the amplitude and phase information of the T-wave data signal and can be processed by low-frequency electronics.

D.2 T-wave receiver

This section gives details of the implementation and the characterization of the optoelectronic Rx used in our experiments. Figure D.1 shows images of our Rx module. The photoconductor [106,108] is connected to the feed points of the bow-tie antenna, see Figure D.1a. The antenna is electrically bonded to a transimpedance amplifier (TIA, Maxim Integrated [111] PHY1097) for processing the downconverted intermediate-frequency current. Note that the TIA is originally designed for amplification of receiver signals in a passive optical network, where the photodiode is reverse-biased by the TIA. In our application, the photoconductor does not require a bias voltage and we hence use a capacitor *C* to decouple the photoconductor from the DC bias at the TIA input terminals. Metal wire bonds are used to electrically connect the output of the TIA to a printed circuit board (PCB) consisting of a gold-plated alumina ceramic substrate. The photoconductor is illuminated from the top with the time-dependent optical power $P_\mathrm{LO}(t)$, which is coupled to the active region of the device from the horizontally positioned fibre by a photonic wire bond [112,191], see inset of Figure D.1a. The assembly is placed on a silicon lens which focuses the T-wave incoming from below onto the antenna, see Figure 4.2c on Page 45. All components are placed in a metal housing for electromagnetic shielding of the Rx circuits and for simplified handing of the assembly. The fully packaged Rx is shown in Figure D.1b. The photonic LO is fed to the Rx with a fibre, and the downconverted RF data signal (‘data out’) is processed further by standard laboratory equipment. In the following, we give a detailed characterization of the Rx in terms of conversion efficiency, bandwidth, and noise.

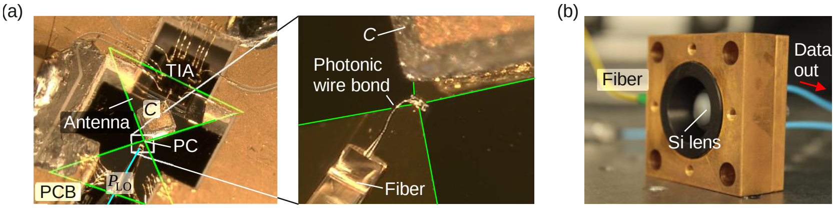

Figure D.1: Optoelectronic coherent T-wave Rx. **(a)** Microscope image of the Rx module. The photoconductor (PC) is connected to an on-chip bow-tie antenna, which is electrically bonded to a transimpedance amplifier (TIA). For better visibility, the contour of the bow-tie antenna is marked by green lines. The capacitor $C = 1$ nF is used to decoupled the photoconductor from the DC bias voltage that is supplied by the TIA at its input. Metal wire bonds are used to electrically connect the output of the TIA to a printed circuit board (PCB) consisting of a gold-plated alumina ceramic substrate. The PCB includes sub-miniature plugs for off-chip RF and DC connections. The photoconductor is illuminated by the time-dependent optical LO power $P_{LO}(t)$ through a fibre and a 3D-printed photonic wire bond, see inset for details. **(b)** Fully packaged Rx module. The photoconductor, antenna, TIA, and PCB are glued to a silicon lens for coupling the T-wave incident from below to the on-chip bow-tie antenna. All components are placed inside a metal housing for electromagnetic shielding of the Rx circuits. The photonic LO is fed to the Rx with a fibre. The downconverted data signal (‘data out’) is processed further by standard RF-equipment connected to the sub-miniature plugs on the PCB. *Reprinted with permission from [J3] © The Optical Society.*

Conversion efficiency

First we quantify the frequency-dependent response of the photoconductor connected to a bow-tie antenna. We define the conversion efficiency η as the ratio of the output power at the intermediate frequency in a $50\,\Omega$ load resistor related to the incident THz power P_{THz}. The conversion efficiency is measured with a photoconductor very similar to the one used for the data transmission experiment. Details are published elsewhere [108].

For this measurement, the same continuous-wave (c.w.) lasers are used for both the Tx and the Rx LO, i. e, $\omega_\mathrm{S} = \omega_\mathrm{LO}$. One of the Tx lasers is phase-modulated [192,193] by a saw-tooth signal with maximum amplitude of 2π and repetition period $2\pi/\omega_\mathrm{m}$ where $\omega_\mathrm{m} = 2\pi \times 15\,\mathrm{kHz}$. The resulting voltage at the Rx antenna feed points is then modulated according to Eq. (D.1), $U(t) = \hat{U}_\mathrm{S}\cos\left((\omega_\mathrm{S} + \omega_\mathrm{m})t + \varphi_\mathrm{S}\right)$. After downconversion, the current according to Eq. (D.7) becomes $I_\mathrm{IF}(t) = \hat{I}_\mathrm{IF}\cos(\omega_\mathrm{m}t + \varphi_\mathrm{S} - \varphi_\mathrm{LO})$ with $\hat{I}_\mathrm{IF} = \frac{1}{2}\hat{G}_\mathrm{LO}\hat{U}_S$. The current amplitude $\hat{I}_\mathrm{IF}$ is measured with a lock-in amplifier (LIA) tuned to the modulation frequency ω_m. We change the T-wave frequency $\omega_\mathrm{S} = \omega_\mathrm{LO}$ and measure $\hat{I}_\mathrm{IF}$ with the LIA along with the incident THz power P_THz using a calibrated pyroelectric thin film detector (Sensor- und Lasertechnik GmbH, THz20). The conversion efficiency η is then found as

$$\eta = \frac{\frac{1}{2}\hat{I}_\mathrm{IF}^2 \times 50\,\Omega}{P_\mathrm{THZ}}. \tag{D.8}$$

In this relation, we model the photoconductor as an ideal current source driving a 50 Ω load impedance. This assumption is justified since the impedance of the photoconductor is much higher than the 50 Ω load, even under strong illumination. Figure D.2 shows the conversion efficiency of the photoconductive Rx in dependence of the frequency f_S for an optical power of $P_\mathrm{LO,0} = \hat{P}_\mathrm{LO,1} = 30\,\mathrm{mW}$. The grey hatched area indicates the frequency range used in our experiments. In general, the T-wave bandwidth of a photoconductor is limited by the lifetime τ of the free carriers that are generated by the incident optical signal. This lifetime can be reduced by low-temperature growth of the associated III-V materials [106]. The frequency response of our device shows a roll-off of the conversion efficiency for frequencies beyond $f_{\mathrm{S},\tau} = 0.2\,\mathrm{THz}$, corresponding to a carrier lifetime of $\tau = 1/\left(2\pi f_{\mathrm{S},\tau}\right) = 0.8\,\mathrm{ps}$. The conversion efficiency drops by 10 dB and remains virtually constant for frequencies in the range $0.3\,\mathrm{THz} \le f_\mathrm{S} \le 0.6\,\mathrm{THz}$.

We further investigate the dependence of the conversion efficiency $\eta\left(\hat{P}_\mathrm{LO,1}\right)$ on the LO power $\hat{P}_\mathrm{LO,1} = P_\mathrm{LO,0}$, see Figure D.3. At a T-wave frequency of

0.31 THz, we find a conversion efficiency η of -63 dB at an LO power of $P_{\mathrm{LO},0} = \hat{P}_{\mathrm{LO},1} = 30\,\mathrm{mW}$. By measuring the LO-power-dependence of the root mean square (RMS) voltage $U_{\mathrm{S,RMS}}\left(\hat{P}_{\mathrm{LO},1}\right)$ of the signal after the transimpedance amplifier, we can estimate the conversion efficiency for a certain LO power by

$$\eta\left(\hat{P}_{\mathrm{LO},1}\right) = \eta(30\,\mathrm{mW})\left(\frac{U_{\mathrm{S,RMS}}\left(\hat{P}_{\mathrm{LO},1}\right)}{U_{\mathrm{S,RMS}}(30\,\mathrm{mW})}\right)^2 . \tag{D.9}$$

In this relation, we use the fact that the oscillation amplitude $\hat{G}_{\mathrm{LO}}$ of the LO photoconductance and hence the current amplitude of $I_{\mathrm{IF}}(t)$ at the intermediate frequency increases in proportion to the optical LO power $\hat{P}_{\mathrm{LO},1} = P_{\mathrm{LO},0}$, see Eq. (D.7). The current I_{IF} at the intermediate frequency is translated into a voltage signal at the output of the transimpedance amplifier, from which the RMS value is taken to obtain $U_{\mathrm{S,RMS}}\left(\hat{P}_{\mathrm{LO},1}\right)$. For the devices used in our current experiments, the conversion efficiency can be increased by roughly 4 dB, if the LO power is increased from 30 mW to 60 mW. Note that the conversion efficiency of our current photoconductor saturates at high optical power

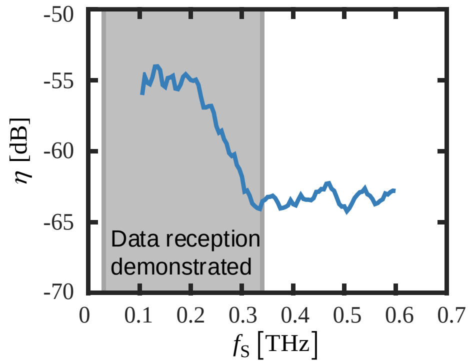

Figure D.2: Conversion efficiency of the photoconductive Rx for an optical power of $P_{\mathrm{LO},0} = \hat{P}_{\mathrm{LO},1} = 30\,\mathrm{mW}$. The gray area marks the frequency range that is used for the data transmission experiments. The conversion efficiency for frequencies larger than 0.34 THz is reduced by 10 dB, but remains constant up to at least 0.6 THz. *Reprinted with permission from [J3] © The Optical Society.*

levels – this aspect might be overcome in the future by optimized device design. The comparatively high optical LO power levels might be reduced to values of below 10 mW by using alternative device concepts such as plasmonic internal photoemission detectors [101].

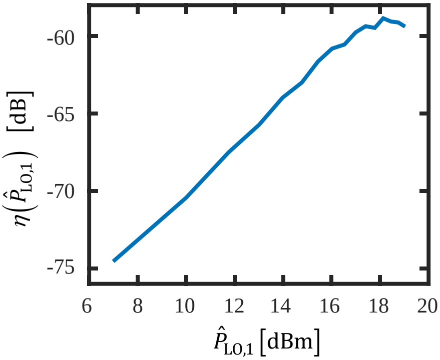

Figure D.3: Photoconductor conversion efficiency η as a function of the optical LO power $\hat{P}_{\mathrm{LO},1} = P_{\mathrm{LO},0}$ for a T-wave frequency of 0.31 THz. *Reprinted with permission from [J3] © The Optical Society.*

Bandwidth

While the optoelectronic part of the T-wave Rx is extremely broadband, the maximum received data rate is limited by the TIA (Maxim Integrated, PHY1097 [111]) which is used for amplifying the downconverted signal $I_{\mathrm{IF}}(t)$. This device features a 3 dB bandwidth of 1.4 GHz, specified for a standard application scenario where the TIA is used in combination with a photodetector in a passive optical network. To measure the overall module bandwidth, we use the setup shown in Figure D.4a. A c.w. T-wave tone at a constant frequency $f_{\mathrm{S}} = \left| f_{\mathrm{S,a}} - f_{\mathrm{S,b}} \right| = 0.1\,\mathrm{THz}$ is generated. At the Rx, the T-wave tone is downconverted using a photonic local oscillator with frequency $f_{\mathrm{LO}} = \left| f_{\mathrm{LO,a}} - f_{\mathrm{LO,b}} \right| \neq f_{\mathrm{S}}$, Eq. (D.7). We then measure the power $\frac{1}{2}\hat{I}_{\mathrm{IF}}^{2} R_{\mathrm{TIA}}$ of the downconverted IF tone at frequency $f_{\mathrm{IF}} = \left| f_{\mathrm{S}} - f_{\mathrm{LO}} \right|$ using an electrical spectrum analyzer (ESA). By tuning the photonic LO frequency f_{LO}, the IF frequency response of the Rx module is obtained. The measured IF frequency response is normalized to its value in the frequency range between $100\,\mathrm{MHz}$ and $200\,\mathrm{MHz}$, and the result is shown in Figure D.4b. The Rx response is fairly constant up to 0.75 GHz and drops quickly for higher frequencies. The measured bandwidth is smaller than expected from the TIA specifications. We attribute this to fact that the impedance of the photoconductor connected to the TIA input differs from that of a high-speed photodiode, for which the device is optimized.

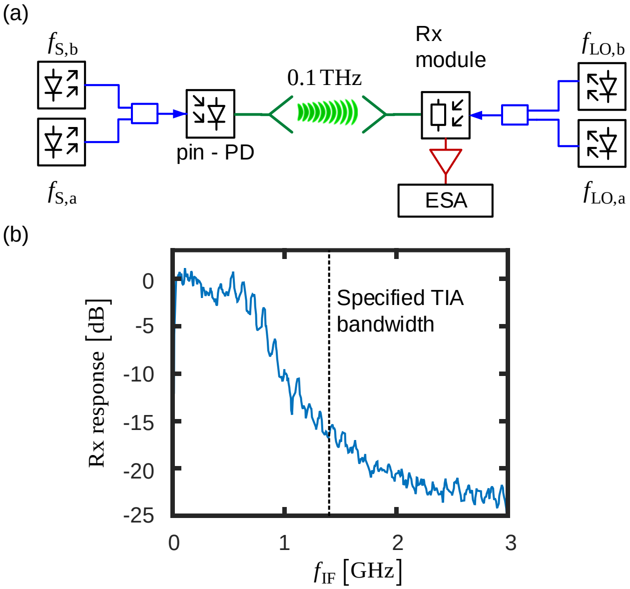

Figure D.4: IF frequency response of the Rx module. **(a)** Measurement setup. A continuous-wave (c.w.) T-wave tone at a constant frequency of $f_S = |f_{S,a} - f_{S,b}| = 0.1\,\text{THz}$ is generated by photomixing of two optical c.w. laser tones. At the Rx, the T-wave signal is downconverted using a photonic local oscillator with frequency $f_{LO} = |f_{LO,a} - f_{LO,b}|$, which differs from f_S by the targeted intermediate frequency $f_{IF} = |f_S - f_{LO}|$. The power of the downconverted c.w. tone is measured by an electrical spectrum analyzer (ESA). By tuning the local oscillator frequency f_{LO}, we obtain the IF frequency response of the Rx. **(b)** Measured IF frequency response of the Rx module. The response drops quickly for frequencies beyond 0.75 GHz. The measured bandwidth is smaller than 1.4 GHz expected from the TIA specifications. We attribute this to the fact that the impedance of the photoconductor connected to the TIA input differs from that of a high-speed photodiode, for which the device is optimized. *Reprinted with permission from [J3] © The Optical Society.*

Noise

Figure D.4 shows the noise characteristics of the packaged Rx module measured without an incident T-wave signal. The power was measured by an electrical spectrum analyzer connected to the Rx output. The photonic LO power $P_{\mathrm{LO}}(t)$ has an amplitude $P_{\mathrm{LO},0} = \hat{P}_{\mathrm{LO},1} = 80\,\mathrm{mW}$ and oscillates with frequency $f_{\mathrm{LO}} \approx 0.31\,\mathrm{THz}$. The noise power measured at the IF output of the Rx module drops significantly for increasing frequencies with a similar characteristic as the Rx response shown in Figure D.4 such that the signal-to-noise power ratio remains essentially constant. The origin of the strong frequency dependence of the Rx response and the Rx noise needs further investigation.

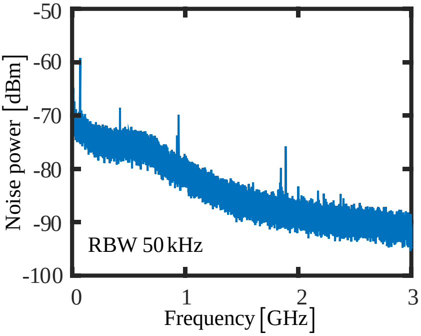

Figure D.5: Noise power measured at the output of the Rx without an incident T-wave. The optical LO power $P_{\mathrm{LO}}(t)$ has an amplitude $P_{\mathrm{LO},0} = \hat{P}_{\mathrm{LO},1} = 80\,\mathrm{mW}$ and oscillates at a frequency $f_{\mathrm{LO}} \approx 0.31\,\mathrm{THz}$. *Reprinted with permission from [J3] © The Optical Society.*

D.3 Wireless T-wave communication link

The detailed experimental setup used for the communication experiments is shown in Figure D.6a. Tunable laser sources with linewidth smaller than 100 kHz (Keysight, N7714A) are used to generate the optical tones for the Tx and the Rx. At the Tx, an arbitrary-waveform generator (‘AWG’) is used to drive an IQ-modulator which is fed by an optical c.w. carrier with frequency $f_{\mathrm{S,a}}$. As a data signal, we use a De-Bruijn sequence [194] of length 2^{13}. The optical signal is sent through an erbium-doped fibre amplifier (‘EDFA’) followed by a 0.6 nm filter to suppress amplified spontaneous emission (ASE) noise. A 50/50-coupler combines the modulated carrier with an unmodulated c.w. tone at frequency $f_{\mathrm{S,b}}$. To ensure strong interference of the two optical signals, we adjust the polarization using two polarization controllers (‘Pol. Contr.’) by maximizing the power after a polarizer (Pol.). An optical attenuator (‘Att’., Keysight N7764A) is used to set the power level $P_{\mathrm{S}}(t)$, and a subsequent optical tap allows for measuring the optical spectra shown in Figure 4.3a and Figure 4.5a,b in Chapter 4. Finally, we adjust the polarization of the combined signal to maximize the current in a high-speed uni-travelling-carrier photodiode (UTC-PD). In the UTC-PD, the optical signal is converted to a T-wave signal with frequency $f_{\mathrm{S}} = \left| f_{\mathrm{S,a}} - f_{\mathrm{S,b}} \right|$ (O/T - conversion). The T-wave is radiated to free space by a horn antenna and a subsequent Polytetrafluoroethylene (PTFE) lens (Thorlabs, LAT200).

After a transmission distance of 58 m, the T-wave is captured by another PTFE lens and coupled to a WR 3.4 hollow waveguide by a horn antenna. The waveguide is connected to the input of two cascaded T-wave amplifiers [22,171], which compensate the free-space transmission loss and amplify the T-wave. In our current design, we use another horn antenna at the output of the second T-wave amplifier in combination with a silicon lens to couple the T-wave to the photoconductor. In the future, the performance of the scheme may be further improved by replacing this assembly with a waveguide-coupled photoconductor. For generating the photonic LO, two c.w. laser tones with optical frequencies $f_{\mathrm{LO,a}}$ and $f_{\mathrm{LO,b}}$ are superimposed using a polarization-maintaining 50/50 coupler, thus generating an optical power beat. The beat signal is amplified by an EDFA followed by a 3 nm filter to reduce ASE noise. A polarization controller is used to maximize the electric IF signal at the output of the polarization-sensitive photoconductor. The optical power P_{LO} coupled to the photoconductor can be adjusted by another optical attenuator (‘Att.’), and a subsequent optical tap is used for measuring the optical spectra shown in Figure 4.3a and Figure 4.5b in Chapter 4. The downconverted IF signal is coupled to the TIA, the output voltage of which is sampled and stored in a real-time oscilloscope (Osc.) for further offline signal processing. Figure D.6b shows a photograph of the wireless transmission link. The image on the left shows the Tx including the UTC-PD and the T-wave PTFE lens. The Rx is 58 m away from the Tx. On the right-hand image, the Rx including the T-wave PTFE

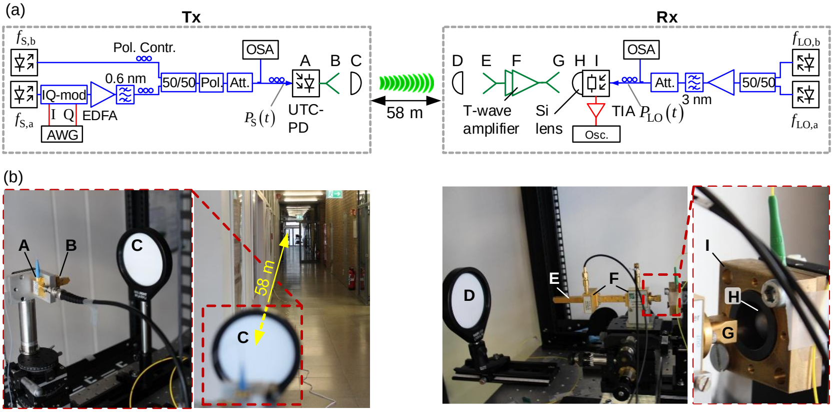

Figure D.6: Details of wireless data transmission link. **(a)** Schematic of the T-wave Tx and Rx used in our experiments. AWG: arbitrary-waveform generator; EDFA: Erbium-doped fibre amplifier; Pol.: Polarizer; Pol. Contr.: Polarization controller; Att.: Optical attenuator; OSA: Optical spectrum analyzer; TIA: Transimpedance amplifier; Osc.: Oscilloscope **(b)** Photograph of Tx and Rx. Components in the schematic of subfigure (a) are marked with letters A…I, which are used as labels in Subfigure (b). At the Tx, the UTC-PD (A), the horn antenna (B), and the PTFE lens (C) are shown. A distance of 58 m is bridged between the Tx and Rx. The Rx setup contains a second PTFE lens (D), a horn antenna (E), the cascaded T-wave amplifiers (F), as well as another horn antenna (G) and a subsequent silicon lens (H) for coupling the T-wave signal to the bow-tie antenna of the photoconductor (not shown) in the T-wave Rx module (I). *Reprinted with permission from [J3] © The Optical Society.*

lens, the T-wave amplifiers and the Rx module is shown in more detail. To facilitate identification of the components shown in the setup sketch of Figure D.6a, we mark them with the letters A … I.

For finding optimum operation parameters, we characterize the performance of the wireless link shown in Figure D.6 for different optical powers $P_S(t)$ and powers $P_{LO}(t)$ at the Tx and the Rx,

$$\begin{aligned} P_S(t) &= P_{S,0} + \hat{P}_{S,1}\cos\left(\omega_S t + \varphi_S(t)\right), & f_S &= \left|f_{S,a} - f_{S,b}\right|, \\ P_{LO}(t) &= P_{LO,0} + \hat{P}_{LO,1}\cos\left(\omega_{LO} t + \varphi_{P,LO}\right), & f_{LO} &= \left|f_{LO,a} - f_{LO,b}\right|. \end{aligned} \tag{D.10}$$

In our measurements, we again adjust the c.w. lasers at the Tx and Rx such that the average power $P_{S,0}$ and $P_{LO,0}$ of the combined optical signal are equal to the amplitude $\hat{P}_{\mathrm{S},1}$ and $\hat{P}_{\mathrm{LO},1}$ of the respective power oscillation, $P_{\mathrm{S},0} = \hat{P}_{\mathrm{S},1}$ and $P_{\mathrm{LO},0} = \hat{P}_{\mathrm{LO},1}$. The Tx and Rx frequencies are set to $f_{\mathrm{S}} = 0.310\,\mathrm{THz}$ and $f_{\mathrm{LO}} = 0.309\,\mathrm{THz}$, respectively. For studying the transmission performance, we generate a quadrature phase-shift keying (QPSK) signal with a line rate of $R_{\mathrm{b}} = 2\,\mathrm{Gbit/s}$ at the Tx and measure its bit error ratio (BER) after downconversion at the Rx.

Figure D.7a shows the BER (red dots) obtained for various average powers $P_{\mathrm{S},0} = \hat{P}_{\mathrm{S},1}$ of the combined optical signal at the Tx and for a constant optical LO power of $P_{\mathrm{LO},0} = \hat{P}_{\mathrm{LO},1} = 80\,\mathrm{mW}$ at the Rx. For some measurement points, the signal quality is that high that we could not measure any errors in a recording length of 10^5 symbols. We therefore estimate the BER from the error vector magnitude [88,89] (blue dots). For an optical power of $\hat{P}_{\mathrm{S},1} > 8\,\mathrm{mW}$, the signal quality decreases because the T-wave amplifiers saturate, see constellation diagrams in the right-hand column of Figure D.7a. In this case, we observe an asymmetric distribution of the noise around the various constellation points, see also Figure 4.3b on Page 47, whereas a symmetric distribution is observed for low optical powers.

Figure D.7b shows the BER measured for a 1 GBd QPSK signal at various average powers $P_{\mathrm{LO},0} = \hat{P}_{\mathrm{LO},1}$ of the combined optical LO signal at the Rx. In this case, the average power of the combined optical Tx signal is kept constant at $P_{\mathrm{S},0} = \hat{P}_{\mathrm{S},1} = 12\,\mathrm{mW}$, close to its optimum point shown in Figure D.7a. The signal quality improves with increasing optical LO power $\hat{P}_{\mathrm{LO},1}$ and is finally limited by the maximum optical power that the photoconductor can withstand. Figure D.7 also indicates that higher-order modulation formats such as 16-state quadrature amplitude modulation (16QAM) might be within reach in future experiments: For a 1 GBd QPSK signal, we estimated a minimum BER of 10^{-9}, Figure D.7a, corresponding to an SNR of roughly 16 dB when assuming that additive white Gaussian noise is the dominating impairment. From Figure 10 of [93], this SNR would lead to a BER of roughly 3×10^{-3} for 16QAM, which would be below the threshold for FEC with 7% coding overhead. With further improvements of the photoconductor and the transimpedance amplifiers, higher-order modulation formats might hence become possible.

If we distribute the T-wave power over multiple channels, see Section 4.3.2 “Multi-channel transmission”, the BER degrades with increasing channel count.

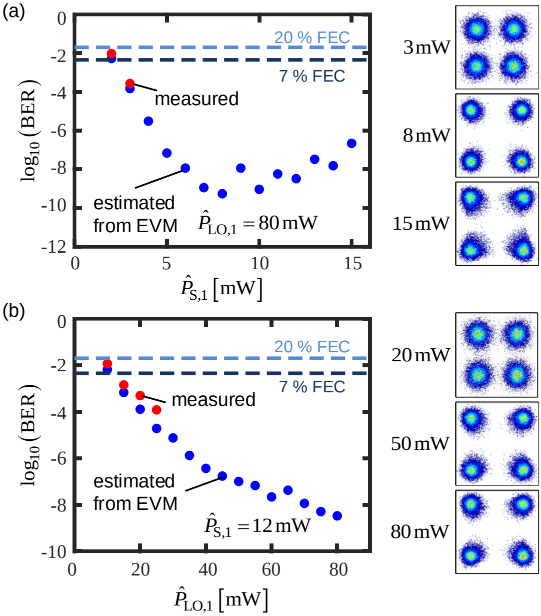

Figure D.7: Measured and estimated bit error ratio (BER) for different optical Tx and LO powers. As a test signal, we transmit a 1 GBd QPSK data signal. The T-wave carrier frequency is set to $f_\text{S} = 0.310\,\text{THz}$. **(a)** BER vs. optical power modulation amplitude $P_{\text{S},0} = \hat{P}_{\text{S},1}$ at the Tx. Red dots denote values that were directly measured, whereas blue dots refer to BER values estimated from the respective error vector magnitude (EVM). Since the length of our signal recordings was limited to 10^5 symbols, the lowest statistically reliable measured BER amounts to 10^{-4}. For measured BER values above this threshold, directly measured and estimated BER show good agreement, giving us confidence that the EVM-based estimations for BER < 10^{-4} are valid. **(b)** BER as a function of the LO power amplitude $P_{\text{LO},0} = \hat{P}_{\text{LO},1}$. The signal quality improves with increasing optical LO power $\hat{P}_{\text{LO},1}$ and is finally limited by the maximum optical power that the photoconductor can withstand. *Reprinted with permission from [J3] © The Optical Society.*

This is mostly caused by the fact that the overall signal power is limited by the T-wave amplifier cascade at the Rx and that hence the per-channel power decreases if more channels are used. This can be equivalently expressed by the degradation of the signal-to-noise power ratio (SNR) for the various channels. From the data shown in Figure D.5, we estimate a root-mean-square (RMS) voltage σ_n = 19 mV of the noise at the output of the transimpedance amplifier in a channel bandwidth of $B = 1$ GHz for the case without any T-wave signal. The corresponding SNR can then be estimated from the RMS voltage $U_{\mathrm{S,RMS}}$ measured for each of the data channel when the T-wave signal is turned on,

$$\mathrm{SNR} = \frac{U_{\mathrm{S,RMS}}^2 - \sigma_{\mathrm{n}}^2}{\sigma_{\mathrm{n}}^2}. \tag{D.11}$$

The SNR measured for the single-channel transmission at a data rate of $R_{\mathrm{b}} = 1.5\,\mathrm{Gbit/s}$ and for the multi-channel transmission with 6, 12 and 20 channels are shown in Figure D.8a. With respect to the single-channel transmission, we expect an SNR reduction of 7.8 dB, 10.8 dB and 13 dB, respectively, through the splitting of the power among 6, 12, and 20 channels. This is in good agreement with our measurement, where we find an average SNR reduction of approximately 6.5 dB, 9.8 dB and 12.3 dB, respectively. For better comparison, we also show the corresponding BER measurements in Figure D.8b, copied from Figure 4.5c of Section 4.3.2. For the symbol rate of 0.75 GBd used here, the bandwidth limitation of the TIA does not play an important role. Signal impairments are hence mainly dictated by the SNR degradation, and the BER is strongly correlated with the SNR.

D.4 T-wave amplifiers and UTC-PD

To compensate the free space T-wave transmission loss, we use a cascade of a low-noise amplifier (LNA) and a medium-power amplifier (MPA) [22,171], designed for operation in the submillimeter H-band (0.220 THz - 0.325 THz), see Figure D.9a. The *S*-parameters for this cascade have been measured with a vector network analyzer (VNA) and are shown in Figure D.9b. In a frequency range from 0.260 THz to 0.335 THz, the total gain is more than 40 dB.

To measure the frequency response of T-wave components and of the complete transmission system, we use the setups shown in Figure D.10. Two unmodulated c.w. laser tones having equal powers and different frequencies $f_{\mathrm{S,a}}$ and $f_{\mathrm{S,b}}$ are superimposed in a 50/50 combiner and coupled to the UTC-PD. The T-wave output power P_{THz} is measured in a calorimeter (VDI, Erickson PM4). By tuning the difference frequency $f_{\mathrm{S}} = \left| f_{\mathrm{S,a}} - f_{\mathrm{S,b}} \right|$ of the two

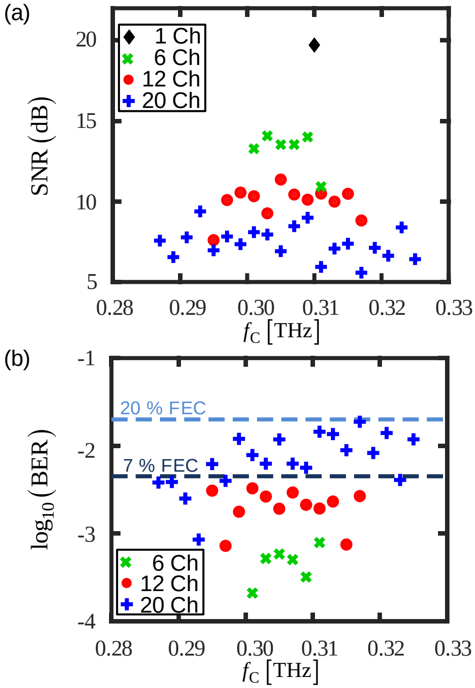

Figure D.8: Signal-to-noise power ratio (SNR) analysis for multi-channel transmission. **(a)** Measured SNR for 1, 6, 12 and 20 channels, each channel carrying a 0.75 GBd QPSK signal. Taking the single-channel transmission experiment as a reference, we find that the SNR reduces by approximately 6.5 dB, 9.8 dB, and 12.3 dB when splitting the limited T-wave power among 6, 12, and 20 channels, respectively. This is in good agreement with the theoretically expected values of 7.8 dB, 10.8 dB, and 13 dB. **(b)** For comparison, we also show the corresponding BER measurements, copied from Figure 4.5c of Section 4.3.2. For the symbol rate of 0.75 GBd used here, the SNR degradation represents the main source of signal impairment, leading to a strong correlation of BER and SNR. *Reprinted with permission from [J3] © The Optical Society.*

lasers, we measured the frequency-dependent output power of the UTC-PD without any amplifier, with the MPA, or with the cascade of LNA and MPA, Figure D.10a-c. Furthermore, we measured the power after T-wave transmission over 58 m with the cascaded LNA and MPA at the Rx, Figure D.10d. The results of all these measurements are shown in Figure D.10e,f. Note that optical input power of the UTC-PD had to be strongly

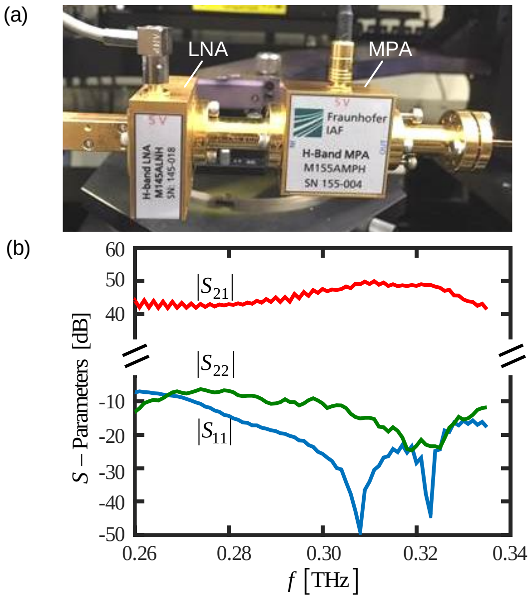

Figure D.9: Characterization of cascaded T-wave amplifiers. **(a)** Photograph of low-noise amplifier (LNA) and medium power amplifier (MPA). **(b)** *S*-parameters measured by a vector network analyzer with frequency extension modules. A total gain of over 40 dB is achieved in a frequency range from 0.260 THz to 0.335 THz. *Reprinted with permission from [J3] © The Optical Society.*

reduced for the case of the cascaded T-wave amplifiers without free-space link to prevent amplifier saturation. For evaluating the measurements, we use the fact that the T-wave output power of the UTC-PD is proportional to the square of the optical power, $P_{\mathrm{THz}} \propto \hat{P}_{s,1}^{2}$. This approach is valid because the UTC-PD is operated far from saturation. The received THz power after the amplifier cascade is more than 0 dBm in a frequency range from 0.29 THz to 0.33 THz for a transmission distance of 58 m. From the measurements shown in Figure D.10 we may also extract the gain of the T-wave amplifier cascade. This leads to a value of 45.5 dB, measured at a T-wave carrier frequency of 0.31 THz, which is in good agreement with the directly measured gain shown in Figure D.9.

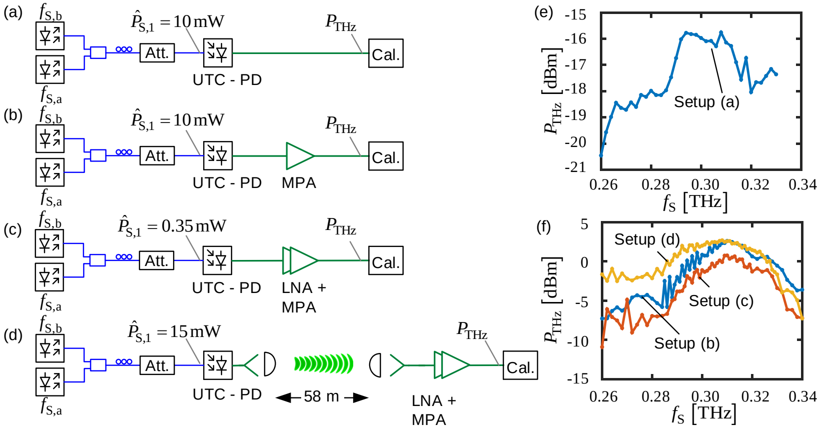

Figure D.10: Setup and results for measuring T-wave output power of UTC-PD and T-wave amplifiers. **(a)** Setup to measure T-wave output power P_{THz} of UTC-PD as a function of frequency $f_S = |f_{S,a} - f_{S,b}|$. **(b)** T-wave output power of UTC-PD and MPA. **(c)** T-wave output power of UTC-PD, LNA and MPA. **(d)** T-wave output power of UTC-PD, 58 m free space transmission, and LNA-MPA cascade. **(e)** Measured T-wave output power P_{THz} in dependence of Tx frequency f_S for UTC-PD. **(f)** Measured T-wave output power P_{THz} for UTC-PD and MPA, setup (b), for UTC-PD and LNA-MPA cascade, setup (c), and for UTC-PD, 58 m free space transmission and LNA-MPA cascade, setup (d). *Reprinted with permission from [J3] © The Optical Society.*

According to the specifications in the datasheet, the LNA has a noise figure of $F_{LNA} = 10$ and a small-signal gain $G_{LNA} = 250$ (24 dB). The noise figure F_{MPA} of the MPA is not exactly known, but has the same order of magnitude as the LNA. According to the Friis formula,

$$F = F_{LNA} + \frac{F_{MPA} - 1}{G_{LNA}}, \tag{D.12}$$

the noise figure F of the cascaded LNA and MPA is dominated by the noise figure of the LNA and amounts to $F \approx 10$ (10 dB).

D.5 Link budget and noise analysis

In this section, we summarize the previous measurements and give a full link budget analysis. From the results shown in Figure D.10, we estimate the LNA gain, the MPA gain, and the total antenna gain of the two horn antennas and the two PTFE lenses that form the free-space transmission link. This analysis is performed at a T-wave frequency of $f_S = 0.31$ THz. We measure an LNA gain of 27 dB and an MPA gain of 18.5 dB. The total antenna gain of the two horn/lens combinations is 87 dBi, which was estimated by comparing the received power with the calculated free-space path loss $\mathrm{FSPL_{dB}}$ for a transmission distance of $d = 58$ m,

$$\mathrm{FSPL_{dB}} = 10\log\left(4\pi d\frac{f_s}{c}\right)^2 = 117\,\mathrm{dB}\,. \tag{D.13}$$

Note that the output of the T-wave amplifier cascade and the photoconductor are connected by a short free-space coupling section, see Figure D.6a. This free-space section consists of a horn antenna at the MPA output and a Si lens for focusing the T-wave beam onto the on-chip bow-tie antenna connected to the photoconductor. While this configuration helped us to avoid laborious co-packaging of the components in our proof-of-concept experiment, it is not an ideal solution and introduces additional losses arising, e.g., from Fresnel reflections at the silicon lens surface, from an impedance mismatch between the bow-tie antenna and the photoconductor, and from the fact that the field generated by the horn antenna and focused to the bow-tie antenna by the silicon lens does not perfectly match the antenna mode. To quantify these losses and to thus estimate the expected performance improvement when using co-integrated devices, we have performed a 3D electromagnetic field simulation using a commercially available numerical time-domain solver (CST Microwave Studio, www.cst.com). see Figure D.11. To keep the numerical effort manageable, we have split the setup into two parts – the T-wave amplifier and the transmitting horn antenna on the one hand and the Si-lens, the receiving bow-tie antenna, and the photoconductor on the other hand. In a first step, we excite the horn antenna with a THz power of 2 mW, corresponding to the highest power of the amplifier cascade that could be measured at its output port using a waveguide-

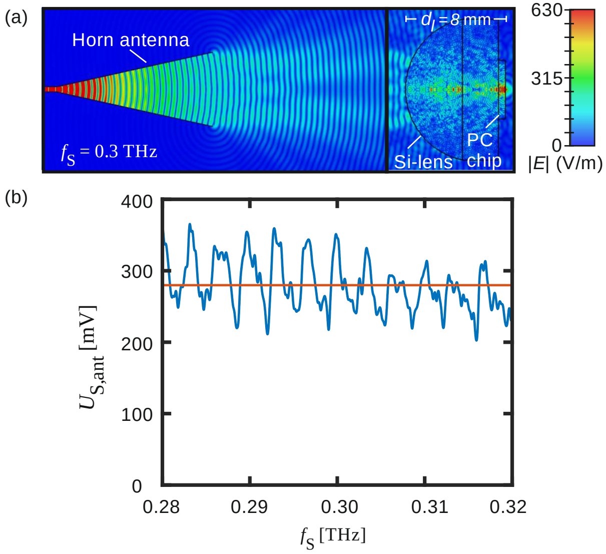

Figure D.11: Simulation of the free-space coupling section between the horn antenna and the photoconductor (PC). **(a)** Magnitude of the electric field at the cross-section of the transmission link for a T-wave power of 2 mW at the input of the horn antenna. To keep the numerical effort manageable, we split the simulation into two parts – the T-wave amplifier and the transmitting horn antenna on the left, and the Si-lens, the receiving bow-tie antenna, and the photoconductor on the right. **(b)** RMS value of the voltage effective across the photoconductor for a T-wave power of 2 mW at the input of the horn antenna. The pronounced ripples are attributed to standing waves within the Si lens. When averaging over the frequency range between 0.28 THz and 0.32 THz, we extract a mean RMS value of $U_{S,ant} = 281\,\text{mV}$ (red line) for the voltage across the photoconductor. *Reprinted with permission from [J3] © The Optical Society.*

coupled calorimeter, and we record the electric field generated in a cross-sectional plane that is 15 mm away from the transmitting aperture of the horn antenna. In a second step, this field is then fed as an excitation into the simulation of the silicon lens, the bow-tie antenna, and the photoconductor. In this simulation, we terminate the bow-tie antenna with a 750 Ω impedance, corresponding to the measured DC impedance of the photoconductor under an illumination with an optical LO power of $P_{LO,0} = 30\,\text{mW}$. The field distribution obtained from the two simulations for an T-wave power of 2 mW at the input of the horn antenna is shown in Figure D.11a. From the simulation, we extract the frequency-dependent RMS value of the voltage that is effective across the photoconductor, see Figure D.11b. We find pronounced variations of this voltage with respect to the T-wave frequency. These ripples exhibit a period of approximately 4 GHz and are attributed to standing waves that form in the Si lens, which features a thickness d_l of approximately 8 mm measured between the rear surface and the apex towards the horn antenna, see Figure D.11a. Averaging the RMS voltage over a frequency range between 0.28 THz and 0.32 THz, we find a mean value of $U_{\mathrm{S,ant}} = 281\,\mathrm{mV}$, see the red horizontal line in Figure D.11b. This value is then compared to the voltage amplitude of $U_{\mathrm{S,dir}} = 1.22\,\mathrm{V}$ that could be expected by coupling the 2 mW T-wave amplifier output to a 750 Ω termination. From the ratio of the two voltages, we extract a potential improvement of $10\log\left(U_{\mathrm{S,dir}}^2 / U_{\mathrm{S,ant}}^2\right) = 12.8\,\mathrm{dB}$ that could be expected from a direct connection between the T-wave amplifier and the photoconductor with an appropriate impedance matching circuit. Direct coupling of the T-wave amplifier could avoid the interference ripples and hence also improve the uniformity of the frequency characteristic of the link. Note that the conversion efficiency shown in Figure D.2 was also measured with an antenna-coupled photoconductor on a silicon lens and therefore already includes the losses introduced by the free-space coupling section. Figure D.12 shows a link budget for an optical power $\hat{P}_{\mathrm{S,1}} = 15\,\mathrm{mW}$ feeding the UTC-PD.

To estimate the influence of the T-wave amplifier noise, we calculate the thermal noise power P_{n} at the output of the cascaded T-wave amplifiers having

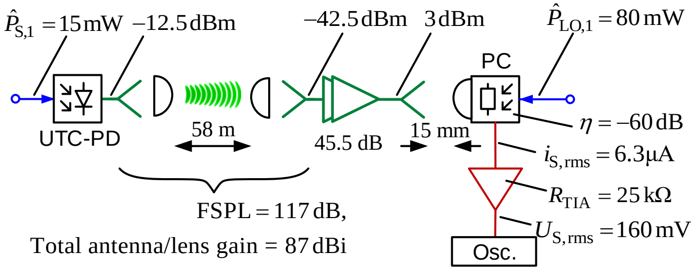

Figure D.12: Link budget for an optical power $\hat{P}_{\mathrm{S,1}} = 15\,\mathrm{mW}$ at the transmitter. Note that the conversion efficiency η of – 60 dB also contains the coupling losses introduced by the free-space section between the output of the T-wave amplifier cascade and the photoconductor. *Reprinted with permission from [J3] © The Optical Society.*

a total noise figure of $F \approx 10$. For a signal bandwidth of $B = 1$ GHz and a power gain G corresponding to 45.5 dB, we find a T-wave noise power at the amplifier output of $P_\mathrm{n} = 4kT_0FBG = 5.9\,\mu\mathrm{W}$, corresponding to -22 dBm. Assuming a photoconductor conversion efficiency η from Eq. (D.8) corresponding to –60 dB and a THz noise power $P_\mathrm{THz} = P_\mathrm{n}$, we can estimate the RMS of the noise current contribution $i_\mathrm{n,RMS}$ in the baseband. To this end, we use the fact that the conversion efficiency was defined for a 50 Ω load impedance at the output of the photoconductor, which itself can be modeled as a current source due to its high internal impedance,

$$i_\mathrm{n,RMS} = \sqrt{\frac{\eta P_n}{50\,\Omega}} = 340\,\mathrm{nA}\,. \tag{D.14}$$

This noise contribution has the same order of magnitude as the typical input-referred noise of 150 nA specified in the data sheet of our TIA [111]. In the experiment, we actually measure a higher RMS noise current of 750 nA at the TIA input, see Figure D.4. We attribute the higher noise currents partially to the additional noise contribution of the photonic LO and partially to the fact that the photoconductor leads to a non-optimum impedance at the input of the TIA, which was designed for operation with-speed photodiodes. We expect that improvements of the photoconductor conversion efficiency, reduced coupling losses and better impedance matching between the T-wave amplifier and the photoconductor, as well as an improved design of the baseband circuitry connecting the photoconductor and the TIA will allow to greatly improve the signal-to-noise ratio of the scheme.

[end of the Supplementary Information of paper [J3]]

E. Silicon-plasmonic integrated circuits

The content of the following sections has been published in Methods and Supplementary Information of the journal publication [J2]. In order to fit the structure and layout of this document, it was adapted accordingly.

> **T. Harter**, S. Muehlbrandt, S. Ummethala, A. Schmid, S. Nellen,
> L. Hahn, W. Freude, and C. Koos, "Silicon-plasmonic integrated
> circuits for terahertz signal generation and coherent detection,"
> *Nature Photonics*, **12**, 625–633 (2018).
> DOI: 10.1038/s41566-018-0237-x © Springer Nature

[start of Methods and Supplementary Information of paper [J2]]

E.1 Methods

Advantages of c.w. signal processing in highly integrated optoelectronic T-wave systems

Optoelectronic generation and detection of T-wave signals can generally rely on photomixing of c.w. carriers or on direct detection of ultra-short laser pulses [195,196]. The focus of our work is on ultra-compact highly scalable T-wave generators and detectors that are amenable to dense integration on highly scalable photonic integration platforms. For such devices, c.w. operation is advantageous as it allows driving of the PIPED by readily available c.w. laser sources that have been developed in the context of optical communications, and that offer small footprints along with narrow optical linewidth and broadband wavelength tunability [197,198]. In contrast to that, chip-scale integration of pulsed laser sources is much more difficult, in particular when ultra-short pulses with durations of well below 1 ps are required. Moreover, when coupled to high-index-contrast semiconductor-based waveguides with small cross-section, pulsed optical signals with low duty cycles are often subject to nonlinear absorption, for example caused by two-photon processes and the resulting free carriers [199].

PIPED device fabrication

The PIPEDs were fabricated on commercially available SOI substrates with a 340-nm-thick device layer. The waveguide structures were defined by electron-beam lithography and reactive ion etching. Directional metal evaporation under various angles allowed deposition of different metals on each side of the silicon core and enabled the fabrication of an asymmetrically metallized silicon core with a width as small as 100 nm (and below [117]). To keep the fabrication simple, we use Au and Ti to metallize the silicon core sidewalls as these materials are readily available in our laboratory. Note that other metals such as Cu or Al with similar optical and electrical properties could also be used, allowing PIPED fabrication using standard CMOS materials. During metallization, an undercut hard mask on top of the silicon core was used to prevent a short circuit between the Au and Ti regions (Figure 5.2a on Page 61). For more information on fabrication of the PIPED see ref. [117].

Coherent T-wave detection

For sensitive detection of the Rx current $\hat{I}_{\mathrm{BB,1}}(t)\cos(\varphi_{\mathrm{BB}})$, a lock-in amplifier was used. To this end, we modulated the Tx bias voltage $U_{\mathrm{Tx,0}}$, leading to modulation of the terahertz Tx current $\hat{I}_{\mathrm{Tx,1}}(t)$, of the received terahertz voltage $\hat{U}_{\mathrm{Rx,1}}(t)$, and of the time-variant part $\hat{I}_{\mathrm{BB,1}}$ of the baseband photocurrent (Eq. (5.12) in Section 5.3). The modulation frequency was set to $f_{\mathrm{LI}} = 12.2\,\mathrm{kHz}$, and the modulated receiver current $\hat{I}_{\mathrm{BB,1}}(t)\cos(\varphi_{\mathrm{BB}})$ was measured by a lock-in amplifier (Toptica TeraControl 110). The phase φ_{BB} of the baseband current depends on the phase $\varphi_{\mathrm{Tx,THz}}$ of the optical power beat at the Tx, the phase $\varphi_{\mathrm{Rx,THz}}$ of the optical power beat at the Rx, as well as on the phase delay φ_{TxRx} gathered during transmission of the T-wave from the Tx to the Rx:

$$\varphi_{\mathrm{BB}} = \varphi_{\mathrm{Tx,THz}} - \varphi_{\mathrm{Rx,THz}} + \varphi_{\mathrm{TxRx}} \,. \tag{E.1}$$

For homodyne detection (see Figure 5.3a in Section 5.4 and Figure 5.4b in Section 5.5), the phase difference $\varphi_{\mathrm{Tx,THz}} - \varphi_{\mathrm{Rx,THz}}$ of the optical power beats depends only on the optical group delay τ_{opt} between the Tx and Rx,

$$\varphi_{\mathrm{Tx,THz}} - \varphi_{\mathrm{Rx,THz}} = \omega_{\mathrm{THz}}\,\tau_{\mathrm{opt}} = 2\pi f_{\mathrm{THz}} n_{\mathrm{g}}\,\Delta L/c\,, \tag{E.2}$$

where c is the speed of light, n_g the optical group refractive index of the single-mode fibres, and ΔL is the path length difference of the optical wave. In this relation, we assumed that the on-chip SOI waveguide at the Tx and Rx have the same length. Scanning the frequency f_THz leads to an oscillation of the $\hat{I}_\mathrm{BB,1}\cos(\varphi_\mathrm{BB})$, where the number of oscillations per frequency interval depends on the time delay τ_opt. We recorded the current $\hat{I}_\mathrm{BB,1}\cos(\varphi_\mathrm{BB})$ as a function of the terahertz frequency f_THz and separated the amplitude $\hat{I}_\mathrm{BB,1}$ from phase φ_BB by means of a Fourier transformation of the received signal $\hat{I}_\mathrm{BB,1}\cos(\varphi_\mathrm{BB}) = \frac{1}{2}\hat{I}_\mathrm{BB,1}\left[e^{\mathrm{j}\varphi_\mathrm{BB}} + e^{-\mathrm{j}\varphi_\mathrm{BB}}\right]$. After Fourier transformation, we numerically removed the negative-frequency components and calculated the inverse Fourier transform to obtain the complex amplitudes $\frac{1}{2}\hat{I}_\mathrm{BB,1}e^{\mathrm{j}\varphi_\mathrm{BB}}$ of the frequency-dependent baseband current. From these complex amplitudes, we can directly read the received current amplitude $\hat{I}_\mathrm{BB,1}$ and the phase φ_BB. Regarding the phase information, we are mainly interested in the phase delay φ_TxRx accumulated by the T-wave during propagation from the Tx to the Rx. To obtain this information, we need to eliminate the phase shifts that are caused by the unknown optical group delay τ_opt between the Tx and the Rx. To this end, we performed two consecutive measurements and exploited the fact that the same PIPED can act both as Tx and Rx. The first measurement was performed as described in Figure 5.4 in Section 5.5. In the second measurement we swapped the role of Tx and Rx by switching the bias conditions of the associated PIPED. Because the optical beam path is unchanged, only the sign of $\varphi_\mathrm{Tx,THz} - \varphi_\mathrm{Rx,THz}$ is inverted, while φ_TxRx is unchanged. For Eq. (E.1), the terahertz phase can then be calculated:

$$\varphi_\mathrm{TxRx} = (\varphi_\mathrm{BB,norm} + \varphi_\mathrm{BB,rev})/2\,. \tag{E.3}$$

The amplitude of the baseband current $\hat{I}_\mathrm{BB,1,rev}$ is not changed by reversing Tx and Rx. In Figure 5.4c-e in Section 5.5 the plotted baseband current $\hat{I}_\mathrm{BB,1}$ was taken as the mean of both measurements

$$\hat{I}_\mathrm{BB,1} = (\hat{I}_\mathrm{BB,1,norm} + \hat{I}_\mathrm{BB,1,rev})/2\,. \tag{E.4}$$

Calibration and traceability of terahertz power measurements

All measurements of terahertz power levels rely on a commercially available reference Tx (Toptica, EK 000724). To ensure traceability of our measurement results, we determined the power emission of the reference Tx using a dedicated pyroelectric thin-film detector (Sensor- und Lasertechnik Dr. W. Bohmeyer, THz20) that was calibrated (calibration certificate 73413-PTB-14) by the Physikalisch-Technische Bundesanstalt (PTB) Berlin (German National Metrology Institute). Note that this detector does not allow the detection of terahertz powers below 1 µW due to limited sensitivity. To detect the sub-1 µW emission powers of our PIPED Tx, we used a commercially available photoconductive Rx (Toptica, EK 000725) to determine the ratio of the PIPED emission power and the known emission power of the Toptica reference Tx (see Eq. (5.13) in Section 5.4 and the corresponding discussion).

3D EM simulations

The frequency response of the terahertz dipole antenna (Figure 5.3b on page 66) and the terahertz resonators (Figure 5.4c–e on page 74) were simulated using a commercially available numerical time-domain solver (CST Microwave Studio, www.cst.com). A crucial aspect is the correct representation of the thin metal layers of the transmission lines and the antennas. Atomic force microscope measurements revealed a 110-nm-thick Au layer on top of a 40-nm-thick Ti layer. In the simulation of transmission lines with dimensions in the millimetre range, a detailed representation of the field within the metal would lead to an unrealistic number of mesh cells that cannot be handled with the available computing resources. Therefore, we used the ‘thin panel’ option of CST Microwave Studio, which relates the tangential electric and magnetic fields on the surface of the metal with the help of surface impedances. The Rx and Tx PIPEDs are described by discrete equivalent circuits. For simulation of the Tx as depicted in Figure 5.3b, the PIPED is represented by a current source in parallel to a capacitance. Details on the antenna simulation are provided in Appendix E.10. The antenna is simulated as a thin metal panel on a silicon substrate with open boundaries to emulate an infinite half-space below. This approach is valid because the silicon chip is in direct contact with a macroscopic silicon lens with dimensions much larger than the terahertz wavelength or the Tx antenna. The total radiated power corresponds to the total power radiated in the lower Si half-space. For a numerical analysis of the terahertz resonator in

Figure 5.4, all transmission line structures are again represented as thin metal panels deposited on a semi-infinite Si substrate. The Tx PIPED is modelled as a current source, and the Rx PIPED is modelled as an open circuit across which the voltage is measured. In both cases, we obtain essentially the same results when replacing the ideal current source or open circuit with infinite internal resistances by devices that feature finite internal resistances of 10 kΩ. This is a worst-case estimate of the real internal PIPED resistance, which is typically well above the assumed value of 10 kΩ (see Appendix E.8). The complex transfer impedance can be calculated by dividing the simulated terahertz voltage amplitude at the Rx by the terahertz current amplitude at the Tx. Alternatively, the complex transfer impedance $\underline{Z}_{21}$ can be derived from numerically calculated scattering parameters of the terahertz resonator (see Appendix E.12). Both methods lead to the same results.

Optical set-up

To generate the optical power beat, two temperature-controlled tunable distributed feedback (DFB) lasers with linewidths of ~1 MHz are used (Toptica #LD-1550-0040-DFB-1). The difference frequency can be tuned from 0 to 1.2 THz with a relative frequency accuracy better than 10 MHz and an absolute frequency accuracy of 2 GHz. To feed light from single-mode fibres to antenna-coupled PIPEDs (Figure 5.3, Section 5.4) we used grating couplers with losses of 5 dB, followed by 0.9-mm-long on-chip SOI waveguides with propagation losses of 2.3 dB/mm, thus leading to a total coupling loss of 7 dB. For the integrated terahertz system (Figure 5.4, Section 5.5), the grating coupler losses amount to 5.3 dB, the waveguide propagation losses to 1.1 dB/mm, and the length of the on-chip waveguide is 0.6 mm. This leads to total coupling losses of 6 dB. The optical path length difference ΔL between the Tx and Rx was between 1.0 m and 1.3 m for the antenna-coupled PIPED (Figure 5.3a, Section 5.3) and 0.6 m for the integrated terahertz system (Figure 5.4). For the antenna-coupled PIPED, the T-wave Tx and Rx characteristics were sampled with steps of 10 MHz (Figure 5.3b,d), and the integration time of the lock-in amplifier was chosen to be between 20 ms and 100 ms. For spectral characterization of the integrated T-wave systems (Figure 5.4c-e), sampling points were taken every 25 MHz, and the integration time was set to 100 ms.

SNR measurements and benchmarking

To characterize the noise performance of our devices, we measured the short-circuit root-mean-square (RMS) noise current $\sqrt{\langle I_{\mathrm{N}}^2 \rangle}$ within a known detection bandwidth *B* for the case with no input T-wave signal [107]. To this end, we used a lock-in amplifier (Toptica TeraControl 110), which, according to the manufacturer, features an equivalent noise bandwidth of $B = 1/(2T)$ for a given integration time *T*. For zero bias current, the device is driven by its internal bias voltage of 0.2 V only, and the noise current is $9\,\mathrm{pA}/\sqrt{\mathrm{Hz}}$. For better comparability to widely used terahertz spectroscopy systems, we also determined the signal-to-noise power ratio (SNR) obtained in our experiment. Using the Toptica reference transmitter (EK 000724), the T-wave power incident on the Rx at 0.3 THz is P_{THz} = -19 dBm and leads to an SNR of 85 dB Hz^{-1}. A similar SNR of $84\,\mathrm{dB\,Hz}^{-1}$ is obtained using the Toptica reference receiver. For the externally applied bias voltage $U_{\mathrm{Rx,0}} = 0.45\,\mathrm{V}$, the RMS noise current increases considerably to values of $190\,\mathrm{pA}/\sqrt{\mathrm{Hz}}$, thus reducing the achieved SNR at 0.3 THz to 65 dB Hz^{-1}, despite the larger conversion factor. The strong noise level for the case of an externally applied bias voltage is attributed to the DC voltage source. Improved noise levels might be achieved by low-pass filtering of the bias voltage.

In Chapter 5 we give the SNR power ratio in units of dB Hz^{-1}, which is independent of the integration time of the lock-in detection. Other groups [106,155] specify the SNR in dB in combination with the integration time *T* of the lock-in detector. To compare these values to our results, we converted the SNR of ref [106] and ref. [155] to dB Hz^{-1}. From Figure 3 in ref. [106] we read an SNR of 93 dB at 0.3 THz. In this measurement, the lock-in filter slope was set to 12 dB per octave and an integration time of *T* = 200 ms was used. This leads to an equivalent noise bandwidth of $B = 1/(8T) = 0.625\,\mathrm{Hz}$ (Research Stanford Systems, www.thinksrs.com/downloads/pdfs/manuals/SR844m.pdf, SR844 user manual) and an SNR value of 91 dB Hz^{-1} as stated in Section 5.4. In ref. [155], the measured SNR value is 47 dB, and an integration time of 23.4 ms was used. The filter slope is not explicitly stated. By assuming a filter slope of 6 dB per octave, we obtain an equivalent noise bandwidth of $B = 1/(4T) = 10.7\,\mathrm{Hz}$ and therefore an SNR of 57 dB Hz^{-1}. The baseband noise background of $28\,\mathrm{nA}/\sqrt{\mathrm{Hz}}$ mentioned in Section 5.4 for ref. [154] was estimated from the noise floor of $-105\,\mathrm{dBm\,Hz}^{-1}$ assuming a 50 Ω load.

E.2 Detailed derivation of formulae

The plasmonic internal-photoemission detector (PIPED) can be used as a T-wave transmitter (Tx) as well as a T-wave receiver (Rx). In the following a detailed explanation of both functionalities is given. As a Tx, the PIPED multiplies two time-dependent optical signals $E_{\mathrm{Tx,a}}(t)$ and $E_{\mathrm{Tx,b}}(t)$ to produce a photocurrent that corresponds to the difference-frequency waveform (O/T conversion). In the following, we assume that the optical signal $E_{\mathrm{Tx,a}}(t)$ oscillates at frequency $f_{\mathrm{Tx,a}} = \omega_{\mathrm{Tx,a}} / (2\pi)$ and carries a (normalized) amplitude modulation $\hat{E}_{\mathrm{Tx,a}}(t)$ and/or a phase modulation $\varphi_{\mathrm{Tx,a}}(t)$, whereas the optical signal $E_{\mathrm{Tx,b}}(t)$ is simply a continuous-wave (c.w.) carrier with constant amplitude $\hat{E}_{\mathrm{Tx,b}}$, frequency $f_{\mathrm{Tx,b}} = \omega_{\mathrm{Tx,b}} / (2\pi)$, and phase $\varphi_{\mathrm{Tx,b}}$,

$$\begin{aligned} E_{\mathrm{Tx,a}}(t) &= \hat{E}_{\mathrm{Tx,a}}(t)\cos\left(\omega_{\mathrm{Tx,a}}t + \varphi_{\mathrm{Tx,a}}(t)\right), \\ E_{\mathrm{Tx,b}}(t) &= \hat{E}_{\mathrm{Tx,b}}\cos\left(\omega_{\mathrm{Tx,b}}t + \varphi_{\mathrm{Tx,b}}\right). \end{aligned} \tag{E.5}$$

The superposition of the two optical signals leads to an optical power $P_{\mathrm{Tx}}(t)$, which oscillates with the difference angular THz frequency $\omega_{\mathrm{Tx,THz}} = \left|\omega_{\mathrm{Tx,a}} - \omega_{\mathrm{Tx,b}}\right|$ and shows a phase $\varphi_{\mathrm{Tx,THz}}(t) = \varphi_{\mathrm{Tx,a}}(t) - \varphi_{\mathrm{Tx,b}}$,

$$\begin{aligned} P_{\mathrm{Tx}}(t) &= \left\langle \left(E_{\mathrm{Tx,a}}(t) + E_{\mathrm{Tx,b}}(t)\right)^2 \right\rangle_{1/f_{\mathrm{Tx,b}}} \\ &= \tfrac{1}{2}\left(\hat{E}^2_{\mathrm{Tx,a}}(t) + \hat{E}^2_{\mathrm{Tx,b}}\right) \\ &\qquad + \hat{E}_{\mathrm{Tx,a}}(t)\hat{E}_{\mathrm{Tx,b}}\cos\left(\omega_{\mathrm{Tx,THz}}t + \varphi_{\mathrm{Tx,THz}}(t)\right) \\ &= P_{\mathrm{Tx,0}}(t) + \underbrace{\hat{P}_{\mathrm{Tx,1}}(t)\cos\left(\omega_{\mathrm{Tx,THz}}t + \varphi_{\mathrm{Tx,THz}}(t)\right)}_{P_{\mathrm{Tx,1}}(t)}. \end{aligned} \tag{E.6}$$

The average $\langle\cdot\rangle$ can be performed over either period of $E_{\mathrm{Tx,a,b}}(t)$. This oscillating power is incident on the PIPED which is biased at a voltage $U_{\mathrm{Tx,0}}$ and has a sensitivity $S_{\mathrm{Tx}}\left(U_{\mathrm{Tx,0}}\right)$. The PIPED output current is in proportion to the optical power, $I_{\mathrm{Tx}}(t) \sim P_{\mathrm{Tx}}(t)$, and can be separated in a slowly varying term $I_{\mathrm{Tx,0}}(t) \sim P_{\mathrm{Tx,0}}(t)$ and a term $I_{\mathrm{Tx,1}}(t) \sim P_{\mathrm{Tx,1}}(t)$ which oscillates at the THz frequency,

$$\begin{aligned} I_{\mathrm{Tx}}(t) &= S_{\mathrm{Tx}}\left(U_{\mathrm{Tx,0}}\right)P_{\mathrm{Tx}}(t) \\ &= I_{\mathrm{Tx,0}}(t) + I_{\mathrm{Tx,1}}(t) \\ &= I_{\mathrm{Tx,0}}(t) + \hat{I}_{\mathrm{Tx,1}}(t)\cos\left(\omega_{\mathrm{Tx,THz}}t + \varphi_{\mathrm{Tx,THz}}(t)\right). \end{aligned} \tag{E.7}$$

In this relation we used the abbreviations

$$\begin{aligned} I_{\mathrm{Tx,0}}(t) &= S_{\mathrm{Tx}}\left(U_{\mathrm{Tx,0}}\right)\tfrac{1}{2}\left(\hat{E}^2_{\mathrm{Tx,a}}(t) + \hat{E}^2_{\mathrm{Tx,b}}\right), \\ \hat{I}_{\mathrm{Tx,1}}(t) &= S_{\mathrm{Tx}}\left(U_{\mathrm{Tx,0}}\right)\hat{E}_{\mathrm{Tx,a}}(t)\hat{E}_{\mathrm{Tx,b}}. \end{aligned} \tag{E.8}$$

Hence, any modulation of the amplitude $\hat{E}_{\mathrm{Tx,a}}(t)$ or the phase $\varphi_{\mathrm{Tx,a}}(t)$ of the optical carrier translates directly to the THz range. The THz current is radiated by an antenna or coupled to a transmission line. Note that for lock-in detection, the transmitter DC bias $U_{\mathrm{Tx,0}}$ could be slowly modulated, leading to a time-dependent quantity $U_{\mathrm{Tx,0}}(t)$.

Similarly, the PIPED can be used for T-wave reception (T/E conversion). In this case, the device combines two functionalities, namely the generation of a THz local oscillator (LO) from two optical carriers, and the downconversion of the received THz signal to the baseband. To this end, the PIPED is fed by a superposition of two unmodulated optical carriers, oscillating at angular frequencies $\omega_{\mathrm{Rx,a}}$ and $\omega_{\mathrm{Rx,b}}$ and having phases $\varphi_{\mathrm{Rx,a}}$ and $\varphi_{\mathrm{Rx,b}}$,

$$\begin{aligned} E_{\mathrm{Rx,a}}(t) &= \hat{E}_{\mathrm{Rx,a}}\cos\left(\omega_{\mathrm{Rx,a}}t + \varphi_{\mathrm{Rx,a}}\right), \\ E_{\mathrm{Rx,b}}(t) &= \hat{E}_{\mathrm{Rx,b}}\cos\left(\omega_{\mathrm{Rx,b}}t + \varphi_{\mathrm{Rx,b}}\right). \end{aligned} \tag{E.9}$$

The superposition of the two optical signals in the Rx has an optical power $P_{\mathrm{Rx}}(t)$, which oscillates with the difference angular frequency $\omega_{\mathrm{Rx,THz}} = \left|\omega_{\mathrm{Rx,a}} - \omega_{\mathrm{Rx,b}}\right|$ and shows a phase $\varphi_{\mathrm{Rx,THz}} = \varphi_{\mathrm{Rx,a}} - \varphi_{\mathrm{Rx,b}}$,

$$\begin{aligned} P_{\mathrm{Rx}}(t) &= \left\langle \left(E_{\mathrm{Rx,a}}(t) + E_{\mathrm{Rx,b}}(t) \right)^2 \right\rangle_{1/f_{\mathrm{Rx,b}}} \\ &= \tfrac{1}{2}\left(\hat{E}_{\mathrm{Rx,a}}^2 + \hat{E}_{\mathrm{Rx,b}}^2 \right) \\ &\quad + \hat{E}_{\mathrm{Rx,a}} \hat{E}_{\mathrm{Rx,b}} \cos\left(\omega_{\mathrm{Rx,THz}} t + \varphi_{\mathrm{Rx,THz}} \right) \\ &= P_{\mathrm{Rx,0}} + \underbrace{\hat{P}_{\mathrm{Rx,1}} \cos\left(\omega_{\mathrm{Rx,THz}} t + \varphi_{\mathrm{Rx,THz}} \right)}_{P_{\mathrm{Rx,1}}(t)}. \end{aligned} \tag{E.10}$$

At the same time, the PIPED is DC-biased with a voltage $U_{\mathrm{Rx,0}}$ and the antenna superimposes a time-variant THz signal $U_{\mathrm{Rx,1}}(t)$. The total time-dependent voltage applied to the PIPED contacts hence reads

$$U_{\mathrm{Rx}}(t) = U_{\mathrm{Rx,0}} + U_{\mathrm{Rx,1}}(t), \tag{E.11}$$

where we introduced the abbreviation

$$U_{\mathrm{Rx,1}}(t) = \hat{U}_{\mathrm{Rx,1}}(t) \cos\left(\omega_{\mathrm{Tx,THz}} t + \varphi_{\mathrm{Tx,THz}}(t) + \varphi_{\mathrm{TxRx}} \right). \tag{E.12}$$

In this relation, the phase at the receiver depends on the phase shift φ_{TxRx} that the THz wave experiences when propagating from the Tx to the Rx. The voltage $U_{\mathrm{Rx}}(t)$ leads to a time-variant PIPED sensitivity $S_{\mathrm{Rx}}\left(U_{\mathrm{Rx}}(t)\right)$. The small-signal approximation reads

$$S_{\mathrm{Rx}}\left(U_{\mathrm{Rx}}(t)\right) = S_{\mathrm{Rx}}\left(U_{\mathrm{Rx,0}}\right) + \left.\frac{\mathrm{d}S_{\mathrm{Rx}}}{\mathrm{d}U_{\mathrm{Rx}}}\right|_{U_{\mathrm{Rx,0}}} U_{\mathrm{Rx,1}}(t). \tag{E.13}$$

The PIPED photocurrent $I_{\mathrm{Rx}}(t)$ is given by the product of this time-variant sensitivity $S_{\mathrm{Rx}}\left(U_{\mathrm{Rx}}(t)\right)$ and the time-variant optical power $P_{\mathrm{Rx}}(t)$,

$$I_{\mathrm{Rx}}(t) = S_{\mathrm{Rx}}\left(U_{\mathrm{Rx}}(t)\right) P_{\mathrm{Rx}}(t). \tag{E.14}$$

Averaging over a THz cycle leads to the downconverted baseband current

$$\begin{aligned} I_{\mathrm{BB}}(t) &= \left\langle I_{\mathrm{Rx}}(t) \right\rangle_{\mathrm{THz}} \\ &= I_{\mathrm{BB},0} + I_{\mathrm{BB},1}(t) \\ &= I_{\mathrm{BB},0} + \hat{I}_{\mathrm{BB},1}(t) \cos\Big(\big(\omega_{\mathrm{Tx,THz}} - \omega_{\mathrm{Rx,THz}}\big)t + \varphi_{\mathrm{BB}}(t)\Big), \end{aligned} \tag{E.15}$$

where we used the abbreviations

$$\begin{aligned} I_{\mathrm{BB},0} &= S_{\mathrm{Rx}}\left(U_{\mathrm{Rx},0}\right) P_{\mathrm{Rx},0}, \\ \hat{I}_{\mathrm{BB},1}(t) &= \tfrac{1}{2} \left.\frac{\mathrm{d}\,S_{\mathrm{Rx}}}{\mathrm{d}U_{\mathrm{Rx}}}\right|_{U_{\mathrm{Rx},0}} \hat{P}_{\mathrm{Rx},1} \hat{U}_{\mathrm{Rx},1}(t) \ , \\ \varphi_{\mathrm{BB}}(t) &= \varphi_{\mathrm{Tx,THz}}(t) - \varphi_{\mathrm{Rx,THz}} + \varphi_{\mathrm{TxRx}} \, . \end{aligned} \tag{E.16}$$

For the special case of homodyne reception, $\omega_{\mathrm{Rx,THz}} = \omega_{\mathrm{Tx,THz}} = \omega_{\mathrm{THz}}$, the baseband photocurrent at the output of the Rx PIPED is given by

$$I_{\mathrm{BB}}(t) = I_{\mathrm{BB},0} + \hat{I}_{\mathrm{BB},1}(t) \cos\left(\varphi_{\mathrm{BB}}(t)\right). \tag{E.17}$$

The time-variant part $I_{\mathrm{BB},1}(t)$ of the photocurrent is proportional to the voltage amplitude $\hat{U}_{\mathrm{Rx},1}(t)$ of Eq. (E.12) and therefore in proportion to the incoming THz field.

E.3 Calibration of T-wave Tx and Rx reference

For the characterization of the antenna-coupled PIPED Tx and Rx, we use a commercially available T-wave Tx (Toptica, EK 000724) and a corresponding Rx (Toptica, EK 000725) as a reference, see Appendix E.1. To ensure traceability of our measurement results, we determine the power emission of the reference Tx by using a dedicated pyroelectric thin-film detector (Sensor- und Lasertechnik Dr. W. Bohmeyer, THz20) that has been calibrated by the National Metrology Institute of Germany (Physikalisch-Technische Bundesanstalt, PTB; calibration certificate 73413-PTB-14). The frequency-dependent measured reference Tx power $P_{\mathrm{THz,\,ref}}$ is shown in Figure E.1a. Based on these results, we calculate the conversion factor of the reference Rx by using the measured current $I_{\mathrm{Rx,ref}}$ of the reference receiver,

$$\Gamma_{\mathrm{ref}} = I_{\mathrm{Rx,ref}} \Big/ \sqrt{P_{\mathrm{THz,\,ref}}}\,. \tag{E.18}$$

The result is shown in Figure E.1b. For the reference Rx, we obtained a noise current of $18\,\mathrm{pA}\big/\sqrt{\mathrm{Hz}}$.

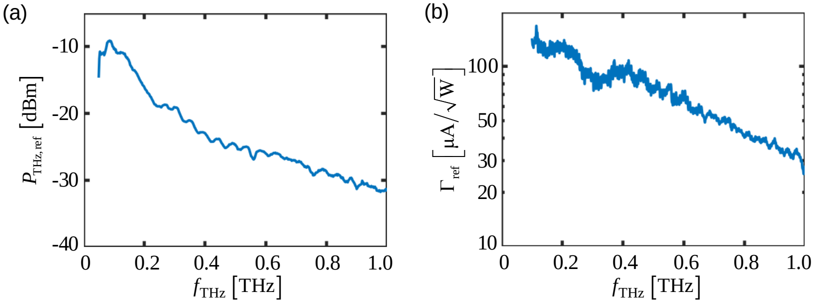

Figure E.1: Characterization of reference Tx and Rx. **(a)** Radiated power of reference transmitter measured by a calibrated pyroelectric thin-film detector. **(b)** Conversion factor Γ_{ref} of reference Rx. *Copyright © Springer Nature.*

E.4 Antenna-coupled Tx and Rx

For characterization of the Tx power and the Rx conversion factor, we couple the PIPED to an on-chip dipole antenna, see Inset 1 of Figure 5.1 on Page 59. The PIPED is placed at the antenna feed point. To supply a bias voltage to the PIPED, we use bias lines equipped with terahertz chokes that prevent leakage of THz signals from the antenna. With this configuration, the T-wave can be transmitted into and received from free space. The antenna and terahertz chokes consists of an approximately 110 nm-thick gold layer on top of a 40 nm-thick titanium layer. The lateral dimensions are given in Figure E.2. The antenna and the chokes where optimized by 3D electromagnetic-simulation [200] to a resonance frequency of 0.385 THz.

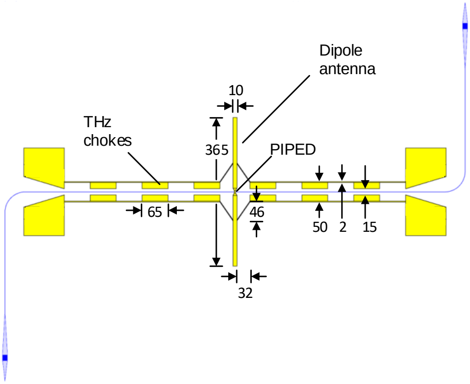

Figure E.2: Dipole antenna used to couple T-wave signals to and from the device. All dimensions are given in µm. *Copyright © Springer Nature.*

E.5 T-wave Rx

In the following, we assume reception of an unmodulated THz voltage amplitude $\hat{U}_{\mathrm{Rx},1} \propto \sqrt{P_{\mathrm{THz}}}$ corresponding to a received THz power P_{THz}, and we experimentally confirm the linear relationship between the baseband photocurrent amplitude $\hat{I}_{\mathrm{BB},1}$ and $\hat{U}_{\mathrm{Rx},1}$ as formulated in Eq. (E.16).

We prove $\hat{I}_{\mathrm{BB},1} \propto \sqrt{P_{\mathrm{THz}}}$ by measuring the baseband current $\hat{I}_{\mathrm{BB},1}$ for various THz powers P_{THz} at a frequency of 0.19 THz, see Figure E.3. The slope defines the conversion factor

$$\Gamma = \frac{\hat{I}_{\mathrm{BB},1}}{\sqrt{P_{\mathrm{THz}}}} \propto \left.\frac{\mathrm{d}S_{\mathrm{Rx}}}{\mathrm{d}U_{\mathrm{Rx}}}\right|_{U_{\mathrm{Rx},0}} \hat{P}_{\mathrm{Rx},1}. \tag{E.19}$$

The data plotted in Figure E.3 correspond to a conversion factor of $70\,\mu\mathrm{A}/\sqrt{\mathrm{W}}$. In Section 5.4 we showed experimentally that the conversion factor Γ is virtually proportional to the slope $\mathrm{d}S_{\mathrm{Rx}}/\mathrm{d}U_{\mathrm{Rx}}|_{U_{\mathrm{Rx},0}}$ of the sensitivity, see Figure 5.3c in Section 5.4. Additionally it is expected from Eq. (E.19) that Γ depends linearly on the optical power amplitude $\hat{P}_{\mathrm{Rx},1}$, which is experimentally confirmed by measurements shown in Figure E.4.

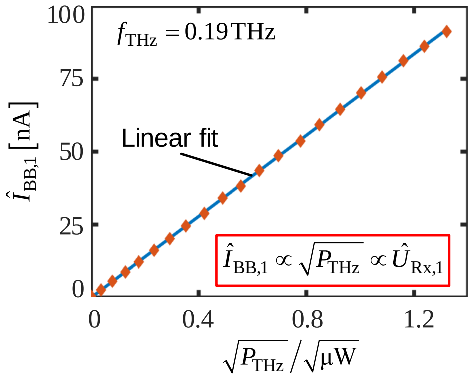

Figure E.3: Baseband current amplitude $\hat{I}_{\mathrm{BB},1}$ in dependence of input THz power amplitude P_{THz} at a frequency of 0.19 THz. The linear fit of the measurement demonstrates the excellent linearity between $\hat{I}_{\mathrm{BB},1}$ and $\sqrt{P_{\mathrm{THz}}}$. *Copyright © Springer Nature.*

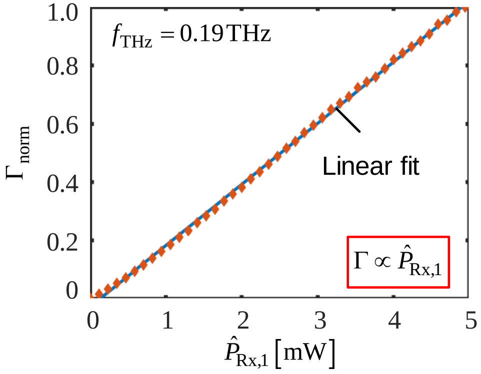

Figure E.4: Normalized conversion factor Γ_{norm} in dependence of the optical power amplitude $\hat{P}_{\mathrm{Rx},1}$, measured at a THz frequency of 0.19 THz. The conversion factor is normalized to the value obtained for the largest optical power amplitude. *Copyright © Springer Nature.*

E.6 Damage threshold

The output power of the Tx PIPED is eventually limited by the damage threshold of the PIPED. In the following section, we estimate the maximum photocurrent that the PIPED can withstand before irreversible damage occurs. To this end, we perform an experiment in which we apply different bias voltages and vary the optical input power in the range of 0 … 7.2 mW. The results are shown in Figure E.5. The device was eventually destroyed for an optical power of 7.2 mW at a bias voltage of 4.3 V. At this voltage, the last reliable measurement point before damaging the device exhibits a photocurrent of 540 µA for an optical input power of 6.5 mW. Note that the PIPED can bear currents that are even bigger than 540 µA at a smaller bias voltage of 4.2 V. Moreover, we have found that PIPEDs can typically withstand even higher bias voltages in excess of 5 V at low optical input powers. We therefore believe that the device damage is caused by a combined thermal effect that depends on both the electrical and the optical power dissipation, and that leads to an electrical short-circuit by melting parts of the metal structures of the active region. We performed similar damage tests with 4 more PIPEDs and found that all of them

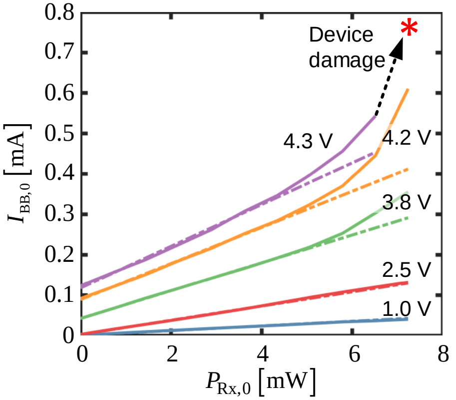

Figure E.5: Estimation of the PIPED damage threshold. For various bias voltages between 1.0 V and 4.2 V, we varied the optical input power $P_{\mathrm{Rx},0}$ in the range of 0 … 7.2 mW. The device was damaged when applying an optical power of 7.2 mW and a bias voltage of 4.3 V, indicated by a star in the diagram. At 4.2 V, the PIPED could withstand currents of 610 µA without being destroyed. *Copyright © Springer Nature.*

withstand currents in the range of 350 µA to 800 µA before damage occurs. Based on these observations, we believe that the operation current of PIPED THz Tx can be further increased in future device generations by improving the thermal coupling of the absorption zone to a proper heat sink.

E.7 Operating conditions of Rx

Figure 5.3a and Figure 5.4b in Chapter 5 show two operating conditions for the Rx PIPED. First, we connect an external DC voltage source $U_{\mathrm{Rx},0}$ by turning the switch to position 1. This allows to set the bias voltage to $U_{\mathrm{Rx},0} = 0.45\,\mathrm{V}$ which maximizes the sensitivity slope $\mathrm{d}S_{\mathrm{Rx}}/\mathrm{d}U_{\mathrm{Rx}}\big|_{U_{\mathrm{Rx},0}}$ and the receiver conversion factor Γ, see Figure 5.3c. Second, we turn the switch to position 0 (open circuit condition). In this case, no DC current flows. We call this situation ‘zero bias-current operation’. The benefit of the latter method is that the effective noise current is reduced from $190\,\mathrm{pA}/\sqrt{\mathrm{Hz}}$ to $9\,\mathrm{pA}/\sqrt{\mathrm{Hz}}$. The large current noise for the case of an externally applied bias voltage is attributed to the DC voltage source. Shot noise is less important for bias currents in the order of $100\,\mu\mathrm{A}$, which leads to an calculated effective shot noise current of only $5\,\mathrm{pA}/\sqrt{\mathrm{Hz}}$.

If an Rx PIPED under zero bias-current operation is illuminated with light, a voltage of roughly $U_{\mathrm{Rx},0} \approx 0.2\,\mathrm{V}$ builds up, which acts as a forward bias for the PIPED. The build-up potential is estimated from the static $I_{\mathrm{Rx},0}$-$U_{\mathrm{Rx},0}$ (current-voltage) characteristic of the receiver PIPED illuminated with optical amplitudes $\hat{E}_{\mathrm{Rx,a}} = 0$, $\hat{E}_{\mathrm{Rx,b}} = \mathrm{const}$, see Figure E.6. The results are shown for three illumination conditions, $P_{\mathrm{Rx},0} = 0\,\mathrm{mW}$, $1\mathrm{mW}$ and $2\,\mathrm{mW}$. Without illumination, the current $I_{\mathrm{Rx},0}$ is negligibly small. For optical input powers of $P_{\mathrm{Rx},0} = 1\mathrm{mW}$ and $2\,\mathrm{mW}$, the currents $I_{\mathrm{Rx},0}$ are zero at a voltage $U_{\mathrm{Rx},0}$ of 0.19 V and 0.21 V, respectively.

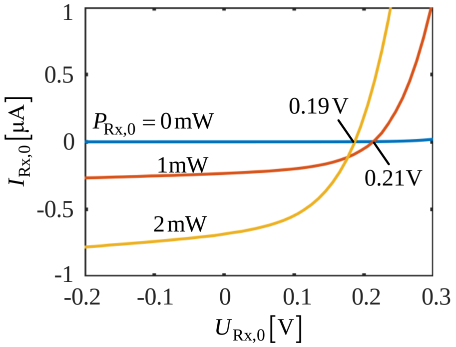

Figure E.6: Estimation of build-up potential of an externally illuminated PIPED with zero bias-current. The static current-voltage characteristic is recorded without illumination, $P_{\mathrm{Rx},0} = 0\,\mathrm{mW}$, as well as for optical input powers of $1\,\mathrm{mW}$ and $2\,\mathrm{mW}$, measured in the silicon waveguide which feeds the PIPED. With an illumination of $P_{\mathrm{Rx},0} = 1\,\mathrm{mW}$ and $P_{\mathrm{Rx},0} = 2\,\mathrm{mW}$, the current $I_{\mathrm{Rx},0}$ vanishes at a voltage $U_{\mathrm{Rx},0}$ of 0.19 V and 0.21 V, respectively. These voltages correspond to the open-circuit voltages that appear with zero bias-current. *Copyright © Springer Nature.*

E.8 Equivalent-circuit of T-wave systems

The schematic of an antenna-coupled Tx PIPED is shown in Figure E.7a, where THz transmitter and receiver carrier are derived from the same optical sources (homodyne reception). The PIPED is directly connected to the antenna feed points and is forward biased by a DC voltage $U_{\mathrm{Tx},0}$, which is applied via a bias line, see Inset 1 in Figure 5.1 on Page 59. This bias line has a low-pass characteristic, which prevents leakage of the THz current to the DC voltage source $U_{\mathrm{Tx},0}$, and is represented by an inductor L_0. The PIPED is illuminated by the optical power $P_{\mathrm{Tx}}\left(t\right)$ defined in Eq. (E.6),

$$P_{\mathrm{Tx}}\left(t\right) = P_{\mathrm{Tx},0}\left(t\right) + \hat{P}_{\mathrm{Tx},1}\left(t\right)\cos\left(\omega_{\mathrm{Tx,THz}}t + \varphi_{\mathrm{Tx,THz}}\right). \tag{E.20}$$

We assume that only the amplitude $\hat{P}_{\mathrm{Tx},1}\left(t\right)$ of the optical power oscillation is modulated, but not its phase $\varphi_{\mathrm{Tx,THz}}$. For analysing the behaviour of the system at THz frequencies, we translate the schematic into an equivalent-circuit representation using small-signal approximations. To this end, the PIPED current is represented by a low-frequency component $I_{\mathrm{Tx},0}\left(t\right)$, and a component with amplitude $\hat{I}_{\mathrm{Tx},1}\left(t\right)$ oscillating at THz frequency $\omega_{\mathrm{Tx,THz}}$, see Eq. (E.7),

$$\begin{aligned} I_{\mathrm{Tx}}(t) &= I_{\mathrm{Tx},0}(t) + I_{\mathrm{Tx},1}(t) \\ &= I_{\mathrm{Tx},0}(t) + \hat{I}_{\mathrm{Tx},1}(t)\cos\left(\omega_{\mathrm{Tx,THz}}t + \varphi_{\mathrm{Tx,THz}}\right). \end{aligned} \tag{E.21}$$

The PIPED voltage is represented in an analogous way,

$$\begin{aligned} U_{\mathrm{Tx}}(t) &= U_{\mathrm{Tx},0}(t) + U_{\mathrm{Tx},1}(t) \\ &= U_{\mathrm{Tx},0}(t) + \hat{U}_{\mathrm{Tx},1}(t)\cos\left(\omega_{\mathrm{Tx,THz}}t + \varphi_{\mathrm{Tx,THz}}\right). \end{aligned} \tag{E.22}$$

Using the small-signal approximation, the behaviour of the Tx PIPED can then be modelled by a linearized voltage-dependent sensitivity,

$$S_{\mathrm{Tx}}\left(U_{\mathrm{Tx}}(t)\right) \approx S_{\mathrm{Tx}}\left(U_{\mathrm{Tx},0}\right) + \left.\frac{\mathrm{d}\,S_{\mathrm{Tx}}}{\mathrm{d}U_{\mathrm{Tx}}}\right|_{U_{\mathrm{Tx},0}} U_{\mathrm{Tx},1}(t). \tag{E.23}$$

The Tx PIPED current is then given by

$$\begin{aligned} I_{\mathrm{Tx}}(t) &= S_{\mathrm{Tx}}\left(U_{\mathrm{Tx}}(t)\right)P_{\mathrm{Tx}}(t) \\ &= \underbrace{S_{\mathrm{Tx}}\left(U_{\mathrm{Tx},0}\right)P_{\mathrm{Tx},0}(t)}_{(1)} \\ &\quad \underbrace{+\frac{1}{2}\left.\frac{\mathrm{d}\,S_{\mathrm{Tx}}}{\mathrm{d}U_{\mathrm{Tx}}}\right|_{U_{\mathrm{Tx},0}} \hat{P}_{\mathrm{Tx},1}(t)\hat{U}_{\mathrm{Tx},1}(t)}_{(2)} \\ &\quad \underbrace{+S\left(U_{\mathrm{Tx},0}\right)\hat{P}_{\mathrm{Tx},1}(t)\cos\left(\omega_{\mathrm{Tx,THz}}t + \varphi_{\mathrm{Tx,THz}}\right)}_{(3)} \\ &\quad \underbrace{+\left.\frac{\mathrm{d}\,S_{\mathrm{Tx}}}{\mathrm{d}U_{\mathrm{Tx}}}\right|_{U_{\mathrm{Tx},0}} P_{\mathrm{Tx},0}(t)\hat{U}_{\mathrm{Tx},1}(t)\cos\left(\omega_{\mathrm{Tx,THz}}t + \varphi_{\mathrm{Tx,THz}}\right)}_{(4)} \\ &\quad \underbrace{+\frac{1}{2}\left.\frac{\mathrm{d}\,S_{\mathrm{Tx}}}{\mathrm{d}U_{\mathrm{Tx}}}\right|_{U_{\mathrm{Tx},0}} \hat{P}_{\mathrm{Tx},1}(t)\hat{U}_{\mathrm{Tx},1}(t)\cos\left(2\omega_{\mathrm{Tx,THz}}t + 2\varphi_{\mathrm{Tx,THz}}\right)}_{(5)}. \end{aligned} \tag{E.24}$$

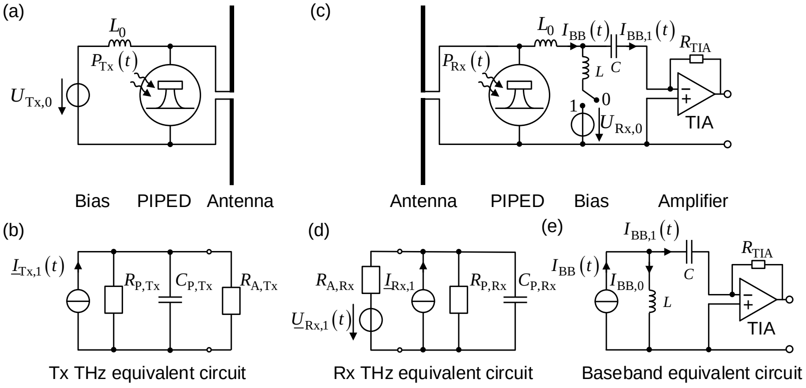

Tx THz equivalent circuit

Rx THz equivalent circuit

Baseband equivalent circuit

Figure E.7: Equivalent circuit of PIPED in T-wave systems. **(a)** Schematic of antenna-coupled T-wave transmitter. The PIPED is directly connected to the antenna feed points and is biased by the voltage $U_{\mathrm{Tx},0}$, which is applied via a bias transmission line acting as a low pass and represented by an inductor L_0. The PIPED is driven by the optical power $P_{\mathrm{Tx}}(t)$. **(b)** Small-signal equivalent-circuit diagram of the Tx at THz frequencies. The PIPED is represented by the THz current source with complex amplitude $\underline{I}_{\mathrm{Tx},1}(t)=S\left(U_{\mathrm{Tx},0}\right)\hat{P}_{\mathrm{Tx},1}(t)\exp\left[\mathrm{j}\varphi_{\mathrm{Tx,THz}}(t)\right]$, the internal resistor $R_{\mathrm{P,Tx}}$ as well as by the capacitor $C_{\mathrm{P,Tx}}$. The antenna is modelled by the radiation resistor $R_{\mathrm{A,Tx}}$. **(c)** Schematic of an antenna coupled to a T-wave receiver. The PIPED is directly connected to the antenna feed points and is biased via transmission lines acting as a low pass and represented by an inductor L_0. The receiver is either operated with an externally applied voltage $U_{\mathrm{Rx},0}$ (switch position 1), or with a zero bias-current (switch position 0). A bias-T, represented by the capacitor C and the inductor L, extracts the time-varying part $I_{\mathrm{BB},1}(t)$ of the total baseband current $I_{\mathrm{BB}}(t)$. A transimpedance amplifier (TIA) with transimpedance R_{TIA} amplifies the baseband current $I_{\mathrm{BB},1}(t)$ and feeds it to a lock-in amplifier (not depicted). **(d)** Small-signal equivalent circuit of the Rx at THz frequencies. The PIPED is modelled by the THz current source with complex amplitude $\underline{I}_{\mathrm{Rx},1}=S\left(U_{\mathrm{Rx},0}\right)\hat{P}_{\mathrm{Rx},1}\exp\left[\mathrm{j}\varphi_{\mathrm{Rx,THz}}(t)\right]$, an internal resistor $R_{\mathrm{P,Rx}}$ and a capacitor $C_{\mathrm{P,Rx}}$, similarly as with the Tx shown in Subfigure (b). The receiving antenna is modelled by a voltage source $\underline{U}_{\mathrm{Rx},1}(t)=\hat{U}_{\mathrm{Rx},1}(t)\exp\left[\mathrm{j}\left(\varphi_{\mathrm{Tx,THz}}+\varphi_{\mathrm{TxRx}}\right)\right]$ and by a radiation resistor $R_{\mathrm{A,Rx}}$. In our experiments, the THz signal and therefore $\hat{U}_{\mathrm{Rx},1}$ are low-frequency modulated for lock-in detection. **(e)** Baseband equivalent circuit. The downconversion leads to a baseband current $I_{\mathrm{BB}}(t)$, see Eq. (E.29). The bias-T branches this current in a constant part $I_{\mathrm{BB},0}$ and in a time-varying part $I_{\mathrm{BB},1}(t)$. The time-varying current component is fed to the TIA. *Copyright © Springer Nature.*

Note that the time dependence of voltages, currents and powers $U_{\mathrm{Tx},0}(t)$, $I_{\mathrm{Tx},0}(t)$, $P_{\mathrm{Tx},0}(t)$, $\hat{U}_{\mathrm{Tx},1}(t)$, $\hat{I}_{\mathrm{Tx},1}(t)$, $\hat{P}_{\mathrm{Tx},1}(t)$ result from an auxiliary low-frequency modulation, which could be imposed for lock-in detection. The quantities $P_{\mathrm{Tx},0}$ and $\hat{P}_{\mathrm{Tx},1}$ have the same order of magnitude. The first two expressions (1) and (2) in Eq. (E.24) describe a low-frequency current. Because $S_{\mathrm{Tx}} \gg \left(\mathrm{d}\,S_{\mathrm{Tx}}/\mathrm{d}U_{\mathrm{Tx}}\right)\hat{U}_{\mathrm{Tx},1}$ holds, subexpression (2) can be neglected compared to subexpression (1), and subexpressions (4), (5) can be neglected compared to subexpression (3). This was the implicit approximation assumed in Eq. (E.8).

From Eq. (E.24), we derive the small-signal equivalent circuit at THz frequencies, see Figure E.7b. The dominating THz current contribution (3) is modelled by a THz current source with a slowly varying complex amplitude,

$$\underline{I}_{\mathrm{Tx},1}(t) = S\left(U_{\mathrm{Tx},0}\right)\hat{P}_{\mathrm{Tx},1}(t)\,\mathrm{e}^{\,\mathrm{j}\varphi_{\mathrm{Tx,THz}}}\,. \tag{E.25}$$

Note that the THz current source is ideal meaning that it features an internal conductance of zero. For a more realistic representation, it may be useful to also consider the impact of a finite source conductance. This is equivalent to considering expression (4) in Eq. (E.24), which describes a contribution to the THz current amplitude $\hat{I}_{\mathrm{Tx},1}(t)$ that increases in proportion to the THz voltage amplitude $\hat{U}_{\mathrm{Tx},1}(t)$. In the equivalent-circuit diagram, this contribution is represented by the PIPED resistance

$$R_{\mathrm{P,Tx}} = \frac{1}{\left.\dfrac{\mathrm{d}\,S_{\mathrm{Tx}}}{\mathrm{d}U_{\mathrm{Tx}}}\right|_{U_{\mathrm{Tx},0}} P_{\mathrm{Tx},0}} = \left.\frac{\mathrm{d}U_{\mathrm{Tx},0}}{\mathrm{d}I_{\mathrm{Tx},0}}\right|_{U_{\mathrm{Tx},0},P_{\mathrm{Tx},0}}\,. \tag{E.26}$$

Furthermore, we introduce the capacitance $C_{\mathrm{P,Tx}}$ into the THz equivalent circuit diagram to account for the tiny, but nonzero capacitance of the metal-coated sidewalls of the PIPED, see Figure 5.2 on Page 61. The antenna is modelled by its radiation resistance $R_{\mathrm{A,Tx}}$.

In an analogous way we describe the PIPED Rx. Figure E.7c shows the schematic of the Rx PIPED. Again, the PIPED is directly connected to the antenna feed points, and the bias line is represented by the inductor L_0. As described in Section 5.4, the Rx PIPED can either be operated with zero bias current if the switch is set to position 0, or with an externally applied bias voltage $U_{\mathrm{Rx},0}$ if the switch is set to position 1. A bias-T, represented by the inductor L and the capacitor C, separates the time varying part $I_{\mathrm{BB},1}(t)$ of the baseband current $I_{\mathrm{BB}}(t)$ from the constant part $I_{\mathrm{BB,0}}$. The current $I_{\mathrm{BB,1}}(t)$ is amplified in a transimpedance amplifier with a transimpedance of $R_{\mathrm{TIA}} = 1\mathrm{M\Omega}$.

To obtain the THz small-signal equivalent circuit of the Rx, we follow the same procedure as with the Tx PIPED. This leads to the equivalent circuit shown in Figure E.7d. In this case, the Rx antenna and the received THz wave are modelled by a radiation resistor $R_{\mathrm{A,Rx}}$ and a voltage source with a slowly varying complex amplitude $\underline{U}_{\mathrm{Rx,1}}(t)$, see Eq. (E.12),

$$\underline{U}_{\mathrm{Rx,1}}(t) = \hat{U}_{\mathrm{Rx,1}}(t)\,\mathrm{e}^{\mathrm{j}\left(\varphi_{\mathrm{Tx,THz}}+\varphi_{\mathrm{TxRx}}\right)}. \tag{E.27}$$

The time-dependence of $\hat{U}_{\mathrm{Rx,1}}(t)$ originates from a modulation of the Tx DC bias voltage $U_{\mathrm{Tx,0}}$, which leads to a varying THz signal amplitude. In contrast, the THz current source

$$\underline{I}_{\mathrm{Rx,1}} = S\left(U_{\mathrm{Rx,0}}\right)\hat{P}_{\mathrm{Rx,1}}\,\mathrm{e}^{\mathrm{j}\varphi_{\mathrm{Rx,THz}}} \tag{E.28}$$

is unmodulated.

The phase and the amplitude of the received THz wave can be extracted from the time-dependent baseband current $I_{\mathrm{BB}}(t)$, see Eqs. (E.16) and (E.17),

$$\begin{aligned} I_{\mathrm{BB}}(t) &= I_{\mathrm{BB,0}} + I_{\mathrm{BB,1}}(t) \\ &= I_{\mathrm{BB,0}} + \hat{I}_{\mathrm{BB,1}}(t)\cos\left(\varphi_{\mathrm{BB}}\right), \end{aligned} \tag{E.29}$$

with the abbreviations

$$\begin{aligned} I_{\mathrm{BB,0}} &= S_{\mathrm{Rx}}\left(U_{\mathrm{Rx,0}}\right)P_{\mathrm{Rx,0}}, \\ \hat{I}_{\mathrm{BB,1}}(t) &= \tfrac{1}{2}\left.\frac{\mathrm{d}S_{\mathrm{Rx}}}{\mathrm{d}U_{\mathrm{Rx}}}\right|_{U_{\mathrm{Rx,0}}} \hat{P}_{\mathrm{Rx,1}}\hat{U}_{\mathrm{Rx,1}}(t)\ , \\ \varphi_{\mathrm{BB}} &= \varphi_{\mathrm{Tx,THz}} - \varphi_{\mathrm{Rx,THz}} + \varphi_{\mathrm{TxRx}}. \end{aligned} \tag{E.30}$$

Note that the Rx PIPED current can be described in analogy to Eq. (E.24) and that the quantities $I_{\mathrm{BB,0}}$ and $I_{\mathrm{BB,1}}(t)$ would correspond to the subexpressions

(1) and (2). The time dependence of $I_{\mathrm{BB}}(t)$ originates from the modulation of the Tx bias voltage $U_{\mathrm{Tx},0}$, which leads to a modulation of the received THz voltage amplitude $\hat{U}_{\mathrm{Rx},1}(t)$. This modulation allows to separate $\hat{I}_{\mathrm{BB},1}(t)$ from the constant current $I_{\mathrm{BB},0}$. The equivalent baseband circuit of the Rx is shown in Figure E.7e. The time-varying current $I_{\mathrm{BB},1}(t)$ is separated from $I_{\mathrm{BB}}(t)$ by the bias-T, which is modelled by the capacitor C and the inductor L. To this end, the high-pass cut-off frequency of the bias-T must be smaller than the modulation frequency for lock-in reception. The baseband current $I_{\mathrm{BB},1}(t)$, which is in proportion to the incoming THz field, is amplified by the transimpedance amplifier, and fed to a subsequent lock-in amplifier.

Since the Tx PIPED features a large internal resistance $R_{\mathrm{P,Tx}}$ and a small capacitance $C_{\mathrm{P,Tx}}$, the corresponding components in the equivalent-circuit representation can often be neglected. To quantify the PIPED resistance, we calculate the differential resistance $\mathrm{d}U_{\mathrm{Tx},0}/\mathrm{d}I_{\mathrm{Tx},0}\big|_{P_{\mathrm{Tx},0}}$ from the static voltage-current characteristics measured for different optical input powers $P_{\mathrm{Tx},0}$, see Figure E.8a and Eq. (E.26). For all operating conditions, we find that the differential resistance is much larger than $10\,\mathrm{k\Omega}$. In addition, the small footprint of the PIPED leads to capacitances well below $2\,\mathrm{fF}$ (ref [117]). Figure E.8b shows the magnitude of the frequency-dependent impedance associated with this capacitance. In the frequency range of interest, the magnitude of the

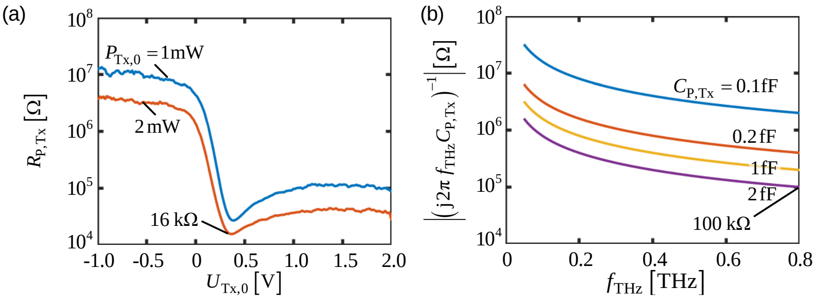

Figure E.8: Estimation of Tx PIPED impedance. **(a)** PIPED resistance $R_{\mathrm{P,Tx}}$ estimated by taking the different resistance $\mathrm{d}U_{\mathrm{Tx},0}/\mathrm{d}I_{\mathrm{Tx},0}\big|_{P_{\mathrm{Tx},0}}$ of the static voltage-current characteristic for different optical input powers $P_{\mathrm{Tx},0}$. For all operation conditions, the differential resistance is larger than $10\,\mathrm{k\Omega}$. **(b)** Magnitude of the impedance $(\mathrm{j}2\pi f_{\mathrm{THz}} C_{\mathrm{P,Tx}})^{-1}$ associated with the PIPED capacitance $C_{\mathrm{P,Tx}}$. In the frequency of interest, the impedance magnitude is larger than 100 kΩ. *Copyright © Springer Nature.*

impedance is larger than 100 $\mathrm{k}\Omega$. Equivalent statements hold for the Rx PIPED. These large internal impedances of the PIPEDs allow to neglect $R_{\mathrm{P,Tx,Rx}}$ in comparison to the antenna radiation resistance $R_{\mathrm{A,Tx,Rx}}$ which is typically in the order of 100 Ω.

Figure E.9a illustrates the equivalent circuit of the monolithically integrated T-wave system, see Figure 5.4 on Page 74. The Tx PIPED and the Rx PIPED are modelled as described in Figure E.7b,d. The transmission line is represented by a complex impedance matrix with components $\underline{Z}_{11}$, $\underline{Z}_{21} = \underline{Z}_{12}$ and $\underline{Z}_{22}$ of a reciprocal two-port network [201]. Making use of the fact that the PIPED impedance is much larger than the impedance matrix elements $\underline{Z}_{ij}$, we simplify the equivalent circuit by eliminating the internal resistors and capacitors of the Rx and Tx PIPED.

Further simplifications are possible, if we modulate the bias $U_{\mathrm{Tx},0}$ of the Tx PIPED and hence the Tx current amplitude $\underline{I}_{\mathrm{Tx},1}(t)$, and exploit lock-in detection of the baseband current $I_{\mathrm{BB}}(t)$. Therefore, we only extract the component that is related to the THz voltage $U_{\mathrm{Rx},1}(t)$ received from the transmitter. The THz current $\underline{I}_{\mathrm{Rx},1}$ is not affected by this modulation, and hence does not influence the lock-in signal. The current source $\underline{I}_{\mathrm{Rx},1}$ can therefore be omitted for the further analysis of the equivalent circuit. This leads to the simplified diagram shown in Figure E.9b and to the relation

$$\underline{U}_{\mathrm{Rx},1}(t) = \underline{Z}_{21}\underline{I}_{\mathrm{Tx},1}(t). \tag{E.31}$$

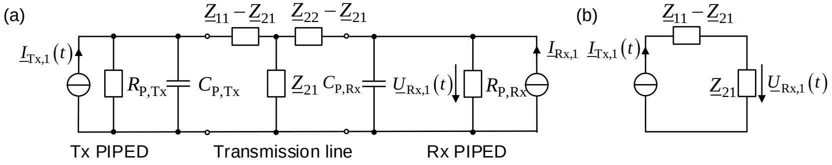

Figure E.9: Equivalent circuit of the monolithically integrated T-wave system. **(a)** Small-signal equivalent circuit. The Tx PIPED and Rx PIPED are modelled as shown in Figure E.7b,d. The transmission line is described by an impedance matrix with elements $\underline{Z}_{11}$, $\underline{Z}_{22}$ and $\underline{Z}_{21} = \underline{Z}_{12}$ for a reciprocal two-port network. **(b)** Simplified equivalent circuit, considering only quantities that are modulated by the lock-in signal of the Tx PIPED bias $U_{\mathrm{Tx},0}(t)$, and exploiting the fact that the PIPED impedance is much larger than the transmission line impedances.

Using this relation we can derive a connection of the complex transfer impedance $\underline{Z}_{21}$ with the baseband current $I_{\mathrm{BB},1}(t)$. With Eq. (E.25), Eq. (E.27), and the definition of the transfer impedance $\underline{Z}_{21} = |\underline{Z}_{21}|\mathrm{e}^{\mathrm{j}\varphi_{21}}$, Eq. (E.31) is written as

$$\hat{U}_{\mathrm{Rx},1}(t)\,\mathrm{e}^{\mathrm{j}(\varphi_{\mathrm{Tx,THz}}+\varphi_{\mathrm{TxRx}})} = |\underline{Z}_{21}|\,\mathrm{e}^{\mathrm{j}\varphi_{21}}\,\hat{I}_{\mathrm{Tx},1}\,\mathrm{e}^{\mathrm{j}\varphi_{\mathrm{Tx,THz}}}\,. \tag{E.32}$$

The relation can be split into one equation for the magnitude $|\underline{Z}_{21}|$ and another equation for the phase φ_{21} of the transfer impedance,

$$\begin{aligned} \hat{U}_{\mathrm{Rx},1}(t) &= |\underline{Z}_{21}|\,\hat{I}_{\mathrm{Tx},1}(t), \\ \varphi_{21} &= \varphi_{\mathrm{TxRx}}. \end{aligned} \tag{E.33}$$

Substituting Eq. (E.33) into Eq. (E.30) leads to

$$\begin{aligned} \hat{I}_{\mathrm{BB},1}(t) &= \tfrac{1}{2}\left.\frac{\mathrm{d}S_{\mathrm{Rx}}}{\mathrm{d}U_{\mathrm{Rx}}}\right|_{U_{\mathrm{Rx},0}} \hat{P}_{\mathrm{Rx},1}\,\hat{I}_{\mathrm{Tx},1}(t)\,|\underline{Z}_{21}|, \\ \varphi_{\mathrm{BB}} &= \varphi_{\mathrm{Tx,THz}} - \varphi_{\mathrm{Rx,THz}} + \varphi_{21}. \end{aligned} \tag{E.34}$$

In this equation the Tx current $\hat{I}_{\mathrm{Tx},1}(t) = \hat{I}_{\mathrm{Tx},1}\cos(\omega_{\mathrm{LI}}t)$ with amplitude $\hat{I}_{\mathrm{Tx},1}$ is subject to a sinusoidal modulation with the lock-in frequency ω_{LI}. The baseband photocurrent $\hat{I}_{\mathrm{BB},1}(t) = \hat{I}_{\mathrm{BB},1}\cos(\omega_{\mathrm{LI}}t)$ with amplitude $\hat{I}_{\mathrm{BB},1}$ can then be used as a measure for the magnitude of the transfer impedance $|\underline{Z}_{21}|$. Substituting $\hat{I}_{\mathrm{Tx},1}(t) = S_{\mathrm{Tx}}(U_{\mathrm{Tx},0})\hat{P}_{\mathrm{Tx},1}$ we write

$$\begin{aligned} \hat{I}_{\mathrm{BB},1} &= \tfrac{1}{2}\left.\frac{\mathrm{d}S_{\mathrm{Rx}}}{\mathrm{d}U_{\mathrm{Rx}}}\right|_{U_{\mathrm{Rx},0}} \hat{P}_{\mathrm{Rx},1}\,\hat{I}_{\mathrm{Tx},1}\,|\underline{Z}_{21}| \\ &= \tfrac{1}{2}\left.\frac{\mathrm{d}S_{\mathrm{Rx}}}{\mathrm{d}U_{\mathrm{Rx}}}\right|_{U_{\mathrm{Rx},0}} \hat{P}_{\mathrm{Rx},1}\,S_{\mathrm{Tx}}(U_{\mathrm{Tx},0})\,\hat{P}_{\mathrm{Tx},1}\,|\underline{Z}_{21}| \\ &= |\underline{Z}_{21}|/a\ . \end{aligned} \tag{E.35}$$

In this relation, the proportionality factor $1/a$ is given by

$$\frac{1}{a} = \tfrac{1}{2} \left. \frac{\mathrm{d} S_{\mathrm{Rx}}}{\mathrm{d} U_{\mathrm{Rx}}} \right|_{U_{\mathrm{Rx,0}}} \hat{P}_{\mathrm{Rx,1}} S_{\mathrm{Tx}} \left(U_{\mathrm{Tx,0}} \right) \hat{P}_{\mathrm{Tx,1}} , \tag{E.36}$$

and has the unit $\left[\mathrm{A} / \Omega \right]$. As a result, we can determine $\left| \underline{Z}_{21} \right|$ by measuring $\hat{I}_{\mathrm{BB,1}}$. In addition, the phase φ_{21} of the transfer impedance $\underline{Z}_{21}$ can be determined by measuring the phase φ_{BB} of the baseband current in Eq. (E.34). We eliminate the influence of the unknown group delay in the optical fibres, see Appendix E.1, by swapping the role of the Tx and the Rx PIPED and recording $\varphi_{\mathrm{BB,\,rev}} = -(\varphi_{\mathrm{Tx,THz}} - \varphi_{\mathrm{Rx,THz}}) + \varphi_{21}$. By adding Eq. (E.34) we finally find φ_{21}.

E.9 Frequency roll-off

For large frequencies, the conversion factor of the Tx PIPED and of the Rx PIPED drop due to limitations by the carrier transit time, see Section 5.3 “PIPED for optoelectronic T-wave processing”. In the following, we characterize the high-speed performance and the frequency roll-off of the PIPED. The frequency response of the Tx and Rx PIPED photocurrent,

$$I_{\mathrm{Tx,Rx}} \left(f_{\mathrm{THz}} \right) = \eta_{\mathrm{Tx,Rx}} \left(f_{\mathrm{THz}} \right) S_{\mathrm{Tx,Rx}} P_{\mathrm{Tx,Rx}} , \tag{E.37}$$

is characterized as an RC low pass characteristic,

$$\eta_{\mathrm{Tx}} \left(f_{\mathrm{THz}} \right) = \eta_{\mathrm{Rx}} \left(f_{\mathrm{THz}} \right) = \frac{1}{\sqrt{1 + \left(f_{\mathrm{THz}} / f_{\mathrm{3dB}} \right)^2}} . \tag{E.38}$$

Figure E.10a shows the simulated magnitude $\left| \underline{Z}_{21,\mathrm{sim}} \left(f_{\mathrm{THz}} \right) \right|$ of the transfer impedance for the $L = 0.01\mathrm{mm}$ long transmission line together with the measured frequency-dependent amplitude $\hat{I}_{\mathrm{BB,1}} \left(f_{\mathrm{THz}} \right)$ of the baseband photocurrent. For an ideal PIPED, $\hat{I}_{\mathrm{BB,1}} \left(f_{\mathrm{THz}} \right) = \left| \underline{Z}_{21} \left(f_{\mathrm{THz}} \right) \right| / a$ would be true, see Eq. (E.35). The real device shows a low pass characteristic. To match the simulation to the measurements, we include the RC low pass characteristic of Eq. (E.38) and find

$$\begin{aligned}\hat{I}_{\mathrm{BB},1}(f_{\mathrm{THz}}) &= \eta_{\mathrm{Tx}}(f_{\mathrm{THz}})\,\eta_{\mathrm{Rx}}(f_{\mathrm{THz}})\left|\underline{Z}_{21,\mathrm{sim}}(f_{\mathrm{THz}})\right|/a \\ &= \frac{1}{1+(f_{\mathrm{THz}}/f_{3\mathrm{dB}})^2}\left|\underline{Z}_{21,\mathrm{sim}}(f_{\mathrm{THz}})\right|/a.\end{aligned} \tag{E.39}$$

The parameters a and $f_{3\mathrm{dB}}$ are obtained from the measurement data by a least-squares fit. This is necessary because the experimental operating conditions of the Tx and Rx PIPED at THz frequencies are only approximately known. We

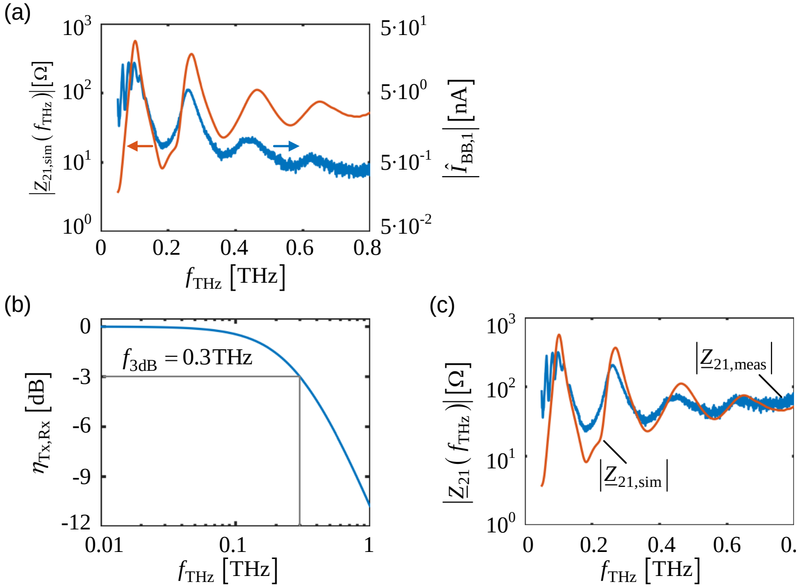

Figure E.10: Characterization of PIPED roll-off frequency $f_{3\mathrm{dB}}$. **(a)** Comparison of simulated magnitude $|\underline{Z}_{21,\mathrm{sim}}(f_{\mathrm{THz}})|$ of the transfer impedance (red, left axis) and the measured amplitude $\hat{I}_{\mathrm{BB},1}(f_{\mathrm{THz}})$ of the baseband photocurrent (blue, right axis) obtained for a transmission line length $L = 0.01\,\mathrm{mm}$. The limited PIPED bandwidth causes a decrease of the current amplitude $\hat{I}_{\mathrm{BB},1}(f_{\mathrm{THz}})$ with respect to the simulated magnitude $|\underline{Z}_{21,\mathrm{sim}}(f_{\mathrm{THz}})|$ at larger frequencies. **(b)** Tx PIPED and Rx PIPED frequency response approximated by an RC low pass. The parameter $f_{3\mathrm{dB}} = 0.3\,\mathrm{THz}$ was obtained by matching in subfigure (a) the two traces. **(c)** Simulated and measured transfer impedance for a transmission line length $L = 0.01\,\mathrm{mm}$. The measured photocurrent amplitudes $\hat{I}_{\mathrm{BB},1}(f_{\mathrm{THz}})$ are expressed by the modulus of the corresponding transfer impedances $|\underline{Z}_{21,\mathrm{meas}}(f_{\mathrm{THz}})|$ using the fitting parameters $a = 21\,\Omega/\mathrm{nA}$ and $f_{3\mathrm{dB}} = 0.3\,\mathrm{THz}$. *Copyright © Springer Nature.*

obtain $a = 21\,\Omega/\text{nA}$ and $f_{3\text{dB}} = 0.3\,\text{THz}$, indicating again the superior bandwidth properties of the PIPED. Figure E.10b shows the double-logarithmic display of the PIPED frequency roll-off. We attribute the same 3 dB bandwidth to various PIPEDs for all measurements in Figure 5.4c-e on Page 74. Residual differences between the PIPEDs employed for measuring with different lengths of the transmission line ($L = 0.63\,\text{mm}$ and $L = 0.95\,\text{mm}$) we compensate by fitting a. Using the parameters a and $f_{3\text{dB}}$, we translate the measured photocurrent amplitude $\hat{I}_{\text{BB},1}\left(f_{\text{THz}}\right)$ into the corresponding transfer impedance $\left|\underline{Z}_{21,\text{meas}}\left(f_{\text{THz}}\right)\right|$, which is plotted along with its simulated counterpart in Figure E.10c; this corresponds to Figure 5.4c on Page 74. Simulation and measurement show good agreement.

E.10 Simulation of frequency-dependent radiated Tx power

The radiated PIPED Tx power shown in Figure 5.3 on Page 66 was simulated using a commercially available numerical time domain solver (CST Microwave Studio [200]). The dipole antenna is excited at the feed point by the equivalent circuit shown in Figure E.11a. The excitation circuit is derived from the equivalent-circuit model shown in Figure E.7b, where the PIPED resistance $R_{\text{P,Tx}} \gg 10\ \text{k}\Omega$ is neglected in comparison to the antenna radiation resistance. Note that even the relatively small PIPED impedance $C_{\text{P,Tx}} < 1$ fF can influence the frequency-dependent radiation characteristics if the PIPED is coupled to a resonant antenna that may have a large radiation resistance. For a quantitative analysis, we estimate the PIPED capacitance using the dimensions indicated in the horizontal cross-sectional view shown Figure E.11b. For a conservative estimate, we use the horizontal cross section of the PIPED close to the upper edge of the Si waveguide core, where the PIPED width d is the smallest, see Figure 5.2 on Page 61. With a PIPED length of $l = 2$ µm, a PIPED width of $d = 0.1$ µm, a silicon height of $h = 0.3$ µm, and the relative permittivity of $\varepsilon_{\text{r,Si}} = 11.9$ we estimate the capacitance of the PIPED core $C_{\text{P,core}}$ by the plate capacitor formula,

$$C_{\text{P,core}} = \varepsilon_0 \varepsilon_{\text{r,Si}} \frac{l \cdot h}{d} = 0.63\,\text{fF}. \tag{E.40}$$

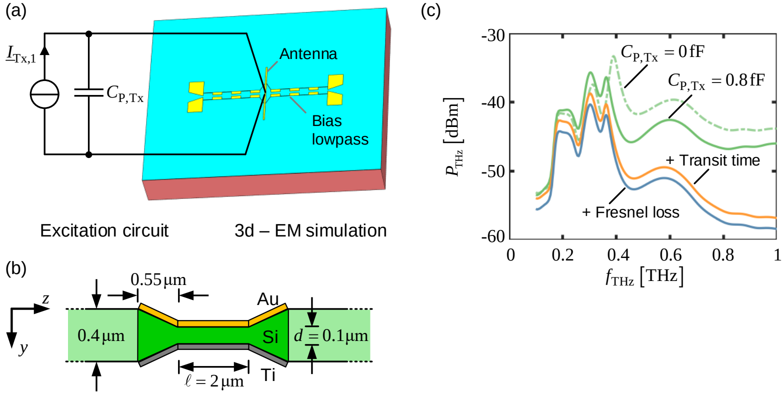

Figure E.11: Simulation of frequency-dependent radiated Tx power. **(a)** Schematic of the 3D electromagnetic-simulation and the equivalent circuit used to emulate the PIPED. **(b)** Horizontal cross section of the PIPED, taken close to the upper edge of the Si waveguide core, where the PIPED width *d* is the smallest, see Figure 5.2 on Page 61. **(c)** Simulated THz power P_{THz} radiated into the acceptance cone of the silicon lens (solid green curve). As a reference, we also plot the radiated power, for the case that the PIPED capacitance would be 0 fF (dashed green curve). The simulation including the PIPED capacitance of 0.8 fF is corrected by a first-order low-pass with $f_{3dB} = 0.3\,\mathrm{THz}$ to take the transit time limitation into account (orange curve), see Appendix E.9 for details. Furthermore, we considered Fresnel loss at the transition from silicon to air (blue curve). *Copyright © Springer Nature.*

In addition, there is a 0.55 µm long taper section to couple the light from the 0.4 µm wide silicon waveguide to the PIPED core. This leads to an estimated taper capacitance $C_{P,tap} = 0.08$ fF on each side. The total PIPED capacitance hence amounts to

$$C_{P,Tx} = C_{P,core} + 2C_{P,tap} = 0.8\,\mathrm{fF}. \tag{E.41}$$

In the current layout the PIPED is symmetrically constructed. This allows to couple the light from both sides to the PIPED and gives more flexibilities in the experimental setup, but is not essential for the operation. The PIPED capacitance can hence be reduced to less than 0.5 fF by omitting one of the tapers and by reducing the length of the plasmonic waveguide to 1 µm. Note that the width of the Si waveguide core and hence the distance between the capacitor plates increases from top to bottom, see Figure 5.2a on Page 61. This leads to a smaller PIPED capacitance as estimated above. Our quantitative analysis is hence to be understood as a conservative estimate, trying to avoid underestimation of the PIPED capacitance.

The simulation result of the power P_{THz} radiated in the direction of the acceptance angle of the silicon lens is shown in Figure E.11c as a solid green curve. To see the influence of the PIPED capacitance, we also simulated the radiated power for a capacitance of 0 fF (dashed green curve). The orange curve in Figure E.11c is obtained by a simulation that includes the PIPED capacitance and additionally considers the bandwidth limitations caused by carrier transit times, which lead to a frequency roll-off $\eta_{\mathrm{Tx}}\left(f_{\mathrm{THz}}\right)$ with a 3 dB frequency of $f_{3\mathrm{dB}} = 0.3\,\mathrm{THz}$, see Appendix E.9 for details. Furthermore, we take into account the Fresnel loss at the silicon-air interface of the THz lens (blue curve). To this end, we approximate the overall power transmission factor T_{Fresnel} by assuming normal incidence of the THz wave onto the interface,

$$T_{\mathrm{Fresnel}} \approx 1 - \left(\frac{\sqrt{\varepsilon_{\mathrm{r,Si}}} - 1}{\sqrt{\varepsilon_{\mathrm{r,Si}}} + 1} \right)^2 = 0.7\,. \tag{E.42}$$

The simulated power transmission characteristic shown in Figure 5.3b on Page 66 corresponds to the blue trace of Figure E.11c.

E.11 Electric field distribution of integrated T-wave system

The transfer impedances of the various THz transmission lines plotted in Figure 5.4c - e on Page 74 exhibit a resonant behaviour. For a better understanding of these resonances, we perform for selected frequencies simulations of the electric field distribution along the transmission line. Figure E.12a-c display the simulation results for the magnitude of the electric field obtained for three different transmission line lengths

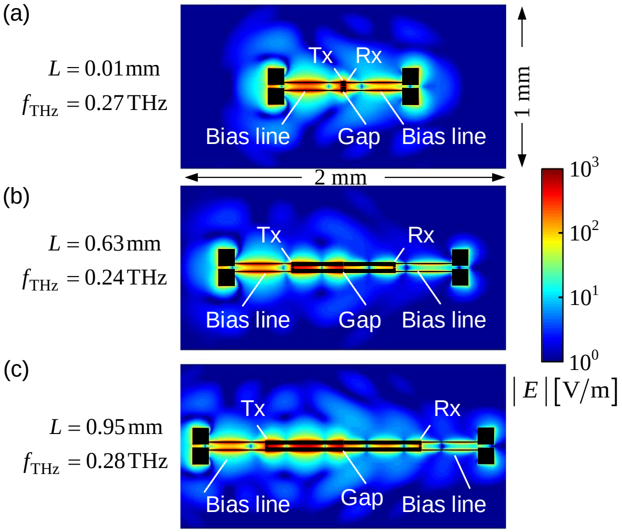

Figure E.12: (a)-(c) Simulated magnitude of the electric field for the resonance frequencies $f_{\mathrm{THz}} = (0.27, 0.24, 0.28)$ THz at the (geometrical) transmission line lengths $L = (0.01, 0.63, 0.95)$ mm. The bias lines have a length of $0.35\,\mathrm{mm}$ each. The Tx is modelled as a THz current source with a current magnitude of $50\,\mu\mathrm{A}$. *Copyright © Springer Nature.*

$L = (0.01, 0.63, 0.95)$ mm. The Tx PIPED is modelled as a THz current source with a magnitude chosen to be $50\,\mu\mathrm{A}$, corresponding to the DC current generated in the PIPED, see Appendix E.1. The frequencies $f_{\mathrm{THz}} = (0.27, 0.24, 0.28)$ THz represent maxima of the transfer impedance magnitude $|Z_{21,\mathrm{sim}}|$ in Figure 5.4c-e. The field simulations exhibit standing wave patterns for the various lengths. We further find that the PIPED bias lines, which have a geometrical length of $0.35\,\mathrm{mm}$, influence the resonance frequencies of the transmission line. Thinner and longer bias lines could reduce this influence.

E.12 Conversion from S-parameters to Z-parameters

The complex transfer impedance $\underline{Z}_{21}$ of the THz resonator can be derived from numerically calculated S-parameters. To this end, we use the following relations [201]:

$$
\begin{aligned}
\underline{Z}_{11} &= Z_0 \frac{(1+\underline{S}_{11})(1-\underline{S}_{22})+\underline{S}_{12}\underline{S}_{21}}{(1-\underline{S}_{11})(1-\underline{S}_{22})-\underline{S}_{12}\underline{S}_{21}} \\
\underline{Z}_{12} &= Z_0 \frac{2\underline{S}_{12}}{(1-\underline{S}_{11})(1-\underline{S}_{22})-\underline{S}_{12}\underline{S}_{21}} \\
\underline{Z}_{21} &= Z_0 \frac{2\underline{S}_{21}}{(1-\underline{S}_{11})(1-\underline{S}_{22})-\underline{S}_{12}\underline{S}_{21}} \\
\underline{Z}_{22} &= Z_0 \frac{(1-\underline{S}_{11})(1+\underline{S}_{22})+\underline{S}_{12}\underline{S}_{21}}{(1-\underline{S}_{11})(1-\underline{S}_{22})-\underline{S}_{12}\underline{S}_{21}} .
\end{aligned}
\tag{E.43}
$$

E.13 Performance improvement

The emitted output power of the PIPED Tx system can be increased by connecting an array of parallel PIPEDs to the feed point of a single antenna or transmission line. This is enabled by the small footprint of an individual PIPED with a typical length of less than 1 µm, by the small capacitance of less than

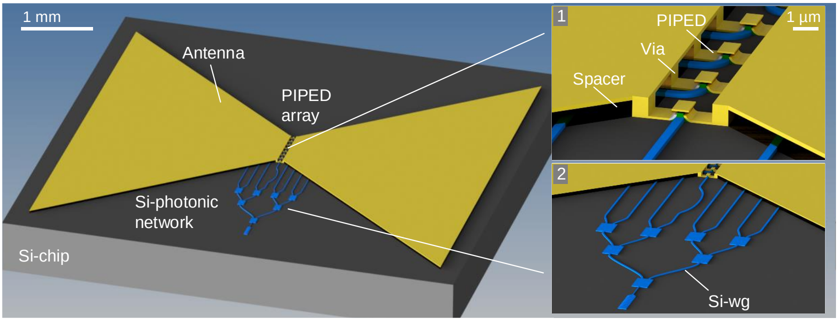

Figure E.13: Multi-PIPED antenna for improving the performance of T-wave Tx and Rx. The small PIPED length of roughly 1 µm, the small capacitance below 1 fF and the large resistance in excess of 10 kΩ allow to connect multiple PIPED to a common antenna feed point (**Inset 1**). For the Tx (Rx), the output power (power conversion factor) increases quadratically with the number of PIPED due to the coherent superposition of the individual currents. The PIPEDs are fed by a Si-photonic power distribution network (**Inset 2**). For efficient optical routing, the antenna is fabricated in a second metal layer, which is separated from the first metal layer and the optical waveguides by a thick dielectric spacer. The PIPEDs are connected to the antenna by a vertical interconnect access (‘Via’) between the first and the second metal layer. *Copyright © Springer Nature.*

1 fF, as well as the high impedance in excess of 10 kΩ, and by the ability to optically address a multitude of devices through on-chip silicon photonic feed networks. This concept is illustrated in Figure E.13. The PIPEDs (Inset 1) are fed by a Si-photonic feed network (Inset 2). The antenna is fabricated on a second metal layer with a spacer layer in-between to enable optical routing underneath the antenna. The PIPEDs are connected to the antenna by a vertical interconnect access (Via) between the first and the second metal layer. Exploiting the coherent superposition of the THz currents obtained from a parallel array of n PIPEDs allows to increase the Tx output power by a factor of n^2, provided that sufficient optical power is available. The same approach can be used at the receiver side, where the power conversion factor could be also increased by n^2 for an array of n devices. For a total of 10 PIPEDs, this would lead to a 20 dB increase both at the transmitter and the receiver.

[end of Methods and Supplementary Information of paper [J2]]

F. Bibliography

[1] "Cisco visual networking index: forecast and trends, 2017–2022," *CISCO White Pap.* (2019).

[2] T. Nagatsuma, G. Ducournau & C. C. Renaud, "Advances in terahertz communications accelerated by photonics," *Nat. Photonics* **10**, 371–379 (2016).

[3] S. S. Dhillon, *et al.*, "The 2017 terahertz science and technology roadmap," *J. Phys. D. Appl. Phys.* **50**, 043001 (2017).

[4] M. Tonouchi, "Cutting-edge terahertz technology," *Nat. Photonics* **1**, 97–105 (2007).

[5] J. G. Proakis & M. Salehi, "*Digital communications*" (McGraw-Hill, 2008).

[6] C. E. Shannon, "A mathematical theory of communication," *Bell Syst. Tech. J.* **27**, 379–423, 623–656 (1948).

[7] ITU, "Recommendation ITU-R P.676-11: Attenuation by atmospheric gases," (2016).

[8] ITU, "Recommendation ITU-R P.840-7: Attenuation due to clouds and fog," (2017).

[9] ITU, "Recommendation ITU-R P.838-3: Specific attenuation model for rain," (2005).

[10] ITU, "Recommendation ITU-R P.837-7: Characteristics of precipitation for propagation modelling," (2017).

[11] R. Mata Calvo, *et al.*, "Optical technologies for very high throughput satellite communications," in *Free-Space Laser Communications XXXI* 10910 (SPIE, 2019).

[12] K. Su, L. Moeller, R. B. Barat & J. F. Federici, "Experimental comparison of performance degradation from terahertz and infrared wireless links in fog," *J. Opt. Soc. Am. A* **29**, 179–184 (2012).

[13] M. A. Khalighi & M. Uysal, "Survey on free space optical communication: A communication theory perspective," *IEEE Commun. Surv. Tutorials* **16**, 2231–2258 (2014).

[14] F. Nadeem, *et al.*, "Weather effects on hybrid FSO/RF communication link," *IEEE J. Sel. Areas Commun.* **27**, 1687–1697 (2009).

[15] H. Kaushal & G. Kaddoum, "Optical communication in space: Challenges and mitigation techniques," *IEEE Commun. Surv. Tutorials* **19**, 57–96 (2017).

[16] J. Federici & L. Moeller, "Review of terahertz and subterahertz wireless communications," *J. Appl. Phys.* **107**, 111101 (2010).

[17] F. Nadeem, T. Javornik, E. Leitgeb, V. Kvicera & G. Kandus, "Continental fog attenuation empirical relationship from measured visibility data," *Radioengineering* **19**, 596–600 (2010).

[18] H. T. Friis, "A note on a simple transmission formula," in *Proceedings of the IRE* **34**, 254–256 (1946).

[19] G. Carpintero, *et al.*, "*Semiconductor terahertz technology: Devices and systems at room temperature operation*" (Wiley-IEEE Press, 2015).

[20] H. Song & T. Nagatsuma, "*Handbook of terahertz technologies: Devices and applications*" (Pan Stanford Publishing, 2015).

[21] K. Sengupta, T. Nagatsuma & D. M. Mittleman, "Terahertz integrated electronic and hybrid electronic–photonic systems," *Nat. Electron.* **1**, 622–635 (2018).

[22] A. Tessmann, *et al.*, "A broadband 220-320 GHz medium power amplifier module," in *2014 IEEE Compound Semiconductor Integrated Circuit Symposium* (IEEE, 2014).

[23] L. John, *et al.*, "A 280–310 GHz InAlAs/InGaAs mHEMT power amplifier MMIC with 6.7–8.3 dBm output power," *IEEE Microw. Wirel. Compon. Lett.* **29**, 143–145 (2019).

[24] A. B. Amado-Rey, *et al.*, "Analysis and development of submillimeter-wave stacked-FET power amplifier MMICs in 35-nm mHEMT technology," *IEEE Trans. Terahertz Sci. Technol.* **8**, 357–364 (2018).

[25] A. El Fatimy, *et al.*, "AlGaN/GaN high electron mobility transistors as a voltage-tunable room temperature terahertz sources," *J. Appl. Phys.* **107**, 024504 (2010).

[26] A. Lisauskas, *et al.*, "Terahertz emission from biased AlGaN/GaN high-electron-mobility transistors," *J. Appl. Phys.* **125**, 151614 (2019).

[27] K. Tae-Woo, J. A. del Alamo, K.-S. Seo, B. Brar & D.-H. Kim, "III–V high-electron-mobility transistors toward terahertz operation," in *Handbook of Terahertz Technologies* (2015).

[28] M. Urteaga, *et al.*, "130nm InP DHBTs with ft >0.52THz and fmax >1.1THz," *Device Res. Conf.* 281–282 (2011).

[29] M. Urteaga, Z. Griffith, M. Seo, J. Hacker & M. J. W. Rodwell, "InP HBT technologies for THz integrated circuits," *Proc. IEEE* **105**, 1051–1067 (2017).

[30] J. C. Rode, *et al.*, "Indium phosphide heterobipolar transistor technology beyond 1-THz bandwidth," *IEEE Trans. Electron Devices* **62**, 2779–2785 (2015).

[31] K. Kasagi, S. Suzuki & M. Asada, "Large-scale array of resonant-tunneling-diode terahertz oscillators for high output power at 1 THz," *J. Appl. Phys.* **125**, 151601 (2019).

[32] T. Maekawa, H. Kanaya, S. Suzuki & M. Asada, "Oscillation up to 1.92 THz in resonant tunneling diode by reduced conduction loss," *Appl. Phys. Express* **9**, 024101 (2016).

[33] M. Asada, S. Suzuki & N. Kishimoto, "Resonant tunneling diodes for sub-terahertz and terahertz oscillators," *Jpn. J. Appl. Phys.* **47**, 4375–4384 (2008).

[34] S. M. Sze & K. K. Ng, "*Physics of semiconductor devices*" (Wiley-Interscience, 2007).

[35] H. Eisele & R. Kamoua, "Submillimeter-wave InP Gunn devices," *IEEE Trans. Microw. Theory Tech.* **52**, 2371–2378 (2004).

[36] E. Bründermann, H.-W. Hübers & M. F. Kimmitt, "*Terahertz techniques*" **151**, (Springer Berlin Heidelberg, 2012).

[37] S. Preu, G. H. Döhler, S. Malzer, L. J. Wang & A. C. Gossard, "Tunable, continuous-wave terahertz photomixer sources and applications," *J. Appl. Phys.* **109**, 061301 (2011).

[38] A. D. J. F. Olvera, H. Lu, A. C. Gossard & S. Preu, "Continuous-wave 1550 nm operated terahertz system using ErAs:In(Al)GaAs photo-conductors with 52 dB dynamic range at 1 THz," *Opt. Express* **25**, 29492–29500 (2017).

[39] S. Koenig, *et al.*, "Wireless sub-THz communication system with high data rate," *Nat. Photonics* **7**, 977–981 (2013).

[40] Q. Wu & X. C. Zhang, "Ultrafast electro-optic field sensors," *Appl. Phys. Lett.* **68**, 1604–1606 (1996).

[41] S. Hisatake & T. Nagatsuma, "Nonpolarimetric technique for homodyne-type electrooptic field detection," *Appl. Phys. Express* **5**, 012701 (2012).

[42] D. Stanze, *et al.*, "Compact cw terahertz spectrometer pumped at 1.5 μm wavelength," *J. Infrared Millim. Terahertz Waves* **32**, 225–232 (2011).

[43] T. Nagatsuma, *et al.*, "Continuous-wave terahertz spectroscopy system based on photodiodes," *PIERS Online* **6**, 390–394 (2010).

[44] A. W. Mohammad, *et al.*, "5 Gbps wireless transmission link with an optically pumped uni-traveling carrier photodiode mixer at the receiver," *Opt. Express* **26**, 2884–2890 (2018).

[45] A. W. Mohammad, *et al.*, "60-GHz transmission link using uni-traveling carrier photodiodes at the transmitter and the receiver," *J. Lightwave Technol.* **36**, 4507–4513 (2018).

[46] X. Li, *et al.*, "1-Tb/s millimeter-wave signal wireless delivery at D-band," *J. Lightwave Technol.* **37**, 196–204 (2019).

[47] F. Boes, *et al.*, "Multi-gigabit E-band wireless data transmission," in *2015 IEEE MTT-S International Microwave Symposium (IMS)* (IEEE, 2015).

[48] I. Kallfass, *et al.*, "64 Gbit/s transmission over 850 m fixed wireless link at 240 GHz carrier frequency," *J. Infrared Millim. Terahertz Waves* **36**, 221–233 (2015).

[49] R. Puerta, S. Rommel, J. J. V. Olmos & I. T. Monroy, "Optically generated single side-band radio-over-fiber transmission of 60 Gbit/s over 50m at W-band," in *Optical Fiber Communication Conference (OFC)* M3E.4 (OSA, 2017).

[50] X. Li, *et al.*, "Delivery of 54-Gb/s 8QAM W-band signal and 32-Gb/s 16QAM K-band signal over 20-km SMF-28 and 2500-m wireless distance," *J. Lightwave Technol.* **36**, 50–56 (2018).

[51] T. Nagatsuma, *et al.*, "300-GHz-band wireless transmission at 50 Gbit/s over 100 meters," in *41st International Conference on Infrared, Millimeter, and Terahertz waves (IRMMW-THz)* 1–2 (IEEE, 2016).

[52] G. Ducournau, *et al.*, "Ultrawide-bandwidth single-channel 0.4-THz wireless link combining broadband quasi-optic photomixer and coherent detection," *IEEE Trans. Terahertz Sci. Technol.* **4**, 328–337 (2014).

[53] X. Li, J. Xiao & J. Yu, "Long-distance wireless mm-wave signal delivery at W-band," *J. Lightwave Technol.* **34**, 661–668 (2016).

[54] S. Jia, *et al.*, "Integrated dual-DFB laser for 408 GHz carrier generation enabling 131 Gbit/s wireless transmission over 10.7 meters," in *Optical Fiber Communication Conference (OFC)* Th1C.2 (OSA, 2019).

[55] R. Puerta, *et al.*, "Single-carrier dual-polarization 328-Gb/s wireless transmission in a D-band millimeter wave 2×2 MU-MIMO radio-over-fiber system," *J. Lightwave Technol.* **36**, 587–593 (2018).

[56] X. Pang, *et al.*, "260 Gbit/s photonic-wireless link in the THz band," in *IEEE Photonics Conference (IPC)* (IEEE, 2016).

[57] X. Li, *et al.*, "132-Gb/s photonics-aided single-carrier wireless terahertz-wave signal transmission at 450 GHz enabled by 64QAM modulation and probabilistic shaping," in *Optical Fiber Communication Conference (OFC)* M4F.4 (OSA, 2019).

[58] S. Jia, *et al.*, "0.4 THz photonic-wireless link with 106 Gb/s single channel bitrate," *J. Lightwave Technol.* **36**, 610–616 (2018).

[59] X. Li, *et al.*, "120 Gb/s wireless terahertz-wave signal delivery by 375 GHz-500 GHz multi-carrier in a 2×2 MIMO system," *J. Lightwave Technol.* **37**, 606–611 (2019).

[60] H. Shams, *et al.*, "100 Gb/s multicarrier THz wireless transmission system with high frequency stability based on a gain-switched laser comb source," *IEEE Photonics J.* **7**, 7902011 (2015).

[61] H. Hamada, *et al.*, "300-GHz, 100-Gb/s InP-HEMT wireless transceiver using a 300-GHz fundamental mixer," in *2018 IEEE/MTT-S International Microwave Symposium (IMS)* 1480–1483 (IEEE, 2018).

[62] K. Liu, *et al.*, "100 Gbit/s THz photonic wireless transmission in the 350-GHz band with extended reach," *IEEE Photonics Technol. Lett.* **30**, 1064–1067 (2018).

[63] T. Nagatsuma & G. Carpintero, "Recent progress and future prospect of photonics-enabled terahertz communications research," *IEICE Trans. Electron.* **E98.C**, 1060–1070 (2015).

[64] T. Nagatsuma, *et al.*, "Terahertz wireless communications based on photonics technologies," *Opt. Express* **21**, 23736–23747 (2013).

[65] N. Oshima, K. Hashimoto, S. Suzuki & M. Asada, "Wireless data transmission of 34 Gbit/s at a 500-GHz range using resonant-tunnelling-diode terahertz oscillator," *Electron. Lett.* **52**, 1897–1898 (2016).

[66] M. F. Hermelo, P.-T. (Boris) Shih, M. Steeg, A. Ng'oma & A. Stöhr, "Spectral efficient 64-QAM-OFDM terahertz communication link," *Opt. Express* **25**, 19360–19370 (2017).

[67] A. Mecozzi, C. Antonelli & M. Shtaif, "Kramers – Kronig coherent receiver," *Optica* **3**, 1220–1227 (2016).

[68] K. Zhong, *et al.*, "Digital signal processing for short-reach optical communications: A review of current technologies and future trends," *J. Lightwave Technol.* **36**, 377–400 (2018).

[69] X. Chen, *et al.*, "Kramers – Kronig receivers for 100-km datacenter interconnects," *J. Lightwave Technol.* **36**, 79–89 (2018).

[70] H. Voelcker, "Demodulation of single-sideband signals via envelope detection," *IEEE Trans. Commun.* **14**, 22–30 (1966).

[71] M. H. A. Kramers, "La diffusion de la lumière par les atomes," *Atti cong intern Fis.* **2**, 545–557 (1927).

[72] R. de L. Kronig, "On the theory of the dispersion of x-rays," *J. Opt. Soc. Am.* **12**, 547–557 (1926).

[73] J. Ma, *et al.*, "Security and eavesdropping in terahertz wireless links," *Nature* **563**, 89–93 (2018).

[74] T. Kawanishi, "THz and photonic seamless communications," *J. Lightwave Technol.* **37**, 1671–1679 (2019).

[75] A. J. Seeds, H. Shams, M. J. Fice & C. C. Renaud, "Terahertz photonics for wireless communications," *J. Lightwave Technol.* **33**, 579–587 (2015).

[76] X. Yu, *et al.*, "160 Gbit/s photonics wireless transmission in the 300-500 GHz band," *APL Photonics* **1**, 081301 (2016).

[77] J. Ma, R. Shrestha, L. Moeller & D. M. Mittleman, "Invited Article: Channel performance for indoor and outdoor terahertz wireless links," *APL Photonics* **3**, 051601 (2018).

[78] G. J. Schneider, J. A. Murakowski, C. A. Schuetz, S. Shi & D. W. Prather, "Radiofrequency signal-generation system with over seven octaves of continuous tuning," *Nat. Photonics* **7**, 118–122 (2013).

[79] G. Carpintero, *et al.*, "Wireless data transmission at terahertz carrier waves generated from a hybrid InP-polymer dual tunable DBR laser photonic integrated circuit," *Sci. Rep.* **8**, 3018 (2018).

[80] T. Harter, *et al.*, "110-m THz wireless transmission at 100 Gbit/s using a Kramers-Kronig schottky barrier diode receiver," in *European Conference on Optical Communication (ECOC)* (IEEE, 2018).

[81] T. S. Rappaport, *et al.*, "Millimeter wave mobile communications for 5G cellular: It will work!," *IEEE Access* **1**, 335–349 (2013).

[82] J. G. Andrews, *et al.*, "What will 5G be?," *IEEE J. Sel. Areas Commun.* **32**, 1065–1082 (2014).

[83] "ITU-R Report M.2410-0: Minimum requirements related to technical performance for IMT-2020 radio interface(s)," (2017).

[84] M. Latva-aho & K. Leppänen, "*Key drivers and research challenges for 6G ubiquitous wireless intelligence*" (2019).

[85] A. J. Lowery, T. Wang & B. Corcoran, "Clipping-enhanced Kramers-Kronig receivers," in *Optical Fiber Communications Conference and Exhibition (OFC)* M1H.2 (2019).

[86] H. Ito, T. Furuta, Y. Muramoto, T. Ito & T. Ishibashi, "Photonic millimetre- and sub-millimetre-wave generation using J-band rectangular-waveguide-output uni-travelling-carrier photodiode module," *Electron. Lett.* **42**, 1424–1425 (2006).

[87] Y. Shoji, K. Hamaguchi & H. Ogawa, "Millimeter-wave remote self-heterodyne system for extremely stable and low-cost broad-band signal transmission," *IEEE Trans. Microw. Theory Tech.* **50**, 1458–1468 (2002).

[88] R. Schmogrow, *et al.*, "Error vector magnitude as a performance measure for advanced modulation formats," *IEEE Photonics Technol. Lett.* **24**, 61–63 (2012).

[89] R. Schmogrow, *et al.*, "Corrections to “Error vector magnitude as a performance measure for advanced modulation formats” [61-63, 2012]," *IEEE Photonics Technol. Lett.* **24**, 2198 (2012).

[90] B. P. Smith, A. Farhood, A. Hunt, F. R. Kschischang & J. Lodge, "Staircase codes: FEC for 100 Gb/s OTN," *J. Lightwave Technol.* **30**, 110–117 (2012).

[91] Z. Li, *et al.*, "Digital linearization of direct-detection transceivers for spectrally efficient 100 Gb/s/λ WDM metro networking," *J. Lightwave Technol.* **36**, 27–36 (2018).

[92] Y. Cai, *et al.*, "FPGA investigation on error-floor performance of a concatenated staircase and Hamming code for 400G-ZR forward error correction," *J. Lightwave Technol.* **37**, 188–195 (2019).

[93] R.-J. R.-J. Essiambre, *et al.*, "Capacity limits of optical fiber networks," *J. Lightwave Technol.* **28**, 662–701 (2010).

[94] IEEE Standard 802.15.3d-2017, "IEEE Standard for High Data Rate Wireless Multi-Media Networks–Amendment 2: 100 Gb/s Wireless Switched Point-to-Point Physical Layer," (2017).

[95] I. F. Akyildiz, J. M. Jornet & C. Han, "Terahertz band: Next frontier for wireless communications," *Phys. Commun.* **12**, 16–32 (2014).

[96] A. Kanno, P. T. Dat, N. Yamamoto & T. Kawanishi, "Millimeter-wave radio-over-fiber network for linear cell systems," *J. Lightwave Technol.* **36**, 533–540 (2018).

[97] H.-J. Song & T. Nagatsuma, "Present and future of terahertz communications," *IEEE Trans. Terahertz Sci. Technol.* **1**, 256–263 (2011).

[98] G. Ducournau, *et al.*, "THz communications using photonics and electronic devices: the race to data-rate," *J. Infrared Millim. Terahertz Waves* **36**, 198–220 (2015).

[99] R. Waterhouse & D. Novak, "Realizing 5G: Microwave photonics for 5G mobile wireless systems," *IEEE Microw. Mag.* **16**, 84–92 (2015).

[100] D. Pérez, I. Gasulla & J. Capmany, "Toward programmable microwave photonics processors," *J. Lightwave Technol.* **36**, 519–532 (2018).

[101] T. Harter, *et al.*, "Silicon–plasmonic integrated circuits for terahertz signal generation and coherent detection," *Nat. Photonics* **12**, 625–633 (2018).

[102] T. Harter, *et al.*, "Wireless THz communications using optoelectronic techniques for signal generation and coherent reception," in *Conference on Lasers and Electro-Optics (CLEO)* SM3J.2 (OSA, 2017).

[103] T. Harter, *et al.*, "Wireless multi-subcarrier THz communications using mixing in a photoconductor for coherent reception," in *IEEE Photonics Conference (IPC)* 147–148 (IEEE, 2017).

[104] Y. Salamin, *et al.*, "Microwave plasmonic mixer in a transparent fibre–wireless link," *Nat. Photonics* **12**, 749–753 (2018).

[105] S. Ummethala, *et al.*, "THz-to-optical conversion in wireless communications using an ultra-broadband plasmonic modulator," *Nat. Photonics* **13**, 519–524 (2019).

[106] T. Göbel, *et al.*, "Telecom technology based continuous wave terahertz photomixing system with 105 decibel signal-to-noise ratio and 3.5 terahertz bandwidth," *Opt. Lett.* **38**, 4197–4199 (2013).

[107] A. Roggenbuck, *et al.*, "Coherent broadband continuous-wave terahertz spectroscopy on solid-state samples," *New J. Phys.* **12**, 043017 (2010).

[108] S. Nellen, B. Globisch, R. B. Kohlhaas, L. Liebermeister & M. Schell, "Recent progress of continuous-wave terahertz systems for spectroscopy, non-destructive testing, and telecommunication," in *Proceedings of SPIE* 105310C (2018).

[109] S. Verghese, *et al.*, "Generation and detection of coherent terahertz waves using two photomixers," *Appl. Phys. Lett.* **73**, 3824 (1998).

[110] D. Saeedkia & S. Safavi-Naeini, "Terahertz photonics: optoelectronic techniques for generation and detection of terahertz waves," *J. Lightwave Technol.* **26**, 2409–2423 (2008).

[111] Maxim Integrated, "PHY1097," Available at: https://datasheets.maximintegrated.com/en/ds/PHY1097.pdf. (Accessed: 3rd December 2018)

[112] M. R. Billah, *et al.*, "Hybrid integration of silicon photonics circuits and InP lasers by photonic wire bonding," *Optica* **5**, 876–883 (2018).

[113] J. Ma, N. J. Karl, S. Bretin, G. Ducournau & D. M. Mittleman, "Frequency-division multiplexer and demultiplexer for terahertz wireless links," *Nat. Commun.* **8**, 729 (2017).

[114] M. Yata, M. Fujita & T. Nagatsuma, "Photonic-crystal diplexers for terahertz-wave applications," *Opt. Express* **24**, 7835–7849 (2016).

[115] M. Giovanni & L. Frecassetti, "E-band and V-band - survey on status of worldwide regulation," *Eur. Telecommun. Stand. Institute, White Pap.* 1–40 (2015).

[116] A. de J. Fernandez Olvera, *et al.*, "International system of units (SI) traceable noise-equivalent power and responsivity characterization of continuous wave ErAs:InGaAs photoconductive terahertz detectors," *Photonics* **6**, 15 (2019).

[117] S. Muehlbrandt, *et al.*, "Silicon-plasmonic internal-photoemission detector for 40 Gbit/s data reception," *Optica* **3**, 741–747 (2016).

[118] H.-J. Song, "Packages for terahertz electronics," *Proc. IEEE* **105**, 1121–1138 (2017).

[119] Semtech, "Transimpedance amplifier GN1081," Available at: https://www.semtech.com/products/signal-integrity/transimpedance-amplifiers/gn1081. (Accessed: 30th November 2018)

[120] A. H. Atabaki, *et al.*, "Integrating photonics with silicon nanoelectronics for the next generation of systems on a chip," *Nature* **556**, 349–354 (2018).

[121] L. M. Augustin, *et al.*, "InP-based generic foundry platform for photonic integrated circuits," *IEEE J. Sel. Top. Quantum Electron.* **24**, 1–10 (2018).

[122] G. Carpintero, *et al.*, "Microwave photonic integrated circuits for millimeter-wave wireless communications," *J. Lightwave Technol.* **32**, 3495–3501 (2014).

[123] G. Ducournau, "Silicon photonics targets terahertz region," *Nat. Photonics* **12**, 574–575 (2018).

[124] J. Capmany & D. Novak, "Microwave photonics combines two worlds," *Nat. Photonics* **1**, 319–330 (2007).

[125] K. Krügener, *et al.*, "Terahertz meets sculptural and architectural art: Evaluation and conservation of stone objects with T-ray technology," *Sci. Rep.* **5**, 14842 (2015).

[126] A. Shalit, S. Ahmed, J. Savolainen & P. Hamm, "Terahertz echoes reveal the inhomogeneity of aqueous salt solutions," *Nat. Chem.* **9**, 273–278 (2016).

[127] S. Fan, Y. He, B. S. Ung & E. Pickwell-MacPherson, "The growth of biomedical terahertz research," *J. Phys. D. Appl. Phys.* **47**, 374009 (2014).

[128] R. I. Stantchev, *et al.*, "Noninvasive, near-field terahertz imaging of hidden objects using a single-pixel detector," *Sci. Adv.* **2**, e1600190 (2016).

[129] M. Naftaly, R. G. Clarke, D. A. Humphreys & N. M. Ridler, "Metrology state-of-the-art and challenges in broadband phase-sensitive terahertz measurements," *Proc. IEEE* **105**, 1151–1165 (2017).

[130] E. R. Brown, K. A. McIntosh, K. B. Nichols & C. L. Dennis, "Photomixing up to 3.8 THz in low-temperature-grown GaAs," *Appl. Phys. Lett.* **66**, 285–287 (1995).

[131] B. Sartorius, D. Stanze, T. Göbel, D. Schmidt & M. Schell, "Continuous wave terahertz systems based on 1.5 µm telecom technologies," *J. Infrared Millim. Terahertz Waves* **33**, 405–417 (2012).

[132] Y.-D. Hsieh, *et al.*, "Terahertz frequency-domain spectroscopy of low-pressure acetonitrile gas by a photomixing terahertz synthesizer referenced to dual optical frequency combs," *J. Infrared Millim. Terahertz Waves* **37**, 903–915 (2016).

[133] S. Hisatake, Y. Koda, R. Nakamura, N. Hamada & T. Nagatsuma, "Terahertz balanced self-heterodyne spectrometer with SNR-limited phase-measurement sensitivity," *Opt. Express* **23**, 26689–26695 (2015).

[134] T. Ishibashi, Y. Muramoto, T. Yoshimatsu & H. Ito, "Unitraveling-carrier photodiodes for terahertz applications," *IEEE J. Sel. Top. Quantum Electron.* **20**, 79–88 (2014).

[135] H.-J. Song, *et al.*, "Uni-travelling-carrier photodiode module generating 300 GHz power greater than 1 mW," *IEEE Microw. Wirel. Compon. Lett.* **22**, 363–365 (2012).

[136] A. Beling, X. Xie & J. C. Campbell, "High-power, high-linearity photodiodes," *Optica* **3**, 328–338 (2016).

[137] C. W. Berry, *et al.*, "High power terahertz generation using 1550 nm plasmonic photomixers," *Appl. Phys. Lett.* **105**, 011121 (2014).

[138] D. Thomson, *et al.*, "Roadmap on silicon photonics," *J. Opt.* **18**, 073003 (2016).

[139] L. Vivien & L. Pavesi, "*Handbook of silicon photonics*" (Taylor & Francis, 2013).

[140] W. Bogaerts, *et al.*, "Nanophotonic waveguides in silicon-on-insulator fabricated with CMOS technology," *J. Lightwave Technol.* **23**, 401–412 (2005).

[141] T. Harter, *et al.*, "Silicon-plasmonic photomixer for generation and homodyne reception of continuous-wave THz radiation," in *Conference on Lasers and Electro-Optics (CLEO)* SM4E.5 (OSA, 2016).

[142] J. Pfeifle, L. Alloatti, W. Freude, J. Leuthold & C. Koos, "Silicon-organic hybrid phase shifter based on a slot waveguide with a liquid-crystal cladding," *Opt. Express* **20**, 15359–15376 (2012).

[143] N. C. Harris, *et al.*, "Efficient, compact and low loss thermo-optic phase shifter in silicon," *Opt. Express* **22**, 10487–10493 (2014).

[144] J.-Y. Kim, *et al.*, "Compact and stable THz vector spectroscopy using silicon photonics technology.," *Opt. Express* **22**, 7178–7185 (2014).

[145] G. T. Reed, G. Mashanovich, F. Y. Gardes & D. J. Thomson, "Silicon optical modulators," *Nat. Photonics* **4**, 518–526 (2010).

[146] C. Koos, *et al.*, "Silicon-organic hybrid (SOH) and plasmonic-organic hybrid (POH) integration," *J. Lightwave Technol.* **34**, 256–268 (2016).

[147] T. Hiraki, *et al.*, "Heterogeneously integrated III–V/Si MOS capacitor Mach–Zehnder modulator," *Nat. Photonics* **11**, 482–485 (2017).

[148] E. Timurdogan, *et al.*, "An ultralow power athermal silicon modulator," *Nat. Commun.* **5**, 4008 (2014).

[149] R. Quay, *et al.*, "High-power microwave GaN/AlGaN HEMTs and MMICs on SiC and silicon substrates for modern radio communication," *Phys. status solidi* **215**, 1700655 (2018).

[150] G. V. Naik, V. M. Shalaev & A. Boltasseva, "Alternative plasmonic materials: Beyond gold and silver," *Adv. Mater.* **25**, 3264–3294 (2013).

[151] C. Canali, G. Majni, R. Minder & G. Ottaviani, "Electron and hole drift velocity measurements in silicon and their empirical relation to electric field and temperature," *IEEE Trans. Electron Devices* **22**, 1045–1047 (1975).

[152] C. C. Renaud, *et al.*, "Antenna integrated THz uni-traveling carrier photodiodes," *IEEE J. Sel. Top. Quantum Electron.* **24**, 8500111 (2018).

[153] P. Latzel, *et al.*, "Generation of mW Level in the 300-GHz band using resonant-cavity-enhanced unitraveling carrier photodiodes," *IEEE Trans. Terahertz Sci. Technol.* **7**, 800–807 (2017).

[154] E. Rouvalis, M. J. Fice, C. C. Renaud & A. J. Seeds, "Millimeter-wave optoelectronic mixers based on uni-traveling carrier photodiodes," *IEEE Trans. Microw. Theory Tech.* **60**, 686–691 (2012).

[155] S. Hisatake, J.-Y. Kim, K. Ajito & T. Nagatsuma, "Self-heterodyne spectrometer using uni-traveling-carrier photodiodes for terahertz-wave generators and optoelectronic mixers," *J. Lightwave Technol.* **32**, 3683–3689 (2014).

[156] G. G. Hernandez-Cardoso, *et al.*, "Terahertz imaging for early screening of diabetic foot syndrome: A proof of concept," *Sci. Rep.* **7**, 42124 (2017).

[157] H. Cheon, J. H. Paik, M. Choi, H.-J. Yang & J.-H. Son, "Detection and manipulation of methylation in blood cancer DNA using terahertz radiation," *Sci. Rep.* **9**, 6413 (2019).

[158] "IEEE standard for definitions of terms for antennas," in *IEEE Std 145-2013 (Revision of IEEE Std 145-1993)* 1–50 (IEEE, 2014).

[159] J. L. Pawsey & R. N. Bracewell, "*Radio astronomy*" (Oxford University Press, 1955).

[160] T. L. Wilson, K. Rohlfs & H. Susanne, "*Tools of radio astronomy*" (Springer, 2008).

[161] H. Ito, *et al.*, "High-speed and high-output InP-InGaAs unitraveling-carrier photodiodes," *IEEE J. Sel. Top. Quantum Electron.* **10**, 709–727 (2004).

[162] T. Ishibashi, T. Furuta, H. Fushimi & H. Ito, "Photoresponse characteristics of uni-traveling-carrier photodiodes," in *Physics and Simulation of Optoelectronic Devices IX* **4283**, 469–479 (2001).

[163] T. Ishibashi, *et al.*, "Uni-traveling-carrier photodiodes," in *Ultrafast Electronics and Optoelectronics* **13**, UC3 (OSA, 1997).

[164] J.-M. Wun, *et al.*, "Photonic high-power continuous wave THz-wave generation by using flip-chip packaged uni-traveling carrier photodiodes and a femtosecond optical pulse generator," *J. Lightwave Technol.* **34**, 1387–1397 (2016).

[165] H. T. Chen, *et al.*, "High-responsivity low-voltage 28-Gb/s Ge p-i-n photodetector with silicon contacts," *J. Lightwave Technol.* **33**, 820–824 (2015).

[166] L. Vivien, *et al.*, "42 GHz p.i.n Germanium photodetector integrated in a silicon-on-insulator waveguide.," *Opt. Express* **17**, 6252–7 (2009).

[167] D.-H. Jun, J.-H. Jang, I. Adesida & J.-I. Song, "Improved efficiency-bandwidth product of modified uni-traveling carrier photodiode structures using an undoped photo-absorption layer," *Jpn. J. Appl. Phys.* **45**, 3475–3478 (2006).

[168] Xin Wang, Ning Duan, Hao Chen & J. C. Campbell, "InGaAs–InP photodiodes with high responsivity and high saturation power," *IEEE Photonics Technol. Lett.* **19**, 1272–1274 (2007).

[169] J. Hesler, K. Hui & T. Crowe, "Ultrafast millimeter wave and THz envelope detectors for wireless communications," *2012 IEEE Int. Top. Meet. Microw. Photonics* 93–94 (2012).

[170] J. L. Hesler & T. W. Crowe, "NEP and responsivity of THz zero-bias Schottky diode detectors," in *2007 Joint 32nd International Conference on Infrared and Millimeter Waves and the 15th International Conference on Terahertz Electronics* 844–845 (IEEE, 2007).

[171] A. Tessmann, *et al.*, "High-gain submillimeter-wave mHEMT amplifier MMICs," in *IEEE MTT-S International Microwave Symposium (IMS)* 53–56 (IEEE, 2010).

[172] J. S. Toll, "Causality and the dispersion relation: logical foundations," *Phys. Rev.* **104**, 1760–1770 (1956).

[173] C. Füllner, *et al.*, "Complexity analysis of the Kramers–Kronig receiver," *J. Lightwave Technol.* **37**, 4295–4307 (2019).

[174] Z. Li, *et al.*, "Joint Optimisation of Resampling Rate and Carrier-to-Signal Power Ratio in Direct-Detection Kramers-Kronig Receivers," in *European Conference on Optical Communication (ECOC)* W2D.3 (2017).

[175] S. J. Savory, "Digital coherent optical receivers: Algorithms and subsystems," *IEEE J. Sel. Top. Quantum Electron.* **16**, 1164–1179 (2010).

[176] C. W. Farrow, "A continuously variable digital delay element," in *1988 IEEE International Symposium on Circuits and Systems* 2641–2645 (IEEE, 1988).

[177] D. N. Godard, "Self-recovering equalization and carrier tracking in two-dimensional data communication system," *IEEE Trans. Commun.* **28**, 1867–1875 (1980).

[178] T. Pfau & S. Hoffmann, "Hardware-efficient coherent digital receiver concept with feedforward carrier recovery for M-QAM constellations," *J. Lightwave Technol.* **27**, 989–999 (2009).

[179] S. Randel, *et al.*, "All-electronic flexibly programmable 864-Gb/s single-carrier PDM-64-QAM," in *Conference on Optical Fiber Communication (OFC)* Th5C.8 (2014).

[180] S. Faruk & S. J. Savory, "Digital signal processing for coherent transceivers employing multilevel formats," *J. Lightwave Technol.* **35**, 1125–1141 (2017).

[181] T. Bo & H. Kim, "Kramers-Kronig receiver operable without digital upsampling," *Opt. Express* **26**, 13810–13818 (2018).

[182] A. Mecozzi, C. Antonelli & M. Shtaif, "Kramers–Kronig receivers," *Adv. Opt. Photonics* **11**, 480–517 (2019).

[183] W. Freude, *et al.*, "Quality metrics for optical signals: Eye diagram, Q-factor, OSNR, EVM and BER," *14th Int. Conf. Transparent Opt. Networks* 1–4 (2012).

[184] X. Chen, S. Chandrasekhar, S. Olsson, A. Adamiecki & P. Winzer, "Impact of O/E Front-End Frequency Response on Kramers-Kronig Receivers and its Compensation," in *European Conference on Optical Communication (ECOC)* (2018).

[185] O. Strobel, "*Optical and Microwave Technologies for Telecommunication Networks*" (John Wiley & Sons, 2016).

[186] R. W. Gerchberg & W. O. Saxton, "A practical algorithm for the determination of phase from image and diffraction plane pictures," *Optik (Stuttg).* **35**, 237–246 (1972).

[187] J. R. Fienup, "Phase retrieval algorithms: a comparison," *Appl. Opt.* **21**, 2758 (1982).

[188] D. J. Kane, "Real-time measurement of ultrashort laser pulses using principal component generalized projections," *IEEE J. Sel. Top. Quantum Electron.* **4**, 278–284 (1998).

[189] T. F. Quatieri & A. V. Oppenheim, "Iterative techniques for minimum phase signal reconstruction from phase or magnitude," *IEEE Trans. Acoust.* **29**, 1187–1193 (1981).

[190] Y. Baek, K. Lee, S. Shin & Y. Park, "Kramers–Kronig holographic imaging for high-space-bandwidth product," *Optica* **6**, 45 (2019).

[191] N. Lindenmann, *et al.*, "Connecting silicon photonic circuits to multicore fibers by photonic wire bonding," *J. Lightwave Technol.* **33**, 755–760 (2015).

[192] D. Stanze, T. Göbel, R. J. B. Dietz, B. Sartorius & M. Schell, "High-speed coherent CW terahertz spectrometer," *Electron. Lett.* **47**, 1292–1294 (2011).

[193] T. Göbel, *et al.*, "Single-sampling-point coherent detection in continuous-wave photomixing terahertz systems," *Electron. Lett.* **45**, 65–66 (2009).

[194] H. Badaoui, Y. Frignac, P. Ramantanis, B. E. Benkelfat & M. Feham, "De Bruijn pseudo random sequences analysis for modeling of quaternary modulation formats," *J. Comput. Sci.* **7**, 35–38 (2010).

[195] C. W. Berry, N. Wang, M. R. Hashemi, M. Unlu & M. Jarrahi, "Significant performance enhancement in photoconductive terahertz optoelectronics by incorporating plasmonic contact electrodes," *Nat. Commun.* **4**, 1622 (2013).

[196] R. J. B. Dietz, *et al.*, "Influence and adjustment of carrier lifetimes in InGaAs/InAlAs photoconductive pulsed terahertz detectors: 6 THz bandwidth and 90dB dynamic range," *Opt. Express* **22**, 19411–19422 (2014).

[197] F. Van Dijk, *et al.*, "Integrated InP heterodyne millimeter wave transmitter," *IEEE Photonics Technol. Lett.* **26**, 965–968 (2014).

[198] L. Ponnampalam, *et al.*, "Monolithically integrated photonic heterodyne system," *J. Lightwave Technol.* **29**, 2229–2234 (2011).

[199] T. Vallaitis, *et al.*, "Optical properties of highly nonlinear silicon-organic hybrid (SOH) waveguide geometries," *Opt. Express* **17**, 17357–17368 (2009).

[200] "CST® STUDIO SUITE® 2017, Release version 2017.05 - Aug 04 2017, User’s handbook,"

[201] D. M. Pozar, "*Microwave Engineering*" (John Wiley & Sons, 2011).

[202] N. Lindenmann, *et al.*, "Photonic wire bonding: a novel concept for chip-scale interconnects.," *Opt. Express* **20**, 17667–17677 (2012).

G. Glossary

G.1 List of abbreviations

2PAM	2-state pulse amplitude modulation
16QAM	16-state quadrature amplitude modulation
5G	5th-Generation
AC	Alternating current
ADC	Analog-to-digital converter
ASE	Amplified spontaneous emission
Att.	Attenuator
Au	Gold
AWG	Arbitrary-waveform generator
AWGN	Additive white Gaussian noise
BER	Bit error ratio
BP	Bandpass
BPF	Bandpass filter
Cal.	Calorimeter
CB	Conduction band
CMA	Constant-modulus algorithm
CMOS	Complementary metal-oxide-semiconductor
CSPR	Carrier-to-signal power ratio
c.w.	Continuous-wave

DAC	Digital-to-analog converter
DC	Direct current
DFB	Distributed feedback
DSP	Digital signal processing
EDFA	Erbium-doped fibre amplifier
EO	Electro-optic
ESA	Electrical spectrum analyzer
EVM	Error vector magnitude
FEC	Forward error correction
FFE	Feed-forward equalizer
FPGA	Field-programmable gate arrays
FSO	Free-space optical
FSPL	Free-space path loss
FT	Fourier transform
GC	Grating couplers
HA	Horn antenna
HBT	Heterojunction bipolar transistor
HBVs	Heterostructure barrier varactors
IF	Intermediate-frequency
IMPATT	Impact ionization avalanche transit-time
Inverse FT	Inverse Fourier Transform
IQ	In-phase/quadrature phase
KK	Kramers-Kronig

LIA	Lock-in amplifier
LNA	Low-noise amplifier
LO	Local oscillator
LP	Low-pass
mHEMT	Metamorphic high-electron-mobility transistor
MIMO	Multiple-input-multiple-output
MMIC	Millimetre-wave integrated circuit
MPA	Medium-power amplifier
NDC	Negative differential conductance
O/T	optical-to-T-wave
OOK	On-off keying
OSA	Optical spectrum analyser
Osc.	Oscilloscope
PC	Photoconductor
PCB	Printed circuit board
PAPR	Peak-to-average power ratio
pdf	Probability density function
PIPED	Plasmonic internal-photoemission detector
Pol.	Polarizer
Pol. contr.	polarization controller
PTFE	Polytetrafluoroethylene
QPSK	Quadrature phase shift keying
RBW	Resolution bandwidth

RMS	Root mean square
RTD	Resonant tunneling diode
Rx	Receiver
SBD	Schottky-barrier diode
SEM	Scanning electron microscopy
Si	Silicon
SISO	Single-input-single-output
SNR	Signal-to-noise power ratio
SOI	Silicon-on-insulator
SPP	Surface plasmon polariton
SSBI	Signal-signal beat interference
T/E	T-wave-to-electronic
THz	Terahertz
Ti	Titanium
TIA	Transimpedance amplifier
TUNNETT	Tunneling transit-time
Tx	Transmitter
UTC-PD	Uni-travelling-carrier photodiode
VB	Valance band
Via	Vertical interconnect access
VNA	Vector network analyze
VOA	Variable optical attenuator
WG	Waveguide

G.2 List of mathematical symbols

Greek symbols

ξ	Constant scaling factor
$\varphi(t), \Phi(t)$	Real-valued phase
Γ	Conversion factor
η	Conversion efficiency
λ	Wavelength
ω	Angular frequency

Latin symbols

$A(t)$	Real-valued amplitude of $\underline{s}(t)$
A	Effective area antenna aperture
$\underline{a}_k$	Complex valued symbol
$a_{k,\mathrm{I}}$	Real part of complex valued symbol $\underline{a}_k$
$a_{k,\mathrm{Q}}$	Imaginary part of complex valued symbol $\underline{a}_k$
a_n	Coefficients of Taylor expansion
B	Signal bandwidth
$B_f(f,T)$	Spectral black-body radiance
$\mathcal{C}$	Channel capacity
C	Capacitance
c	Speed of light in vacuum
CSPR	Carrier-to-signal power ratio

D	Antenna directivity
d	Distance
$E(t)$	Electric field
f	Frequency
f_{max}	Maximum oscillation frequency of transistors
FSPL	Free-space path loss
$\tilde{g}$	Input-output characteristic of an ideal, instantaneous nonlinear element
g	Input-output characteristic of SBD
G_{A} , G_{Tx} , G_{Rx}	Antenna gain
$G(t)$	Photoconductor conductivity
$\mathcal{G}$	Sensitivity of the photoconductor
$I(t), i(t)$	Current
$i_{\mathrm{I}}(t)$	Output of in-phase mixer
$i_{\mathrm{Q}}(t)$	Output of quadrature phase mixer
j	Imaginary unit
L_{a}	Atmospheric loss
ℓ	Length of PIPED
M	Number of symbols of an alphabet
N_0	Noise power density
P_{s}, P_{n}	Signal power, noise power
P_{Tx}, P_{Rx}	Power at the transmitter, power at the receiver
P_{THz}	Terahertz power

$\mathcal{P}$	Cauchy principle value
$p(t)$	Pulse shape
$\Re\{.\}$	Real part
R_b	Bit rate
R_s	Symbol rate
R	Resistance
S	Sensitivity
$\underline{s}(t)$	Complex baseband signal
$s_\mathrm{I}(t)$	Real part of complex baseband signal $\underline{s}(t)$
$s_\mathrm{Q}(t)$	Imaginary part of complex baseband signal $\underline{s}(t)$
t	Time
T_s	Symbol duration
$U(t)$	Real valued voltage
U_0	Constant voltage
$\underline{U}(t)$	Complex envelope
$\lvert\underline{U}_\mathrm{R}\rvert$	Reconstructed THz voltage amplitude
$\underline{U}_\mathrm{s}(t)$	Analytic data signal
$u_\mathrm{THz}(t)$	Terahertz voltage signal
W	Energy
$\underline{Z}$	Complex impedance

Danksagung

Diese Dissertation entstand während meiner Zeit am Institut für Photonik und Quantenelektronik (IPQ) und am Institut für Mikrostrukturtechnik (IMT) am Karlsruher Institut für Technologie. An dieser Stelle bedanke ich mich bei allen Personen, durch deren Unterstützung diese Arbeit ermöglicht wurde.

Besonders bedanken möchte ich mich bei meinem Doktorvater, Prof. Christian Koos, für das in mich gesetzte Vertrauen und die ausgezeichnete Betreuung meiner Arbeit. Seine schnelle Auffassungsgabe und die Fähigkeit komplizierte Dinge einfach zu erklären fasziniert mich und gab mir immer wieder neue Denkanstöße für meine eigene Arbeit. Seine zahlreichen Ideen und seine Begeisterung für das Thema haben stark zum Erfolg dieser Arbeit beigetragen. Ebenso großer Dank gebührt Prof. Wolfgang Freude unter anderem für die zahlreichen, offenen und fruchtbaren Diskussionen, die maßgeblich zum Gelingen dieser Arbeit beigetragen haben. Professor Guillermo Carpintero-del-Barrio danke ich herzlich für die freundliche Betreuung als Korreferent. Auch Prof. Sebastian Randel unterstützte meine Arbeit vor allem durch seine fundierten Kenntnisse in der digitalen Signalverarbeitung – vielen Dank hierfür.

Ein weiterer Dank gilt unseren Kooperationspartnern Simon Nellen, Björn Globisch vom Fraunhofer-Institut für Nachrichtentechnik, Heinrich-Hertz-Institut (HHI), sowie Axel Tessmann und Martin Walther vom Fraunhofer-Institut für Angewandte Festkörperphysik (IAF). Danke an Prof. Thomas Zwick, Florian Boes und Andreas Lipp vom Institut für Hochfrequenztechnik und Elektronik (IHE) für die Hilfe beim Aufbau und der Vermessung unserer Demonstratoren und an Erik Bründermann, Johannes L. Steinmann und Miriam Brosi vom Institut für Beschleunigerphysik und Technologie (IBPT) für die Unterstützung bei den Messungen mit dem Hüllkurvendetektor. Ebenso wertvoll waren die Diskussionen mit Jeffrey L. Hesler über den Hüllkurvendetektor.

Viele in dieser Arbeit gezeigten experimentellen Demonstrationen verwenden die UTC-PD von NTT-NEL als Transmitter. Für die großzügige Leihgabe möchte ich mich an dieser Stelle herzlich bedanken. Die Arbeit wurde finanziell sowie durch lehrreiche Seminare durch die Helmholtz International Research School for Teratronics (HIRST) unterstützt. Vielen Dank an Prof. Alexey Ustinov, der meine Arbeit innerhalb der HIRST betreut hat. Die Arbeit war eingebunden in das EU-Projekt Terashape und in das DFG-Projekt GOSPEL.

Ganz herzlich möchte ich mich bei meinen Kollegen bedanken, die meine Promotionszeit besonders geprägt haben und mit denen ich eine großartige Zeit verbringen konnte. Allen voran Sascha Mühlbrandt und Sandeep Ummethala, die mich bereits in meiner Masterarbeit betreut haben und von denen ich nicht nur fachlich sehr viel lernen konnte. Außerdem danke ich meinen Kollegen Clemens Kieninger und Heiner Zwickel für die bereichernden Diskussionen, die ich seit unserer gemeinsamen Zeit der Masterarbeit sehr schätze. Die Zusammenarbeit mit meinen Kollegen Muhammad Billah, Matthias Blaicher, Philipp Dietrich, Carsten Eschenbaum, Dengyang Fang, Christoph Füllner, Denis Ganin, Tilahun Gutema, Wladislaw Hartmann, Tobias Hoose, Adib Hossain, Juned Kemal, Daria Kohler, Kira Köhnle, Alexander Kotz, Yasar Kutuvantavida, Matthias Lauermann, Salek Mahmud, Pascal Maier, Pablo Marin, Argishti Melikyan, Johannes Milvich, Aleksandar Nesic, Jörg Pfeifle, Norbert Schneider, Simon Schneider, Stefan Singer, Mareike Trappen, Philipp Trocha, Claudius Weimann, Stefan Wolf, Sentayehu Wondimu und Yilin Xu hat mir enorm viel Spass bereitet und ich konnte viel von euch lernen. Es war die beste Gruppe die man sich wünschen konnte. Vielen Dank für die super Zeit und jede einzelne Kaffeepause.

Sehr herzlich bedanke ich mich bei Tatiana Gassmann, Maria-Luise Koch, Bernadette Lehmann und Andrea Riemensperger für die administrative Hilfe. Danke auch an unser Techniker-team David Guder, Steffen Herzog, Marco Hummel, Lisa Nolte, Steffen Pfeifer, Oswald Speck und Martin Winkeler für die Unterstützung beim Aufbau unserer Experimente.

Herzlichen Dank auch an Aritrio Bandyopadhyay, Christoph Füllner, Adib Hossain, Alexander Kotz, Christian Kriso, Marco Merboldt, Alexander Schmid und Marco Weber, deren Abschlussarbeiten ich betreuen durfte, und die wesentlich zum Erfolg dieser Dissertation beigetragen haben.

Tausend Dank an meine Eltern Helga und Karl, meine Großeltern sowie an meine Geschwister Daniel, Michael, Markus, Timo, Sara und Annabell. Danke, dass ihr immer hinter mir steht und mich in Allem unterstützt.

Besonders bedanken möchte ich mich bei Mariann, für ihre Liebe, ihr Verständnis und ihren mentalen Beistand bei dieser Arbeit.

List of publications

Journal publications

[J1] Muehlbrandt, S.; Melikyan, A.; **Harter, T.**; Koehnle, K.; Muslija, A.; Vincze, P.; Wolf, S.; Jakobs, P. -J.; Fedoryshyn, Y.; Freude, W.; Leuthold, J.; Koos, C.; Kohl, M., "Silicon-plasmonic internal-photoemission detector for 40 Gbit/s data reception," *Optica* **3**, 741-747 (2016), DOI: 10.1364/OPTICA.3.000741

[J2] **Harter, T.**; Muehlbrandt, S.; Ummethala, S.; Schmid, A.; Nellen, S.; Hahn, L.; Freude, W.; Koos, C., "Silicon–plasmonic integrated circuits for terahertz signal generation and coherent detection," *Nature Photonics* **12**, 625-633 (2018), DOI: 10.1038/s41566-018-0237-x

[J3] **Harter, T.**; Ummethala, S.; Blaicher, M.; Muehlbrandt, S.; Wolf, S.; Weber, M.; Adib, M.M.H.; Kemal, J. N.; Merboldt, M.; Boes, F.; Nellen, S.; Tessmann, A.; Walther, M.; Globisch, B.; Zwick, T.; Freude, W.; Randel, S.; Koos, C. "Wireless THz link with optoelectronic transmitter and receiver," *Optica* **6**, 1063-1070 (2019), DOI: 10.1364/OPTICA.6.001063

[J4] **Harter, T.**; Füllner, C.; Kemal, J. N.; Ummethala, S.; Steinmann, J. L.; Brosi, M.; Hesler, J. L.; Bründermann E.; Müller, A.-S.; Freude, W.; Randel, S., Koos, C., "Generalized Kramers-Kronig Receiver for Coherent THz Communications," *Nature Photonics **14**, 601-606* (2020), DOI: 10.1038/s41566-020-0675-0

[J5] Ummethala, S.; **Harter, T.**; Koehnle, K.; Li, Z.; Muehlbrandt, S.; Kutuvantavida, Y.; Kemal, J.; Marin-Palomo, P.; Schaefer, J.; Tessmann, A.; Garlapati, S. K.; Bacher, A.; Hahn, L.; Walther, M.; Zwick, T.; Randel, S.; Freude, W.; Koos, C., "THz-to-optical conversion in wireless communications using an ultra-broadband plasmonic modulator, " *Nature Photonics* **13**, 519-524 (2019), DOI: 10.1038/s41566-019-0475-6

Conference publications

[C1] Muehlbrandt, S.; Melikyan, A.; Koehnle, K.; **Harter, T.**; Muslija, A.; Vincze, P.; Wolf, S.; Jakobs, P. -J.; Fedoryshyn, Y.; Freude, W.; Leuthold, J.; Koos, C.; Kohl, M., "Plasmonic Internal Photoemission Detectors with Responsivities above 0.12 A/W," *Conf. on Lasers and Electro-Optics (CLEO'15), San Jose (CA), USA, May 10-15*, paper FTh3E.3 (2015), DOI: 10.1364/CLEO_QELS.2015.FTh3E.3

[C2] **Harter, T.**; Muehlbrandt, S.; Ummethala, S.; Schmid, A.; Bacher, A.; Hahn, L.; Kohl, M.; Freude, W.; Koos, C., "Silicon-Plasmonic Photomixer for Generation and Homodyne Reception of Continuous-Wave THz Radiation," *Conf. on Lasers and Electro-Optics (CLEO'16), San Jose (CA), USA, June 5-10* , paper SM4E.5 (2016), DOI: 10.1364/CLEO_SI.2016.SM4E.5

[C3] Koos, C.; Freude, W.; Leuthold, J.; Dalton, L. R.; Wolf, S.; Muehlbrandt, S.; Melikyan, A.; Zwickel, H.; Kutuvantavida, Y.; **Harter, T.**; Lauermann, M.; Elder, D. L., "Nanophotonic modulators and photodetectors using silicon photonic and plasmonic device concepts," *SPIE Physics and Simulation of Optoelectronic Devices XXV (OPTO-SPIE'17), San Francisco (CA), USA, Jan. 28-Feb. 2*, paper 10098-6 (2017), DOI: 10.1117/12.2256536

[C4] **Harter, T.**; Weber, M.; Muehlbrandt, S.; Wolf, S.; Kemal, J. N.; Boes, F.; Nellen, S.; Goebel, T.; Giesekus, J.; Zwick, T.; Randel, S.; Freude, W.; Koos, C., "Wireless THz Communications Using Optoelectronic Techniques for Signal Generation and Coherent Reception," *Conf. on Lasers and Electro-Optics (CLEO'17), San Jose (CA), USA, May 14-19*, paper SM3J.2 (2017), DOI: 10.1364/CLEO_SI.2017.SM3J.2

[C5] Freude, W.; Muehlbrandt, S.; **Harter, T**.; Melikyan, A.; Koehnle, K.; Muslija, A.; Vincze, P.; Wolf, S.; Jakobs, P. -J.; Fedoryshyn, Y.; Leuthold, J.; Kohl, M.; Zwick, T.; Randel, S.; Koos, C., "PIPED: A silicon-plasmonic high-speed photodetector," *19th Intern. Conf. on Transparent Optical Networks (ICTON'17), Girona, Spain, July 2-6*, paper Mo.D4.1 (2017), DOI: 10.1109/ICTON.2017.8024803

[C6] Koos, C.; Freude, W.; Guber, A. E.; Schimmel, T.; Lauermann, M.; Schneider, S.; Weimann, C.; Muehlbrandt, S.; **Harter, T.**; Wondimu, S. F.; Wienhold, T.; von der Ecken, S.; Dietrich, P.-I.; Goering, G., ”Photonic Integration for Metrology and Sensing,” *OSA Integrated Photonics Research, Silicon, and Nano- Photonics (IPR), New Orleans, Louisiana, USA, 24-27 July*, paper ITh1A.1 (2017), DOI: 10.1364/IPRSN.2017.ITh1A.1

[C7] **Harter, T.**; Adib, M.; Wolf, S.; Muehlbrandt, S.; Weber, M.; Blaicher, M.; Boes, F.; Massler, H.; Tessmann, A.; Nellen, S.; Goebel, T.; Giesekus, J.; Walther, M.; Zwick, T.; Freude, W.; Randel, S.; Koos, C., “Wireless Multi-Subcarrier THz Communications Using Mixing in a Photoconductor for Coherent Reception,” *IEEE Photonics Conference (IPC2017), Orlando, Florida, USA, 1-5 October* , paper MA4.2 (2017), DOI: 10.1109/IPCon.2017.8116044

[C8] Ummethala, S.; **Harter, T.**; Koehnle, K.; Muehlbrandt, S.; Kutuvantavida, Y.; Kemal, J. N.; Schaefer, J.; Massler, H.; Tessmann, A.; Kumar Garlapati, S.; Bacher, A.; Hahn, L.; Walther, M.; Zwick, T.; Randel, S.; Freude, W.; Koos, C., “Terahertz-to-Optical Conversion Using a Plasmonic Modulator,” *Conf. on Lasers and Electro-Optics (CLEO'18), San Jose (CA), USA, May 13–18* , paper STu3D.4 (2018), DOI: 10.1364/CLEO_SI.2018.STu3D.4

[C9] Freude, W.; **Harter, T**.; Ummethala, S.; Muehlbrandt, S.; Blaicher, M.; Wolf, S.; Weber, M.; Boes, F.; Massler, H.; Tessmann, A.; Kutuvantavida, Y.; Kemal, J. N.; Nellen, S.; Hahn, L.; Goebel, T.; Walther, M.; Zwick, T.; Randel, S.; Koos, C.; “Wireless THz communications using optoelectronic techniques,” *Light: Science & Applications, Light Conference (Light Conference'18), Changchun, China, July 16-18* (2018) (invited)

[C10] Koos, C.; Randel, S.; Freude, W.; Dalton, L. R.; Wolf, S.; Kieninger, C.; Kutuvantavida, Y.; Lauermann, M.; Elder, D. L.; Muehlbrandt, S.; Zwickel, H.; Melikyan, A.; **Harter, T.**; Ummethala, S.; Billah, M. R.; Blaicher, M.; Dietrich, P.-I.; Hoose, T., "Hybrid Photonic Integration and Plasmonic Devices: New Perspectives for High-Speed Communications and Ultra-Fast Signal Processing," *Pacific Rim Conference on Lasers and Electro-Optics (CLEO-PR 2018), Hong Kong, July 29 – August 3* (2018), (invited), DOI: 10.1364/CLEOPR.2018.W4J.1

[C11] **Harter, T.**; Ummethala, S.; Muehlbrandt, S.; Blaicher, M.; Koehnle, K.; Adib, M.; Weber, M.; Wolf, S.; Kutuvantavida, Y.; Kemal, J. N.; Nellen, S.; Hahn, L.; Tessmann, A.; Walther, M.; Zwick, T.; Randel, S.; Freude, W.; Koos, C., "Wireless terahertz communications using optoelectronic techniques," *Progress in Electromagnetics Research Symposium 2018 (PIERS 2018), Toyama, Japan, August 1-4* (2018), (invited)

[C12] **Harter, T.**; Fuellner, C.; Kemal, J. N.; Ummethala, S.; Brosi, J.-M.; Bruendermann, E.; Freude, W.; Randel, S.; Koos, C., "110-m THz Wireless Transmission at 100 Gbit/s Using a Kramers-Kronig Schottky Barrier Diode Receiver," *44th European Conference on Optical Communication (ECOC'18), Rome, Italy, September 23-27*, paper Th3F.7 (2018), (postdeadline), DOI: 10.1109/ECOC.2018.8535174

[C13] Ummethala, S.; **Harter, T**.; Koehnle, K.; Li, Z.; Muehlbrandt, S.; Kutuvantavida, Y.; Kemal, J. N.; Schaefer, J.; Massler, H.; Tessmann, A.; Kumar Garlapati, S.; Bacher, A.; Hahn, L.; Walther, M.; Zwick, T.; Randel, S.; Freude, W.; Koos, C., "Wireless Transmission at 0.3 THz Using Direct THz-to-Optical Conversion at the Receiver," *44th European Conference on Optical Communication (ECOC'18), Rome, Italy, September 23-27*, paper We4H.3 (2018), DOI: 10.1109/ECOC.2018.8535490

[C14] Freude, W.; **Harter, T**.; Ummethala, S.; Muehlbrandt, S.; Blaicher, M.; Wolf, S.; Weber, M.; Boes, F.; Massler, H.; Tessmann, A.; Kutuvantavida, Y.; Kemal, J. N.; Nellen, S.; Hahn, L.; Goebel, T.; Walther, M.; Zwick, T.; Randel, S.; Koos, C., “Terahertz communications meets photonics,” *14th Intern. Conf. on Fiber Optics & Photonics (Photonics'18), Indian Institute of Technology Delhi (IIT Delhi), Delhi, India, December 12–15* (2018) (invited)

[C15] Ummethala, S.; Kemal, J. N.; Lauermann, M.; Alam, A. S.; Zwickel, H.; **Harter, T**.; Kutuvantavida, Y.; Hahn, L.; Nandam, S. H.; Elder, D. L.; Dalton, L. R.; Freude, W.; Randel, S.; Koos, C., “Capacitively Coupled Silicon-Organic Hybrid Modulator for 200 Gbit/s PAM-4 Signaling,” *Conf. on Lasers and Electro-Optics (CLEO'19), San Jose (CA), USA, May 5–10*, paper JTh5B.2 (2019) (postdeadline), DOI: 10.1364/CLEO_AT.2019.JTh5B.2

[C16] Freude, W.; **Harter, T**.; Ummethala, S.; Muehlbrandt, S.; Blaicher, M.; Wolf, S.; Weber, M.; Boes, F.; Massler, H.; Tessmann, A.; Kutuvantavida, Y.; Kemal, J. N.; Nellen, S.; Hahn, L.; Globisch, B.; Walther, M.; Zwick, T.; Randel, S.; Koos, C., “Wireless terahertz communications” *Conf. on Lasers and Electro-Optics (CLEO/Europe-EQEC 2019), Munich, Germany, June 23-27* (2019)

[C17] Freude, W.; **Harter, T**.; Muehlbrandt, S.; Ummethala, S.; Nellen, S.; Hahn, L.; Randel, S.; Koos, C., “Silicon photonics for coherent terahertz generation and detection,” *21th Intern. Conf. on Transparent Optical Networks (ICTON'19), Angers, France, July 9-13* (2019) (invited)

[C18] Freude, W.; Ummethala, S.; **Harter, T**.; Koehnle, K.; Li, Z.; Muehlbrandt, S.; Kutuvantavida, Y.; Kemal, J. N.; Marin-Palomo, P.; Schaefer, J.; Tessmann, A.; Kumar Garlapati, S.; Bacher, A.; Hahn, L.; Walther, M.; Zwick, T.; Randel, S.; Koos, C., “Wireless THz-to-optical conversion with an electro-optic plasmonic modulator,” *Light: Science & Applications, Light Conference (Light Conference'19), Changchun, China, July 16-18* (2019) (invited)

[C19] **Harter, T**.; Füllner, C.; Kemal, J. N.; Ummethala, S.; Steinmann, J. L.; Brosi, M.; Hesler, J. L.; Bründermann, E.; Freude, W.; Randel, S.; Koos C., “Generalized Kramers-Kronig Receiver for 16QAM Wireless THz Transmission at 110 Gbit/s,” *45th European Conference on Optical Communication (ECOC'19), Dublin, Irland, September 22-26*, paper TH.2.C (2019) (highly scored)

[C20] Randel, S.; **Harter, T**.; Fuellner, C.; Ummethala, S.; Koos, C.; Freude, W, “Opto-Electronic Terahertz Transceivers for Wireless 5G Backhaul,” *Optical Fiber Communication Conference (OFC'20), San Diego (CA), USA, March 8-12*, paper M4I.6 (2020) (invited)

Karlsruhe Series in Photonics & Communications, Vol. 24
Edited by Profs. C. Koos, W. Freude and S. Randel

Karlsruhe Institute of Technology (KIT)
Institute of Photonics and Quantum Electronics (IPQ)
Germany

Data transmission at carrier frequencies between 0.1 THz and 1 THz could overcome the current limitations of wireless networks offering data rates beyond 100 Gbit/s at transmission distances of hundreds of meters. Widespread deployment of THz links in real systems, however, still requires a reduction of the footprint, cost, and energy consumption of the associated devices.

In this book, novel device concepts and signal processing schemes are introduced and experimentally confirmed. Advanced THz systems are demonstrated which combine electronic methods with optoelectronic and digital signal processing. Thereby, record-high data rates of 115 Gbit/s are transmitted over a distance of 110 m, while the complexity of the receiver hardware could be reduced. Moreover, a THz communication system using an optoelectronic receiver and a photonic local oscillator is shown for the first time, and a new class of devices for THz transmitters and receivers is investigated which enables a monolithic co-integration of THz components with advanced silicon photonic circuits.

About the Author

Tobias Harter was born 1987 in Villingen-Schwenningen, Germany. In 2014, he received the Master degree in Optics and Photonics from Karlsruhe Institute of Technology (KIT). In 2019, he was awarded the Dr.-Ing. (Ph.D) degree in Electrical Engineering and Information Technology of KIT. His research focuses on high-speed optoelectronic devices and signal processing techniques for wireless THz communications.

ISSN 1865-1100
ISBN 978-3-7315-1083-3

Gedruckt auf FSC-zertifiziertem Papier

ISBN 978-3-7315-1083-3
9 783731 510833 >